Modelling the Carding of Recycled Carbon Fibre



Joe Roberts
Mansfield College
University of Oxford

A thesis submitted for the degree of
Doctor of Philosophy
Michaelmas 2023

Acknowledgements

I would like to thank the following people for all their contributions in the last four years:

My academic supervisors Professor Peter Howell and Dr Hilary Ockendon for all the advice, help, guidance, and encouragement throughout my DPhil project.

My former industrial supervisor Mathilde Poulet who provided insight and support when only virtual meetings were possible, and my current industrial supervisor Mohammed Riaz who continued this support, and always made me feel welcome at Gen 2 Carbon.

All the staff at Gen 2 Carbon who made me feel welcome and were happy to help and answer any questions.

Professor Chris Breward, Professor Colin Please, and everyone involved with the InFoMM CDT, for the opportunities it has provided me with, and the continued support everyone has given me throughout my time in Oxford.

The EPSRC for funding my research.

All the friends, family, and colleagues who have supported, helped, and encouraged me, and without whom this work would not have been possible.

Abstract

Carbon fibre is a very versatile material with applications in many different industries from medical, electronics, marine, to space. The demand for carbon fibre composites is increasing yearly and therefore the amount of waste carbon fibre is rising. This waste can be recovered and turned into a material that can be used in industry. The waste carbon fibre is converted into a "nonwoven" form using a carding process. This is carried out in a carding machine, with the aim of producing a homogeneous web of aligned fibres.

A continuum model is derived for a web of carbon fibre in the carding machine. Properties such as the density and order of fibres vary through the machine. This work gives insight into the key parameters in producing a web of aligned fibres, and is the first step in making the process more efficient. The combing effect of carding teeth is then modelled at the microscale level, with focus on the force required to both comb and break different arrangements of fibres.

The breaking up of "tows" of fibres in the carding machine is also studied, by focusing on microscale and probabilistic models. The tows are modelled in 2D as two joined elasticas that are 'peeled' apart by a circular tooth. The results depend on properties such as the force and radius of the tooth, and the bending stiffness of the tows. To model the breakup of a distribution of tows, a master equation is derived for the change in tow properties in the region between two rollers. The distribution of tow size and length is studied as the material moves through several of these regions. Transition probabilities are proposed that describe tow splitting, tow breakage, and transfer between carding rollers.

Finally, an example is presented where manufactured data is used to fit the probability parameters. It is then discussed how these models could be used to improve the carding process in the future. This work was conducted at the University of Oxford, in collaboration with Gen 2 Carbon.

Contents

1 Introduction **1**

1.1 Background and Motivation 1

1.2 The Carding Process 2

1.2.1 The Carding Machine 2

1.2.2 Feedstock and Products 4

1.3 Literature Review 5

1.4 Thesis Overview 8

2 A Continuum Model for a web of Carbon Fibre **9**

2.1 Overview and Literature Review 9

2.2 Model Derivation 10

2.2.1 General Set-up 10

2.2.2 The Stress Tensor 11

2.2.3 Kinematic Condition 13

2.2.4 The Order Parameter 14

2.3 Governing Equations 15

2.4 Lubrication Model 16

2.4.1 Nondimensionalisation 16

2.4.2 Model Simplifications 19

2.5 Uniform Viscosity Model 19

2.5.1 Simplified Model 19

2.5.2 Solution in Swift-Worker Region 20

2.5.3 Results in Swift-Worker Region 22

2.5.4 Solution in Worker-Stripper Region 23

2.5.5 Results in Worker-Stripper Region 26

2.6 Full Lubrication Model 27

2.6.1 Density Model 27

2.6.1.1 Model Simplification 27

2.6.1.2 Density Model Reformulation 28
2.6.1.3 Density Model Results 31
2.6.2 Order and Density Model 34
2.6.2.1 Full Model 34
2.6.2.2 Full Model Results 34
2.7 Conclusions 39

3 A Microscale Combing Model **41**
3.1 Overview and Literature Review 41
3.2 Two Fibre Model 41
3.3 Symmetric Three-Fibre Model 47
3.4 Generalised Three-Fibre Model 50
3.5 Conclusions 54

4 Opening of Carbon Fibre Tows **56**
4.1 Background and Literature Review 56
4.2 Model Derivation 57
4.3 Model Results 63
4.4 Elastica Wrapping Model 65
4.5 Wrapping Model Results 69
4.6 Conclusions 71

5 A Probabilistic Model for Multiple Tows **73**
5.1 The Carding Machine 73
5.2 Literature Review 73
5.3 A Probabilistic Model 75
5.3.1 The Master Equation 75
5.3.2 Model results 80
5.4 A Model to Include Length 83
5.4.1 Master Equations 83
5.4.2 Results 88
5.5 A Continuous Model for Carbon Fibre Tows 95
5.5.1 Governing Equations 95
5.5.2 A Simple Model for Tow Size 97
5.5.3 Numerical Solution 99
5.5.3.1 Derivation of Numerical Scheme 99
5.5.3.2 Ignoring Length 101

5.5.3.3 Size and Length . . . 105
5.6 A Simpler Model . . . 107
5.6.1 Alternative Derivation . . . 107
5.6.2 Extension to Include Length . . . 113
5.7 Conclusions . . . 115

6 A Data Case Study **117**
6.1 Overview . . . 117
6.2 Tow Size . . . 118
6.2.1 The Model . . . 118
6.2.2 Example Distributions . . . 119
6.2.3 Fitting . . . 121
6.3 Tow Size and Length . . . 123
6.3.1 The Model . . . 123
6.3.2 Example Data . . . 125
6.3.3 Fitting . . . 126
6.4 Conclusions . . . 129

7 Discussion, Conclusions and Further Work **130**
7.1 Discussion and Conclusions . . . 130
7.2 Further Work . . . 132

A A Numerical Scheme for Method of Lines **134**

B Analysis and Numerical Solution of the Full Lubrication Model **137**

Bibliography **142**

List of Figures

1.1 Example of a Carding machine, taken from [67]. 2
1.2 Movement of a fibre through the carding machine. 3
1.3 A photo of a web of carbon fibres before carding (from Gen 2 Carbon). 4
1.4 A photo of a web of carbon fibres after carding (from Gen 2 Carbon). 4
1.5 Example photo of a collection of carbon fibre tows before carding, from Gen 2 Carbon 5
1.6 A photo of the final product produced by Gen 2 Carbon. 6

2.1 Sketches of possible arrangements of fibres for different values of the order parameter 11
2.2 A diagram of the evolution of a line element 14
2.3 Sketch of the "nip" region between the worker and the main cylinder. 17
2.4 Distribution of the density of fibres. 22
2.5 Distribution of the order parameter with different velocity ratios. . . 23
2.6 Plot of ϕ at the downstream end point. 24
2.7 Picture showing the region between the stripper and the main cylinder. 24
2.8 Picture showing the region between the stripper and the worker. . . . 25
2.9 Stream plots of the velocity field in the region between the worker and the stripper 27
2.10 Distribution of the density of fibres with different velocity ratios. . . . 33
2.11 Distribution of the order of fibres with different velocity ratios. 33
2.12 Distribution of the density of fibres with different velocity ratios for a balance between the viscosity parameters. 36
2.13 Distribution of the order of fibres with different velocity ratios for a balance between the viscosity parameters. 37
2.14 Distribution of the density of fibres with different velocity ratios when isotropic components of the viscosity dominate. 37
2.15 Distribution of the order of fibres with different velocity ratios when isotropic components of the viscosity dominate. 38

2.16 Distribution of the density of fibres with different velocity ratios when anisotropic components of the viscosity dominate. 38
2.17 Distribution of the order of fibres with different velocity ratios when anisotropic components of the viscosity dominate. 39

3.1 Schematic of a pin being dragged downwards to comb two overlapping fibres. 42
3.2 Force diagram of the pin being pushed with force F. 43
3.3 Diagram of the forces on fibre 1. 45
3.4 The angle θ as the tooth is moved through the fibres at a constant speed against time. 46
3.5 The tension, T_2, in the fibre as the tooth is moved through the fibres at a constant speed, against time. 46
3.6 The force required to move the tooth through the fibres at a constant speed, against time. 47
3.7 Schematic of a pin being dragged downwards to comb three overlapping fibres that interact at crossing points (a), (b), and (c). 48
3.8 The force and tension against time for the 3-fibre model. 49
3.9 The area of triangle (a)-(b)-(c) against time. 50
3.10 Schematic of a pin being dragged downwards to comb three overlapping fibres. 51
3.11 Frictional forces acting on the third nonhorizontal fibre. 52
3.12 The area of triangle (a)-(b)-(c), the angle, α, and $\pi/2 - \theta$, against time. 53
3.13 The system of 3 fibres at different times. 54

4.1 Photo of a collection of carbon fibre tows before carding, from Gen 2 Carbon 57
4.2 A photo of the final product, from Gen 2 Carbon 58
4.3 A tow modelled as two elasticas 58
4.4 Values of the contact angle and coefficient of friction that satisfy the inequality 61
4.5 Plot of the contact angle against dimensionless tension for different values of μ 62
4.6 The critical values of dimensionless tension and the contact angle . . 63
4.7 Solutions for the elastica shapes 64
4.8 The dimensionless curvature at $s = 0$ against dimensionless tension . 64
4.9 Plots of the dimensionless parameter T^* against a^* 65

4.10 Schematic of an elastica in contact with a tooth 66
4.11 The contact angles against dimensionless tension 69
4.12 Solution for the shape of the elastica, with a contact region along the tooth 70
4.13 The dimensionless curvature at $s = 0$ against dimensionless tension for both the single contact point and elastica wrapping models 71
4.14 The dimensionless parameter T^* against a^* for both the single contact point and elastica wrapping models 71

5.1 Example of a Carding machine 74
5.2 Two distributions of tows along two rollers entering and leaving a nip region in the carding machine 75
5.3 Schematic diagrams of example tows splitting into two daughter tows 76
5.4 Diagram of the probabilistic model for the size of carbon fibre tows . 77
5.5 The tow distributions on the swift and another roller meeting it. . . . 79
5.6 The probability distributions on the swift and 2 worker-stripper pairs (represented by one roller for each pair). 80
5.7 Plots of distribution $s_m(n)$ and volume density at successive positions 81
5.8 Plots of the distribution after the fifth top roller for different parameter values 82
5.9 Schematic diagrams of example tows splitting and breaking into two daughter tows 84
5.10 Diagram showing the probabilistic model for the size and length of carbon fibre tows 85
5.11 Plots of distribution $s_m(n, l)$ at successive positions 90
5.12 Plots of distribution $s_6(n, l)$ for different α_w and α_s 91
5.13 Plots of distribution $s_6(n, l)$ for different β_s 91
5.14 Plots of distribution $s_6(n, l)$ for different β_w 92
5.15 Plots of distribution $s_6(n, l)$ for different γ 92
5.16 Plots of distributions $s_4(n, l)$ and $s_6(n, l)$ for different critical sizes . . 94
5.17 Plots of continuous distribution, $s_m(x)$, and volume density, $xs_m(x)$. 98
5.18 Plots of the absolute error in $s_m(x)$ between the continuous and discrete models 99
5.19 Plot of the maximum absolute error in $s_m(x)$ against $1/N$ 100
5.20 Plots of the absolute error in the distribution $s_m(b_n)$ using the new discretization against b_n for different numbers of bins 103

5.21 Plot of the maximum absolute error in the distribution, $s_6(1)$, against $1/B^2$ using the new discretization 103
5.22 Plots of the absolute error in the distribution $s_m(b_n)$ using the new discretization against b_n for different values of n_c. 104
5.23 Plot of the maximum absolute error in the distribution, $s_6(1)$, using the new discretization against n_c for different values of B 104
5.24 Plots of the distribution $s_m(b_n, b_l)$ using the new discretization against b_n and b_l for different number of bins, B. 105
5.25 Plots of the absolute error in the distribution $s_m(b_n, b_l)$ using the new discretization against b_n and b_l for different numbers of bins 106
5.26 Plot of the maximum absolute error in the distribution, $s_6(b_n, b_l)$, using the new discretization for different numbers of bins 106
5.27 Plot of the computation time versus number of bins. 107
5.28 The probability distributions on the swift and a worker-stripper pair. 108
5.30 Plots of distribution $s_m(n)$ at successive positions for different values of α_s 110
5.31 Plots of volume density $ns_m(n)/N$ at successive positions for different values of α_s 111
5.32 Plots of final distribution and volume density from equations (5.6.1) and (5.6.3) 112
5.34 Plots of distribution $s_m(n, l)$ at successive positions using the new formulation 115

6.1 Plots of the example data for the initial distribution 120
6.2 Plots of tow size distribution for both example initial distributions . . 120
6.3 Plots of the manufactured data for the final distribution 121
6.4 The final data and fitted solutions 122
6.5 Final distributions for examples 1 and 2 for the fitted and original parameters for different velocity ratios 122
6.6 Manufactured initial and final data for the distribution of tows 125
6.7 Final distribution for the parameters from (6.3.8) 126
6.8 Absolute error in the final distribution for the parameters from (6.3.8) compared to the original chosen parameters 127
6.9 Final distributions for different velocity ratios 128

Chapter 1

Introduction

1.1 Background and Motivation

In recent years the demand for carbon fibre has increased, mainly due to the wide variety of potential industrial applications, including the use of carbon fibre-reinforced materials in the aerospace, automotive, and defence industries [30, 45]. Carbon fibre has a number of advantageous properties that make it suitable for this wide range of applications, for example a very high tensile strength and low density [32]. The current high demand, and predicted high demand in the future, mean that the amount of waste carbon fibre is increasing. This project was carried out alongside Gen 2 Carbon, a company that focuses on recovering carbon fibre waste from the aerospace industry and turning it into non-woven materials that can be used in other industries, primarily the automotive and electronic industries.

The processing of waste carbon fibre involves multiple stages. First the material is pyrolysed, to remove all components other than carbon fibre from the composite material. The next stage is the carding of these fibres, a mechanical process that separates and then intermixes fibres by passing them through a "carding machine". This process produces a homogeneous web of carbon fibres that can then be impregnated with a resin, resulting in a fibre-reinforced composite material that can be used in the industries discussed above.

In this thesis we focus on modelling the movement of fibres through the carding machine, providing an alternative to time consuming practical experiments. This approach will allow us to examine how the properties of the carding machine can be varied to efficiently produce a quasi-isotropic web of fibres. We will use modelling at both the macroscopic and microscopic levels to gain understanding of the process as well as providing models that can be used to optimise the machine settings. The models presented in this thesis are informed by both the literature and discussions

with Gen 2 Carbon. We were able to see the machines running, though it proved difficult to gain any quantitative data so it has not yet been possible to validate our models using real experimental data. We start by examining the setup of the carding machine, giving some background to the problem, before reviewing existing and relevant work in this field.

1.2 The Carding Process

1.2.1 The Carding Machine

Carding machines are widely used in the textile industry, and consist of a set of interlocking toothed rollers of different sizes, moving at different velocities (see figure 1.1). The fibres are fed onto the carding machine by a rotating feed sheet and then a pass along a number of rotating cylinders, such as the "feedrollers" and "lickerin". They then move onto the main cylinder, or "swift". They travel around this main cylinder, which has several pairs of cylinders along its edge. The two cylinders in each pair are called the "worker" and the "stripper". In reality there are multiple worker-stripper pairs, but for simplicity only a single pair is shown in figure 1.1. After the fibres have travelled along the main cylinder, passing through each worker/stripper pair, they are then taken off by the "fancy" and the "doffer" cylinders. The orientation of the teeth along each roller can also be seen in figure 1.1. The teeth play an important role in combing the web of carbon fibres and will be discussed in more detail in chapters 3 and 4.

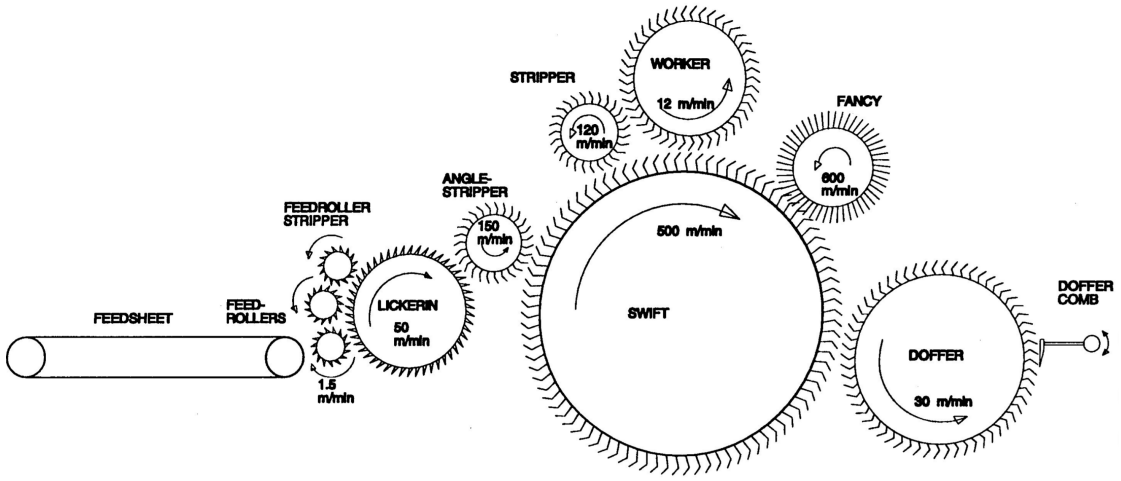


Figure 1.1: Example of a Carding machine, taken from [67].

In this thesis we focus on the carbon fibres moving through the regions between the workers, strippers, and swift, where the majority of the carding action takes place (although many of the models presented in this thesis could also be applied to other parts of the machine). The main cylinder, along with one worker-stripper pair, is shown in figure 1.2. The numbers (1)-(7) show the order in which a typical fibre moves through this part of a carding machine. However, in the thin region between any two cylinders, the fibres have the possibility of joining either cylinder. This means a fibre can move straight through this region of the machine or go around the worker and stripper several times. We use this behaviour to motivate the derivation of a probabilistic model in chapter 5. We can also see the relative sizes and directions of rotation of the three cylinders in figure 1.2. The typical orders of magnitude for some relevant parameters are shown in table 1.1; these parameters have important effects on the quality of the final product, which we aim to predict and understand.

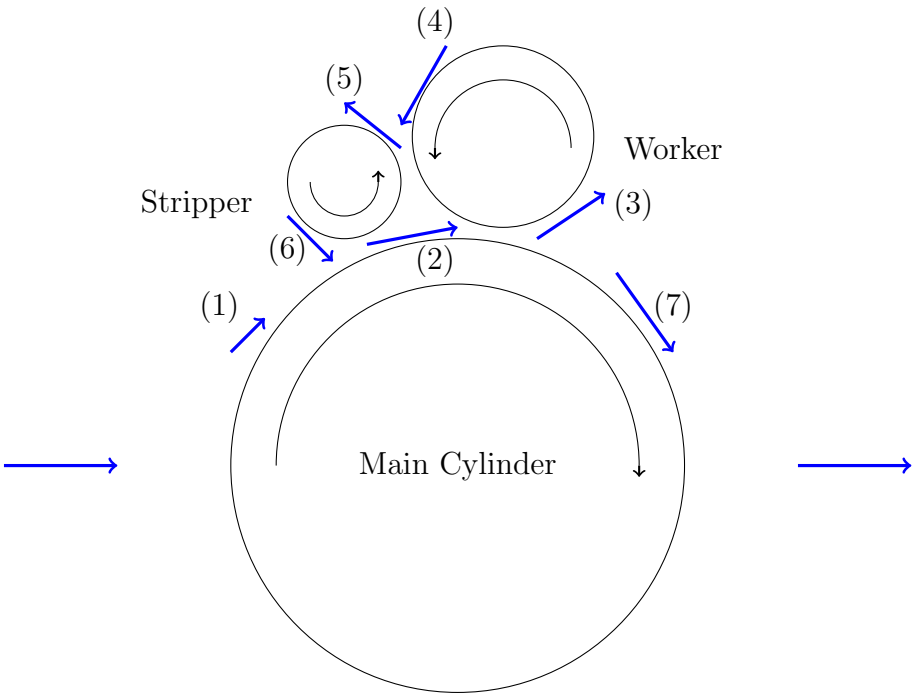


Figure 1.2: Movement of a fibre (shown in blue) through the carding machine, only showing one worker-stripper pair. The path of a typical fibre is shown by numbers (1)-(7).

Parameter	Swift (Main Cylinder)	Worker	Stripper
Surface velocity (m/s)	10-30	0.01-0.1	0.1-1
Radius (m)	1	0.1	0.01
Tooth density (teeth per inch)	1	1	1

Table 1.1: Table showing typical parameter values for the different cylinders.

Observations suggest that most of the carding action (intermixing of fibres and forming of a homogeneous web) takes place in the region between the main cylinder and the worker. The purpose of the stripper is then to transfer fibres from the worker back onto the swift.

1.2.2 Feedstock and Products

To appreciate the action of the carding machine, we now discuss the different forms of carbon fibre that are fed onto the machine. An example of the evolution of a web of carbon fibre is shown in figures 1.3 and 1.4. We can see that the initially disordered web has been homogenised and aligned by the carding machine. Throughout this thesis we refer to the fibres fed onto the machine (figure 1.3) as feedstock and the fibres leaving the machine (figure 1.4) as the product.



Figure 1.3: A photo of a web of carbon fibres before carding (from Gen 2 Carbon).



Figure 1.4: A photo of a web of carbon fibres after carding (from Gen 2 Carbon).



Figure 1.5: Example photo of a collection of carbon fibre tows before carding, from Gen 2 Carbon.

One particular form of feedstock that we focus on in the second half of the thesis is "tows" of fibres. A carbon fibre tow is a clump of typically thousands of individual fibre filaments, as shown in figure 1.5. We note that these tows need to be broken up in the machine to form a homogeneous, aligned web of fibres that, after more stages such as folding and needling, becomes the product, as shown in figure 1.6. The aligning of the fibres in the machine is an important part of the carding process, and in chapter 2 we introduce an 'order' parameter to quantify this.

1.3 Literature Review

A number of mathematical models for carding machines and the carding process already exist, mainly focused on applications in the processing of textile materials such as wool and cotton. The continuum model of Lee and Ockendon [38] forms the basis of our study in chapter 2. In this work a continuum model for a web of fibres moving through a revolving flats carding machine is derived and analysed. We will discuss what changes we can make to this model when considering the process shown in figure 1.2 for carbon fibres. For example, carbon fibres are naturally straight and so they do not entangle with each other to the same extent as typical fibres in the



Figure 1.6: A photo of the final product produced by Gen 2 Carbon.

textile industry.

A model for a single fibre moving through the carding machine is discussed in the thesis of Lee [37] and the paper of Lee and Ockendon [39]. This model focuses on the transfer of a fibre from one part of the carding machine to the next, with particular reference to the aerodynamic forces present in different regions of the carding machine. We will discuss similar ideas in chapter 5 when we focus on the transfer process. The thesis [37] goes on to discuss a model for the action of a tooth withdrawing an individual fibre from a web of fibres. The teeth along the surfaces of the cylinders play an important role in the performance of a carding machine, and we will consider them in detail in chapters 3 and 4.

Other approaches to the mathematical modelling of the carding machine include that of Rust and Gutierrez [49], in which each cylinder is characterized by its "collecting power". This collecting power represents the ability of a cylinder to remove a fibre from of the main cylinder [49], and can therefore be used to predict the journey of a fibre through a carding machine. The paper goes on to consider the relative velocities of the cylinders, transfer of fibres, and comparison with experimental results.

Cherkassky [10] discusses the need for a two-dimensional model for carding. This model considers transfer of fibres in both the longitudinal and transverse directions, where there is deterministic transfer in the longitudinal direction, and random transfer

in the transverse. It is stated here that the dominant process for the longitudinal transport of fibres is the transfer of fibres along the surface of the main cylinder, which can be seen in figure 1.2.

Models for the carding process are derived in the thesis of Wibberly [65], motivated by the use of carding in the textile industry. The models focus on the movement of fibre mass through the machine, including descriptions of transfer between card rollers and air flow in the regions between these rollers [66]. The models of Wibberly [65] are then used to examine the dynamics of individual fibres. We consider a similar carding machine in this thesis, and focus on the behaviour of fibre webs and tows in the machine.

An important process to consider when examining the efficiency of a carding machine is fibre breakage. A high frequency of breakage will result in a low efficiency of the carding machine and lower quality of the final product. Fibre breakage is modelled by Carnaby [8] through examining the distribution of fibre lengths of wool fibres in a carding machine, and the forces on a fibre being withdrawn by a tooth. The model is evaluated by Wood, Stanley-Boden, and Carnaby [68], who go on to fit the model parameters using published data, obtaining predictions of the fibre length distribution in good agreement with experimental evidence.

Komori and Makishima [34,35] use the method of geometric probability to present a relationship between the distribution of orientation and the number density of fibre cross-sections in fibre assemblies. These papers are used in the model of Lee and Ockendon [38] to estimate that the number of contact points between fibres in a randomly orientated web is proportional to the square of the density. The orientation of fibres is an important property of the web and is studied in chapter 2.

There are also a number of experimental studies that focus on carbon fibres, such as [69], which examines fibre alignment and its effect on the mechanical properties of recycled carbon fibre composites. The study [22] highlights the importance of recycling carbon fibre, due to high demand, and one of their key findings is that fibres of longer length result in greater fibre orientation, and therefore a higher quality product. The experimental work of Jlassi, Berthet, and Bernhart [29] also suggests that fibre length is a key influence on the mechanical properties of carbon fibre-reinforced polymer composites. Fibre length is therefore an important property that we will consider in this thesis.

1.4 Thesis Overview

The work presented in thesis was carried out alongside Gen 2 Carbon, a company based in the West Midlands whose focus is on taking waste carbon fibre from different industries and recycling it so it can be used again. Discussions between academics at the University of Oxford and employees at Gen 2 Carbon, along with the literature review presented above, revealed two key processes that take place in the carding machine; the aligning of carbon fibres, and the breaking up of fibrous tows. The focus of this work was therefore to model these two processes in the carding machine.

In chapters 2 and 3 we focus on the aligning of a web of fibres in the carding machine. We use the model of Lee and Ockendon [38] as a starting point for our model in chapter 2, which we adapt to describe carbon fibres instead of textiles fibres, and the geometry of our particular carding machine. This model is used to examine how different parameters affect the ordering and aligning of fibres through different sections of the carding machine. In chapter 3 we present microscale models for the interaction between a tooth and individual fibres, revealing insights into how the 'combing' action of the teeth contributes towards the processes of aligning and breaking fibres.

In chapters 4 and 5 we focus in detail on the breakup of fibre tows in the carding machine. Our first approach is to model an individual tow as two joined elasticas, with a tooth being pulled through. We discuss how we can quantify the breakup, or 'opening', of a tow, and what physical processes are important in this action. In chapter 5 we present a probabilistic model for a distribution of tows moving through the carding machine, deriving a tool that can be used to predict the final distribution of tow sizes given the initial distribution. In chapter 6 we give an example of how this probabilistic model could be used in combination with experimental data to inform the carding machine control parameters in the future. Finally, in chapter 7 we draw our conclusions and discuss future work that would extend our models.

Chapter 2

A Continuum Model for a web of Carbon Fibre

2.1 Overview and Literature Review

In this chapter we derive and solve a continuum model for a web of carbon fibres moving through different regions of the carding machine. We adapt the existing model of Lee and Ockendon [38] to reflect the properties of carbon fibre. In the model of Lee and Ockendon [38], equations are derived using conservation of mass and momentum, a constitutive law for the order of fibres, and equations for the evolution of entanglement and mean direction of fibres. The web is moving through a region between two flat, rigid boundaries, and subjected to a shear force, and analytical solutions are presented to a one-dimensional model.

The model we derive in this chapter is similar to many models found in the areas of continuum mechanics and liquid crystals, with some key differences. For example, the form of our constitutive relation for the stresses comes from the theory of anisotropic viscous fluids. Spencer [53] shows that, for a fluid with a director, and a linear stress-rate-of-strain relation, the stress tensor must be of the form we use. Spencer [54] uses the resulting ideas to study a fibre-reinforced fluid. The model is similar to the one we use, with the difference that Spencer models the fluid as incompressible, whereas a web of fibres is not. A similar continuum model for a fibre-reinforced fluid is applied to flow when the fluid is squeezed between two rigid plates by Rogers [47], again assuming incompressibility and fibre-inextensibility. Green and Friedman [16] consider extensional flow of an incompressible, transversely isotropic viscous fluid in 2D. A thin-film approximation is made to find a leading order solution, and the results suggest that the fibres align in the direction of extension, provided the tension and extensional viscosity are sufficiently small. Similar models can be found in

biological applications, such as the model by Holloway, Smith, and Dyson [23], which is motivated by the change in fluid rheology caused by the presence of suspended fibres in DNA and synthetic biological nanofibres, and the study of Dyson and Jensen [13] who model oriented cellulose microfibrils in plant cell walls as extensible fibres.

We also use ideas from the theory of liquid crystals. For example, we use an order parameter to quantify the alignment of fibres, as in Lee and Ockendon [38]. This order parameter is commonly used in relation to liquid crystals, and is taken from the work of de Gennes and Prost [15]. Ericksen also discusses liquid crystals with a variable degree of orientation [14]. Flow of nematic liquid crystals with variable degree of orientation is studied, for example, in [7, 9]. In particular, [7] presents a similar form of the stress tensor to ours, and then discusses constraints on the relevant viscosity coefficients.

We derive a continuum model for a web of carbon fibres in sections 2.2-2.3, and discuss how we exploit the geometry of the swift-worker region of the carding machine in section 2.4. We then present analytical and numerical solutions to the model in sections 2.5 and 2.6 respectively. We make a number of simplifying assumptions so that we can solve the model analytically in section 2.5, and discuss the full model in section 2.6.

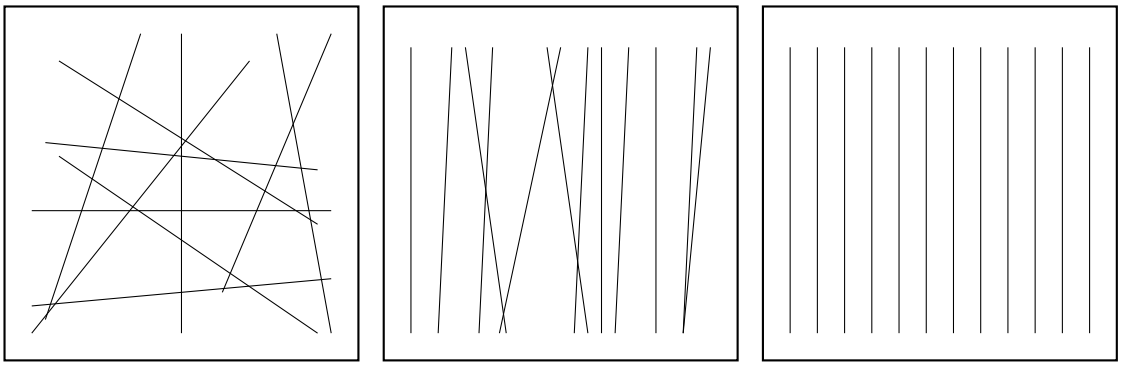
2.2 Model Derivation

2.2.1 General Set-up

We model a web of carbon fibres using a continuum approach, as in [38], through making a few important changes to this model. We begin by considering dependence on three spatial variables, (x, y, z), with the average velocity of the fibres represented by $\boldsymbol{u} = (u(x, y, z, t), v(x, y, z, t), w(x, y, z, t))$. Later we will reduce the model to two dimensions as it can be shown that the average motion is in two dimensions. The remaining important dependent variables in the model of Lee and Ockendon [38] are the density of the web, ρ, order parameter, ϕ, director, $\boldsymbol{a}$, and entanglement, κ. Since we are considering the carding of carbon fibres, which are naturally straight, we will neglect the effect of entanglement. The director, $\boldsymbol{a}$, is defined as the unit vector representing the mean fibre direction at each point.

We will use the same order parameter as adopted by Lee and Ockendon [38], which is taken from the theory of liquid crystals [15] and defined by

$$\phi(\boldsymbol{x}, t) = \int_S \left(\frac{3\cos^2\Theta - 1}{2} \right) \psi(\boldsymbol{x}, t, \Theta) dS, \tag{2.2.1}$$



(a) $\phi \approx 0$ (b) $0 < \phi < 1$ (c) $\phi = 1$

Figure 2.1: Sketches of possible arrangements of fibres for different values of the order parameter, ϕ.

where ψ is the probability density function that a fibre at position $\boldsymbol{x}$ and time t makes an angle Θ with the director, $\boldsymbol{a}$, and S represents the unit sphere in 3D. We can see from this definition that, if $\phi = 1$ then all the fibres are perfectly aligned, and if $\phi = 0$ then the fibre orientations are randomly distributed, as illustrated in figure 2.1. Other methods have been used to characterize the order of fibres. For example, Khurshid, Abdkader and Cherif [30, 31] use the orientation index, which is defined as

$$\text{Orientation Index} = \left(1 - \frac{E}{N}\right) \times 100, \tag{2.2.2}$$

where E is the "weight" of the extended part of fibres, and N is the "weight" of the remaining fibres.

Provided inertia is negligible, conservation of mass and linear momentum lead to the equations

$$\frac{\partial \rho}{\partial t} + \frac{\partial}{\partial x}(\rho u) + \frac{\partial}{\partial y}(\rho v) + \frac{\partial}{\partial z}(\rho w) = 0, \tag{2.2.3a}$$

$$F_i + \frac{\partial \sigma_{ik}}{\partial x_k} = 0, \tag{2.2.3b}$$

using index notation, where F_i represents body forces, and σ_{ij} is the stress tensor.

2.2.2 The Stress Tensor

Following [37,38], we propose a constitutive relation for σ_{ij} with contributions from an isotropic stress when fibres are randomly aligned, σ^I, and non-isotropic components caused by the directionality of the fibres, σ^N. The stress tensor should depend on the

number of contact points between the fibres per unit volume, which was shown by Komori and Makishima [34] to be proportional to the square of the density of fibres. We therefore propose the relation

$$\sigma_{\alpha\beta} = \rho^2 \left[(1-\phi)\sigma^I_{\alpha\beta} + \phi\sigma^N_{\alpha\beta} \right]. \tag{2.2.4}$$

We assume that the stress tensor is linearly dependent on the rate-of-strain, so the isotropic stress is written as

$$\sigma^I_{\alpha\beta} = \mu_1 e_{\alpha\beta} + \mu_2 e_{kk}\delta_{\alpha\beta}, \tag{2.2.5}$$

where

$$e_{ij} = \frac{1}{2}\left(\frac{\partial u_i}{\partial x_j} + \frac{\partial u_j}{\partial x_i} \right), \tag{2.2.6}$$

is the rate-of-strain tensor, and μ_1, μ_2 are isotropic viscosity coefficients.

In what follows we derive the form of the transversely isotropic stress tensor, σ^N, by following the methods described in [24] and [37]. We assume a linear relation between the stress, σ_{ij}, and rate-of-strain, e_{ij}, given by

$$\sigma_{ij} = B_{ijkl} e_{kl}, \tag{2.2.7}$$

where B_{ijkl} is a fourth order tensor. Since both stress and rate-of-strain are symmetric we have

$$B_{ijkl} = B_{jikl} = B_{ijlk} = B_{jilk}. \tag{2.2.8}$$

Next, we consider a rotation by an orthogonal matrix $\boldsymbol{P}$, represented by

$$\sigma'_{ij} = B'_{ijkl} e'_{kl}, \quad B'_{ijkl} = P_{im}P_{jn}P_{kr}P_{ls}B_{mnrs}. \tag{2.2.9}$$

The relationship between $\boldsymbol{\sigma'}$ and $\boldsymbol{e'}$ must be the same as that between $\boldsymbol{\sigma}$ and $\boldsymbol{e}$ for each $\boldsymbol{P}$ representing a material symmetry [24]. It follows that, for every such $\boldsymbol{P}$,

$$B_{ijkl} = P_{im}P_{jn}P_{kr}P_{ls}B_{mnrs}. \tag{2.2.10}$$

We consider a material with a single preferred direction, which for now is identified with the $z-$axis. We therefore require that (2.2.10) is satisfied with the family of orthogonal transformations

$$\boldsymbol{P} = \begin{pmatrix} \cos\theta & \sin\theta & 0 \\ -\sin\theta & \cos\theta & 0 \\ 0 & 0 & 1 \end{pmatrix}. \tag{2.2.11}$$

It follows that the tensor $\boldsymbol{B}$ can be expressed in terms of just five viscosity coefficients λ_k, viz.

$$\begin{aligned}
&B_{1111} = B_{2222} = \lambda_1 + \lambda_2,\ B_{1122} = B_{2211} = \lambda_2,\\
&B_{1133} = B_{2233} = B_{3311} = B_{3322} = \lambda_2 + \lambda_4,\ B_{1313} = B_{2323} = \lambda_1 + \frac{\lambda_3}{2},\\
&B_{3333} = \lambda_1 + \lambda_2 + 2\lambda_3 + 2\lambda_4 + \lambda_5,\ B_{1212} = \lambda_1,
\end{aligned} \tag{2.2.12}$$

which may be summarised as

$$\begin{aligned}
B_{ijkl} =&\lambda_1\delta_{ik}\delta_{jl} + \lambda_2\delta_{ij}\delta_{kl} + \lambda_3\left(\frac{\delta_{j3}\delta_{k3}\delta_{il} + \delta_{i3}\delta_{l3}\delta_{jk} + \delta_{i3}\delta_{k3}\delta_{jl} + \delta_{j3}\delta_{l3}\delta_{ik}}{2}\right)\\
&+ \lambda_4\left(\delta_{i3}\delta_{j3}\delta_{kl} + \delta_{ij}\delta_{k3}\delta_{l3}\right) + \lambda_5\delta_{i3}\delta_{j3}\delta_{k3}\delta_{l3}.
\end{aligned} \tag{2.2.13}$$

Now, following Lee [37], to generalise (2.2.13) for a general director $\boldsymbol{a}$ we rotate the vector $(0, 0, 1)$ using an orthogonal matrix, t_{ij}, such that $a_i = t_{i3}$, resulting in

$$\sigma'_{\alpha\beta} = t_{\alpha i}t_{\beta j}t_{rk}t_{sl}B_{ijkl}e'_{rs}. \tag{2.2.14}$$

The first term in (2.2.13) thus becomes

$$t_{\alpha i}t_{\beta j}t_{rk}t_{sl}\lambda_1\delta_{ik}\delta_{jl}e'_{rs} = \lambda_1\delta_{\alpha r}\delta_{\beta s}e'_{rs} = \lambda_1 e'_{\alpha\beta}. \tag{2.2.15}$$

Following a similar method for the remaining four terms in (2.2.13) leads to the transversly isotropic linear constitutive relation

$$\begin{aligned}
\sigma^N_{\alpha\beta} =&\lambda_1 e_{\alpha\beta} + \lambda_2 e_{kk}\delta_{\alpha\beta} + \lambda_3(a_\alpha a_i e_{\beta i} + a_\beta a_i e_{i\alpha})\\
&+ \lambda_4(a_\alpha a_\beta e_{kk} + \delta_{\alpha\beta}a_k a_l e_{kl}) + \lambda_5 a_\alpha a_\beta a_k a_l e_{kl},
\end{aligned} \tag{2.2.16}$$

where we have dropped the $'$s. Equation (2.2.16) is the tensor that we use in the model.

2.2.3 Kinematic Condition

We continue to follow Lee [37] to derive a governing equation for the director, $\boldsymbol{a}$, using kinematics. We consider an infinitesimal line element given by $s(t)\boldsymbol{a}(t)$ at time t which is convected by a velocity field $\boldsymbol{u}$, as shown in figure 2.2. By Taylor expansion, a small time δt later the element is convected to

$$s\left(t+\delta t\right)\boldsymbol{a}\left(t+\delta t\right) \sim s\left(t\right)\boldsymbol{a}\left(t\right) + s\delta t\left(\boldsymbol{a}\cdot\boldsymbol{\nabla}\right)\boldsymbol{u} + O\left(s^2, \delta t^2\right). \tag{2.2.17}$$

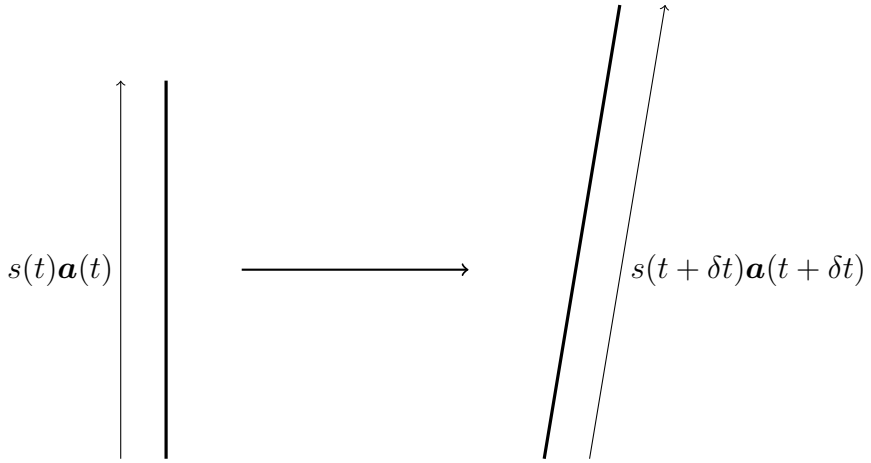


Figure 2.2: A diagram of the evolution of a line element, $s(t)\boldsymbol{a}(t)$, with director, $\boldsymbol{a}(t)$, as presented in Lee [37].

Taking the limit $\delta t \to 0$ leads to

$$\frac{\mathrm{d}}{\mathrm{d}t}\left(s\boldsymbol{a}\right) = s\left(\boldsymbol{a}\cdot\boldsymbol{\nabla}\right)\boldsymbol{u}, \tag{2.2.18}$$

which we write as

$$\frac{\partial \boldsymbol{a}}{\partial t} + \left(\boldsymbol{u}\cdot\boldsymbol{\nabla}\right)\boldsymbol{a} + \frac{1}{s}\frac{\mathrm{d}s}{\mathrm{d}t}\boldsymbol{a} = \left(\boldsymbol{a}\cdot\boldsymbol{\nabla}\right)\boldsymbol{u}. \tag{2.2.19}$$

The term $(1/s)\mathrm{d}s/\mathrm{d}t$ represents the rate of extension of the material element. Although we assume that individual fibres are inextensible, this term describes fibres slipping over one another, leading to a macroscopic extensibility, as discussed by Lee [37]. We now restrict $\boldsymbol{a}$ to be a unit vector, and thus $a_k a_k = 1$. The apparent extension rate is thus given by

$$\frac{\dot{s}}{s} = \boldsymbol{a}\cdot\left[\left(\boldsymbol{a}\cdot\boldsymbol{\nabla}\right)\boldsymbol{u}\right], \tag{2.2.20}$$

allowing us to eliminate s and write equation (2.2.19) as

$$\frac{\partial a_i}{\partial t} + u_k\frac{\partial a_i}{\partial x_k} + a_k a_l\frac{\partial u_k}{\partial x_l}a_i = a_k\frac{\partial u_i}{\partial x_k}. \tag{2.2.21}$$

This is the governing equation for the director, $\boldsymbol{a}$.

2.2.4 The Order Parameter

We assume that the evolution of the order parameter, ϕ, is proportional to the rate-of-extension of a material element [37, 38]. To respect the constraint that $0 < \phi < 1$, Lee [37] proposes the model

$$\frac{\partial \phi}{\partial t} + \left(\boldsymbol{u}\cdot\boldsymbol{\nabla}\right)\phi = \beta\left(1-\phi\right)\frac{1}{s}\frac{\mathrm{d}s}{\mathrm{d}t}, \tag{2.2.22}$$

where $\beta > 0$ is a material constant. Equation (2.2.22) implies that if the web of fibres is under compression in the fibre direction, the order will decrease. This is not physically realistic, as it would result in no net change ordering of the material when the web is first compressed and then stretched. We therefore modify (2.2.22) to make the ordering process irreversible. After using (2.2.20) to eliminate s, we arrive at the evolution equation

$$\frac{\partial \phi}{\partial t} + u_k \frac{\partial \phi}{\partial x_k} = \left[\beta(1-\phi) a_k a_l \frac{\partial u_k}{\partial x_l} \right]^+ . \tag{2.2.23}$$

Equation (2.2.23) states that the order of the web only increases when the web is stretched.

2.3 Governing Equations

Combining the equations derived in sections 2.2.2-2.2.4, we have the mass- and momentum-conservation equations in the form

$$\frac{\partial \rho}{\partial t} + \frac{\partial}{\partial x}(\rho u) + \frac{\partial}{\partial y}(\rho v) + \frac{\partial}{\partial z}(\rho w) = 0, \tag{2.3.1a}$$

$$F_i + \frac{\partial \sigma_{ik}}{\partial x_k} = 0, \tag{2.3.1b}$$

$$\sigma_{\alpha\beta} = (1-\phi)\sigma^I_{\alpha\beta} + \phi \sigma^N_{\alpha\beta}, \tag{2.3.1c}$$

$$\sigma^I_{\alpha\beta} = \rho^2 \left(\mu_1 e_{\alpha\beta} + \mu_2 e_{kk} \delta_{\alpha\beta} \right), \tag{2.3.1d}$$

$$\begin{aligned} \sigma^N_{\alpha\beta} = \rho^2 \Big(& \lambda_1 e_{\alpha\beta} + \lambda_2 e_{kk} \delta_{\alpha\beta} + \lambda_3 (a_\alpha a_i e_{\beta i} + a_\beta a_i e_{i\alpha}) \\ & + \lambda_4 (a_\alpha a_\beta e_{kk} + \delta_{\alpha\beta} a_k a_l e_{kl}) + \lambda_5 a_\alpha a_\beta a_k a_i e_{kl} \Big), \end{aligned} \tag{2.3.1e}$$

where we have redefined $\sigma^I_{\alpha\beta}$ and $\sigma^N_{\alpha\beta}$ to include the dependence on ρ^2. In general, we can write the director in terms of two Euler angles (θ, α) as

$$\boldsymbol{a} = (\cos\alpha \cos\theta, \cos\alpha \sin\theta, \sin\alpha) . \tag{2.3.2}$$

This substitution allows us to write the order evolution equation (2.2.23) as

$$\begin{aligned} & \frac{\partial \phi}{\partial t} + u\frac{\partial \phi}{\partial x} + v\frac{\partial \phi}{\partial y} + w\frac{\partial \phi}{\partial z} \\ & \quad = \beta(1-\phi) \Bigg[\cos^2\alpha \left(\cos^2\theta \frac{\partial u}{\partial x} + \sin^2\theta \frac{\partial v}{\partial y} + \sin\theta\cos\theta \left(\frac{\partial u}{\partial y} + \frac{\partial v}{\partial x} \right) \right) \\ & \qquad + \sin\alpha\cos\alpha \left(\cos\theta \left(\frac{\partial u}{\partial z} + \frac{\partial w}{\partial x} \right) + \sin\theta \left(\frac{\partial v}{\partial z} + \frac{\partial w}{\partial y} \right) \right) \\ & \qquad + \sin^2\alpha \frac{\partial w}{\partial z} \Bigg]^+ , \end{aligned} \tag{2.3.3}$$

and the kinematic equation (2.2.21) leads to

$$\frac{\partial\theta}{\partial t}+u\frac{\partial\theta}{\partial x}+v\frac{\partial\theta}{\partial y}+w\frac{\partial\theta}{\partial z}=\sin\theta\cos\theta\left(\frac{\partial v}{\partial y}-\frac{\partial u}{\partial x}\right)+\cos^2\theta\frac{\partial v}{\partial x}-\sin^2\theta\frac{\partial u}{\partial y}+\tan\alpha\left(\cos\theta\frac{\partial v}{\partial z}-\sin\theta\frac{\partial u}{\partial z}\right), \tag{2.3.4a}$$

$$\frac{\partial\alpha}{\partial t}+u\frac{\partial\alpha}{\partial x}+v\frac{\partial\alpha}{\partial y}+w\frac{\partial\alpha}{\partial z}=-\cos\alpha\sin\alpha\left(\cos^2\theta\frac{\partial u}{\partial x}+\cos\theta\sin\theta\left(\frac{\partial u}{\partial y}+\frac{\partial v}{\partial x}\right)+\sin^2\theta\frac{\partial v}{\partial y}\right)-\sin^2\alpha\left(\cos\theta\frac{\partial u}{\partial z}+\sin\theta\frac{\partial v}{\partial z}\right)+\cos\alpha\left(\cos\alpha\cos\theta\frac{\partial w}{\partial x}+\cos\alpha\sin\theta\frac{\partial w}{\partial y}+\sin\alpha\frac{\partial w}{\partial z}\right). \tag{2.3.4b}$$

We then calculate the stresses by substituting (2.3.2) into equations (2.3.1c), (2.3.1d), and (2.3.1e). In the next section we will simplify the model by examining a particular region of the carding machine and using the geometry to make a lubrication-type approximation.

2.4 Lubrication Model

2.4.1 Nondimensionalisation

In this section we will apply the above model, (2.3.1)-(2.3.4), to the regions between two cylinders. We have identified three important cylinders, the swift (or main cylinder), the worker, and the stripper. Initially, we will consider the region between the main cylinder and the worker, shown schematically in figure 2.3. We can see from figure 2.3 that the main cylinder's and the worker's surfaces are moving in the same direction but at different speeds, u_1 and u_2 respectively. The radius of the main cylinder in the carding machine is much greater than the radius of the worker, and we therefore approximate the surface of the main cylinder as flat. We assume the process has reached a steady state and so neglect time derivatives. For now, we neglect the action of the teeth (the orientations of which can be seen in figure 2.3) which will be discussed in chapters 3 and 4.

The region the fibres occupy between the worker and the main cylinder is very thin compared to its length, and we can therefore use analysis similar to lubrication theory, which will simplify the problem. We start by nondimensionalising the system of equations (2.3.1)-(2.3.4) using a horizontal length-scale $L=\sqrt{h_0R}$, and define $\delta=h_0/L=\sqrt{h_0/R}$, where h_0 is the minimum gap thickness between the

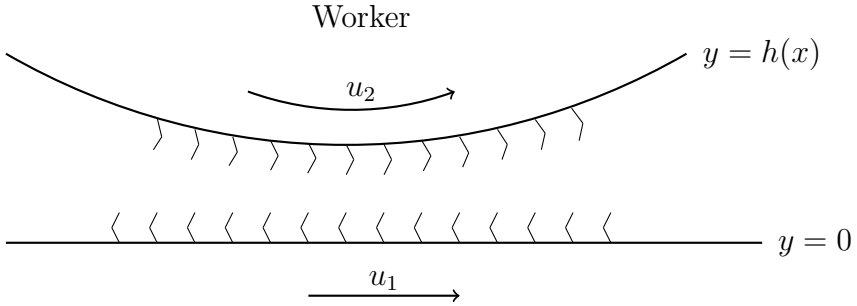


Figure 2.3: Sketch of the "nip" region between the worker, moving at speed u_2, and the main cylinder, moving at speed u_1.

cylinders, and R is the radius of the worker. Using typical parameter values we have that $\delta = O(0.01)$. Given that θ is the mean angle that the fibres make with the x-axis, we assume that $\theta = O(\delta)$. We thus nondimensionalise using the scalings

$$\begin{aligned} &x = L\hat{x}, \quad y = \delta L\hat{y}, \quad z = L\hat{z}, \quad u = u_1\hat{u}, \quad v = \delta u_1\hat{v}, \quad w = u_1\hat{w}, \\ &h = \delta L\hat{h}, \quad \rho = \rho_0\hat{\rho}, \quad \theta = \delta\hat{\theta}, \end{aligned} \tag{2.4.1}$$

where ρ_0 is the initial density of fibres.

Using the scalings (2.4.1), and keeping leading-order terms in δ, we find that the mass conservation equation (2.3.1a) becomes

$$\frac{\partial}{\partial\hat{x}}\left(\hat{\rho}\hat{u}\right) + \frac{\partial}{\partial\hat{y}}\left(\hat{\rho}\hat{v}\right) + \frac{\partial}{\partial\hat{z}}\left(\hat{\rho}\hat{w}\right) = 0, \tag{2.4.2}$$

while the governing equations (2.3.3)-(2.3.4) for the order and the director become

$$\begin{aligned} \hat{u}\frac{\partial\phi}{\partial\hat{x}} + \hat{v}\frac{\partial\phi}{\partial\hat{y}} + \hat{w}\frac{\partial\phi}{\partial\hat{z}} = \beta(1-\phi)\Bigg[&\cos^2\alpha\left(\frac{\partial\hat{u}}{\partial\hat{x}} + \hat{\theta}\frac{\partial\hat{u}}{\partial\hat{y}}\right) \\ &+ \sin\alpha\cos\alpha\left(\frac{\partial\hat{u}}{\partial\hat{z}} + \frac{\partial\hat{w}}{\partial\hat{x}} + \hat{\theta}\frac{\partial\hat{w}}{\partial\hat{y}}\right) \\ &+ \sin^2\alpha\frac{\partial\hat{w}}{\partial\hat{z}}\Bigg]^{+}, \end{aligned} \tag{2.4.3}$$

and

$$\hat{u}\frac{\partial\hat{\theta}}{\partial\hat{x}}+\hat{v}\frac{\partial\hat{\theta}}{\partial\hat{y}}+\hat{w}\frac{\partial\hat{\theta}}{\partial\hat{z}}=\hat{\theta}\left(\frac{\partial\hat{v}}{\partial\hat{y}}-\frac{\partial\hat{u}}{\partial\hat{x}}\right)+\frac{\partial\hat{v}}{\partial\hat{x}}-\hat{\theta}^2\frac{\partial\hat{u}}{\partial\hat{y}}+\tan\alpha\left(\frac{\partial\hat{v}}{\partial\hat{z}}-\hat{\theta}\frac{\partial\hat{u}}{\partial\hat{z}}\right), \quad (2.4.4a)$$

$$\begin{aligned}\hat{u}\frac{\partial\alpha}{\partial\hat{x}}+\hat{v}\frac{\partial\alpha}{\partial\hat{y}}+\hat{w}\frac{\partial\alpha}{\partial\hat{z}} =& -\cos\alpha\sin\alpha\left(\frac{\partial\hat{u}}{\partial\hat{x}}+\hat{\theta}\frac{\partial\hat{u}}{\partial\hat{y}}\right)-\sin^2\alpha\frac{\partial\hat{u}}{\partial\hat{z}}\\ &+\cos\alpha\left[\cos\alpha\left(\frac{\partial\hat{w}}{\partial\hat{x}}+\hat{\theta}\frac{\partial\hat{w}}{\partial\hat{y}}\right)+\sin\alpha\frac{\partial\hat{w}}{\partial\hat{z}}\right]. \quad (2.4.4b)\end{aligned}$$

We then calculate the stresses using equations (2.3.1c), (2.3.1d), (2.3.1e), and (2.3.2). Under the lubrication-type approximation the momentum equations then become

$$\frac{\partial}{\partial\hat{y}}\left[\hat{\rho}^2\left(\frac{\partial\hat{u}}{\partial\hat{y}}\left\{\mu_1(1-\phi)+\left(\lambda_1+\lambda_3\cos^2\alpha\right)\phi\right\}+\frac{\partial\hat{w}}{\partial\hat{y}}\lambda_3\cos\alpha\sin\alpha\phi\right)\right]=0, \quad (2.4.5a)$$

$$\begin{aligned}&\frac{1}{2}\frac{\partial}{\partial\hat{x}}\left[\hat{\rho}^2\left(\frac{\partial\hat{u}}{\partial\hat{y}}\left\{\mu_1(1-\phi)+\left(\lambda_1+\lambda_3\cos^2\alpha\right)\phi\right\}+\frac{\partial\hat{w}}{\partial\hat{y}}\lambda_3\cos\alpha\sin\alpha\phi\right)\right]\\ &+\frac{\partial}{\partial\hat{y}}\left[\hat{\rho}^2\left(\left\{\mu_2(1-\phi)+(\lambda_2+\lambda_4\cos^2\alpha)\phi\right\}\frac{\partial\hat{u}}{\partial\hat{x}}+(\lambda_3+\lambda_4)\hat{\theta}\cos^2\alpha\phi\frac{\partial\hat{u}}{\partial\hat{y}}\right.\right.\\ &+\left\{(\mu_1+\mu_2)(1-\phi)+(\lambda_1+\lambda_2)\phi\right\}\frac{\partial\hat{v}}{\partial\hat{y}}\\ &+\left\{\mu_2(1-\phi)+\left(\lambda_2+\lambda_4\sin^2\alpha+\lambda_5\cos^2\alpha\sin^2\alpha\right)\phi\right\}\frac{\partial\hat{w}}{\partial\hat{z}}\\ &\left.\left.+\lambda_4\cos\alpha\sin\alpha\left(\frac{\partial\hat{u}}{\partial\hat{z}}+\frac{\partial\hat{w}}{\partial\hat{x}}\right)\phi+(\lambda_3+\lambda_4)\hat{\theta}\cos\alpha\sin\alpha\phi\frac{\partial\hat{w}}{\partial\hat{y}}\right)\right]\\ &+\frac{1}{2}\frac{\partial}{\partial\hat{z}}\left[\hat{\rho}^2\left(\lambda_3\cos\alpha\sin\alpha\phi\frac{\partial\hat{u}}{\partial\hat{y}}+\frac{\partial\hat{w}}{\partial\hat{y}}\left\{\mu_1(1-\phi)+(\lambda_1+\lambda_3\sin^2\alpha)\phi\right\}\right)\right]=0, \quad (2.4.5b)\end{aligned}$$

$$\frac{\partial}{\partial\hat{y}}\left[\hat{\rho}^2\left(\lambda_3\cos\alpha\sin\alpha\phi\frac{\partial\hat{u}}{\partial\hat{y}}+\left\{\mu_1(1-\phi)+\left(\lambda_1+\lambda_3\sin^2\alpha\right)\phi\right\}\frac{\partial\hat{w}}{\partial\hat{y}}\right)\right]=0, \quad (2.4.5c)$$

where we have neglected body forces. The governing equations for $(\hat{u},\hat{v},\hat{w})$, $\hat{\rho}$, ϕ, $\hat{\theta}$, and α under our lubrication-type approximation are equations (2.4.2)-(2.4.5).

We assume no-slip boundary conditions on the upper and lower cylinders, namely

$$\hat{u}=1,\ \hat{v}=0,\ \hat{w}=0,\ \text{at}\ \hat{y}=0, \quad (2.4.6a)$$

$$\hat{u}=\bar{u},\ \hat{v}=\bar{u}\frac{d\hat{h}}{d\hat{x}},\ \hat{w}=0,\ \hat{y}=\hat{h}(\hat{x}), \quad (2.4.6b)$$

where $\bar{u}=u_2/u_1\approx 0.1$, and $\hat{h}(\hat{x})=1+(1/2)\hat{x}^2$ is the leading order approximation of the circular upper roller surface.

We also require upstream boundary conditions for $\hat{\rho}$, ϕ, $\hat{\theta}$, and α. We assume that these are all specified functions of y at some upstream point, $\hat{x} = -\xi$, which is assumed to be where the web enters the nip region between the rollers, i.e.

$$\hat{\rho} = \rho_{\text{in}}(\hat{y}),\ \phi = \phi_{\text{in}}(\hat{y}),\ \hat{\theta} = \theta_{\text{in}}(\hat{y}),\ \alpha = \alpha_{\text{in}}(\hat{y}),\ \text{at } \hat{x} = -\xi. \tag{2.4.7}$$

2.4.2 Model Simplifications

The full problem is defined by equations (2.4.2)-(2.4.5), but we note that equations (2.4.4b) and (2.4.5c) governing α and $\hat{w}$ are satisfied identically if $\alpha = \hat{w} = 0$. Provided the fibres entering the domain from the left are (on average) aligned in the $(\hat{x}, \hat{y})$ plane (i.e. $\alpha_{\text{in}}(\hat{y}) = 0$) then they remain so and the problem can be reduced to two dimensions. With $\alpha = 0$, we note further that equation (2.4.4a) is satisfied identically by $\hat{\theta} = \hat{v}/\hat{u}$, and we focus henceforth on this specific solution for the director. With these assumptions, the model (2.4.2)-(2.4.5) simplifies to

$$\frac{\partial}{\partial \hat{x}}(\hat{\rho}\hat{u}) + \frac{\partial}{\partial \hat{y}}(\hat{\rho}\hat{v}) = 0, \tag{2.4.8a}$$

$$\hat{u}\frac{\partial \phi}{\partial \hat{x}} + \hat{v}\frac{\partial \phi}{\partial \hat{y}} = \beta(1-\phi)\left[\left(\frac{\partial \hat{u}}{\partial \hat{x}} + \frac{\hat{v}}{\hat{u}}\frac{\partial \hat{u}}{\partial \hat{y}}\right)\right]^{+}, \tag{2.4.8b}$$

$$\frac{\partial}{\partial \hat{y}}\left[\hat{\rho}^2\frac{\partial \hat{u}}{\partial \hat{y}}\left(\frac{\mu_1}{\lambda_1} + \left(\frac{\lambda_1 + \lambda_3 - \mu_1}{\lambda_1}\right)\phi\right)\right] = 0, \tag{2.4.8c}$$

$$\begin{aligned}
&\frac{1}{2}\frac{\partial}{\partial \hat{x}}\left[\hat{\rho}^2\frac{\partial \hat{u}}{\partial \hat{y}}\left(\frac{\mu_1}{\lambda_1} + \left(\frac{\lambda_1 + \lambda_3 - \mu_1}{\lambda_1}\right)\phi\right)\right] \\
&+ \frac{\partial}{\partial \hat{y}}\left[\hat{\rho}^2\left(\left(\frac{\mu_2}{\lambda_1} + \left(\frac{\lambda_2 + \lambda_4 - \mu_2}{\lambda_1}\right)\phi\right)\frac{\partial \hat{u}}{\partial \hat{x}} + \left(\frac{\lambda_3 + \lambda_4}{\lambda_1}\right)\phi\frac{\hat{v}}{\hat{u}}\frac{\partial \hat{u}}{\partial \hat{y}}\right.\right. \\
&\qquad\left.\left. + \left(\frac{\mu_1 + \mu_2}{\lambda_1} + \left(\frac{\lambda_1 + \lambda_2 - \mu_1 - \mu_2}{\lambda_1}\right)\phi\right)\frac{\partial \hat{v}}{\partial \hat{y}}\right)\right] = 0.
\end{aligned} \tag{2.4.8d}$$

2.5 Uniform Viscosity Model

2.5.1 Simplified Model

Even with the simplifications made in section 2.4, the full lubrication model (2.4.8) remains difficult to solve in general. To make some progress, we first consider a simplified version where all the viscosity coefficients are constant. We remove the dependence on $\hat{\theta}$ by setting $\lambda_3 + \lambda_4 = 0$, and neglect the dependence on $\hat{\rho}$ and ϕ by approximating $\hat{\rho} \approx 1$ and $\phi \approx 1$ in (2.4.8c) and (2.4.8d). The resulting simplified

model is represented by equations

$$\frac{\partial}{\partial x}(\rho u) + \frac{\partial}{\partial y}(\rho v) = 0, \tag{2.5.1a}$$

$$u\frac{\partial \phi}{\partial x} + v\frac{\partial \phi}{\partial y} = \beta(1-\phi)\left[\left(\frac{\partial u}{\partial x} + \frac{v}{u}\frac{\partial u}{\partial y}\right)\right]^{+}, \tag{2.5.1b}$$

$$\frac{\partial^2 u}{\partial y^2} = 0, \tag{2.5.1c}$$

$$m_1\frac{\partial^2 u}{\partial x \partial y} + m_2\frac{\partial^2 v}{\partial y^2} = 0, \tag{2.5.1d}$$

where $m_1 = (\lambda_1 + \lambda_3 + 2(\lambda_2 + \lambda_4))/(2\lambda_1)$, $m_2 = (\lambda_1 + \lambda_2)/\lambda_1$, and the hats have now been dropped. The momentum equations (2.5.1c) and (2.5.1d), under this approximation, are linear and no longer depend on ρ, θ, or ϕ. These two equations therefore decouple and can be solved for the velocities u and v, which can then be substituted into the remaining three equations to solve for ρ, θ, and ϕ.

2.5.2 Solution in Swift-Worker Region

Solving equations (2.5.1c) and (2.5.1d) subject to boundary conditions (2.4.6) leads to the following solutions for velocity components:

$$u(x,y) = 1 - (1-\bar{u})\frac{y}{h(x)}, \tag{2.5.2a}$$

$$v(x,y) = \frac{h'(x)y}{h(x)}\left(\bar{u} + m_1\frac{(1-\bar{u})}{2m_2}\frac{(h(x)-y)}{h(x)}\right). \tag{2.5.2b}$$

It is convenient here to introduce the new variable

$$Y = \frac{y}{h(x)}. \tag{2.5.3}$$

The region between the two rollers, $0 \le y \le h(x)$, is thus mapped to the fixed interval $0 \le Y \le 1$, and (2.5.2) reads

$$u(x,Y) = 1 - (1-\bar{u})Y, \tag{2.5.4}$$

$$v(x,Y) = h'(x)Y\left(\bar{u} + \frac{(1-\bar{u})m_1}{2m_2}(1-Y)\right). \tag{2.5.5}$$

The mass conservation equation (2.5.1a) with respect to new variables (x, Y) reads

$$u\frac{\partial \rho}{\partial x} + \frac{v - Yuh'}{h}\frac{\partial \rho}{\partial Y} = \frac{\rho}{h}\left(Yh'\frac{\partial u}{\partial Y} - \frac{\partial v}{\partial Y}\right). \tag{2.5.6}$$

The characteristics of this hyperbolic PDE (the streamlines of the flow) satisfy

$$\frac{dY}{dx} = \frac{v - Yuh'}{uh} = \frac{(2m_2 - m_1)(\bar{u} - 1)}{2m_2} \frac{h'}{h} \frac{Y(1-Y)}{1-(1-\bar{u})Y}. \tag{2.5.7}$$

We parametrise the upstream boundary conditions (2.4.7) using the new variable Y so that

$$Y = \eta, \quad \rho = \rho_0(\eta), \quad \phi = \phi_0(\eta), \quad \theta = \theta_0(\eta) \quad \text{at} \quad x = -\xi, \tag{2.5.8}$$

where $\rho_0(\eta) = \rho_{\text{in}}(h(-\xi)\eta)$, $\phi_0(\eta) = \phi_{\text{in}}(h(-\xi)\eta)$, and $\theta_0(\eta) = \theta_{\text{in}}(h(-\xi)\eta)$. Solving equation (2.5.7) subject to (2.5.8) gives the result

$$\frac{(1-\eta)^{\bar{u}}}{\eta} = \frac{(1-Y)^{\bar{u}}}{Y} \left(\frac{h(-\xi)}{h(x)} \right)^{\frac{(2m_2 - m_1)(1-\bar{u})}{2m_2}}. \tag{2.5.9}$$

The streamlines of the flow are given by lines of constant η in (2.5.9). With $Y(x;\eta)$ determined implicitly by equation (2.5.9) we can now solve equation (2.5.6) for the parametric form of the density, namely

$$\rho(Y;\eta) = \rho_0(\eta) \frac{\eta(1-\eta)}{Y(1-Y)} \left[\frac{(1-\eta)^{\bar{u}} Y}{(1-Y)^{\bar{u}} \eta} \right]^{\frac{2m_2}{(2m_2 - m_1)(1-\bar{u})}}. \tag{2.5.10}$$

In principle we can solve (2.5.9) for η, in $x > -\xi$, and substitute into (2.5.10) to find ρ as a function of x and Y.

We recall that we take the specific solution for the director angle, which can be written as

$$\theta(x,Y) = \frac{v(x,Y)}{u(x,Y)} = \left(\frac{2m_2\bar{u} + m_1(1-\bar{u})(1-Y)}{2m_2} \right) \frac{h'Y}{1-(1-\bar{u})Y}. \tag{2.5.11}$$

Finally we turn to equation (2.5.1b) for the order parameter. We recall that the worker moves at a velocity significantly slower than the main cylinder and in the same direction, and therefore $0 < \bar{u} < 1$. Using this information, it can be shown that

$$\frac{\partial u}{\partial x} + \frac{v}{u} \frac{\partial u}{\partial y} \begin{cases} > 0, \text{ for } x > 0, \\ < 0, \text{ for } x < 0, \end{cases} \tag{2.5.12}$$

and therefore the solution to equation (2.5.1b) is given parametrically by

$$\phi(x,Y) = \begin{cases} \phi_0(\eta), \ x \leq 0, \\ 1 - (1 - \phi_0(\eta)) \left(\frac{1+(\bar{u}-1)\nu}{1+(\bar{u}-1)Y} \right)^{\beta}, \ x \geq 0, \end{cases} \tag{2.5.13}$$

where $Y = \nu$ at $x = 0$. Equations (2.5.2), (2.5.9), (2.5.10), (2.5.11), and (2.5.13) represent the solution to the simplified 2D lubrication model in the region between the worker and the main cylinder.

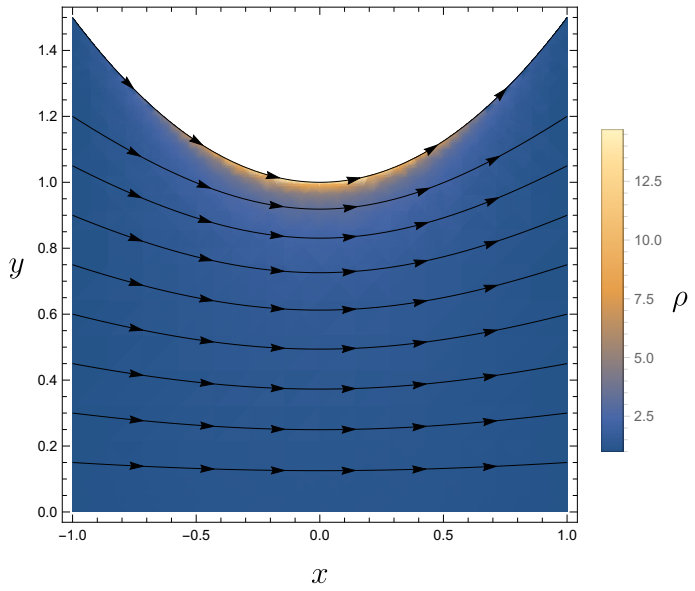


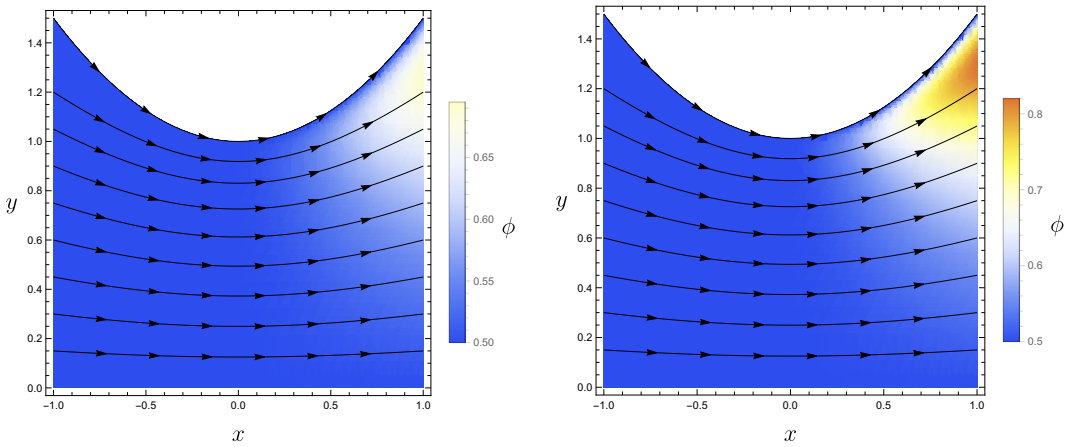
Figure 2.4: Distribution of the density of fibres, with $\rho_0 = 1$, $\xi = 1$, $\bar{u} = 0.1$, $m_1 = 1.5$ and $m_2 = 2$. The streamlines are shown in black.

2.5.3 Results in Swift-Worker Region

The solutions derived in the previous subsection allow us to examine the evolution of the properties of the web as it passes through the region between the swift and the worker. In figures 2.4 and 2.5 we use constant initial values for ρ and ϕ. It is also assumed that the swift is moving a lot faster than the worker, which is typical in most carding machines, and hence we take $\bar{u} = 0.1$ in figures 2.4 and 2.5a and $\bar{u} = 0.05$ in figure 2.5b. This velocity ratio is an important control parameter in practice, and we therefore want to examine the effect of it on the properties of the final product.

The distribution of the density of fibres, using typical parameter values, is plotted in figure 2.4. Taking a constant density, $\rho_0 = 1$, at the upstream point, $x = -\xi = -1$, we observe that the density increases as the web moves into the middle of the region, and then decreases to the initial density at the end point $x = 1$. The initial uniformity is temporarily lost, as a very high density of fibres is observed in a thin region near the worker at the centre of the nip region, but the distribution is symmetric about $x = 0$, so ρ returns to being uniform again at $x = 1$.

We see in figure 2.5 that the order parameter, ϕ, of the fibres remains constant in $x < 0$ as the web is compressed, but starts to increase in $x > 0$ where the web is being stretched. We also see the order parameter achieving its maximum value at an interior point near the worker. Comparing figures 2.5a and 2.5b we observe that



(a) Distribution for $\bar{u} = 0.1$.

(b) Distribution for $\bar{u} = 0.05$.

Figure 2.5: Distribution of the order parameter ϕ with different velocity ratios, with $\phi_0 = 0.5$, $\xi = 1$, $m_1 = 1.5$ and $m_2 = 2$. The streamlines are shown in black.

a lower $\bar{u}$, equivalent to a larger difference between the velocities of the cylinders, results in a higher order achieved in the region of interest.

In figure 2.6 we further examine the influence of the control parameter, $\bar{u}$, by plotting the order parameter against $\bar{u}$ and y at some assumed end point, $x = \xi$. We see that, as $\bar{u}$ is increased, the maximum value of ϕ reached at this end point decreases. We also see that if the cylinders are moving at the same velocity, i.e. $\bar{u} \to 1$, then $\phi \to \phi_0$ and the order of the fibres doesn't increase. A large difference between the velocities, equivalent to a low $\bar{u}$, results in a larger maximum order being achieved. This result for the dependence of ordering on relative velocity agrees qualitatively with experimental results [30, 33].

So far, our model suggests that the larger the velocity difference, the more efficient the carding; however, we have not introduced the possibility of fibre breakage. Fibre breakage has an adverse affect on the product and is observed to depend on the velocities of the cylinders. This breakage is discussed more in chapters 3 and 5.

2.5.4 Solution in Worker-Stripper Region

Previously we have looked at the region of the carding machine between the worker and the swift. The stripper-swift and worker-stripper regions are shown schematically in figures 2.7 and 2.8 respectively. The problem in the stripper-swift region is analogous to the one discussed above, but, the region between the stripper and the worker is qualitatively different because the cylinders are moving in opposite directions. Thus the material enters the nip region from both sides, changing the boundary conditions

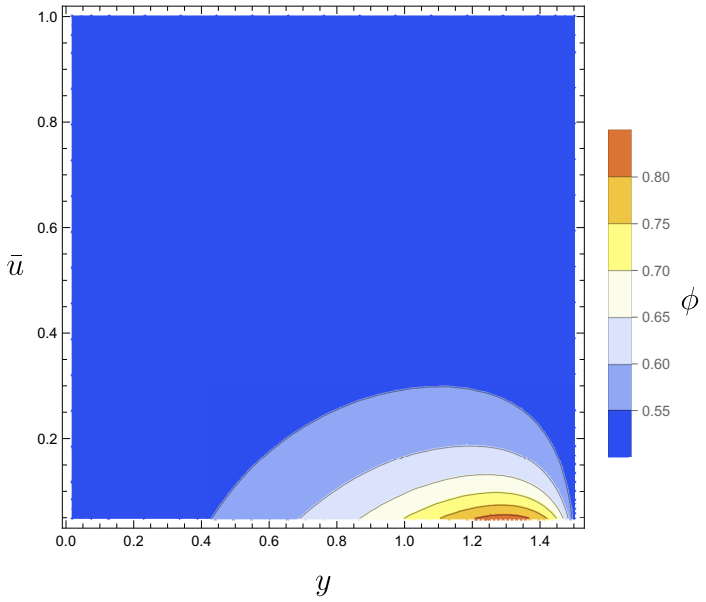


Figure 2.6: Plot of ϕ at the downstream end point, $x = \xi$, varying y and $\bar{u}$, with $\phi_0 = 0.5$, $\xi = 1$, $m_1 = 1.5$, and $m_2 = 2$.

we need to use, and therefore the solution. For simplicity, we again approximate the surface of the larger cylinder, the worker in this case, as flat.

The velocities of the cylinders are such that $|u_2| < |u_3|$, and we define the velocity ratio as

$$\bar{\bar{u}} = -\frac{u_3}{u_2} \geq 1. \tag{2.5.14}$$

We take the positive x-direction to be from left to right in figure 2.8, so when we do our lubrication nondimensionalisation we now scale the velocity with $-u_2$. This change in velocity scale means the governing equations, given by (2.5.1), remain the

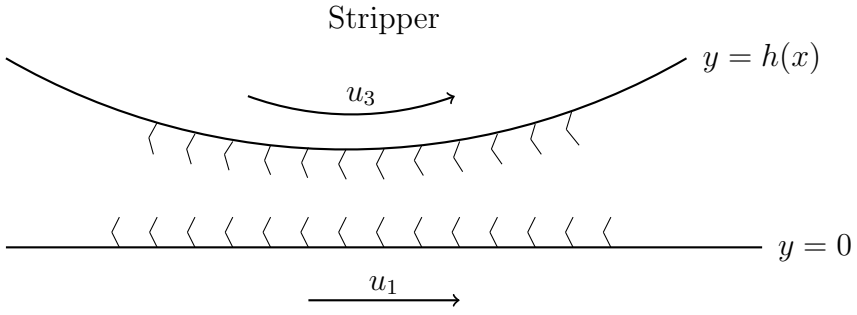


Figure 2.7: Picture showing the region between the stripper, moving at velocity u_3, and the main cylinder, moving at velocity u_1.

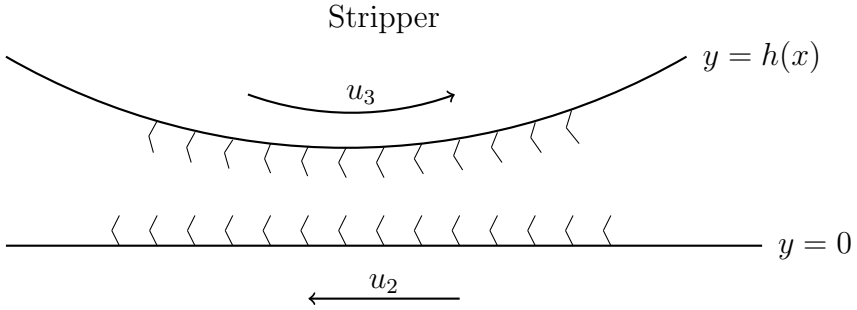


Figure 2.8: Picture showing the region between the stripper, moving at velocity u_3, and the worker, moving at velocity u_2.

same, but the dimensionless boundary conditions (2.4.6) for u and v are replaced by

$$u = -1, \quad v = 0, \quad \text{at} \quad y = 0, \tag{2.5.15a}$$

$$u = \bar{\bar{u}}, \quad v = \bar{\bar{u}}\frac{\mathrm{d}h}{\mathrm{d}x}, \quad \text{at} \quad y = h(x). \tag{2.5.15b}$$

For the swift-worker region we imposed upstream boundary conditions on ρ, θ, and ϕ. We want to do the same here, however also taking into account the fact that some material enters the region from the left, and some from the right. Specifically, we see that characteristics of the hyperbolic equations (2.5.1) enter from the left if the horizontal velocity, u, is positive at the starting left-hand value of $x = -\xi$, and they enter from the right if u is negative at the right-hand point of $x = \xi$. We therefore impose the boundary conditions

$$\rho = \rho_1(y), \ \phi = \phi_1(y), \ \text{at } x = \xi, \ u(\xi, y) < 0, \tag{2.5.16a}$$

$$\rho = \rho_2(y), \ \phi = \phi_2(y), \ \text{at } x = -\xi, \ u(-\xi, y) > 0. \tag{2.5.16b}$$

We solve equations (2.5.1c), (2.5.1d) subject to boundary conditions (2.5.15) to obtain the velocity components

$$u(x, Y) = (1 + \bar{\bar{u}})\, Y - 1, \tag{2.5.17a}$$

$$v(x, Y) = h'(x) Y \left(\bar{\bar{u}} + \frac{m_1 \,(1 + \bar{\bar{u}})\,(Y - 1)}{2m_2} \right), \tag{2.5.17b}$$

where again we set $Y = y/h(x)$. We can thus write the boundary conditions (2.5.16) as

$$Y = \eta, \ \rho = \rho_1(\eta), \ \phi = \phi_1(\eta), \ \text{at } x = \xi, \ \eta < \frac{1}{1 + \bar{\bar{u}}}, \tag{2.5.18a}$$

$$Y = \eta, \ \rho = \rho_2(\eta), \ \phi = \phi_2(\eta), \ \text{at } x = -\xi, \ \eta > \frac{1}{1 + \bar{\bar{u}}}. \tag{2.5.18b}$$

We use the method of characteristics to solve equation (2.5.1a), as shown in section 2.5.2. The characteristics (i.e. streamlines) are given by

$$\frac{(1-\eta)^{-\bar{\bar{u}}}}{\eta} = \frac{(1-Y)^{-\bar{\bar{u}}}}{Y}\left(\frac{h(x)}{h(\xi)}\right)^{\frac{(m_1-2m_2)(1+\bar{\bar{u}})}{2m_2}}, \tag{2.5.19}$$

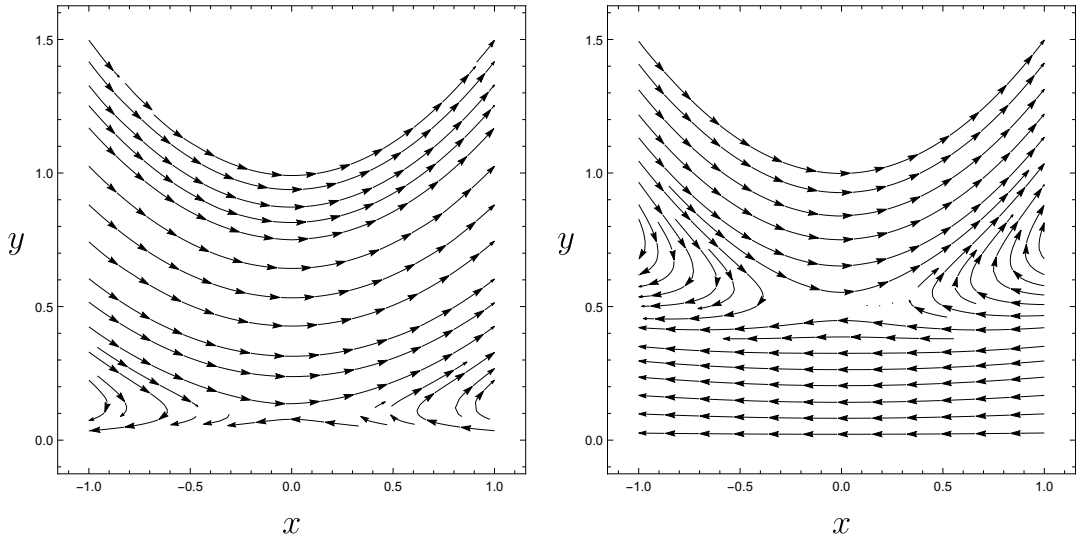
which can be used to solve for the density of fibres, ρ, in the parametric form

$$\rho(Y;\eta) = \begin{cases} \rho_1(\eta)\frac{\eta(1-\eta)}{Y(1-Y)}\left[\frac{(1-\eta)^{\bar{\bar{u}}}\eta}{(1-Y)^{\bar{\bar{u}}}Y}\right]^{\frac{2m_2}{(m_1-2m_2)(1+\bar{\bar{u}})}}, & 0<\eta<\frac{1}{1+\bar{\bar{u}}}, \\ \rho_2(\eta)\frac{\eta(1-\eta)}{Y(1-Y)}\left[\frac{(1-\eta)^{\bar{\bar{u}}}\eta}{(1-Y)^{\bar{\bar{u}}}Y}\right]^{\frac{2m_2}{(m_1-2m_2)(1+\bar{\bar{u}})}}, & \frac{1}{1+\bar{\bar{u}}}<\eta<1. \end{cases} \tag{2.5.20}$$

2.5.5 Results in Worker-Stripper Region

In this section we will examine the behaviour of fibres across the new region of interest, between the worker and the stripper. In figure 2.9 we show stream plots of the velocity field, (u, v), given by equation (2.5.17). We see, as expected, that some of the streamlines enter the nip region from the left, assumed to be along the stripper, and some enter from the right, along the worker. For a high velocity ratio, $\bar{\bar{u}}$, meaning the stripper moves much faster than the worker, most streamlines enter the region along the stripper. When the velocities of the two cylinders are kept the same, streamlines enter equally from the left and from the right. Most streamlines cross the region, but there are regions where the streamlines change direction and exit at the same side as they enter. There is always a stagnation point at $x = 0$ and $Y = 1/(1+\bar{\bar{u}})$.

There is a dividing streamline that separates material coming from the left, and material coming from the right. In the previous section we assumed a constant density of fibres entering the region along both cylinders. This is no longer a physically realistic assumption however as most of the fibres on the stripper are observed to rejoin the swift before reaching this nip region. Our underlying assumption that the whole region is filled with fibres is therefore not necessarily the right option here. We see from figure 2.9a that most streamlines entering from the right leave on the right, supporting the industrial observations that the web transfers from the worker to the stripper without mixing in this region. We therefore assume that the region between the worker and the stripper does not contribute to the ordering of fibres.



(a) A stream plot of the velocity field, (2.5.17a), (2.5.17b), for $\bar{\bar{u}} = 10$.

(b) A stream plot of the velocity field, (2.5.17a), (2.5.17b), for $\bar{\bar{u}} = 1$.

Figure 2.9: Stream plots of the velocity field, (u, v), in the region between the worker and the stripper with $\xi = 1$, $\phi_0 = 0.5$, and $m_1 = 1.5$ and $m_2 = 2$.

2.6 Full Lubrication Model

2.6.1 Density Model

2.6.1.1 Model Simplification

In this section we return to the full lubrication model, which is represented by equations (2.4.8). We begin by examining a simplified version of the problem by making particular choices for some of the constants μ_1, μ_2, λ_1–λ_5. We first outline a solution method for the simplified problem and then apply this method to the full problem. We focus on the region between the swift and the worker, shown in figure 2.3, and so both cylinders are moving in the same direction.

We can decouple ϕ and θ in equations (2.4.8) by setting

$$\lambda_3 = \lambda_4 = 0, \tag{2.6.1a}$$

$$\mu_1 = \lambda_1, \tag{2.6.1b}$$

$$\mu_2 = \lambda_2. \tag{2.6.1c}$$

We note that by making these parameter choices we are neglecting the effect of the order but, crucially, retaining the effect of the density on the viscosity. Equations (2.4.8)

then become

$$\frac{\partial}{\partial x}(\rho u) + \frac{\partial}{\partial y}(\rho v) = 0, \tag{2.6.2a}$$

$$\frac{\partial}{\partial y}\left(\rho^2 \frac{\partial u}{\partial y}\right) = 0, \tag{2.6.2b}$$

$$\frac{\partial}{\partial x}\left(\rho^2 \frac{\partial u}{\partial y}\right) + \frac{\partial}{\partial y}\left[\rho^2\left(2m_3 \frac{\partial u}{\partial x} + 2(1+m_3)\frac{\partial v}{\partial y}\right)\right] = 0, \tag{2.6.2c}$$

$$u\frac{\partial \phi}{\partial x} + v\frac{\partial \phi}{\partial y} = \beta(1-\phi)\left[\left(\frac{\partial u}{\partial x} + \frac{v}{u}\frac{\partial u}{\partial y}\right)\right]^+, \tag{2.6.2d}$$

where

$$m_3 = \frac{\mu_2}{\mu_1}. \tag{2.6.3}$$

Equations (2.6.2) require boundary conditions, which in the swift-worker region are

$$u = 1,\ v = 0,\ \text{at } y = 0, \tag{2.6.4a}$$

$$u = \bar{u},\ v = \bar{u}\frac{\mathrm{d}h}{\mathrm{d}x},\ \text{at } y = h(x), \tag{2.6.4b}$$

$$\rho = \rho_{\text{in}}(y),\ \phi = \phi_{\text{in}}(y),\ \text{at } x = -\xi. \tag{2.6.4c}$$

2.6.1.2 Density Model Reformulation

In this section we present a method for solving the system of coupled partial differential equations (2.6.2)–(2.6.4). Our method is to first map our equations onto a fixed domain, and then manipulate the resulting system of equations to obtain a set of equations with derivatives in only one of the spatial variables, and one explicit equation stepping forwards in x. This system can then be solved using the method of lines.

We note that equation (2.6.2d) is a PDE that determines ϕ which decouples. We therefore focus on equations (2.6.2a)-(2.6.2c). From equations (2.6.2b) and (2.6.2c) we can write

$$\rho^2 \frac{\partial u}{\partial y} = \sigma(x), \tag{2.6.5a}$$

$$\rho^2\left(2m_3\frac{\partial u}{\partial x} + 2(m_3+1)\frac{\partial v}{\partial y}\right) = F(x) - y\sigma'(x), \tag{2.6.5b}$$

where $F(x)$ and $\sigma(x)$ are unknown functions of x. We then make a change of coordinate system defined by

$$X = x, \quad Z = \frac{1-u(x,y)}{1-\bar{u}}, \tag{2.6.6}$$

so that, after using conditions (2.6.4) the domain $0 \leq y \leq h(x)$ is mapped onto the fixed domain $0 \leq Z \leq 1$. Making this change of variables we find that governing equations (2.6.2a) and (2.6.5) become

$$(1-(1-\bar{u})Z)\,\frac{\partial y}{\partial Z}\frac{\partial \rho}{\partial X} + \left(v-(1-(1-\bar{u})Z)\,\frac{\partial y}{\partial X}\right)\frac{\partial \rho}{\partial Z} + \left(\frac{\partial v}{\partial Z}+(1-\bar{u})\frac{\partial y}{\partial X}\right)\rho = 0, \tag{2.6.7a}$$

$$\rho^2 = -\frac{\sigma(X)}{1-\bar{u}}\frac{\partial y}{\partial Z}, \tag{2.6.7b}$$

$$2(m_3+1)\frac{\partial v}{\partial Z} = -(1-\bar{u})\left(2m_3\frac{\partial y}{\partial X}+\frac{F(X)}{\sigma(X)}-\frac{\sigma'(X)}{\sigma(X)}y\right). \tag{2.6.7c}$$

Now, combining equations (2.6.7) and rearranging gives

$$\begin{aligned}\mathcal{L}v \equiv & \frac{2(m_3+1)}{(1-\bar{u})^2}\frac{\partial^2 v}{\partial Z^2} - \frac{1}{1-\bar{u}}\left(-\frac{4}{1-(1-\bar{u})Z}+\frac{2(m_3+1)}{1-\bar{u}}\frac{\frac{\partial^2 y}{\partial Z^2}}{\frac{\partial y}{\partial Z}}\right)\frac{\partial v}{\partial Z} \\ & - \left(\frac{2m_3\frac{\partial^2 y}{\partial Y^2}}{(1-\bar{u})\,(1-(1-\bar{u})Z)\,\frac{\partial y}{\partial Z}}\right)v \\ = & \left(\frac{\sigma'(X)}{\sigma(X)}y-\frac{F(X)}{\sigma(X)}\right)\left(-\frac{1}{1-\bar{u}}\frac{\frac{\partial^2 y}{\partial Z^2}}{\frac{\partial y}{\partial Z}}+\frac{2}{(1-(1-\bar{u})Z)}\right)+\frac{(2m_3+1)\sigma'(X)}{(1-\bar{u})\sigma(X)}\frac{\partial y}{\partial Z},\end{aligned} \tag{2.6.8}$$

where we define the operator $\mathcal{L}$. Equation (2.6.8) defines a boundary-value problem for v and y with boundary conditions

$$v = y = 0, \text{ at } Z = 0, \tag{2.6.9a}$$

$$v = \bar{u}h'(X),\ y = h(X), \text{ at } Z = 1. \tag{2.6.9b}$$

We aim to derive a system where only one of the equations contains an explicit X-derivative. This will allow us to use the method of lines more easily in solving our system. We therefore split v into components v_0, v_1, and v_2 so the vertical velocity v is given by

$$v(X,Z) = v_0(X,Z)\bar{u}h'(X) + \frac{\sigma'(X)}{\sigma(X)}v_1(X,Z) + \frac{F(X)}{\sigma(X)}v_2(X,Z). \tag{2.6.10}$$

This means equations (2.6.7c) and (2.6.8) become

$$\mathcal{L}v_0 = 0, \tag{2.6.11a}$$

$$\mathcal{L}v_1 = y\left(\frac{2}{(1-(1-\bar{u})Z)} - \frac{1}{1-\bar{u}}\frac{\frac{\partial^2 y}{\partial Z^2}}{\frac{\partial y}{\partial Z}}\right) + \left(\frac{2m_3+1}{1-\bar{u}}\right)\frac{\partial y}{\partial Z}, \tag{2.6.11b}$$

$$\mathcal{L}v_2 = \frac{1}{1-\bar{u}}\frac{\frac{\partial^2 y}{\partial Z^2}}{\frac{\partial y}{\partial Z}} - \frac{2}{1-(1-\bar{u})Z)}, \tag{2.6.11c}$$

$$2m_3\frac{\partial y}{\partial X} = -\frac{2\bar{u}(m_3+1)h'(X)}{1-\bar{u}}\frac{\partial v_0}{\partial Z} + \frac{\sigma'(X)}{\sigma(X)}\left(y - \frac{2(m_3+1)}{1-\bar{u}}\frac{\partial v_1}{\partial Z}\right) - \frac{F(X)}{\sigma(X)}\left(1 + \frac{2(m_3+1)}{1-\bar{u}}\frac{\partial v_2}{\partial Z}\right), \tag{2.6.11d}$$

with boundary conditions

$$v_0(X,0) = 0,\ v_0(X,1) = 1, \tag{2.6.12a}$$

$$v_1(X,0) = v_1(X,1) = 0, \tag{2.6.12b}$$

$$v_2(X,0) = v_2(X,1) = 0, \tag{2.6.12c}$$

$$y(X,0) = 0,\ y(X,1) = h(X). \tag{2.6.12d}$$

Upon implementing the y boundary conditions (2.6.12d), and letting

$$\sigma'(X) = \alpha_1(X)h'(X)\sigma(X), \tag{2.6.13a}$$

$$F(X) = \alpha_2(X)h'(X)\sigma(X), \tag{2.6.13b}$$

we derive the governing equation

$$2m_3\frac{\partial y}{\partial X} = h'(X)\left[-\frac{2(m_3+1)\bar{u}}{1-\bar{u}}\frac{\partial v_0}{\partial Z} + \alpha_1(X)\left(y - \frac{2(m_3+1)}{1-\bar{u}}\frac{\partial v_1}{\partial Z}\right) - \alpha_2(X)\left(1 + \frac{2(m_3+1)}{1-\bar{u}}\frac{\partial v_2}{\partial Z}\right)\right]. \tag{2.6.14}$$

We note that, equations (2.6.11a)-(2.6.11c) do not contain any X-derivatives, and therefore equation (2.6.14) is an explicit equation for stepping forwards in X. The

functions $\alpha_1(X)$ and $\alpha_2(X)$ are the solutions of the system

$$\begin{pmatrix} -\dfrac{2(m_3+1)}{1-\bar{u}}\dfrac{\partial v_1}{\partial Z}(X,0) & -\dfrac{2(m_3+1)}{1-\bar{u}}\dfrac{\partial v_2}{\partial Z}(X,0)-1 \\ h(X)-\dfrac{2(m_3+1)}{1-\bar{u}}\dfrac{\partial v_1}{\partial Z}(X,1) & -\dfrac{2(m_3+1)}{1-\bar{u}}\dfrac{\partial v_2}{\partial Z}(X,1)-1 \end{pmatrix} \begin{pmatrix} \alpha_1(X) \\ \alpha_2(X) \end{pmatrix} = \begin{pmatrix} \dfrac{2(m_3+1)\bar{u}}{1-\bar{u}}\dfrac{\partial v_0}{\partial Z}(X,0) \\ 2m_3+\dfrac{2(m_3+1)\bar{u}}{1-\bar{u}}\dfrac{\partial v_0}{\partial Z}(X,1) \end{pmatrix}. \tag{2.6.15}$$

Our remaining equations for variables ρ and ϕ are

$$\rho^2 = -\frac{\sigma(X)}{1-\bar{u}}\frac{\partial y}{\partial Z}, \tag{2.6.16}$$

$$(1-(1-\bar{u})Z)\frac{\partial \phi}{\partial X}+\left(\frac{v-(1-(1-\bar{u})Z)\dfrac{\partial y}{\partial X}}{\dfrac{\partial y}{\partial Z}}\right)\frac{\partial \phi}{\partial Z} = \beta(1-\phi)(1-\bar{u})\left[\frac{(1-(1-\bar{u})Z)\dfrac{\partial y}{\partial X}-v}{(1-(1-\bar{u})Z)\dfrac{\partial y}{\partial Z}}\right]^{+}. \tag{2.6.17}$$

This problem lends itself to the method of lines, whereby we discretize governing equations (2.6.11a)-(2.6.11c), (2.6.12a)-(2.6.12c), and (2.6.13)-(2.6.17) in Z. From (2.6.11a)-(2.6.11c), (2.6.12a)-(2.6.12c), and (2.6.15)-(2.6.16) we derive algebraic equations, and (2.6.13a), (2.6.14) and (2.6.17) lead to ODEs in X. We then use an ODE solver to solve the resulting system of differential-algebraic equations (DAEs). This discretization is discussed in detail in appendix A. To maintain accuracy we introduce ghost points on the Z boundaries, and solve the system using MATLAB's in-built solver ode15s [27,51]. This is a variable-step, variable order numerical method, and we set the relative and absolute error tolerances to 10^{-6}.

2.6.1.3 Density Model Results

In this section we discuss the results of the model that includes the fibre density in the viscosities, represented by equations (2.6.11)-(2.6.17). As mentioned previously we solve this system using the method of lines, for which the discretization in Z can be found in appendix A.

We need to define 'upstream' conditions at some entry point $X = -\xi$ for variables ρ, ϕ, v_0, v_1, v_2, and y for the solver to use. We impose initial density and order

that are constant in Z, and use equations (2.6.13) and (2.6.16) to derive the upstream conditions

$$\rho(-\xi, Z) = \rho_{\text{in}}, \tag{2.6.18a}$$

$$\phi(-\xi, Z) = \phi_{\text{in}}, \tag{2.6.18b}$$

$$y(-\xi, Z) = h(-\xi)Z, \tag{2.6.18c}$$

$$\sigma(-\xi) = -\frac{(1-\bar{u})\rho_{\text{in}}^2}{h(-\xi)}. \tag{2.6.18d}$$

We use conditions (2.6.18) to solve algebraic equations (A.2a), (A.2b), (A.2c), (A.2e), and (A.2f) defined in appendix A, giving $v_0(-\xi, Z_i)$, $v_1(-\xi, Z_i)$, $v_2(-\xi, Z_i)$, $\alpha_1(-\xi)$, and $\alpha_2(-\xi)$. This provides us with all the required 'upstream' conditions that can be used to solve the DAE system (A.2)-(A.5).

We solve the DAE system in coordinate system (X, Z), and then use our solution for $y(X, Z)$ to then plot results in the (x, y)-plane. We plot the distribution of density and order in the swift-worker region of the carding machine in figures 2.10 and 2.11 respectively. We note that the parameters used for the uniform viscosity model and the density model are

$$m_1 = \frac{\lambda_1 + \lambda_3 + 2(\lambda_2 + \lambda_4)}{2\lambda_1} = \frac{\lambda_1 + 2\lambda_2}{2\lambda_1}, \tag{2.6.19}$$

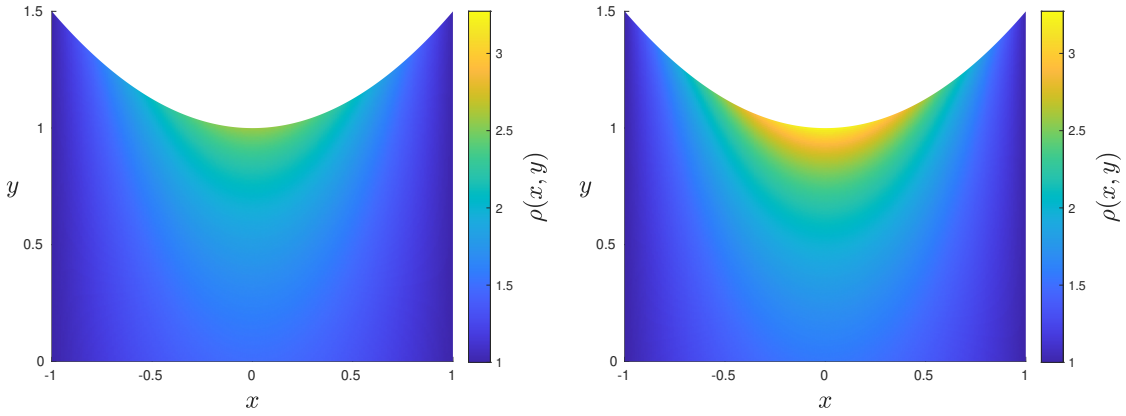
$$m_2 = \frac{\lambda_1 + \lambda_2}{\lambda_1}, \tag{2.6.20}$$

$$m_3 = \frac{\mu_2}{\mu_1} = \frac{\lambda_2}{\lambda_1}, \tag{2.6.21}$$

where we also use equations (2.6.1). Therefore to choose analogous parameters to those chosen in section 2.5 we use $m_3 = 1$ (i.e. $\lambda_1 = \lambda_2 = 1$).

In figure 2.10 we again observe an increase in fibre density in the centre of the carding region, before the initial uniform distribution is recovered at the 'downstream' endpoint. Comparing figures 2.10a and 2.4 we see that including the density in the viscosities removes the very localised increase in the density near the top roller, and the maximum density does not reach the same peak. Including the effect of ρ on the viscosities spreads out the compression of the web more — as ρ increases, the viscosity increases quadratically, making the material harder to deform. This important physical effect is not captured by the "uniform viscosity" model.

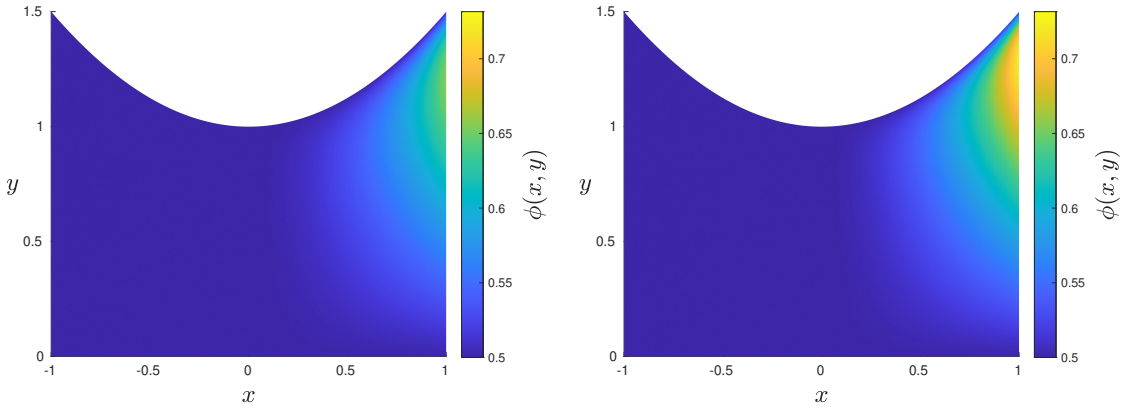
We plot the order of fibres in figure 2.11 for two different values of $\bar{u}$, and again observe the order increasing as the web is stretched, achieving its maximum at an interior point near the worker. Comparing these results with figure 2.5 we see that the



(a) Distribution for $\bar{u} = 0.1$.

(b) Distribution for $\bar{u} = 0.05$.

Figure 2.10: Distribution of the density of fibres with different velocity ratios, with $\rho_{\text{in}} = 1$, $\xi = 1$, and $m_3 = 1$.



(a) Distribution for $\bar{u} = 0.1$.

(b) Distribution for $\bar{u} = 0.05$.

Figure 2.11: Distribution of the order of fibres with different velocity ratios, with $\phi_{\text{in}} = 0.5$, $\xi = 1$, and $m_3 = 1$.

order also becomes far less localised when the uniform viscosity assumption is relaxed, with the maximum order occurring further away from the worker. This again is due to the density terms in the viscosity resulting in a material that becomes harder to deform as it is compressed. Comparing figures 2.10a and 2.10b, and 2.11a and 2.11b we recover the expected result that decreasing $\bar{u}$ leads to a higher maximum in the density of fibres, and a higher order being achieved. This result therefore also suggests that a larger velocity difference between two rollers leads to more efficient ordering.

2.6.2 Order and Density Model

2.6.2.1 Full Model

We now return to the full lubrication model, defined by equations (2.4.8), to include ϕ in the viscosities. The governing equations can be written

$$\frac{\partial}{\partial x}(\rho u) + \frac{\partial}{\partial y}(\rho v) = 0, \tag{2.6.22a}$$

$$u\frac{\partial \phi}{\partial x} + v\frac{\partial \phi}{\partial y} = \beta(1-\phi)\left[\left(\frac{\partial u}{\partial x} + \frac{v}{u}\frac{\partial u}{\partial y}\right)\right]^{+}, \tag{2.6.22b}$$

$$\frac{\partial}{\partial y}\left[\rho^2 \frac{\partial u}{\partial y}\left(1 + A_1\phi\right)\right] = 0, \tag{2.6.22c}$$

$$\frac{\partial}{\partial x}\left[\rho^2 \frac{\partial u}{\partial y}\left(1 + A_1\phi\right)\right] + \frac{\partial}{\partial y}\left[\rho^2\left(\left(A_2 + A_3\phi\right)\frac{\partial u}{\partial x} + A_4\phi\frac{v}{u}\frac{\partial u}{\partial y} + \left(A_5 + A_6\phi\right)\frac{\partial v}{\partial y}\right)\right] = 0, \tag{2.6.22d}$$

where

$$A_1 = \frac{\lambda_1 + \lambda_3 - \mu_1}{\mu_1}, \quad A_2 = \frac{2\mu_2}{\mu_1}, \quad A_3 = \frac{2\left(\lambda_2 + \lambda_4 - \mu_2\right)}{\mu_1},$$
$$A_4 = \frac{2\left(\lambda_3 + \lambda_4\right)}{\mu_1}, \quad A_5 = \frac{2\left(\mu_1 + \mu_2\right)}{\mu_1}, \quad A_6 = \frac{2\left(\lambda_1 + \lambda_2 - \mu_1 - \mu_2\right)}{\mu_1}. \tag{2.6.23}$$

Equations (2.6.22) are subject to boundary conditions

$$u = 1,\ v = 0,\ \text{at } y = 0, \tag{2.6.24a}$$

$$u = \bar{u},\ v = \bar{u}\frac{\mathrm{d}h}{\mathrm{d}x},\ \text{at } y = h(x), \tag{2.6.24b}$$

$$\rho = \rho_{\text{in}}(y),\ \phi = \phi_{\text{in}}(y) \text{ at } x = -\xi. \tag{2.6.24c}$$

In the next section we present a solution method and results for the full lubrication model (2.6.22)-(2.6.24).

2.6.2.2 Full Model Results

We present the analysis of the full model (2.6.22)-(2.6.24) in appendix B, where we follow a very similar method to that used in section 2.6.1.2. The resulting system again lends itself to the method of lines. We therefore discretise in Z using the same discretisation as for the density model (see appendix A). This leaves a DAE system which we solve using ode15s in MATLAB [27, 51], again introducing ghost points at

the Z boundaries to maintain accuracy. We define upstream conditions

$$\rho(-\xi, Z) = \rho_{\text{in}}, \tag{2.6.25a}$$

$$\phi(-\xi, Z) = \phi_{\text{in}}, \tag{2.6.25b}$$

$$y(-\xi, Z) = h(-\xi)Z, \tag{2.6.25c}$$

$$\sigma(-\xi) = -\frac{(1-\bar{u})\rho_{\text{in}}^2(1+A_1\phi_{\text{in}})}{h(-\xi)}, \tag{2.6.25d}$$

from which we can solve a system of algebraic equations for $v_0(-\xi, Z)$, $v_1(-\xi, Z)$, and $v_2(-\xi, Z)$. We can then use the ode solver to solve the DAE system in the fixed domain $-\xi < X < \xi$, $0 < Z < 1$.

We now look at the solutions to the model in three distinct cases. The first is the case of constant viscosity parameters, i.e. $\lambda_i = 1$, $1 \leq i \leq 5$, $\mu_i = 1$, $i = 1, 2$, and thus there is a balance between the isotropic and anisotropic contributions to the stress. This means we have

$$A_1 = 1, \quad A_2 = A_3 = 2, \quad A_4 = A_5 = 4, \quad A_6 = 0. \tag{2.6.26}$$

In the second case isotropic contributions dominate, i.e. $\lambda_k \ll \mu_k$, and so we set

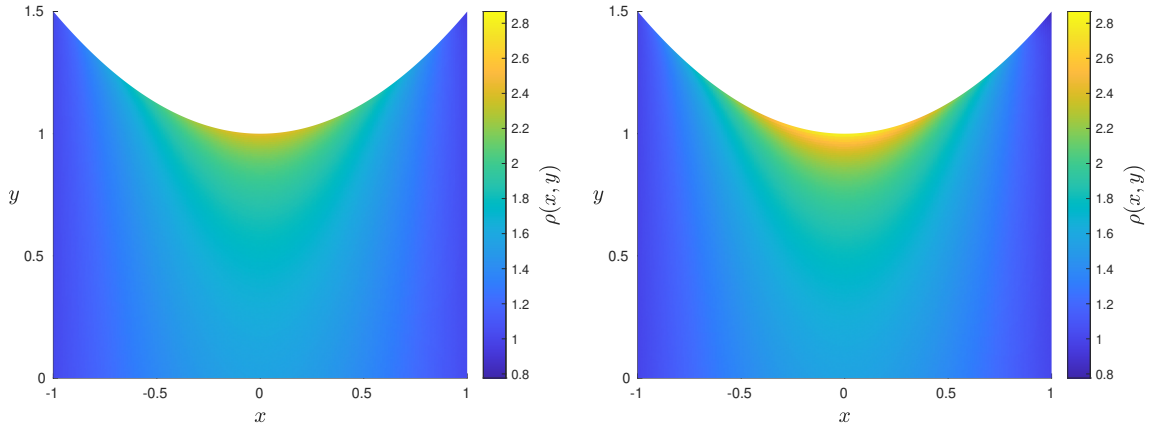
$$A_1 = -1, \quad A_2 = 2, \quad A_3 = -2, \quad A_4 = 0, \quad A_5 = 4, \quad A_6 = -4. \tag{2.6.27}$$

In the third case anisotropic terms dominate, i.e. $\lambda_k \gg \mu_k$. To represent this case we take $\lambda_k/\mu_k = O(10^2)$ and therefore let

$$A_1 = 199, \quad A_2 = 2, \quad A_3 = 398, \quad A_4 = 400, \quad A_5 = 4, \quad A_6 = 396. \tag{2.6.28}$$

We plot results for all three of these cases in figures 2.12-2.17, where we see the same qualitative behaviour as previously, namely an increase in the density in the middle of the region with a higher density near the top roller, and the order increasing for $X > 0$, with a maximum order being achieved at an interior point at $X = \xi$. We also see that decreasing the parameter $\bar{u}$, i.e. increasing the difference in the roller velocities, leads to higher maximum density and order being achieved. A key difference in this model, when compared with the density model in section 2.6.1, is that the symmetry about $x = 0$ is lost, and the density no longer returns to being uniform as the web leaves the region.

Comparing figures 2.14 and 2.15 and figures 2.16 and 2.17 we can examine the effect of the isotropic and anisotropic viscosity parameters on the behaviour of the web. When isotropic components dominate, the increase in the order of fibres leads to



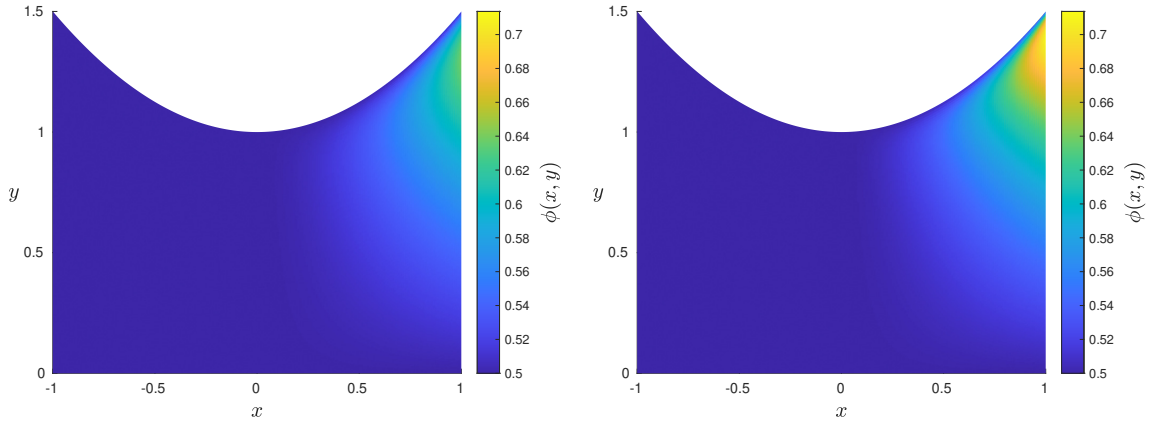
(a) Distribution for $\bar{u} = 0.1$.

(b) Distribution for $\bar{u} = 0.05$.

Figure 2.12: Distribution of the density of fibres with different velocity ratios for a balance between the viscosity parameters, with $\rho_{\text{in}} = 1$, $\xi = 1$, and parameters (2.6.26).

a decrease in the viscosity, and therefore the material becomes easier to deform. We therefore see, in figures 2.14 and 2.15, that the exiting web has a higher density than the 'initial' web at $X = -\xi$, with the exiting density increasing with y. We also see the distribution of the order becoming less localized as isotropic parameters increase compared to anisotropic parameters, as the material becomes easier to deform as the order increases.

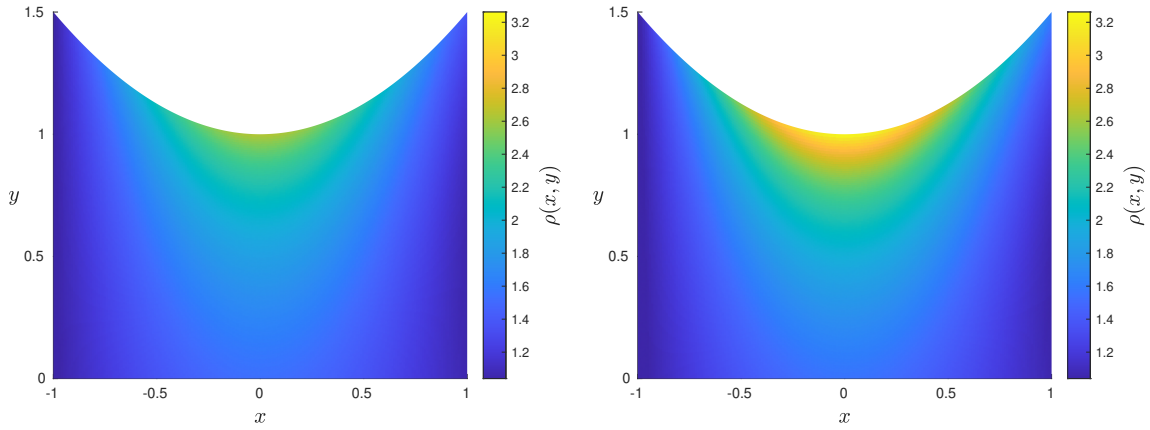
When anisotropic viscosity parameters dominate (see figures 2.16 and 2.17) we see that the density of the exiting web is less than the density of the entry web. In this case, the increase in order leads to an increase in the viscosity, and therefore the material becomes harder to deform, which also results in a very localized maximum order near the top roller. This time the density of the exiting distribution decreases with y, reaching a minimum near the top roller. Comparison with experimental data would be needed to determine which of the cases (2.6.26), (2.6.27), or (2.6.28) is relevant for carbon fibre.



(a) Distribution for $\bar{u} = 0.1$.

(b) Distribution for $\bar{u} = 0.05$.

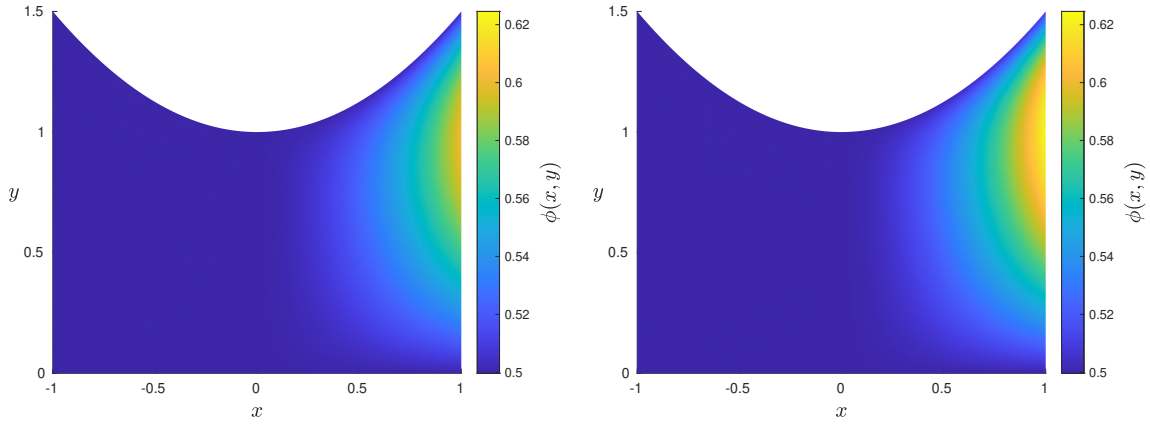
Figure 2.13: Distribution of the order of fibres with different velocity ratios for a balance between the viscosity parameters, with $\phi_{\text{in}} = 0.5$, $\xi = 1$, and parameters (2.6.26).



(a) Distribution for $\bar{u} = 0.1$.

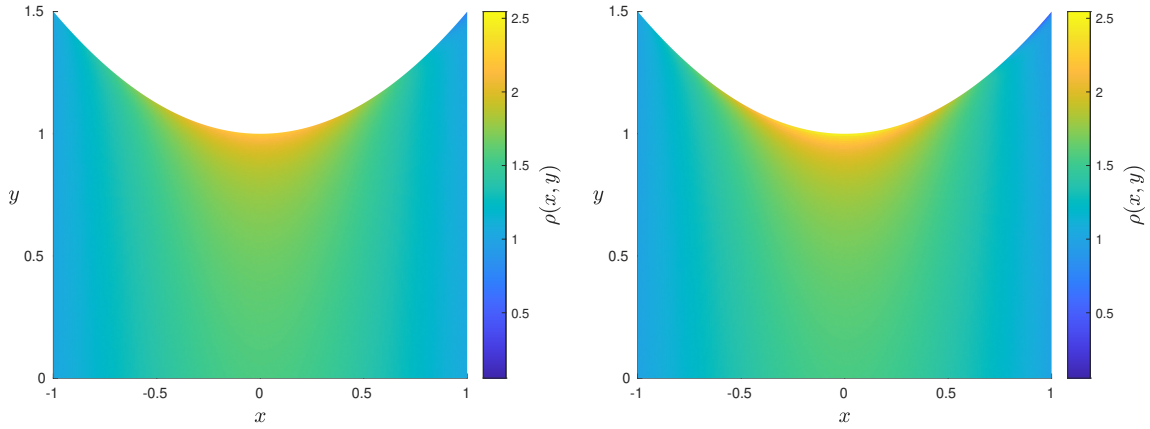
(b) Distribution for $\bar{u} = 0.05$.

Figure 2.14: Distribution of the density of fibres with different velocity ratios when isotropic components of the viscosity dominate, with $\rho_{\text{in}} = 1$, $\xi = 1$, and parameters (2.6.27).



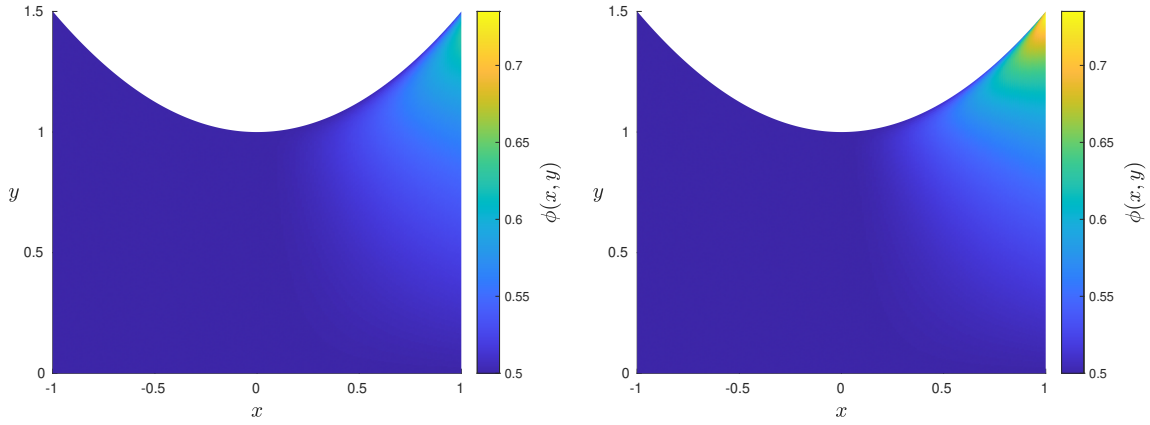
(a) Distribution for $\bar{u} = 0.1$. (b) Distribution for $\bar{u} = 0.05$.

Figure 2.15: Distribution of the order of fibres with different velocity ratios when isotropic components of the viscosity dominate, with $\phi_{\text{in}} = 0.5$, $\xi = 1$, and parameters (2.6.27).



(a) Distribution for $\bar{u} = 0.1$. (b) Distribution for $\bar{u} = 0.05$.

Figure 2.16: Distribution of the density of fibres with different velocity ratios when anisotropic components of the viscosity dominate, with $\rho_{\text{in}} = 1$, $\xi = 1$, and parameters (2.6.28).



(a) Distribution for $\bar{u} = 0.1$.

(b) Distribution for $\bar{u} = 0.05$.

Figure 2.17: Distribution of the order of fibres with different velocity ratios when anisotropic components of the viscosity dominate, with $\phi_{\text{in}} = 0.5$, $\xi = 1$, and parameters (2.6.28).

2.7 Conclusions

We have presented a continuum model for a web of fibres moving through regions of the carding machine, using the work of Lee [38], which models the carding of polyester and cotton, as a starting point. We derived governing equations using conservation of mass, conservation of momentum, and a kinematic condition on the director. We then proposed constitutive laws for the stress tensor and the ordering of fibres, initially described in the work of Lee [38]. The stress-rate-of-strain relation is derived by treating the web as an anisotropic viscous fluid. The evolution equation for the order parameter assumes that the order of the fibres increases due to the web being stretched, but can never decrease. We then used the slender geometry of the nip region to make a lubrication-type approximation.

We showed that the model can be reduced to 2D, and, with the simplifying assumption of uniform viscosity, were then able to solve the resulting PDE system using the method of characteristics. This simplified model gave us insight into how the density and order of fibres changes in the region between the worker and swift in the carding machine. Relaxing the uniform viscosity assumption, we then presented a numerical scheme to solve the resulting coupled PDE system. The numerical solution involved deriving a finite difference scheme, discretizing in one transformed spatial direction, and solving the resulting DAE system using the method of lines. We showed that including the effect of density on the viscosities is important for realistic results.

Including the order in the viscosities then allowed us to study how the isotropic and anisotropic viscosity parameters contribute towards the deformation of the web.

We focused on the region between the swift and the worker, which both move in the same direction, and found that the density of fibres increases in the middle of the region, with a greater density being observed near the worker. The order parameter increases across this region, with the maximum order being achieved at an interior point near the worker, with the position of this maximum depending on the viscosity parameters. We showed that the maximum order parameter achieved increases as the velocity ratio, $\bar{u}$, between the cylinders decreases, equivalent to a greater difference in the velocities. Given that the worker generally moves at a lower velocity than the stripper, this model prediction supports industrial observations that most of the ordering takes place between the worker and the swift. Here we see better ordering with a greater velocity contrast but later on we will see that there is an optimisation problem for the velocities because at some point the fibres will start to break.

A possible extension to this approach is to derive an elastic/plastic model that is likely more physically realistic. This would include reversible deformation of the web when subject to low stresses, and irreversible when the stress is above some yield stress. Another limitation is that the model presented in this chapter assumes that the web is always continuous. This allows us to describe ordering of fibres, but not how clumps or "tows" of fibres are broken up, which is one of the main aims of carding. Models for this process are derived in chapters 4 and 5.

Chapter 3

A Microscale Combing Model

3.1 Overview and Literature Review

In this section we derive simple microscale models examining the interaction between carding teeth and individual fibres. There are various ideas from the literature that we use in these models. Wang and Johnson [59] model the disentangling of two twisted fibres by a combing pin, focusing on how fibre breakage relates to the pin speed. In our situation we do not have twisted fibres, so instead we model the fibres being rotated and straightened, with frictional forces acting between them. Maltin and Mayer [43] model the disentanglement of a fibre from a clump in the textile industry, by relating the tensions in the fibre to the frictions and normal forces at the crossing points with other fibres. In our models we discuss possible frictional behaviours both at fibre-fibre interaction points, and at fibre-tooth interaction points. This work is extended by Li and Johnson [41] who conclude that if a fibre is withdrawn from being entangled with other fibres and combing pins, there is a critical withdrawal speed, above which the strain in the fibre will cause it to break. We carry out similar analysis, with a focus on straight carbon fibres.

In section 3.2 we derive a model for a pin combing through two fibres, focusing on the frictional forces between the fibres and the tooth, as well as the tension in the fibres. In section 3.3 we extend this model to include a third horizontal fibre, and then generalise this model in section 3.4.

3.2 Two Fibre Model

In this section we derive a simple microscale model for the 'combing' effect of a tooth pushing through a web of fibres. We follow a similar problem to that presented in [59] for the disentangling of two twisted fibres by a combing pin. We have the

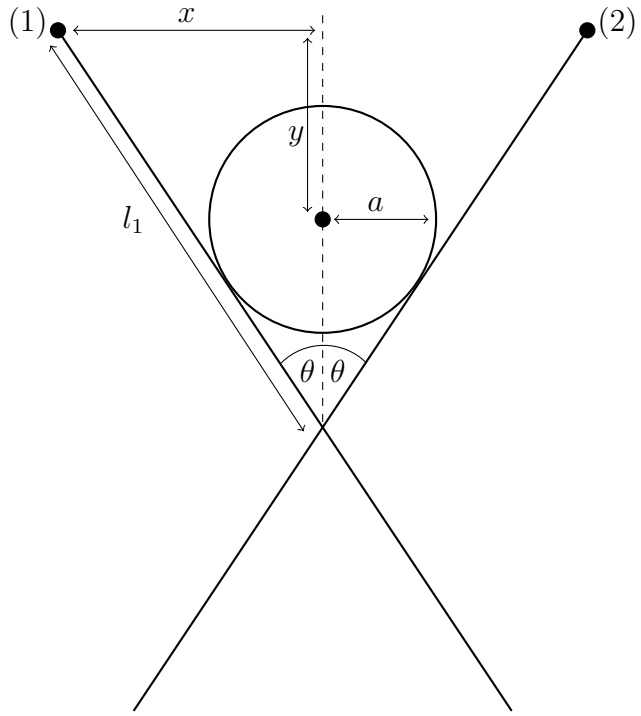


Figure 3.1: Schematic of a pin being dragged downwards to comb two overlapping fibres.

key difference that the carbon fibres we are modelling are naturally straight, and do not need to be 'untwisted', but instead 'aligned'. We start by examining the simple model problem of a tooth (or pin) moving through two overlapped fibres, modelled as rigid straight rods, as shown schematically in figure 3.1.

We assume that the two fibres are held a distance $2x$ apart at their ends, at points (1) and (2), due to the presence of other fibres in the surrounding web. From this point on we refer to the fibre fixed at (1) as fibre 1, and the fibre fixed at (2) as fibre 2. We assume that the circular tooth of radius a is dragged through the fibres with force F. For simplicity, we take the tooth to move along the mid-line between the two end points (1) and (2). The forces acting on the tooth are shown in figure 3.2, where N_1 and f_1 are the normal and frictional forces on the pin respectively, due to the contact between the pin and the fibres. We assume Coulomb friction at these contact points between the pin and the fibres, as in [43], and assume that the frictional force at the crossing point of the two fibres is proportional to the relative velocity of the two. We therefore do not need to consider forces out of the plane, and can use a simple 2D model to begin with.

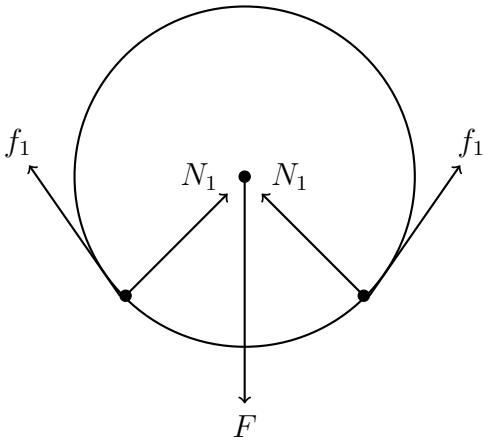


Figure 3.2: Force diagram of the pin being pushed with force F.

Performing a force balance on the pin, using figure 3.2, leads to

$$2f_1 \cos\theta + 2N_1 \sin\theta - F = 0, \tag{3.2.1}$$

where θ is the angle shown in figure 3.1. The distance y moved by the centre of the tooth relative to the fibre end points is related to θ by

$$a = x\cos\theta - y\sin\theta. \tag{3.2.2}$$

Using Coulomb's law of friction, and assuming the system to be slipping, we have

$$f_1 = \mu N_1, \tag{3.2.3}$$

where μ is the coefficient of friction between the fibre and the tooth which is assumed to be constant.

We now turn our attention to the forces on the fibres. To calculate the frictional force at the crossover point of the fibres, we have to calculate the relative velocity at this point. If we let $l_1 = x/\sin\theta$ be the distance from the fixed point (1) to the crossing point, as seen in figure 3.1, we find that the velocity of fibre 1 with respect to fibre 2 at the crossing point is given by

$$\boldsymbol{v} = l_1\dot{\theta}\begin{pmatrix} 2\cos\theta \\ 0 \end{pmatrix}, \tag{3.2.4}$$

where $\dot{\theta}$ is the first derivative of θ with respect to time. The frictional force, $\boldsymbol{f}_2$, on fibre 1 acts horizontally to oppose this velocity, and is therefore given by

$$\boldsymbol{f}_2 = -2Al_1\dot{\theta}\cos\theta\begin{pmatrix} 1 \\ 0 \end{pmatrix} = f_2\begin{pmatrix} 1 \\ 0 \end{pmatrix}, \tag{3.2.5}$$

where

$$f_2 = -2Ax\dot{\theta}\cot\theta, \tag{3.2.6}$$

and A is a scalar. We will take A to be constant for now, although it could also depend on both $|\boldsymbol{v}|$ and l_1 [43]. We note that we expect θ to decrease as the pin is moved downwards, and therefore f_2 is positive.

As shown in figure 3.3, performing a moment balance on fibre 1 about the fixed point (1) yields the equation

$$\frac{N_1}{\sin\theta}\left(a\cos\theta - x\right) + \frac{f_2 x}{\tan\theta} = 0. \tag{3.2.7}$$

If we rearrange (3.2.7) and substitute equation (3.2.5) in we get the result

$$N_1 = -\frac{2Ax\dot{\theta}\cos^2\theta}{\sin\theta\left(1 - \frac{a}{x}\cos\theta\right)}. \tag{3.2.8}$$

Substituting (3.2.8) and (3.2.3) into (3.2.1) we get a relation between the force, F, applied to the tooth, and the rate at which the fibres open, namely

$$F = -\frac{4Ax^2\dot{\theta}\cos^2\theta}{\sin\theta\left(x - a\cos\theta\right)}\left(\mu\cos\theta + \sin\theta\right). \tag{3.2.9}$$

The frictional forces at the contact points and crossing point induce tensions in the fibres. The tension induced in fibre 1 between the two contact points is given by

$$T_2 = -2Ax\dot{\theta}\cos\theta. \tag{3.2.10}$$

In the carding machine, the teeth move through fibres at constant velocity due to the rotation of the surfaces of the rollers. We therefore assume the motion of the tooth to be vertically downwards at constant speed, V, so the position of the midpoint of the tooth is represented by

$$y = y_0 + Vt. \tag{3.2.11}$$

Differentiating with respect to t leads to

$$\dot{\theta} = -\frac{V\sin^2\theta}{(x - a\cos\theta)}. \tag{3.2.12}$$

As anticipated above, for positive V, θ is decreasing, as we would expect for the fibres to be straightened and the tooth to move through. For the fibres to be completely combed, we require θ to decrease to

$$\theta_{\min} = \sin^{-1}\left(\frac{x}{L}\right), \tag{3.2.13}$$

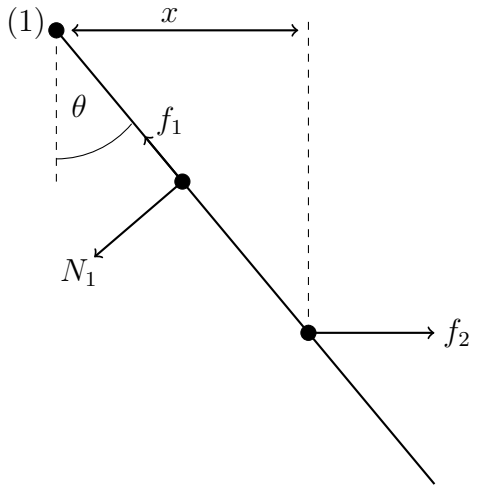


Figure 3.3: Diagram of the forces on fibre 1.

at which point the two fibres are no longer in contact, where L is the full length of the fibres.

Substituting equation (3.2.12) into (3.2.9) and (3.2.10) gives

$$F = \frac{4AVx^2\cos^2\theta\sin\theta}{(x - a\cos\theta)^2}\left(\mu\cos\theta + \sin\theta\right), \tag{3.2.14}$$

$$T_2 = \frac{2AVx\cos\theta\sin^2\theta}{(x - a\cos\theta)}. \tag{3.2.15}$$

We note that the forces F and T_2 are both proportional to the velocity V. We expect a higher tension to result in a higher chance that the fibres will break. Relation (3.2.15) therefore suggests that if the tooth is moving at a higher velocity, the fibres are more likely to break. In our continuum modelling, in chapter 2, we concluded that a high velocity difference between cylinders is optimal to achieve maximum ordering. This will however result in higher tooth velocity, V, and therefore could lead to more breakage. This prediction is, however, dependent on our assumption that A is constant.

We now use (3.2.2), (3.2.11), (3.2.14), and (3.2.15) to plot how the forces F and T_2 vary with time. Without loss of generality, we normalize the problem such that $x = V = 1$, and we also choose the constant parameters $\mu = A = 1$. The decrease of the combing angle θ with time is shown in figure 3.4, and the evolution of the tension T_2 in the fibre and the force F required to drag the tooth through are shown in figures 3.5 and 3.6 respectively. We observe that both F and T_2 initially increase to maximum values. We infer that it initially becomes harder to comb through the fibres until a certain angle is overcome, after which it becomes easier.

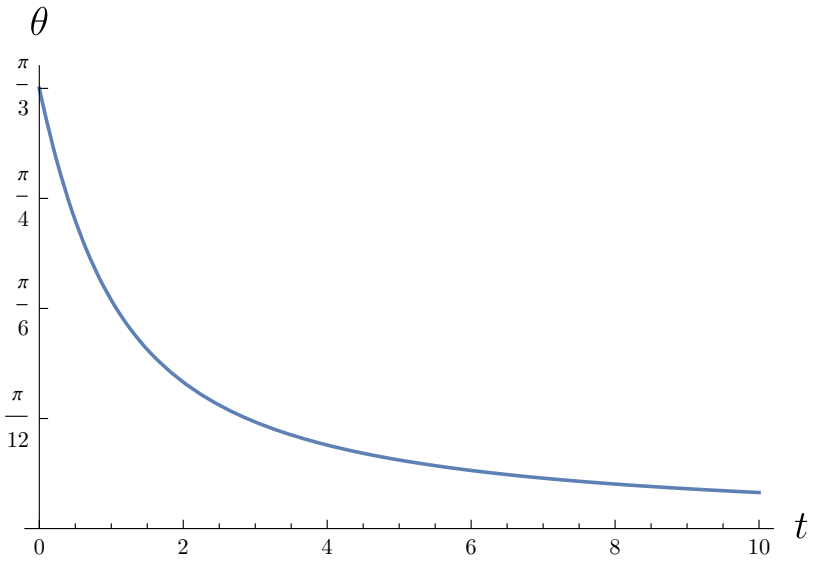


Figure 3.4: The angle θ as the tooth is moved through the fibres at a constant speed against time with $a = 0.1$ and $\theta(0) = \pi/3$.

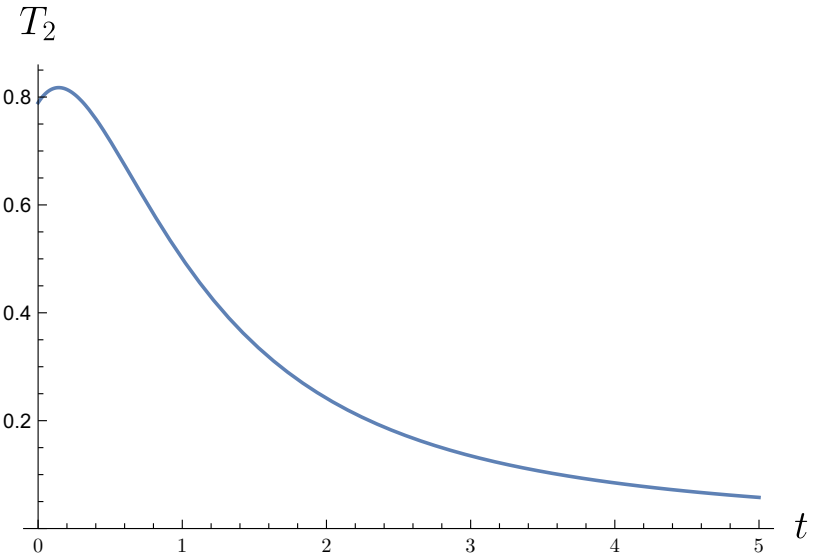


Figure 3.5: The tension, T_2, in the fibre as the tooth is moved through the fibres at a constant speed, against time, t, with $a = 0.1$, $\mu = 1$, and $\theta(0) = \pi/3$.

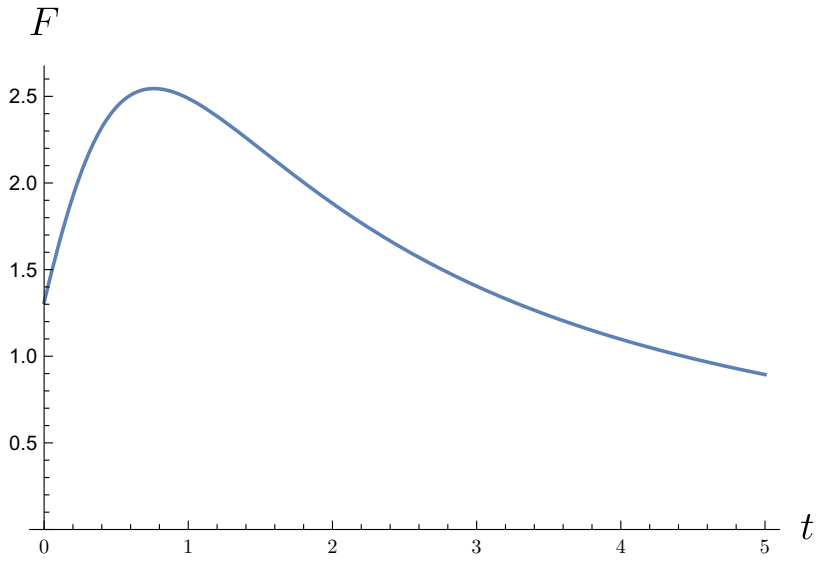


Figure 3.6: The force, F, required to move the tooth through the fibres at a constant speed, against time, t, with $a = 0.1$, $\mu = 1$, and $\theta(0) = \pi/3$.

In the model problem studied above, the tooth will always comb through the fibres, although if the velocity is too high the tension in the fibres could increase above the breaking stress. In the next section we will consider a more complex problem by adding another fibre.

3.3 Symmetric Three-Fibre Model

In this section we consider a web of 3 crossed fibres, and the key question we want to answer is: can the fibres be combed, or do they become knotted together and break? We start by examining the system shown in figure 3.7, where a horizontal fibre is added a distance z below the fixed points (1) and (2). We now have 3 fibre crossing points, which we denote (a), (b), and (c). We assume that all 3 fibres are the same length, and that the system is symmetrical.

The relative velocity of fibre 1 to fibre 3 at point (c) is given by

$$\boldsymbol{v} = \begin{pmatrix} l_2\dot{\theta}\cos\theta \\ l_2\dot{\theta}\sin\theta + \dot{z} \end{pmatrix}, \tag{3.3.1}$$

where l_2 is the length from fixed point (1) to the crossing point, (c). The vertical component of the friction between the two fibres must be zero for the forces on the horizontal fibre to balance. Our assumption that the friction is proportional to the relative velocity therefore implies that

$$\dot{z} + l_2\dot{\theta}\sin\theta = 0. \tag{3.3.2}$$

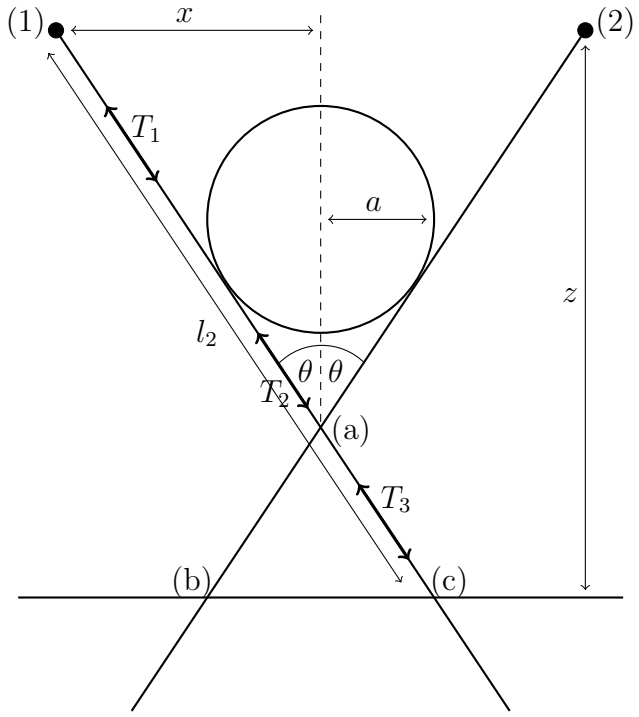


Figure 3.7: Schematic of a pin being dragged downwards to comb three overlapping fibres that interact at crossing points (a), (b), and (c).

Since $z = l_2 \cos\theta$, it follows from equation (3.3.2) that $\dot{l}_2 = 0$ so, as the fibres are combed, the length l_2 remains constant. Substituting (3.3.2) into (3.3.1) leads to

$$\boldsymbol{v} = l_2 \dot{\theta} \cos\theta \begin{pmatrix} 1 \\ 0 \end{pmatrix}. \tag{3.3.3}$$

Making the same constitutive assumption as in section 3.2, we deduce that the horizontal interaction force at point (c) is given by

$$f_3 = -A l_2 \dot{\theta} \cos\theta, \tag{3.3.4}$$

where A is taken as a constant. The force balance on the pin remains the same as in the previous section, and results in equation (3.2.1). A moment balance on fibre 1 leads to the result

$$N_1 = \frac{f_2 \cos\theta + f_3 \frac{z}{x} \sin\theta}{1 - \frac{a}{x}\cos\theta}, \tag{3.3.5}$$

where f_2 is the horizontal friction at (a), given by (3.2.5). If we say that T_1, T_2, and T_3 are the tensions in fibre 1 between (1) and the pin, between the pin and (a), and between (a) and (c), respectively, then we deduce that

$$T_2 - T_3 = f_2 \sin\theta = -2A l_2 \dot{\theta} \cos\theta \sin\theta, \tag{3.3.6}$$

$$T_3 = f_3 \sin\theta = -A l_2 \dot{\theta} \cos\theta \sin\theta, \tag{3.3.7}$$

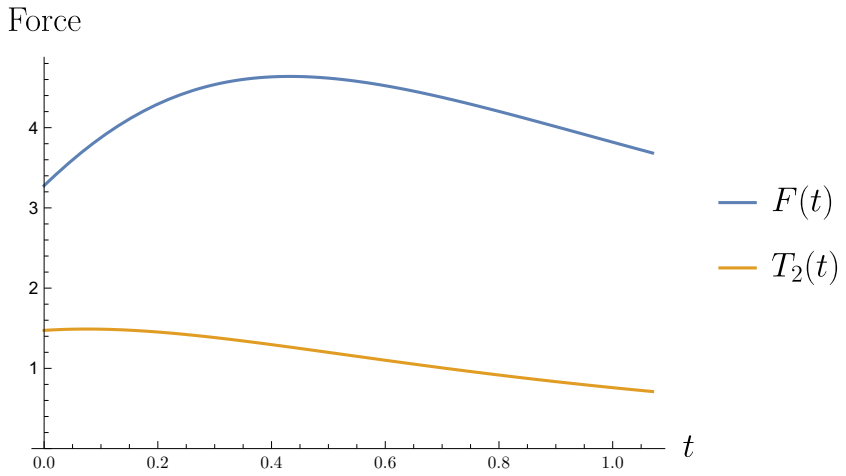


Figure 3.8: The force, F, and tension, T_2, against time, t, using equations (3.3.9) and (3.3.10) respectively, plotted for $a = 0.1$, $\mu = 1$, $l_2 = 2$, and $\theta(0) = \pi/3$.

which leads to the result

$$T_2 = -A\left(2l_1 + l_2\right)\dot{\theta}\cos\theta\sin\theta. \tag{3.3.8}$$

Using equations (3.2.1), (3.2.3), (3.2.5), (3.2.12), (3.3.4), (3.3.5), and (3.3.8), we obtain the equations

$$F = \frac{2AV\cos^2\theta\sin\theta\left(2x + \frac{l_2^2}{x}\sin^2\theta\right)}{x\left(1 - \frac{a}{x}\cos\theta\right)^2}\left(\mu\cos\theta + \sin\theta\right), \tag{3.3.9}$$

$$T_2 = \left(2x + l_2\sin\theta\right)\frac{AV\cos\theta\sin^2\theta}{x\left(1 - \frac{a}{x}\cos\theta\right)}. \tag{3.3.10}$$

As in section 3.2, θ is determined by

$$x\cos\theta - \left(y_0 + Vt\right)\sin\theta = a. \tag{3.3.11}$$

We again normalize such that $x = V = 1$ without loss of generality and choose parameters $\mu = A = 1$. We plot F and T_2 versus t in figure 3.8, observing similar behaviour to the 2-fibre case, i.e. both forces initially increasing, and then decreasing after a critical time where maximum is achieved.

Now, as in the previous setup with 2 fibres, there will be a point when the model breaks down or changes, in this case either because the crossing points (b) and (c) detach, or because the triangle (a)-(b)-(c) shrinks to zero area. We want to know which of these possibilities occurs first, and at what time. We have already determined that l_2 is a constant so, assuming that the fibres are crossed initially, points (c) and (b) stay the same distance away from (1) and (2), respectively. These two crossover points

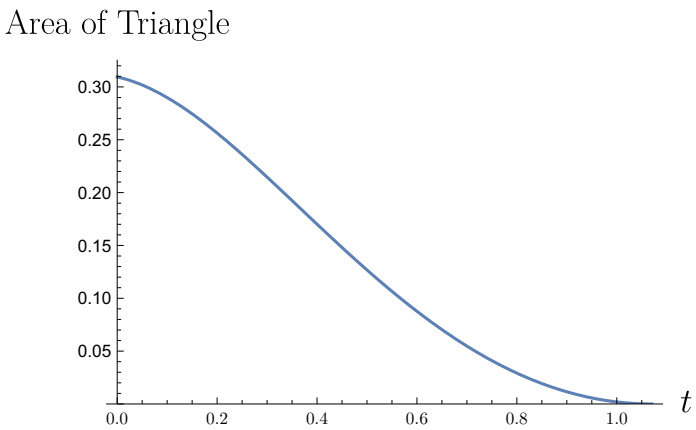


Figure 3.9: The area of triangle (a)-(b)-(c) against time for $a = 0.1$, $l_2 = 2$, and $\theta(0) = \pi/3$.

are therefore not combed out, but eventually converge, when $x = l_2 \sin\theta$, and all three points meet at the same time. Indeed, the area of triangle (a)-(b)-(c) is given by

$$\text{Area} = \cot\theta(l_2 \sin\theta - x)^2. \tag{3.3.12}$$

In figure 3.9 we show that the area of the triangle (a)-(b)-(c) quickly reduces to 0, before anything can be combed. At that point, a knot has formed in the web, and the only way for the tooth to carry on through is for the fibres to break.

3.4 Generalised Three-Fibre Model

In the previous section we added a horizontal fibre that preserves the reflectional symmetry of the other two fibres. In this section we generalise this setup by adding a fibre at an angle α to the horizontal, as shown schematically in figure 3.10. We define l_2 as the length along fibre 1 from point (1) to crossing point (c), and l_3 as the length along fibre 2 from point (2) to crossing point (b). We define $(X_3, -Z_3)$ as the centroid of fibre 3, while d_1 and d_2 denote the distances of this point from crossing points (c) and (b), respectively.

We carry out a similar analysis to that in section 3.3, noting that the system is no longer symmetric. The vertical force balance on the tooth now gives

$$(N_1 + N_2)\sin\theta + (f_1 + f_2)\cos\theta - F = 0, \tag{3.4.1}$$

where the subscripts 1 and 2 correspond to the interactions with fibre 1 and fibre 2 respectively. Again assuming Coulomb friction between the fibres and the pin, we have that

$$F = (N_1 + N_2)(\sin\theta + \mu\cos\theta). \tag{3.4.2}$$

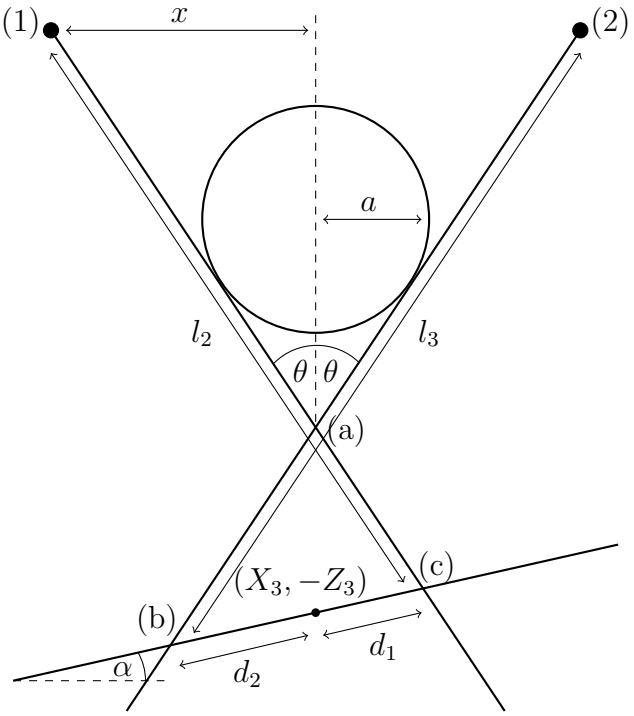


Figure 3.10: Schematic of a pin being dragged downwards to comb three overlapping fibres.

In section 3.3 we found that the distance l_2 from the fixed point (1) to the crossover point (c) remains constant. Now we will argue that an equivalent conservation principle holds for the crossover points (b) and (c) in figure 3.10. Indeed, whenever a fibre has two crossover points but is subject to no other forces, the frictional forces at the crossover points must be equal and opposite and, by a moment balance, must therefore be parallel to the fibre, as depicted in figure 3.11. Since the frictional force is assumed to be parallel to the relative velocity, it follows that the contact points can only move parallel to the highlighted fibre in figure 3.11 and not along either of the two fibres that cross it.

We deduce that the two lengths l_2 and l_3 in figure 3.10 must remain constant (as may also be shown in a more long-winded exercise as in section 3.3). It then follows by trigonometry that the angle α and the distance $d_1 + d_2$ between the crossover points in figure 3.10 are given by

$$\tan\alpha = \frac{(l_3 - l_2)\cos\theta}{(l_2 + l_3)\sin\theta - 2x}, \tag{3.4.3}$$

$$(d_1 + d_2)^2 = (l_3 - l_2)^2 + 4\,(l_2\sin\theta - x)\,(l_3\sin\theta - x)\,. \tag{3.4.4}$$

The reaction forces N_1 and N_2 are determined from moment balances on fibres 1 and 2,

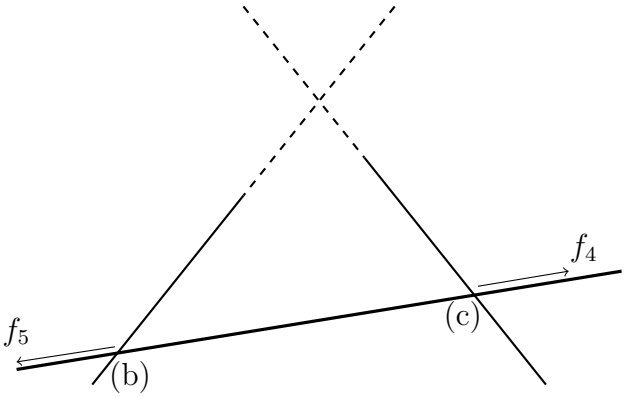


Figure 3.11: Frictional forces acting on the third nonhorizontal fibre.

which lead to

$$N_1 + N_2 = \frac{\sin\theta}{(x - a\cos\theta)}\left[2f_3 x\cot\theta + f_4\left(l_3\cos\left(\theta+\alpha\right) + l_2\cos\left(\theta-\alpha\right)\right)\right], \quad (3.4.5)$$

where f_3 and f_4 are the magnitudes of the interaction forces at crossover points (a) and (b), respectively. As above, we take these forces to be proportional to the relative velocity between the fibres at the crossover points, so that

$$f_3 = -2Ax\dot{\theta}\cot\theta, \quad (3.4.6)$$

and

$$\begin{aligned} f_4 &= -\frac{A}{2}\left(\dot{d}_1 + \dot{d}_2\right) \\ &= -\frac{A\dot{\theta}\cos\theta\left(2l_2 l_3\sin\theta - (l_2+l_3)x\right)}{d_1+d_2}. \end{aligned} \quad (3.4.7)$$

Putting everything together, we find that the force on the tooth is given by

$$F = -\frac{2A\cos^2\theta\left(\sin\theta+\mu\cos\theta\right)\dot{\theta}}{(x-a\cos\theta)\sin\theta}\left[2x^2 + \frac{\sin^2\theta\left(2l_2 l_3\sin\theta - (l_2+l_3)x\right)^2}{(d_1+d_2)^2}\right]. \quad (3.4.8)$$

Using equations (3.2.12) and (3.4.3), we see that $\dot{\alpha} > 0$ if $\alpha > 0$, which we assume without loss of generality, and so α increases with time.

Examining figure 3.10 we can see that, if the area of triangle (a)-(b)-(c) reduces to 0 before α reaches $\pi/2-\theta$ then the system will behave as in section 3.3: a knot will form and the fibres will break. If the reverse is true however, then fibre 3 will become parallel to fibre 2, and points (a) and (c) will meet. This situation can then be treated in a similar way to the 2-fibre case, and the system will be combed. Without loss of

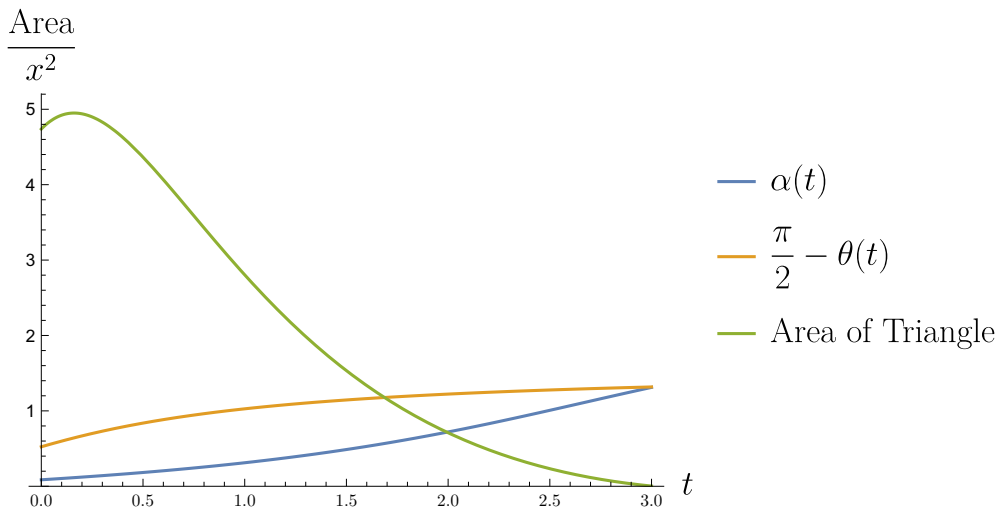


Figure 3.12: The area of triangle (a)-(b)-(c), the angle, α, and $\pi/2-\theta$, against time, t. Plotted for $\theta(0) = \pi/3$, $a = 0.1$, $l_2/x = 4$, and $l_3/x = 5$.

generality, suppose that $l_2 < l_3$ and recall that both are constant. It may then be shown that the triangle cannot shrink to zero area before fibre 3 is parallel to fibre 2.

The area of triangle (a)-(b)-(c) is given by

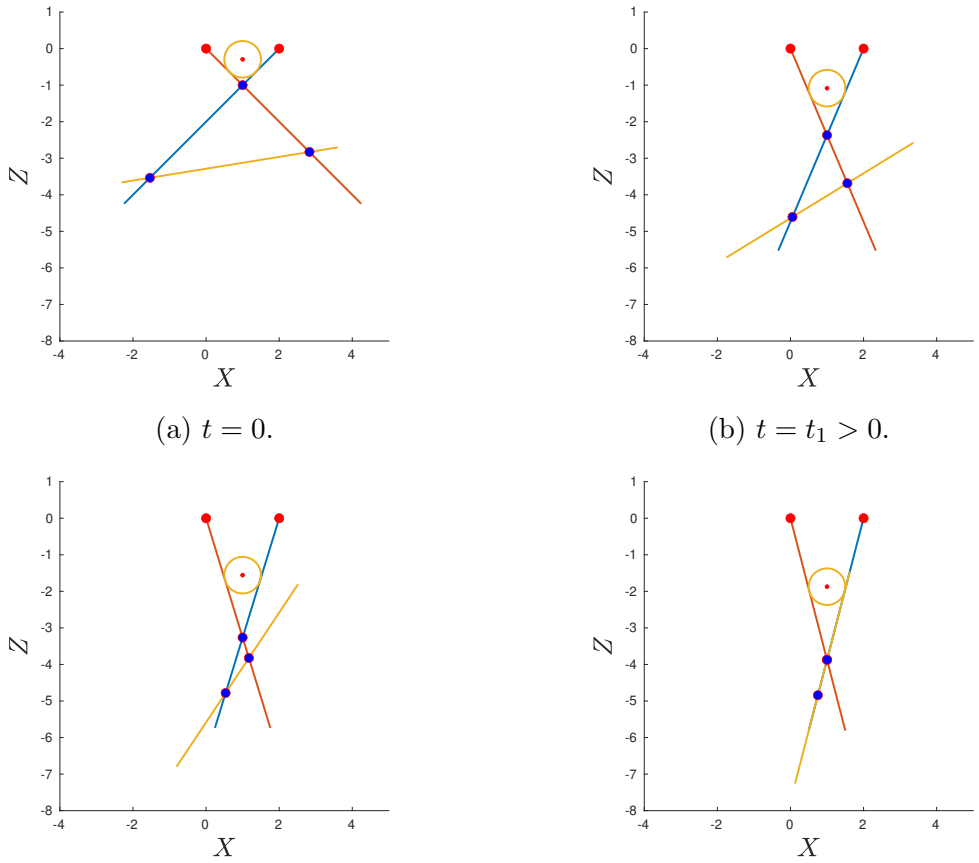
$$\text{Area} = \cot\theta\,(l_2\sin\theta - x)\,(l_3\sin\theta - x)\,. \tag{3.4.9}$$

We plot this area, along with angles α and $\pi/2-\theta$ in figure 3.12. We see that the area reaches zero precisely when $\alpha = \pi/2-\theta$. Indeed, equation (3.4.3) may be rearranged to

$$\tan(\alpha+\theta) = \tan\theta + \frac{l_3 - l_2}{2\cos\theta\,(l_2\sin\theta - x)}, \tag{3.4.10}$$

which shows that $\alpha \to \pi/2-\theta$ as $\sin\theta \to x/l_2$.

We show the three fibres being combed by a tooth in figure 3.13 at different times from $t = 0$ to $t = t_{\text{end}}$, where the final time, t_{end}, is such that $\sin\theta = x/l_2$. We again normalise such that $x = 1$ and prescribe initial conditions with $l_3 > l_2$. We observe that the crossover points (a) and (c) coalesce, at which point fibres 2 and 3 become parallel. The problem is then reduced to that of only two fibres, which can be combed, as shown in section 3.2. Given that $l_2 < l_3$ and they are both constant, the three crossover points can never all meet at the same point, and the tooth will always be able to pass through without breaking the fibres. This suggests that the symmetric case presented in section 3.3 is degenerate because as soon as any symmetry is lost a knot does not form, and so in practice we will not observe knots forming.



(a) $t = 0$.

(b) $t = t_1 > 0$.

(c) $t = t_2 > t_1$.

(d) $t = t_{\text{end}}$.

Figure 3.13: The system of 3 fibres at different times for $\theta(0) = \pi/4$, $a = 0.5$, $l_2 = 4$, and $l_3 = 5$.

3.5 Conclusions

In this chapter we have presented three microscale model problems for a carding tooth combing through a finite set of fibres. We started by focusing on a symmetric system of two fibres crossing at a point. Our analysis allowed us to model the evolution of the fibre arrangement with time, while deriving expressions for the tooth force and tensions in the fibres. This model was then extended in sections 3.3 and 3.4 to include interaction with a third fibre. We showed that for a horizontal fibre the system cannot be 'combed out' and the fibres must therefore break for the tooth to continue through. For the general three-fibre model presented in section 3.4, we showed that no knot forms, and therefore the only mechanism for fibre breakage is the increase of fibre tension above the breaking stress. In all these models the force of the tooth and the tension in the fibres were shown to be proportional to the velocity

of the tooth, suggesting that more breakage will occur for faster teeth.

These models could be expanded further to develop a fully generalised model for a network of fibres, where any number of fibres and crossover points could be considered. This would require a network model that could give insight into how tension and frictional forces propagate through a network of fibres, and therefore provide a more detailed description of fibre breakage.

Chapter 4

Opening of Carbon Fibre Tows

4.1 Background and Literature Review

This chapter concerns a particular type of feedstock used in the carbon fibre carding process, namely 'tows' of fibres. A tow is a bundle of typically thousands of individual fibres held together by a resin and adhesion between the fibres. Photos of typical tows are shown in figure 4.1. One of the main functions of the carding process is to create a homogeneous web of fibres, shown in figure 4.2, which requires these large tows to be broken up, or 'individualized' [19]. Throughout this chapter we refer to this breakup as the 'opening' of tows. In this chapter we derive and solve mechanical models for an individual tow being split apart by a tooth in the carding machine. Then, in chapter 5, we present a probabilistic model for a distribution of tows moving through the carding machine.

There are a number of existing studies that focus on fibre tows. The frictional behaviour of two carbon fibre tows in contact is studied in [11]. This work proposes an experiment where a tow is wrapped around a metal friction drum, a problem similar to the one presented in section 4.4, where a Capstan relation is used to model the tension in a tow wrapped around a tooth. Similar experiments were studied in [12], again focusing on Capstan-style problems.

A microscale model of the interaction between a fibre and the carding teeth is studied in [36]. They describe that an important factor is the retention of the fibres on a roller against the centrifugal force it produces. We will discuss this idea in more detail in chapter 5. Another microscale model is found in [21], where the setup of the carding teeth is examined.

We model a single tow using the elastica equation [40,42,58]. The elastica equation has been used in modelling a variety of applications, including a ruck in a rug [56] and the deflection of a diving board [25]. The work of Obreimoff [44] models the splitting



Figure 4.1: Photo of a collection of carbon fibre tows before carding, from Gen 2 Carbon.

of mica using the elastica equation, and focuses on the energy required to overcome the adhesion of mica. Obreimoff deduces that the curvature, κ, at the splitting point is related to adhesive surface energy density Q by

$$Q = \frac{B\kappa^2}{4b}, \tag{4.1.1}$$

where B and b are the bending stiffness and breadth, respectively, of the mica layer. We deduce from equation (4.1.1) that, to overcome the adhesion energy and split the mica, a critical curvature, κ_0, must be reached, and this critical curvature is given by

$$\kappa_0 = \sqrt{\frac{4bQ}{B}}. \tag{4.1.2}$$

We use equation (4.1.2) in section 4.3 to model the splitting of a carbon fibre tow.

4.2 Model Derivation

We begin by focusing on a simple problem to determine when a tow will open due to interaction with a single tooth. We model the tow as two joined identical elasticas being pushed apart by a tooth of radius a, as shown schematically in figure 4.3. A tension, T_∞, is applied by pushing the circular tooth through horizontally while holding the elasticas' ends. In reality this holding is done by the other tows or a web of fibres analogous to the one discussed in chapter 2. In what follows we focus on the top elastica, as the analysis for the bottom one follows by symmetry.



Figure 4.2: A photo of the final product, from Gen 2 Carbon.

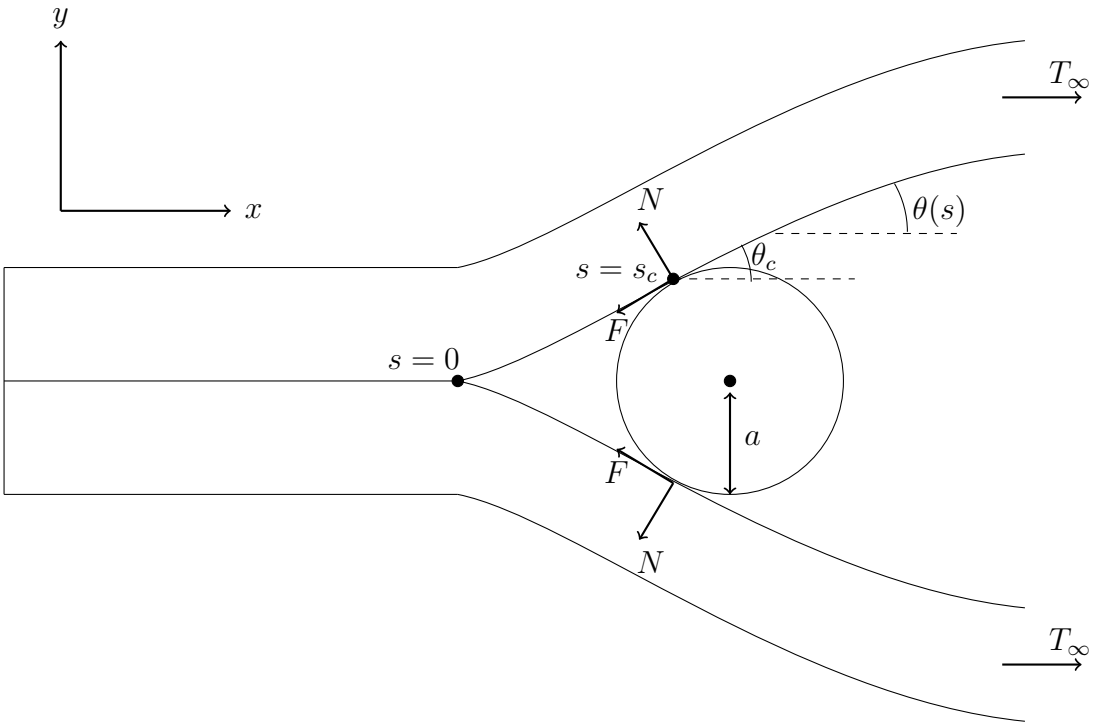


Figure 4.3: Schematic of a tooth interacting with a tow, modelled as two elasticas.

We define the angle the elastica makes with the horizontal as $\theta(s)$, where s measures arclength along the elastica from the meeting point of the two. We introduce the notation $\theta(s_c) = \theta_c$, where $s = s_c$ at the contact point with the tooth, where there are normal and frictional forces between the tooth and elastica, denoted by N and F.

The governing equations for the elastica [25, 40, 58] are

$$B\frac{\mathrm{d}^2\theta}{\mathrm{d}s^2} = F_x \sin\theta - F_y \cos\theta, \tag{4.2.1a}$$

$$\frac{\mathrm{d}F_x}{\mathrm{d}s} = (N\sin\theta_c + F\cos\theta_c)\,\delta\,(s - s_c)\,, \tag{4.2.1b}$$

$$\frac{\mathrm{d}F_y}{\mathrm{d}s} = (-N\cos\theta_c + F\sin\theta_c)\,\delta\,(s - s_c)\,, \tag{4.2.1c}$$

where (F_x, F_y) are the internal force components in the elastica, B is the bending stiffness, and δ is the Dirac delta-function. We have an applied horizontal force at ∞ and zero force to the left of the tooth, and we therefore impose the boundary conditions

$$F_x \to T_\infty, \quad F_y \to 0 \quad \text{as} \quad s \to \infty, \tag{4.2.2}$$

$$F_x(0) = 0. \tag{4.2.3}$$

From the geometrical setup of the problem, we also have

$$\int_0^{s_c} \sin\theta \; \mathrm{d}s = a\cos\theta_c, \tag{4.2.4}$$

$$\theta(0) = 0, \quad \theta\,(s_c) = \theta_c, \quad \theta(\infty) = 0. \tag{4.2.5}$$

We assume limiting Coulomb friction, i.e.

$$F = \mu N, \tag{4.2.6}$$

where μ is the coefficient of friction. We note that (4.2.1) defines a 4th-order system of ODEs, with additional unknowns N, F, s_c, and θ_c, so the 8 conditions (4.2.2)-(4.2.6) are needed to define a well-posed problem.

We suppose that there is a prescribed maximum curvature, κ_0, such that, when the curvature at $s = 0$ is less than κ_0, the contact point is stuck and, when $\mathrm{d}\theta/\mathrm{d}s(0) = \kappa_0$, the elasticas peel apart. This hypothesis is supported by equation (4.1.2) derived using a model for the splitting of mica [44]. Thus for $\mathrm{d}\theta/\mathrm{d}s(0) < \kappa_0$, the elasticas are stuck together and T_∞ is specified, and when $\mathrm{d}\theta/\mathrm{d}s(0) = \kappa_0$, the elasticas are peeling apart, and the corresponding tension, T_∞, is determined as part of the solution.

Using (4.2.6), and performing a force balance at the contact point, we have

$$\frac{F}{\mu} = N = \frac{T_\infty}{\sin\theta_c + \mu\cos\theta_c}, \tag{4.2.7}$$

which allows us to solve (4.2.1b) and (4.2.1c) subject to (4.2.2), leading to

$$F_x = T_\infty \mathcal{H}(s - s_c), \tag{4.2.8a}$$

$$F_y = \frac{T_\infty\left(\cos\theta_c - \mu\sin\theta_c\right)}{\sin\theta_c + \mu\cos\theta_c}\mathcal{H}(s_c - s) = T_\infty\cot(\theta_c + \phi)\mathcal{H}(s_c - s), \tag{4.2.8b}$$

where $\phi = \tan^{-1}\mu$ is the angle of friction and $\mathcal{H}(s)$ is the Heaviside function. The problem (4.2.1a), (4.2.4), and (4.2.5) therefore becomes

$$B\frac{\mathrm{d}^2\theta}{\mathrm{d}s^2} = T_\infty\sin\theta,\ \ s_c < s < \infty, \tag{4.2.9a}$$

$$B\frac{\mathrm{d}^2\theta}{\mathrm{d}s^2} = -T_\infty\cot(\theta_c + \phi)\cos\theta,\ \ 0 < s < s_c, \tag{4.2.9b}$$

$$\theta(0) = 0,\quad \theta(s_c) = \theta_c,\quad \theta \to 0 \ \text{ as } \ s \to \infty, \tag{4.2.9c}$$

$$\int_0^{s_c}\sin\theta\ \mathrm{d}s = a\cos\theta_c, \tag{4.2.9d}$$

where we require continuity of θ and $\mathrm{d}\theta/\mathrm{d}s$ at $s = s_c$.

We solve equation (4.2.9a) analytically, giving the result

$$\theta(s) = 4\arctan\left[\tan\left(\frac{\theta_c}{4}\right)\exp\left(\sqrt{\frac{T_\infty}{B}}\,(s_c - s)\right)\right],\ \ s > s_c. \tag{4.2.10}$$

We note that equation (4.2.10) implies that $\mathrm{d}\theta/\mathrm{d}s\,(s_c) < 0$ and since, from figure 4.3, we expect $\mathrm{d}\theta/\mathrm{d}s\,(0) > 0$, there must be an inflection point $s = s_0 \in (0, s_c)$, where the maximum value of θ is achieved. In the region $0 < s < s_c$, we therefore write the first integral of (4.2.9b) as

$$\frac{\mathrm{d}\theta}{\mathrm{d}s} = \begin{cases} +\sqrt{\dfrac{2T_\infty}{B}\left(1 + \dfrac{\left(\sin\theta\left(\mu\sin\theta_c - \cos\theta_c\right) - \mu\right)}{\sin\theta_c + \mu\cos\theta_c}\right)},\ \text{for}\ \ 0 < s < s_0,\ \ \theta(0) = 0, \\ -\sqrt{\dfrac{2T_\infty}{B}\left(1 + \dfrac{\left(\sin\theta\left(\mu\sin\theta_c - \cos\theta_c\right) - \mu\right)}{\sin\theta_c + \mu\cos\theta_c}\right)},\ \text{for}\ \ s_0 < s < s_c,\ \ \theta(s_c) = \theta_c. \end{cases} \tag{4.2.11}$$

We use (4.2.11) to determine the maximum angle as

$$\theta_{\max} = \theta\left(s_0\right) = \arcsin\left(\frac{\sin\theta_c - \mu(1 - \cos\theta_c)}{\cos\theta_c - \mu\sin\theta_c}\right). \tag{4.2.12}$$

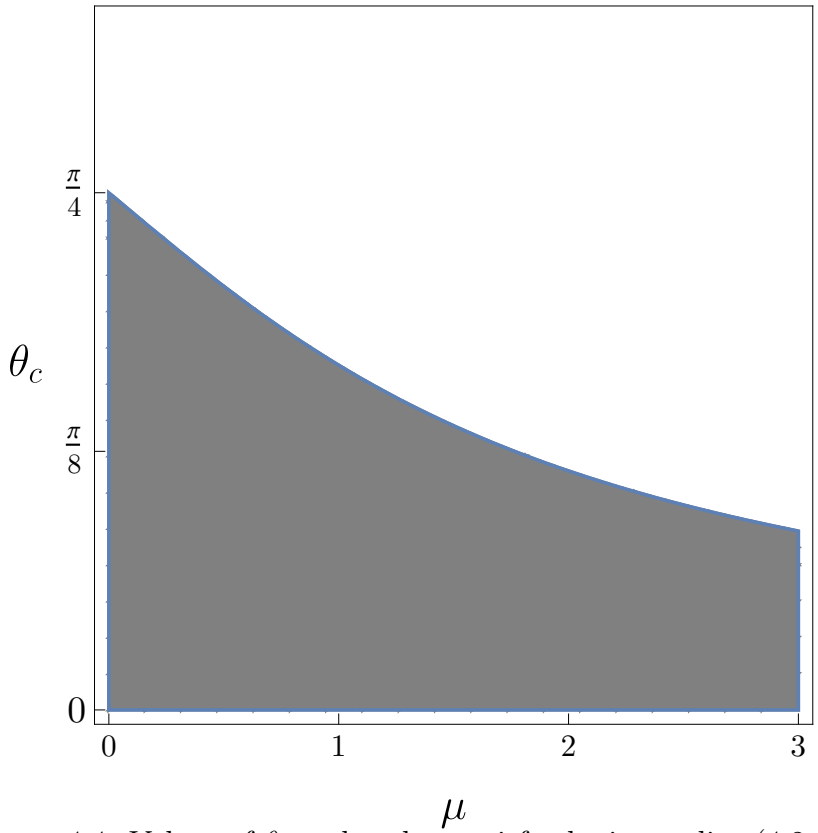


Figure 4.4: Values of θ_c and μ that satisfy the inequality (4.2.13).

Given that this inflection point must exist, we deduce a constraint on μ and θ_c given by

$$\frac{\sin\theta_c - \mu(1-\cos\theta_c)}{\cos\theta_c - \mu\sin\theta_c} \leq 1, \tag{4.2.13}$$

where it can be shown that the numerator and denominator are both non-negative. The values of μ and θ_c that satisfy inequality (4.2.13) are shown in figure 4.4, where, upon rearranging (4.2.13), the region can be defined by

$$\theta_c \leq \tan^{-1}\left(\frac{1-\mu^2+\mu\sqrt{2+\mu^2}}{1+2\mu}\right). \tag{4.2.14}$$

We see that, for a given coefficient of friction between tow and tooth, there is an upper bound on the contact angle θ_c. For example, for $\mu = 1$, we require $\theta_c < \pi/6$, and θ_c can never exceed $\pi/4$ for any value of μ.

Using equations (4.2.9d) and (4.2.11) we find

$$\sqrt{\tau}\cos\theta_c = \int_0^{\theta_{\max}} f(\mu,\theta_c,\theta)\,\mathrm{d}\theta + \int_{\theta_c}^{\theta_{\max}} f(\mu,\theta_c,\theta)\,\mathrm{d}\theta, \tag{4.2.15}$$

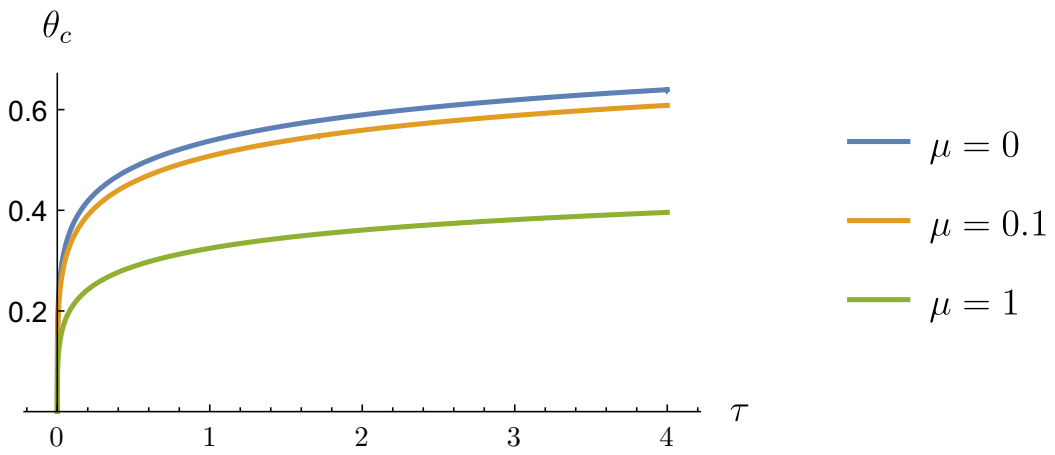


Figure 4.5: Plot of θ_c against τ for different values of μ.

where

$$f(\mu, \theta_c, \theta) = \frac{\sin\theta}{\sqrt{1 + \left(\dfrac{\sin\theta\,(\mu\sin\theta_c - \cos\theta_c) - \mu}{\sin\theta_c + \mu\cos\theta_c}\right)}}, \tag{4.2.16}$$

and we define the dimensionless tension parameter

$$\tau = \frac{2a^2 T_\infty}{B}. \tag{4.2.17}$$

If a and B are constant for a given tow and tooth, then τ is proportional to the force with which the tooth is pushed through the tow. Equation (4.2.15) determines the contact angle, θ_c, as a function of τ and μ, as can be seen in figure 4.5.

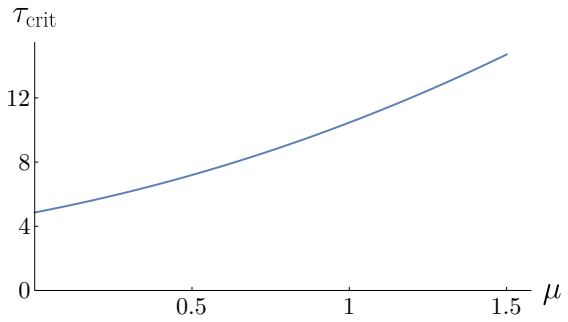
We have assumed so far that there is only a single contact point between the elastica and tooth, which is true provided the curvatures satisfy the inequality

$$\left|\frac{\mathrm{d}\theta}{\mathrm{d}s}\right| < \frac{1}{a} \text{ at } s = s_c. \tag{4.2.18}$$

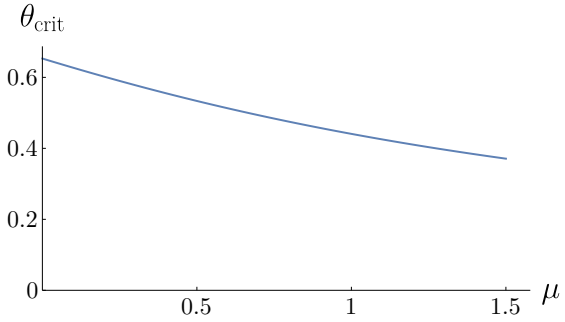
Using (4.2.11), this constraint may be expressed as

$$\sqrt{\tau} < \frac{1}{\sqrt{2}\sin\left(\frac{\theta_c}{2}\right)}. \tag{4.2.19}$$

When condition (4.2.18) is not satisfied we have a contact region instead of a point, which is addressed in section 4.4. Equation (4.2.15) and inequality (4.2.19) mean that, if τ is too large, or equivalently if θ_c is too large, then the assumption of a single contact point fails. The critical values of τ and θ_c, denoted τ_{crit} and θ_{crit}, for different values of μ are shown in figures 4.6a and 4.6b respectively. We note that this constraint on θ_c is stronger than (4.2.13); for example for $\mu = 1$ we now require $\theta_c < 0.440766 < \pi/6$. Provided the inequality (4.2.19) is satisfied, we are in a position to solve the model, and thus determine the elastica configuration.



(a) The critical dimensionless tension τ_{crit}.



(b) The critical contact angle θ_{crit}.

Figure 4.6: The critical values of τ and θ_c, above which the assumption of a single contact point fails, plotted versus the coefficient of friction, μ.

4.3 Model Results

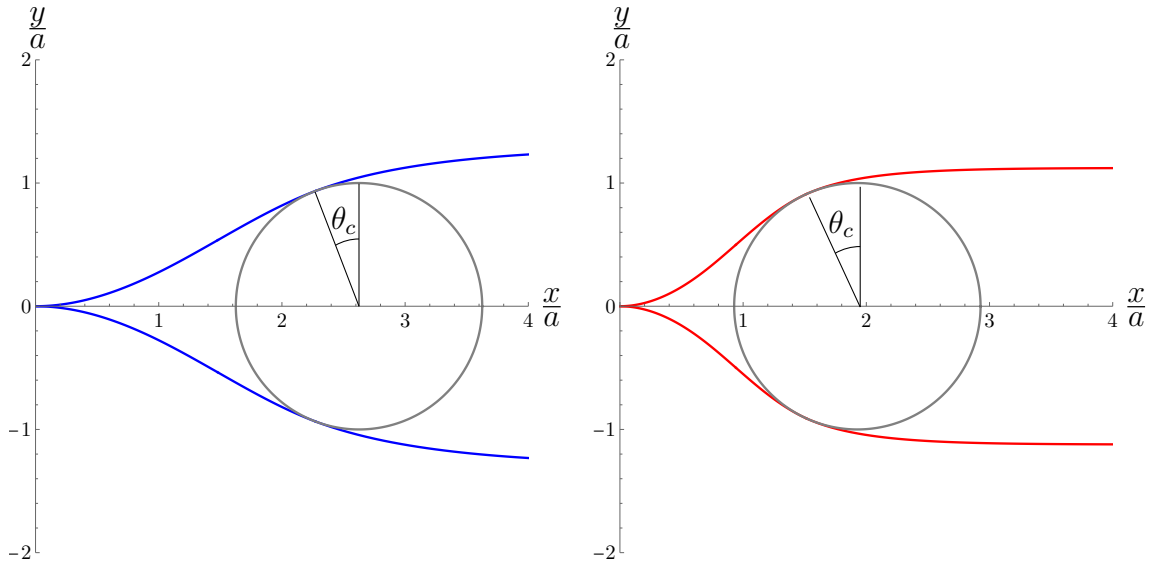
The model for a pair of elasticas being prised apart by a tooth is represented by equations (4.2.10), (4.2.11), (4.2.12), (4.2.15), (4.2.16), and (4.2.17). For given values of μ and τ we first solve equations (4.2.12) and (4.2.15) for θ_c and $\theta_{\max}$. Then equations (4.2.10) and (4.2.11) determine the solution for $\theta(s)$ across the whole elastica.

The solution shapes for $\mu = 1$ and two different values of the dimensionless tension $\tau = 2$ and $\tau = 8$ are shown in figure 4.7. We note from figure 4.6 that $\tau_{\text{crit}} \approx 10.36$ when $\mu = 1$, so both of these solutions are in the region where there is a single contact point. As τ is increased, we see the tooth move to the left. The elastica to the right of the tooth becomes flatter while the segment to the left of the tooth becomes more deformed. We note from figure 4.5 that, as τ increases, so does θ_c, which means the contact point moves anticlockwise away from the "top" of the tooth, as can be seen in figure 4.7.

As discussed in section 4.1, one of the key questions we want to answer is: when will a tow be opened by a tooth? We propose that, if the curvature of the elastica at $s = 0$ reaches some yield value, κ_0, then the tow will start to open, consistent with the mechanism proposed for mica in [44]. The dimensionless curvature at $s = 0$ is given by

$$\kappa^* = a\frac{\mathrm{d}\theta}{\mathrm{d}s}(0) = \sqrt{\tau\left(1 - \frac{\mu}{\sin\theta_c + \mu\cos\theta_c}\right)}, \tag{4.3.1}$$

where we recall that θ_c is determined by equation (4.2.15) as a function of τ and μ. This dimensionless curvature at the splitting point is plotted against the dimensionless tension τ in figure 4.8 for $\mu = 0$, $\mu = 0.1$, and $\mu = 1$. We see that κ^* increases with τ



(a) $\tau = 2$, $\mu = 1$. (b) $\tau = 8$, $\mu = 1$.

Figure 4.7: Solutions for the elastica shapes, with coefficient of friction $\mu = 1$ and two different dimensionless tensions, τ.

so, for a given tooth, pulling with a greater force makes the tow more likely to open, as expected.

We can examine the effect of the tooth size on tow splitting as follows. Defining the critical value of the curvature for the tow to split to be κ_0, and using equation (4.3.1), we find that the tow will split when

$$\frac{\sin\theta_c + \mu\cos\theta_c}{\sin\theta_c + \mu\left(\cos\theta_c - 1\right)} = \frac{2T_\infty}{B\kappa_0^2} = \frac{\tau}{a^{*2}} = T^*, \tag{4.3.2}$$

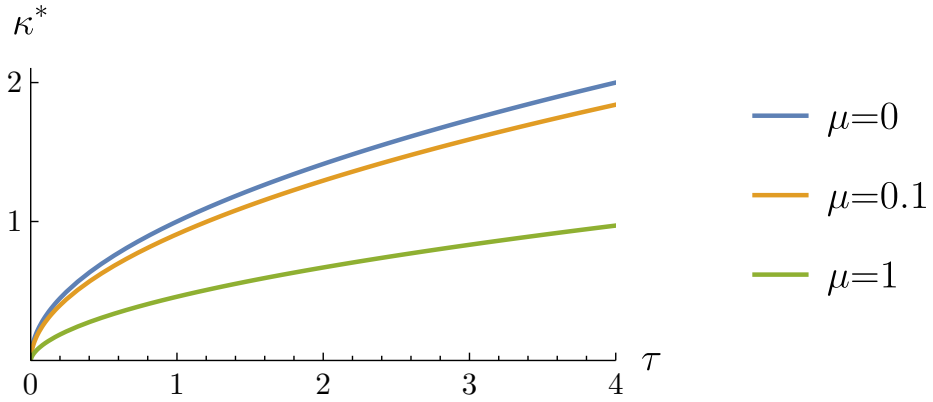


Figure 4.8: The dimensionless curvature at $s = 0$ against dimensionless tension τ for different values of μ.

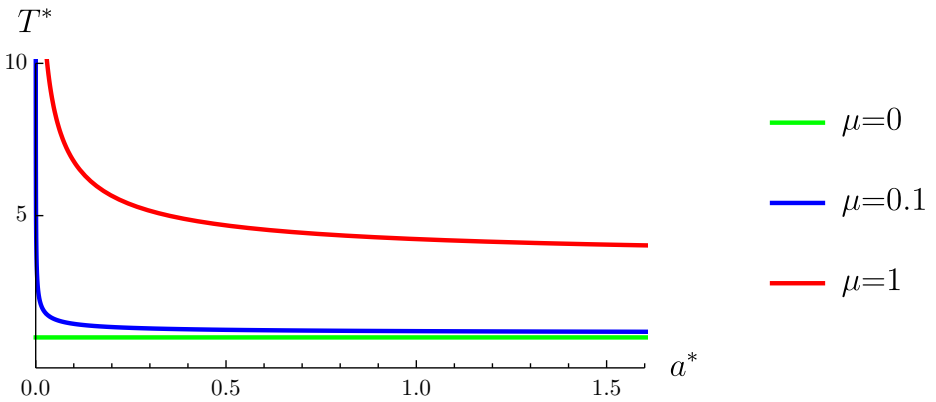


Figure 4.9: Plots of the dimensionless parameter T^* against a^* for different values of μ.

say, where

$$a^* = a\kappa_0. \tag{4.3.3}$$

The contact angle when the tow is splitting is thus given by

$$\theta_c = -\phi + \sin^{-1}\left(\frac{T^* \sin\phi}{T^* - 1}\right), \tag{4.3.4}$$

where we recall that $\phi = \tan^{-1}\mu$. We can then express a^* as a function of T^* and μ, using

$$a^* = \frac{1}{\sqrt{T^*}\cos\theta_c}\left\{\int_0^{\theta_{\max}} f\left(\mu, \theta_c, \theta\right) \mathrm{d}\theta + \int_{\theta_c}^{\theta_{\max}} f\left(\mu, \theta_c, \theta\right) \mathrm{d}\theta\right\}, \tag{4.3.5}$$

where f is again given by (4.2.16).

Plots of T^* against a^* for different values of μ are shown in figure 4.9, where we note that $T^* = 1$ for a smooth tooth with $\mu = 0$, independently of the tooth radius. Otherwise we see that a smaller tooth radius requires a larger force to open the tow. We also see that a larger force is required if the coefficient of friction, μ, is higher. We therefore propose that larger/smoother teeth will open tows more easily. However we have assumed so far that the tooth is already embedded in the tow. A three-dimensional model would be required to describe how the point of the tooth initially penetrates between the fibres so that the subsequent splitting described in this section can proceed.

4.4 Elastica Wrapping Model

In this section we extend the model discussed above by relaxing the assumption that the elastica makes contact with the tooth at a single point, which relies on the

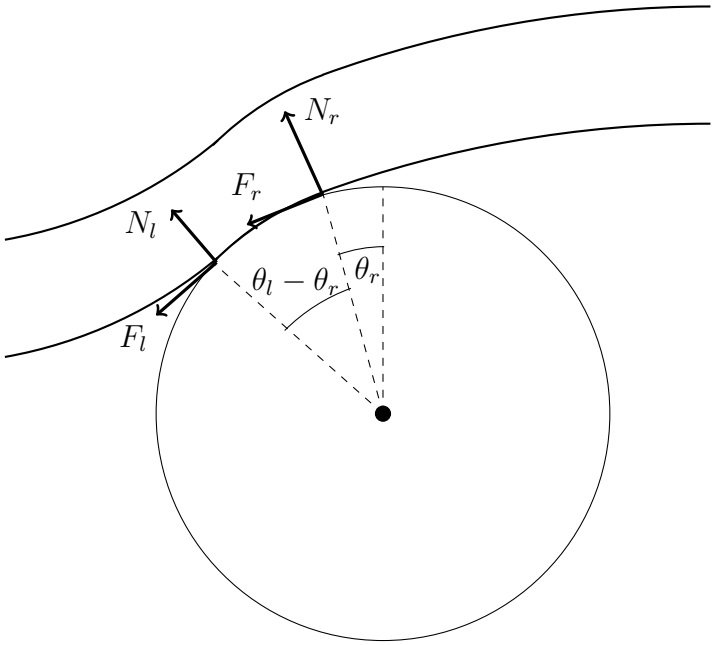


Figure 4.10: Schematic of an elastica in contact with a tooth in the region $s_l < s < s_r$.

constraint (4.2.18). When this inequality is no longer satisfied, we have the situation shown schematically in figure 4.10. Instead of touching the tooth at one point, the elastica will 'wrap' around the tooth, forming a contact set with two ends on the left and right, which we define as $s = s_l$, $\theta = \theta_l$ and $s = s_r$, $\theta = \theta_r$ respectively. We now have a classical free boundary problem, where the contact region needs to be found as part of the solution.

The shape of the elastica in each of the three regions is defined by

$$B\frac{\mathrm{d}^2\theta}{\mathrm{d}s^2} = F_x \sin\theta - F_y \cos\theta, \quad 0 < s < s_l, \tag{4.4.1a}$$

$$\frac{\mathrm{d}\theta}{\mathrm{d}s} = -\frac{1}{a}, \quad s_l < s < s_r, \tag{4.4.1b}$$

$$\theta = 4\arctan\left\{\exp\left[\sqrt{\frac{T_\infty}{B}}\,(s_r - s)\right]\tan\frac{\theta_r}{4}\right\}, \quad s > s_r, \tag{4.4.1c}$$

$$\theta(0) = 0, \quad \theta(s_l) = \theta_l, \quad \theta(s_r) = \theta_r, \tag{4.4.1d}$$

where (4.4.1a) is the same as equation (4.2.1a), and solution (4.4.1c) is obtained as in section 4.2. From equation (4.4.1b), the length of the contact region is given by

$$s_r - s_l = a\,(\theta_l - \theta_r)\,. \tag{4.4.2}$$

From equations (4.4.1b) and (4.4.1c), and continuity of curvature at $s = s_r$, we obtain the equation

$$\theta_r = 2 \arcsin\left(\frac{1}{\sqrt{2\tau}}\right), \tag{4.4.3}$$

where $\tau = 2a^2 T_\infty / B$, as before. We note that we must have $0 < \theta_r < \pi/2$, which, from (4.4.3) means we require $\tau > 1$. We already know however, from figure 4.6a, that for the contact problem to be relevant we must have $\tau > \tau_{\text{crit}} > 1$ for all μ.

Since $\mathrm{d}^2\theta/\mathrm{d}s^2$ is in general discontinuous at s_l and s_r there must be localized normal and frictional forces N_l, F_l, and N_r, F_r at $s = s_l$ and $s = s_r$ respectively, as shown in figure 4.10. The jumps in force across these two points must satisfy

$$F_x(s_r^+) - F_x(s_r^-) = N_r \sin\theta_r + F_r \cos\theta_r, \tag{4.4.4a}$$

$$F_y(s_r^+) - F_y(s_r^-) = F_r \sin\theta_r - N_r \cos\theta_r, \tag{4.4.4b}$$

$$F_x(s_l^+) - F_x(s_l^-) = N_l \sin\theta_l + F_l \cos\theta_l, \tag{4.4.4c}$$

$$F_y(s_l^+) - F_y\left(s_l^-\right) = F_l \sin\theta_l - N_l \cos\theta_l, \tag{4.4.4d}$$

where the superscripts s^- and s^+ define forces to the left and right of point s respectively. As previously, we assume that there is a horizontal tension, T_∞, at infinity, and there is no horizontal force in the elastica to the left of the contact region. If we additionally assume limiting Coulomb friction, equations (4.4.4) lead to

$$N_r\left(\sin\theta_r + \mu\cos\theta_r\right) = T_\infty - T\left(s_r^-\right)\cos\theta_r, \tag{4.4.5a}$$

$$N_r\left(\mu\sin\theta_r - \cos\theta_r\right) = -T\left(s_r^-\right)\sin\theta_r, \tag{4.4.5b}$$

$$N_l\left(\sin\theta_l + \mu\cos\theta_l\right) = T\left(s_l^+\right)\cos\theta_l, \tag{4.4.5c}$$

$$N_l\left(\mu\sin\theta_l - \cos\theta_l\right) = T\left(s_l^+\right)\sin\theta_l - F_y\left(s_l^-\right), \tag{4.4.5d}$$

where $T(s)$ is the tension in the elastica at s.

Solving equations (4.4.5) leads to the two 'jump' conditions

$$T\left(s_r^-\right) = T_\infty\left(\cos\theta_r - \mu\sin\theta_r\right), \tag{4.4.6a}$$

$$F_y\left(s_l^-\right) = \frac{T\left(s_l^+\right)}{\sin\theta_l + \mu\cos\theta_l}. \tag{4.4.6b}$$

Assuming that the elastica can only be in tension and not compression, we require $T\left(s_r^-\right) > 0$, which leads to

$$\tan\theta_r < \frac{1}{\mu}. \tag{4.4.7}$$

Using equation (4.4.3) we deduce the inequality

$$\tau > 1 + \mu^2 + \mu\sqrt{1+\mu^2}, \tag{4.4.8}$$

which is stronger than the constraint $\tau > 1$ obtained above for $\mu > 0$.

We use similar analysis to the Capstan problem [11, 12] to solve for the tension across the contact region, and therefore find from (4.4.6a) that

$$T\left(s_l^+\right) = T_\infty \left(\cos\theta_r - \mu \sin\theta_r\right) e^{-\mu(\theta_l - \theta_r)}. \tag{4.4.9}$$

Therefore equation (4.4.6b) gives the vertical stress in $s < s_l$ as

$$F_y \equiv F_y\left(s_l^-\right) = \frac{T_\infty \left(\cos\theta_r - \mu\sin\theta_r\right) e^{-\mu(\theta_l - \theta_r)}}{\sin\theta_l + \mu\cos\theta_l}. \tag{4.4.10}$$

The elastica equation for $0 < s < s_l$ is then given by

$$B\frac{\mathrm{d}^2\theta}{\mathrm{d}s} = -F_y \cos\theta. \tag{4.4.11}$$

We can now use equations (4.4.1) and (4.4.11) to obtain θ in all relevant regions. We have to solve the first-order ODE problems

$$\frac{\mathrm{d}\theta}{\mathrm{d}s} = \begin{cases} +\sqrt{\dfrac{1}{a^2} + \dfrac{2F_y}{B}\left(\sin\theta_l - \sin\theta\right)}, & \theta(0) = 0 \quad \text{for} \quad 0 < s < s_0, \qquad (4.4.12a) \\ -\sqrt{\dfrac{1}{a^2} + \dfrac{2F_y}{B}\left(\sin\theta_l - \sin\theta\right)}, & \theta(s_l) = \theta_l \quad \text{for} \quad s_0 < s < s_l, \qquad (4.4.12b) \end{cases}$$

where $s = s_0$ is the inflection point, and

$$\theta(s) = \begin{cases} \theta_l - \dfrac{(s - s_l)}{a}, \text{ for } s_l < s < s_r, & (4.4.13a) \\ 4\arctan\left\{\exp\left[\sqrt{\dfrac{T_\infty}{B}}\left(s_r - s\right)\right]\tan\dfrac{\theta_r}{4}\right\}, \text{ for } s > s_r. & (4.4.13b) \end{cases}$$

As in the previous sections, to close the model we specify the height of the contact point at $s = s_l$, allowing us to write the integral equation

$$\cos\theta_l = \int_0^{\theta_{\max}} \frac{\sin\theta \mathrm{d}\theta}{\sqrt{1 + \dfrac{2F_y a^2}{B}\left(\sin\theta_l - \sin\theta\right)}} + \int_{\theta_l}^{\theta_{\max}} \frac{\sin\theta \mathrm{d}\theta}{\sqrt{1 + \dfrac{2F_y a^2}{B}\left(\sin\theta_l - \sin\theta\right)}}. \tag{4.4.14}$$

Equations (4.4.12)-(4.4.14) define our contact problem and can be solved for the shape of the elastica, given the parameters a, B, T_∞, and μ.

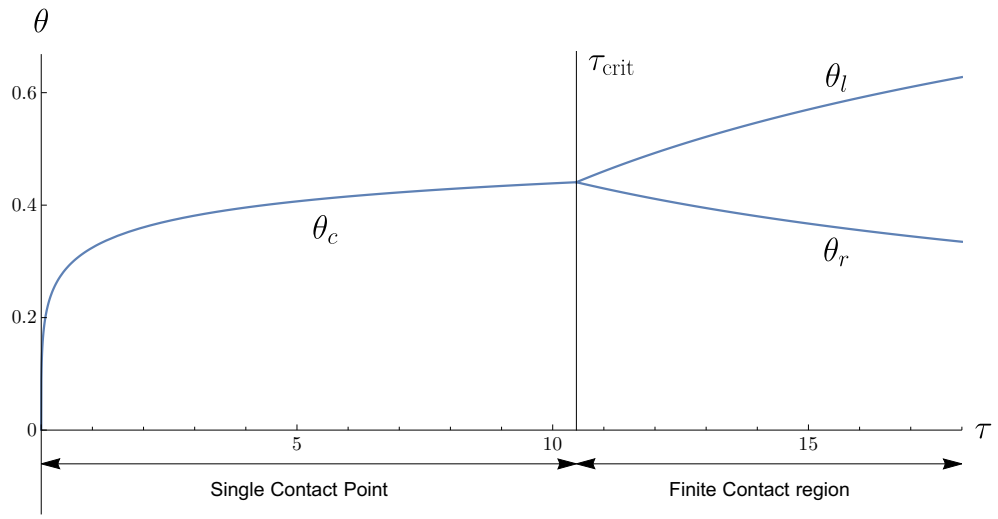


Figure 4.11: The contact angles θ_c, θ_l, and θ_r against dimensionless tension τ for $\mu = 1$.

4.5 Wrapping Model Results

For $\tau < \tau_{\text{crit}}$ we have a single contact point and the solution can be obtained from the governing equations (4.2.10), (4.2.11), (4.2.12), (4.2.15), and (4.2.17); and then for $\tau > \tau_{\text{crit}}$ the equations are (4.4.12)-(4.4.14). This change with increasing τ from one contact angle, θ_c, to two, θ_l and θ_r, is shown in figure 4.11 with $\mu = 1$. We plot the shape of the tow with $\tau > \tau_{\text{crit}}$ in figure 4.12, where we see a region of the tow wrapped around the tooth. This region is our contact set.

As before, we propose that the tow will split if the curvature at $s = 0$ reaches some yield value, κ_0. For the wrapping model, the dimensionless curvature at $s = 0$ is given by

$$\kappa_c^* = a\frac{\mathrm{d}\theta}{\mathrm{d}s}(0) = \sqrt{1 + \tau\left(\frac{\sin\theta_l\,(\cos\theta_r - \mu\sin\theta_r)\,e^{-\mu(\theta_l-\theta_r)}}{\sin\theta_l + \mu\cos\theta_l}\right)}. \tag{4.5.1}$$

One can verify that this expression agrees with (4.3.1) when we set $\theta_l = \theta_r = \theta_{\text{crit}}$ and $\tau = \tau_{\text{crit}}$. The dimensionless curvature at the splitting point is plotted against dimensionless tension τ in figure 4.13, for $\mu = 0$, $\mu = 0.1$, and $\mu = 1$. We indicate the values of τ_{crit} for different coefficients of friction μ, using (4.2.19). We see that, following on from the previous model, if we continue to pull the tooth through with a greater force, the curvature at $s = 0$ continues to grow and the tow will be more likely to open.

Following section 4.3 the dimensionless parameters $a^* = a\kappa_0$ and $T^* = \tau/a^{*2}$ can

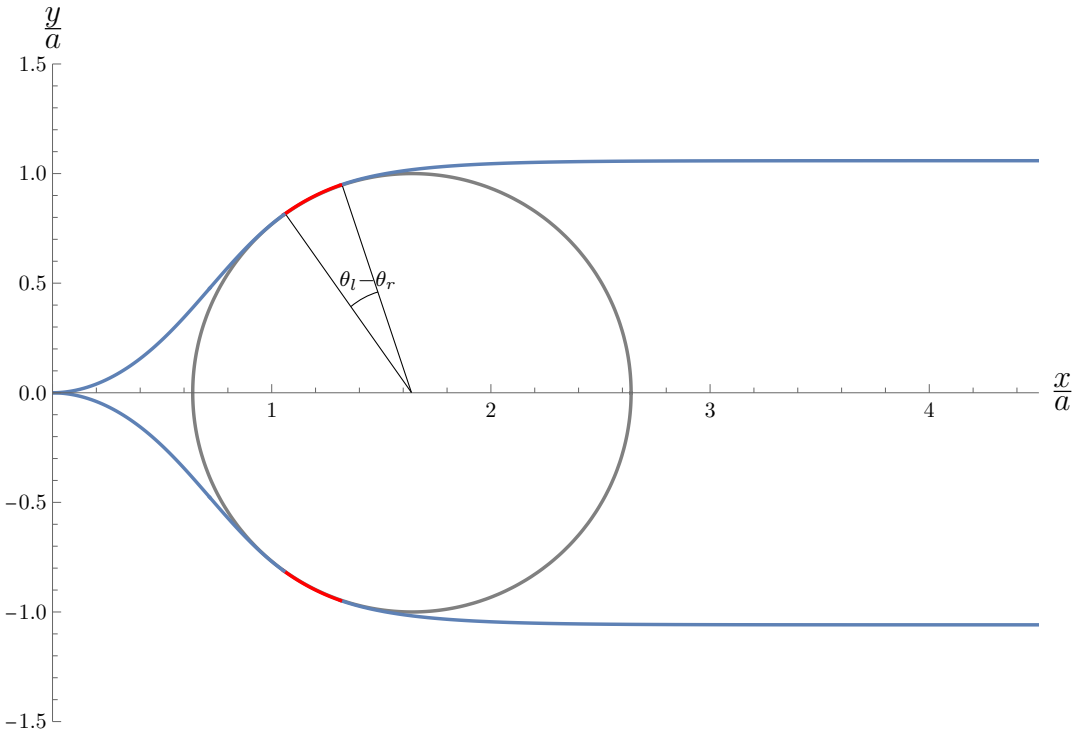


Figure 4.12: Solution for the shape of the elastica, with a contact region along the tooth, with coefficient of friction $\mu = 1$, and dimensionless tension $\tau = 18$.

be deduced by solving the system

$$T^* = \left(1 - \frac{1}{a^{*2}}\right) \frac{1}{g(\mu, \theta_l, \theta_r) \sin\theta_l}, \tag{4.5.2a}$$

$$\cos\theta_l = \int_0^{\theta_{\max}} \frac{\sin\theta \mathrm{d}\theta}{\sqrt{1 + a^{*2} T^* \left(\sin\theta_l - \sin\theta\right) g(\mu, \theta_l, \theta_r)}} + \int_{\theta_l}^{\theta_{\max}} \frac{\sin\theta \mathrm{d}\theta}{\sqrt{1 + a^{*2} T^* \left(\sin\theta_l - \sin\theta\right) g(\mu, \theta_l, \theta_r)}}, \tag{4.5.2b}$$

where

$$g(\mu, \theta_l, \theta_r) = \frac{\left(\cos\theta_r - \mu \sin\theta_r\right) e^{-\mu(\theta_l - \theta_r)}}{\sin\theta_l + \mu\cos\theta_l}. \tag{4.5.3}$$

One can verify that the solution of the system (4.5.2)-(4.5.3) agrees with (4.3.2) and (4.3.5) when $\theta_l = \theta_r = \theta_{\text{crit}}$ and $\tau = \tau_{\text{crit}}$. Plots of T^* against a^* for different values of μ for both models are shown in figure 4.14. We again note that $T^* = 1$ for a smooth tooth with $\mu = 0$. We see that as the radius of the tooth is increased, the wrapping model becomes relevant, and there is less dependence of the force required to open the tow on the tooth radius. We again see that the required force is larger if the coefficient of friction, μ, is higher.

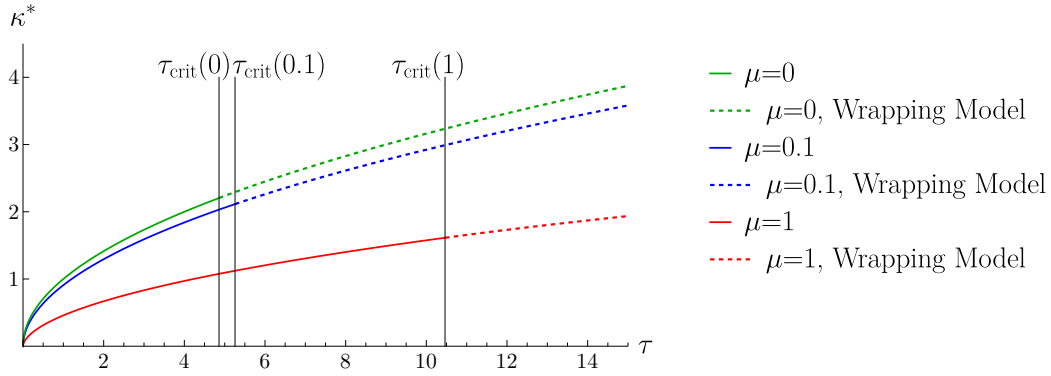


Figure 4.13: The dimensionless curvature at $s = 0$ against dimensionless tension τ for different values of μ for both the single contact point and elastica wrapping models.

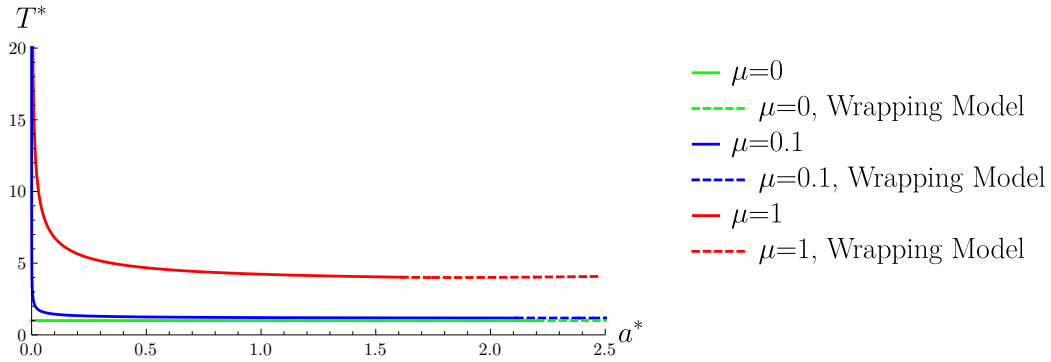


Figure 4.14: The dimensionless parameter T^* against a^* for different values of μ for both the single contact point and elastica wrapping models.

4.6 Conclusions

In this chapter, we formulated and solved a simple problem modelling the interaction between a fibre tow and a single carding tooth, with the aim of understanding the opening of tows. We modelled the tow as two joined elasticas, put under tension by pushing a circular tooth between them. The resulting model yields two distinct types of contact problem; a single contact point between the elastica and the tooth, and a contact set when the elastica 'wraps' around the tooth. We showed that the force with which the tow is pushed through determines which of these cases is relevant, and presented analysis in both cases.

We solved the equations to plot the solution shapes of the elastica as the parameters are varied. We proposed a law for opening of the tow based on the curvature of the elasticas at the meeting point reaching a critical value. We thus determined how the opening of the tow depends on parameters such as the applied force and

the radius of the tooth. We found that the curvature, and therefore the chances of opening the tow, increases with the dimensionless tension, τ, i.e., that tows are more likely to open if the tooth is pushed through the tow with a greater force for constant tooth radius and tow bending stiffness. We also showed that for a tooth of smaller radius, a larger force is required to open the tow.

The next step in this modelling approach would be to derive a full 3D model that incorporates the action of a tooth embedding itself into a tow. The results of the model so far have provided insight into the key parameters affecting the process of tow opening in the carding machine. In the next chapter we derive a probabilistic model for a distribution of tows moving through different regions of the carding machine. The insight provided by the microscale models in this chapter can be used to inform some of the parameters that are highlighted by this probabilistic model. A method for carrying out this analysis is presented in chapter 6.

Chapter 5

A Probabilistic Model for Multiple Tows

5.1 The Carding Machine

In this section we focus on the properties of carbon fibre tows as they move through the carding machine. Tows are fed onto the machine by a rotating feed sheet and then move through the machine, following the same process as described for a web of fibres in chapters 1 and 2. A diagram of a generic carding machine is shown again in figure 5.1. The difference here is that we now model the carbon fibre as being divided into discrete tows, rather than being a continuous web.

We focus on the fibre tows moving along the main cylinder (or 'swift'), the workers, and the strippers. As discussed previously, in the thin region between any two cylinders, the probabilities of the fibres joining either cylinder are determined by key parameters including roller size, roller speed, and tooth orientation. These parameters are also important in determining the probability of a tow splitting in these regions, as discussed in chapter 4. The picture in figure 5.1 shows a single worker-stripper pair, whereas our model generalises to consider any number of these pairs. The aim of this work is to model how fibre tows move through this part of the machine, and how the properties of the tows change as they do so. The aim of the carding process is to split tows consisting of thousands of filaments into tows consisting of hundreds or smaller, without breaking the tows, i.e. reducing the length.

5.2 Literature Review

To model the evolution of tows moving through the carding machine we use the theory of fragmentation and breakup, an area of modelling that is found in a number

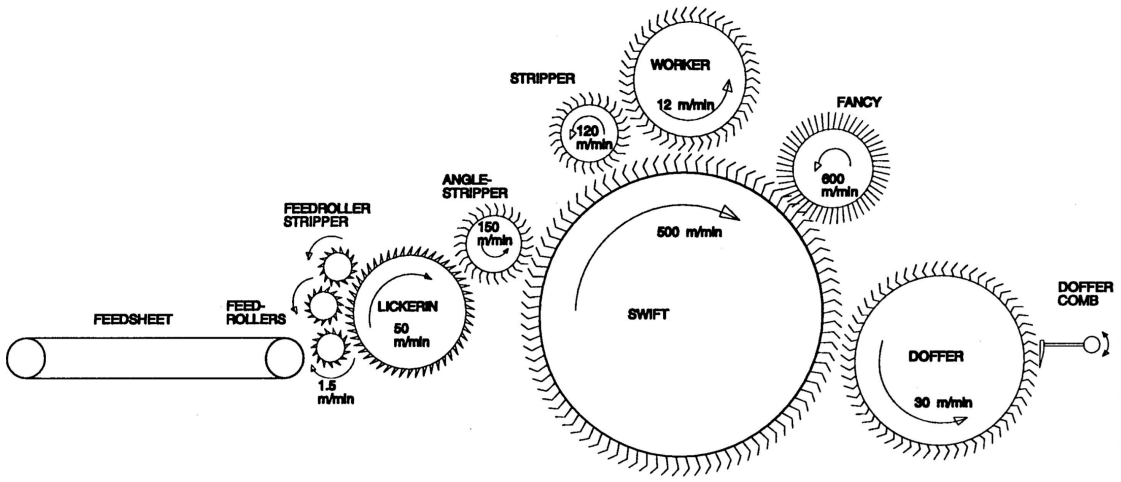


Figure 5.1: Example of a Carding machine, taken from [67].

of different applications. Banasiak and Lamb [3] present a continuous, time-dependent model for the division and aggregation of phytoplankton cells. Rooney et al [48] derive a discrete model for particles being broken up in a blender with the aim of predicting how the size distribution of particles evolves with time. We will present a similar formulation where tows are broken up in regions of the carding machine, allowing us to predict the size and length distributions of tows after different numbers of rollers. Other studies of pure fragmentation processes similar to that of tow splitting and breakage are discussed in [26] and [50].

Wattis [61] presents a summary of these modelling techniques, focusing on the mathematical framework rather than particular applications. These models make use of the Smoluchowski equations [52] and the Becker-Döring equations [4, 63] for coagulation and fragmentation. These two theories have been used in a number of applications that involve the coagulation and aggregation of groups of particles in clusters. The Smoluchowski equations are derived by writing down a master equation, from which a number of rates or probabilities emerge [1, 61]. The Becker-Döring equations are a specific case of the Smoluchowski equations where there is stepwise loss and gain of single particles to form clusters [17]. Applications of this approach include micellar surfactants [17, 18], mechanical alloying [20], polymer degradation [71], and droplet breakage [2,70]. Many models also use this theory to model a balance between aggregation and fragmentation [55], for example Brilliantov et al. [5] model the size distribution of particles in Saturn's rings. In section 5.4 we include both tow splitting and breakage, thus providing us with a multi-component model. Multi-component coagulation-fragmentation models [60] are more rare than single-component models

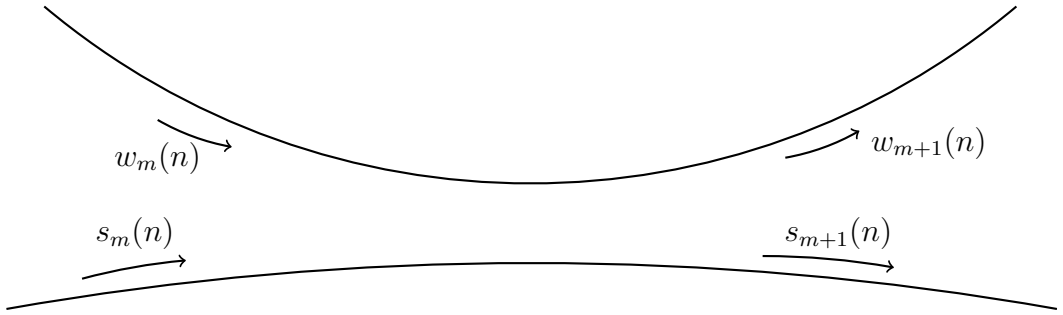


Figure 5.2: Two distributions, $w_m(n)$ and $s_m(n)$, of tows along two rollers entering and leaving a nip region in the carding machine.

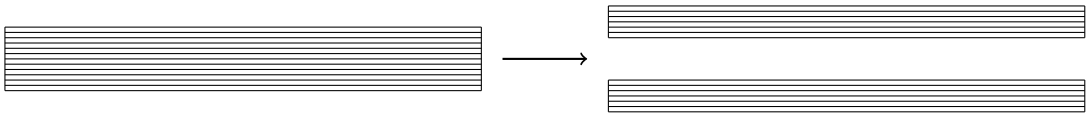
but have been shown to be relevant in applications such as polymerization [62] and mixed miscelle distributions [57].

As well as the breakup of tows, it is also important to include the transfer of fibres between different rollers in the model. As discussed previously, in the thin regions between any two cylinders, fibre tows have the possibility of moving from one cylinder to the other. The model of Cherkassy [10] considers transfer of fibres in both the longitudinal (along the rollers) and transverse (transfer between rollers) directions, where there is deterministic transfer in the longitudinal direction, and random transfer in the transverse [10]. Rust and Gutierrez [49] characterize each carding roller by its collecting power, which represents the ability of a cylinder to take a fibre off the main cylinder [49]. In the models we derive in this chapter probabilities associated with transfer between cylinders are important in the model results.

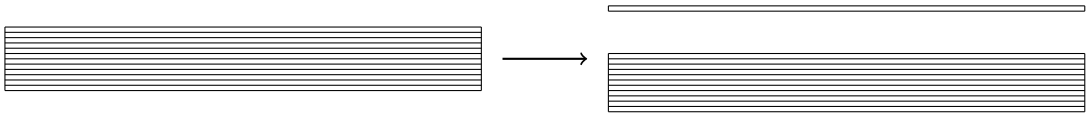
5.3 A Probabilistic Model

5.3.1 The Master Equation

We define the *size* of a fibrous tow as the number, n, of individual filaments that make up the tow. We begin by examining a typical region of the carding machine between the worker and the swift, shown in figure 5.2. Considering this region, we define the distributions $w_m(n)$ and $s_m(n)$ as the average number of tows per unit time of size n entering the position m on the top and bottom rollers respectively. The index m increases by one every time the tows pass through one of these "nip" regions. To begin with we assume all tows are of the same length and remain that way throughout the machine. We we will build change in tow length into the model in section 5.4.



(a) Tow splitting into two daughter tows of equal size.



(b) Tow splitting into two daughter tows of different sizes.

Figure 5.3: Schematic diagrams of example tows splitting into two daughter tows.

We assume that when a tow moves through a region such as the one shown in figure 5.2, one of three things can happen. It can either transfer from one roller to another without splitting, interact with the other roller and split into two or more daughter tows, as shown in figure 5.3, or do neither and remain on the same roller with the same size. The possible routes taken by a tow are shown in figure 5.4, where we define our probabilities as

$g_w(k)$ = Probability a tow of size k on the top roller interacts with the bottom roller and splits,

$g_s(k)$ = Probability a tow of size k on the bottom roller interacts with the top roller and splits,

$p_w(k)$ = Probability a tow of size k on the top roller transfers to the bottom roller without splitting,

$p_s(k)$ = Probability a tow of size k on the bottom roller transfers to the top roller without splitting,

$F(k, n)$ = Average number of daughter tows of size n produced when a tow of size k splits,

$h(k)$ = Probability a daughter tow of size k joins the top roller.

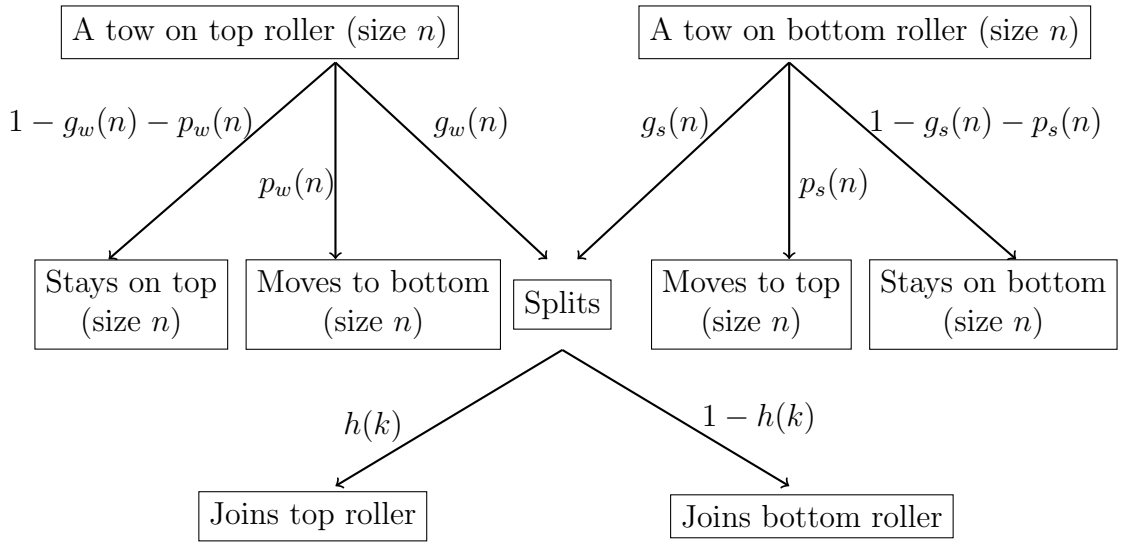


Figure 5.4: Diagram of the probabilistic model for the size of carbon fibre tows.

Using these definitions and assuming a steady state, we pose the master equations

$$\begin{aligned} s_{m+1}(n) &= (1 - g_s(n) - p_s(n))\, s_m(n) + p_w(n) w_m(n) \\ &\quad + (1 - h(n)) \sum_{k=n+1}^{N} F(k,n) \left\{ g_w(k) w_m(k) + g_s(k) s_m(k) \right\}, \qquad (5.3.1a) \\ w_{m+1}(n) &= (1 - g_w(n) - p_w(n))\, w_m(n) + p_s(n) s_m(n) \\ &\quad + h(n) \sum_{k=n+1}^{N} F(k,n) \left\{ g_w(k) w_m(k) + g_s(k) s_m(k) \right\}, \qquad (5.3.1b) \end{aligned}$$

for $1 \leq n \leq N$, where N is the maximum size of a tow, i.e. the size of the tows at the beginning of the carding process. The first terms in equations (5.3.1) describe tows remaining on the same rollers, and not changing in size, the second terms describe tows transferring from one roller to another, but not splitting, and the third terms describe the tows splitting, and then joining either roller. Equations (5.3.1) also require "boundary" conditions

$$\begin{aligned} s_{m+1}(N) &= (1 - g_s(N) - p_s(N))\, s_m(N) + p_w(N) w_m(N), \qquad (5.3.2a) \\ w_{m+1}(N) &= (1 - g_w(N) - p_w(N))\, w_m(N) + p_s(N) s_m(N), \qquad (5.3.2b) \end{aligned}$$

where $n = N$ is not a boundary in space but a finite maximum tow-size. The first terms in these boundary conditions describe tows of size N entering position m that remain on the same roller, and the second terms describe those that are transferred from the other roller.

We define the total number of tows entering stage m as

$$T_m(n) = w_m(n) + s_m(n), \tag{5.3.3}$$

and those that split as

$$I_m(n) = g_w(n)w_m(n) + g_s(n)s_m(n). \tag{5.3.4}$$

Therefore, upon summing equations (5.3.1), and using (5.3.3) and (5.3.4), we write the net master equation as

$$T_{m+1}(n) = T_m(n) - I_m(n) + \sum_{k=n+1}^{N} F(k,n)I_m(k). \tag{5.3.5}$$

We define the total number of individual fibres per unit time at position m as

$$M_m = \sum_{n=1}^{N} nT_m(n), \tag{5.3.6}$$

which, combined with equation (5.3.5), implies

$$\begin{aligned} M_{m+1} - M_m &= \sum_{n=1}^{N} nT_{m+1}(n) - \sum_{n=1}^{N} nT_m(n) \\ &= -\sum_{n=1}^{N} nI_m(n) + \sum_{k=1}^{N} I_m(k) \sum_{n=1}^{k-1} nF(k,n). \end{aligned} \tag{5.3.7}$$

Therefore, to make sure mass (or number of fibres) is conserved, we require

$$\sum_{n=1}^{k-1} nF(k,n) = k, \tag{5.3.8}$$

which states that the number of fibres contained in all the daughter tows is the same as those in the parent, as shown in figure 5.3. We assume for simplicity that $F(k,n)$ is independent of n, so the distribution of daughter tows is uniform and (5.3.8) leads to

$$F(k) = \frac{2}{k-1}. \tag{5.3.9}$$

The form of $F(k)$ in (5.3.9) is the same as derived in other studies, for example [48].

We model a worker-stripper pair as one effective roller, and note that in a steady state all fibres that leave the nip region on the top roller (worker-stripper) are put back into the region from the left, as shown in figure 5.5. Assuming the tows do not

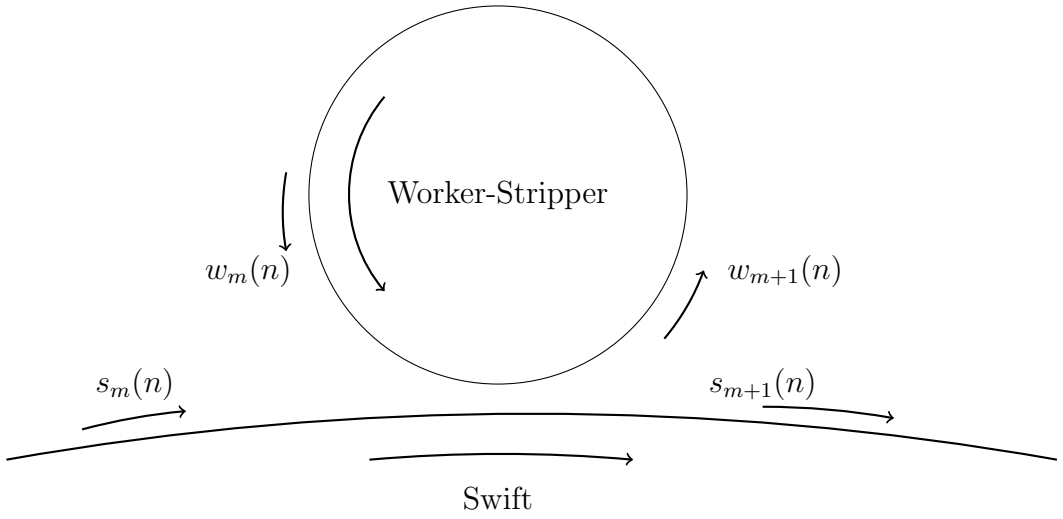


Figure 5.5: The tow distributions on the swift and another roller meeting it.

change size along this top roller, we set $w_{m+1}(n) = w_m(n)$ in equation (5.3.1b) which means our new system of equations is

$$\begin{aligned} s_{m+1}(n) &= (1 - g_s(n) - p_s(n))\, s_m(n) + p_w(n) w_m(n) \\ &\qquad + (1 - h(n)) \sum_{k=n+1}^{N} F(k) \left\{ g_w(k) w_m(k) + g_s(k) s_m(k) \right\}, \qquad \text{(5.3.10a)} \\ s_{m+1}(N) &= (1 - g_s(N) - p_s(N))\, s_m(N) + p_w(N) w_m(N), \qquad \text{(5.3.10b)} \\ w_m(n) &= \frac{p_s(n) s_m(n) + h(n) \sum_{k=n+1}^{N} F(k) \left\{ g_w(k) w_m(k) + g_s(k) s_m(k) \right\}}{g_w(n) + p_w(n)}, \qquad \text{(5.3.10c)} \\ w_m(N) &= \frac{p_s(N) s_m(N)}{g_w(N) + p_w(N)}. \qquad \text{(5.3.10d)} \end{aligned}$$

We therefore redefine the distribution $w_m(n)$ as the average number of tows per unit time of size n on the top roller m. This formulation is shown for two top rollers in figure 5.6. Given the distribution $s_m(n)$ of tows entering from the left we first solve (5.3.10c) and (5.3.10d) for $w_m(n)$; the matrix system is upper triangular and easily solvable by back substitution. Then the exiting distribution $s_{m+1}(n)$ is determined explicitly by (5.3.10a) and (5.3.10b), and fed in as the entry distribution for the next region.

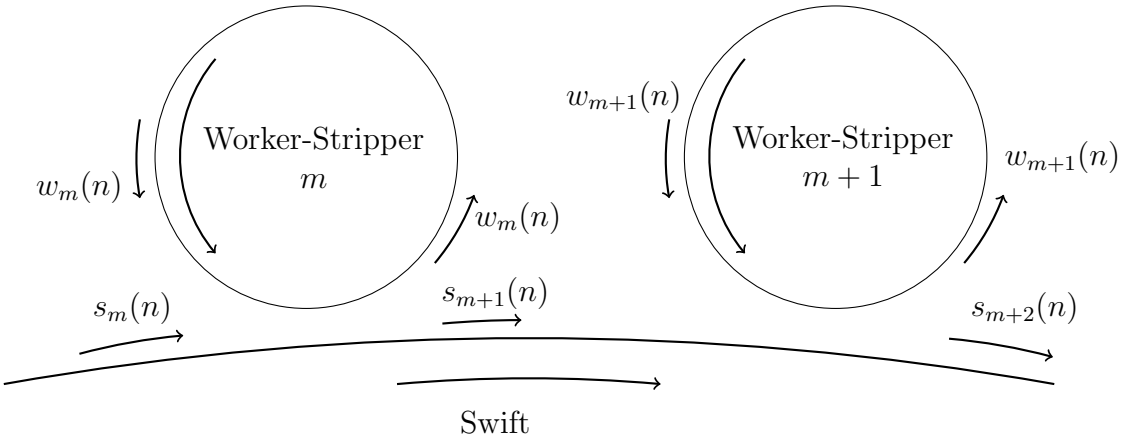


Figure 5.6: The probability distributions on the swift and 2 worker-stripper pairs (represented by one roller for each pair).

5.3.2 Model results

To solve the model (5.3.10) we need to define the probabilities $g_w(n)$, $g_s(n)$, $p_w(n)$, and $p_s(n)$. To make sure the model is physically realistic, we impose the constraints

$$0 \leq g_w(n),\ g_s(n),\ p_w(n),\ p_s(n),\ h(n) \leq 1, \quad \forall\ 1 \leq n \leq N, \tag{5.3.11a}$$

$$g_w(n) + p_w(n) \leq 1, \quad g_s(n) + p_s(n) \leq 1, \quad \forall\ 1 \leq n \leq N, \tag{5.3.11b}$$

$$g_w(1) = g_s(1) = 0, \quad \forall\ 1 \leq n \leq N, \tag{5.3.11c}$$

where (5.3.11c) ensures that tows of the minimum size (corresponding to an individual fibre filament) cannot be split any further. We propose that larger tows are more likely to be split in the region, for example because teeth are more likely to interact with large tows, as discussed in chapter 4. We therefore start by choosing

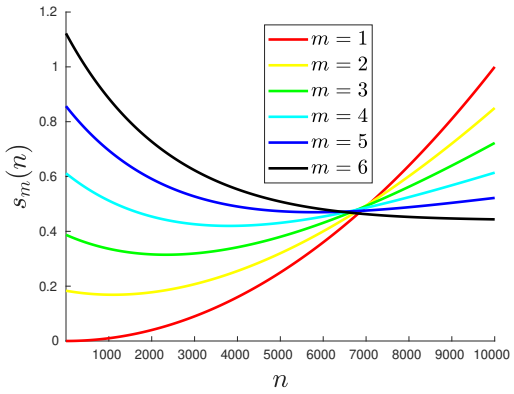
$$g_w(n) = \alpha_w \frac{n-1}{N-1}, \quad g_s(n) = \alpha_s \frac{n-1}{N-1}, \tag{5.3.12a}$$

$$p_w(n) = \beta_w, \quad p_s(n) = \beta_s, \quad h(n) = h, \tag{5.3.12b}$$

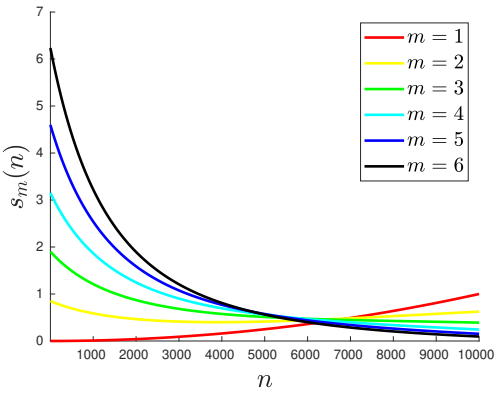
for constants α_w, α_s, β_w, β_s, and h all between 0 and 1. Later on in this chapter, and in chapter 6, we will use the properties of the rollers, and the results of chapter 4, to pose forms for these constants. We note that (5.3.11b) implies that

$$\alpha_w + \beta_w \leq 1, \quad \alpha_s + \beta_s \leq 1. \tag{5.3.13}$$

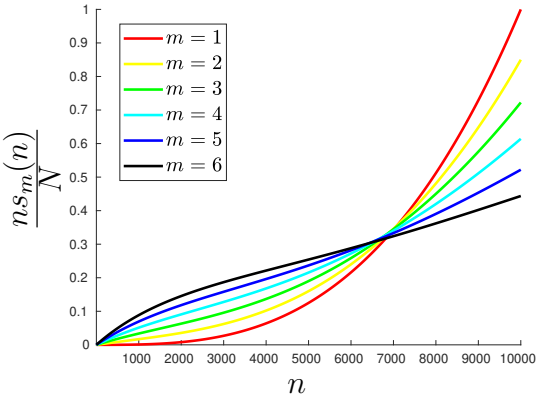
With the constitutive relations (5.3.12) and equation (5.3.9) for $F(k)$, our govern-



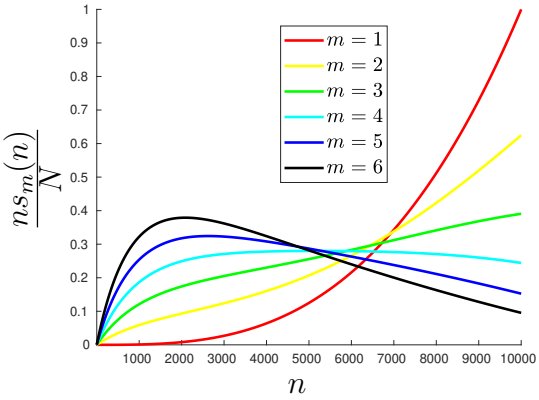
(a) $\alpha_w = \alpha_s = 0.1$.



(b) $\alpha_w = \alpha_s = 0.3$.



(c) Volume density plot for $\alpha_w = \alpha_s = 0.1$.



(d) Volume density plot for $\alpha_w = \alpha_s = 0.3$.

Figure 5.7: Plots of distribution $s_m(n)$ and volume density, $ns_m(n)/N$, at successive positions $m = 1, ..., 6$; plotted for $\beta_w = \beta_s = 0.1$, and $h = 0.5$.

ing master equations (5.3.10) become

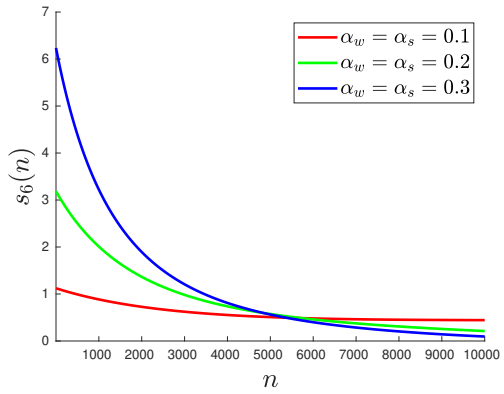
$$w_m(n) = \frac{\beta_s(N-1)s_m(n) + 2h\sum_{k=n+1}^{N}\{\alpha_w w_m(k) + \alpha_s s_m(k)\}}{\alpha_w(n-1) + \beta_w(N-1)}, \tag{5.3.14a}$$

$$w_m(N) = \frac{\beta_s s_m(N)}{\alpha_w + \beta_w}, \tag{5.3.14b}$$

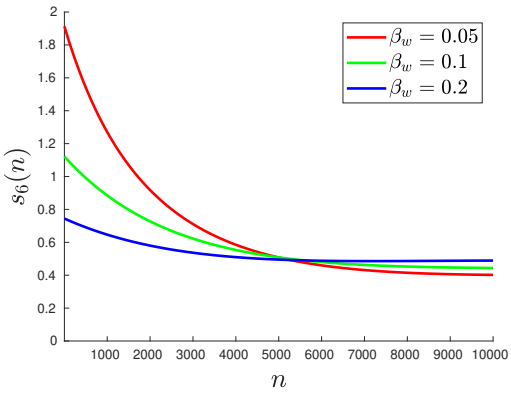
$$\begin{aligned} s_{m+1}(n) = &\left(1 - \alpha_s\left(\frac{n-1}{N-1}\right) - \beta_s\right) s_m(n) + \beta_w w_m(n) \\ &+ \frac{2(1-h)}{N-1}\sum_{k=n+1}^{N}\{\alpha_w w_m(k) + \alpha_s s_m(k)\}, \end{aligned} \tag{5.3.14c}$$

$$s_{m+1}(N) = (1 - \alpha_s - \beta_s)\, s_m(N) + \beta_w w_m(N). \tag{5.3.14d}$$

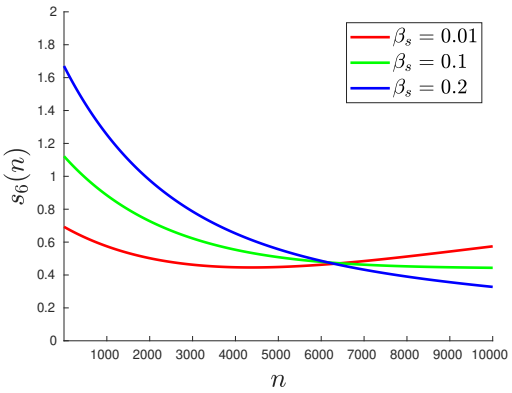
We plot initial results of our model, defined by (5.3.14), in figures 5.7 and 5.8. We set $N = 10,000$ and choose an initial distribution $s_1(n) = n^2/N^2$, with tows of all sizes but more of larger sizes, and we simulate the model for five top rollers. In



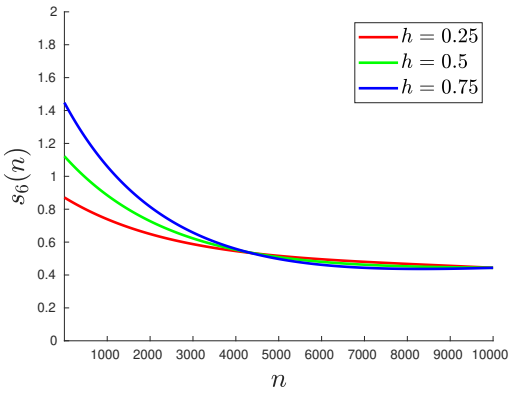
(a) Plot varying $\alpha_w = \alpha_s$, for $\beta_w = \beta_s = 0.1$, and $h = 0.5$.



(b) Plot varying β_w, for $\alpha_w = \alpha_s = \beta_s = 0.1$, and $h = 0.5$.



(c) Plot varying β_s, for $\alpha_w = \alpha_s = \beta_w = 0.1$, and $h = 0.5$.



(d) Plot varying h, for $\alpha_w = \alpha_s = \beta_w = \beta_s = 0.1$.

Figure 5.8: Plots of the distribution after the fifth top roller, $s_6(n)$, for different parameter values.

figure 5.7 we see that, as the tows step through the machine, the average number of smaller tows increases, and the average number of larger tows decreases, as we would expect. We see that increasing α_w and α_s, i.e. the probability of splitting, from figure 5.7a to 5.7b, results in the average number of smaller tows increasing much more quickly. This means that fewer top rollers are required to achieve a distribution dominated by smaller tows. We also plot the volume density of filaments in the tows, given by $ns_m(n)/N$, in figures 5.7c and 5.7d. These give us insight into the size of tows containing the majority of filaments. We see in figure 5.7c that the majority of filaments in the final distribution are contained in tows of size N, and in figure 5.7d the majority of filaments are contained in tows of size $n \approx N/5$. As stated previously the aim of the carding process is to produce a homogeneous web. Therefore a volume density distribution with a sharper peak is desired. We see the region around the

maximum becoming more narrow for the final distribution as α is increased, resulting in a more homogeneous final product.

We vary the constant parameter values and plot the final distribution $s_6(n)$ in figure 5.8. We see in figure 5.8a that increasing α_w and α_s, i.e. the probability of splitting in each nip region, results in more breakup of tows. Increasing the rate of transfer from the bottom roller to the top rollers, which is equivalent to increasing β_s and h, also leads to more breakup because the tows will go through the nip regions a higher average number of times and therefore have more chances to split. This effect is seen in figures 5.8c and 5.8d. The opposite is shown in figure 5.8b, as increasing transfer from the top rollers to the bottom, i.e. increasing β_w, results in a lower average number of cycles through the nip regions, and therefore less splitting.

5.4 A Model to Include Length

5.4.1 Master Equations

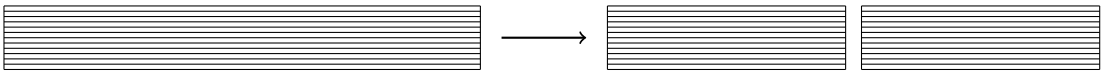
It is not only the average tow size that changes through the carding machine. The average length of the tows is also observed to decrease, and this can only happen if the fibres break. From this point we refer to the reduction in size as *splitting*, and the reduction in length as *breaking*.

We now derive a generalised model with the aim of analysing how to optimise splitting while minimising fibre breakage, as longer fibres lead to a stronger product [29]. We assume for simplicity that in each nip region a tow can either break (see figure 5.9a), split (see figure 5.9b), or do neither, but not both. We assume that when a tow breaks, it breaks at the same point across all the fibres it consists of, as seen in figure 5.9a. The new model to include length is illustrated schematically in figure 5.10, where we now define the distributions $w_m(n, l)$ and $s_m(n, l)$ as the average number of tows of size n and length l entering step m per unit time on the top and bottom rollers, respectively. We note that in reality length should be a continuous variable but to start with, for simplicity, we treat it in the same way as n.

We redefine our probabilities as follows:

$g_w(n, l)$ = Probability a tow of size n and length l on the top roller interacts with the bottom roller and either splits or breaks,

$g_s(n, l)$ = Probability a tow of size n and length l on the bottom roller interacts with the top roller and either splits or breaks,



(a) Tow breaking into two daughter tows of the same length.



(b) Tow splitting into two daughter tows of the same size.

Figure 5.9: Schematic diagrams of example tows splitting and breaking into two daughter tows.

$p_w(n,l)$ = Probability a tow of size n and length l on the top roller transfers to the bottom roller without splitting or breaking,

$p_s(n,l)$ = Probability a tow of size n and length l on the bottom roller transfers to the top roller without splitting or breaking,

$f(n,l)$ = Probability a tow splits, given that it either splits or breaks,

$F_1(k,n)$ = Average number of daughter tows of size n produced when a tow of size k splits,

$F_2(k,l)$ = Average number of daughter tows of length l produced when a tow of length k breaks,

$h_1(n,l)$ = Probability a daughter tow of size n and length l joins the top roller,

$h_2(n,l)$ = Probability a daughter tow of size n and length l joins the top roller,

where we require

$$f(1,l) = 0, \quad f(n,1) = 1, \quad g_w(1,1) = g_s(1,1) = 0. \tag{5.4.1}$$

Constraints (5.4.1) ensure that tows of the minimum thickness cannot split and tows of the minimum length cannot break.

We follow a similar process to the previous section and use these probability

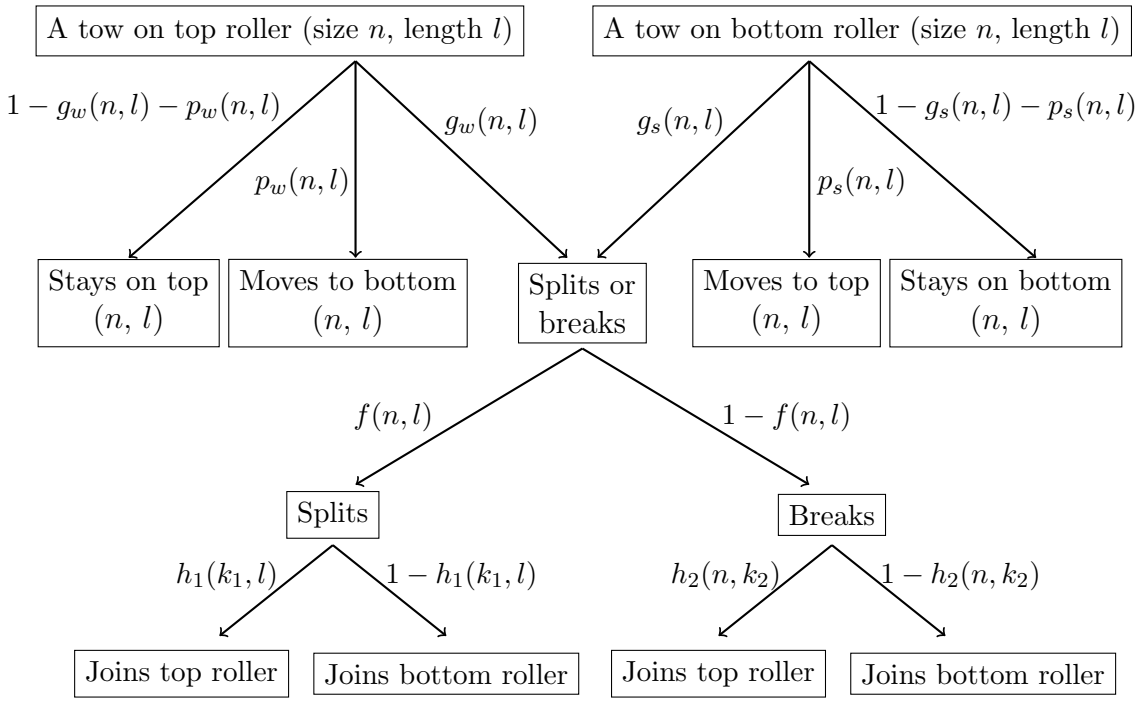


Figure 5.10: Diagram showing the probabilistic model for the size and length of carbon fibre tows.

definitions, and figure 5.10, to write the master equations

$$\begin{aligned} s_{m+1}(n,l) &= \left(1 - g_s(n,l) - p_s(n,l)\right) s_m(n,l) + p_w(n,l) w_m(n,l) \\ &\quad + \left(1 - h_2(n,l)\right) \sum_{k=l+1}^{L} \left(1 - f(n,k)\right) F_2(k,l) \left[g_s(n,k) s_m(n,k) + g_w(n,k) w_m(n,k)\right] \\ &\quad + \left(1 - h_1(n,l)\right) \sum_{k=n+1}^{N} f(k,l) F_1(k,n) \left[g_s(k,l) s_m(k,l) + g_w(k,l) w_m(k,l)\right], \end{aligned} \tag{5.4.2a}$$

$$\begin{aligned} w_{m+1}(n,l) &= \left(1 - g_w(n,l) - p_w(n,l)\right) w_m(n,l) + p_s(n,l) s_m(n,l) \\ &\quad + h_2(n,l) \sum_{k=l+1}^{L} \left(1 - f(n,k)\right) F_2(k,l) \left[g_s(n,k) s_m(n,k) + g_w(n,k) w_m(n,k)\right] \\ &\quad + h_1(n,l) \sum_{k=n+1}^{N} f(k,l) F_1(k,n) \left[g_s(k,l) s_m(k,l) + g_w(k,l) w_m(k,l)\right]. \end{aligned} \tag{5.4.2b}$$

The first terms in equations (5.4.2) describe tows remaining on the same rollers, and not changing in size and length, the second terms describe tows transferring between rollers, but not splitting or breaking, the third terms describe breaking and then joining either roller, and the fourth terms describe splitting and then joining either roller.

We again must ensure that the total mass of fibres is conserved, and we begin by defining the total rate of tows entering stage m as

$$T_m(n,l) = w_m(n,l) + s_m(n,l), \tag{5.4.3}$$

and the tows in the "split or break" region by

$$I_m(n,l) = g_w(n,l)w_m(n,l) + g_s(n,l)s_m(n,l). \tag{5.4.4}$$

We can thus sum (5.4.2) and then write the net master equation as

$$\begin{aligned} T_{m+1}(n,l) =& T_m(n,l) - I_m(n,l) \\ &+ \sum_{k=l+1}^{L} (1 - f(n,k))F_2(k,l)I_m(n,k) \\ &+ \sum_{k=n+1}^{N} f(n,k)F_1(k,n)I_m(k,l). \end{aligned} \tag{5.4.5}$$

Defining the total mass of tows entering position m per unit time as

$$M_m = \sum_{n=1}^{N}\sum_{l=1}^{L} nlT_m(n,l), \tag{5.4.6}$$

we derive the net conservation equation

$$M_{m+1} - M_m = -\sum_{n=1}^{N}\sum_{l=1}^{L} nlI_m(n,l) + S_1 + S_2, \tag{5.4.7}$$

where

$$S_1 = \sum_{n=1}^{N}\sum_{k=1}^{L}\left[\sum_{l=1}^{k-1} lF_2(k,l)\right] n(1 - f(n,k))I_m(n,k), \tag{5.4.8}$$

$$S_2 = \sum_{l=1}^{L}\sum_{k=1}^{N}\left[\sum_{n=1}^{k-1} nF_1(k,n)\right] lf(k,l)I_m(k,l). \tag{5.4.9}$$

To ensure mass conservation, i.e. $M_{m+1} = M_m$, we therefore require

$$\sum_{n=1}^{k-1} nF_1(k,n) = \sum_{l=1}^{k-1} lF_2(k,l) = k. \tag{5.4.10}$$

As in the previous section, we assume that F_1 and F_2 are independent of n and l respectively, i.e. splitting and breaking are both uniformly distributed with respect to size and length, and thus obtain

$$F_1(k) = F_2(k) = \frac{2}{k-1}. \tag{5.4.11}$$

Ensuring that the tows taken up by the top roller then feed back into the region from the left, as in figures 5.5 and 5.6, we set $w_{m+1} = w_m$ in master equations (5.4.2) to give the governing equations

$$\begin{aligned} s_{m+1}(n,l) &= (1 - g_s(n,l) - p_s(n,l))\, s_m(n,l) + p_w(n,l) w_m(n,l) \\ &\quad + (1 - h_2(n,l)) \sum_{k=l+1}^{L} (1 - f(n,k)) F_2(k) \big[g_s(n,k) s_m(n,k) + g_w(n,k) w_m(n,k) \big] \\ &\quad + (1 - h_1(n,l)) \sum_{k=n+1}^{N} f(k,l) F_1(k) \big[g_s(k,l) s_m(k,l) + g_w(k,l) w_m(k,l) \big], \end{aligned} \tag{5.4.12a}$$

$$\begin{aligned} w_m(n,l) &= \frac{1}{g_w(n,l) + p_w(n,l)} \Bigg\{ p_s(n,l) s_m(n,l) \\ &\quad + h_2(n,l) \sum_{k=l+1}^{L} (1 - f(n,k)) F_2(k) \big[g_s(n,k) s_m(n,k) + g_w(n,k) w_m(n,k) \big] \\ &\quad + h_1(n,l) \sum_{k=n+1}^{N} f(k,l) F_1(k) \big[g_s(k,l) s_m(k,l) + g_w(k,l) w_m(k,l) \big] \Bigg\}, \end{aligned} \tag{5.4.12b}$$

with conditions

$$s_{m+1}(N,L) = (1 - g_s(N,L) - p_s(N,L))\, s_m(N,L) + p_w(N,L) w_m(N,L), \tag{5.4.13a}$$

$$\begin{aligned} s_{m+1}(N,l) &= (1 - g_s(N,l) - p_s(N,l))\, s_m(N,l) + p_w(N,l) w_m(N,l) \\ &\quad + (1 - h_2(N,l)) \sum_{k=l+1}^{L} (1 - f(N,k)) F_2(k) \big[g_s(N,k) s_m(N,k) + g_w(N,k) w_m(N,k) \big], \end{aligned} \tag{5.4.13b}$$

$$\begin{aligned} s_{m+1}(n,L) &= (1 - g_s(n,L) - p_s(n,L))\, s_m(n,L) + p_w(n,L) w_m(n,L) \\ &\quad + (1 - h_1(n,L)) \sum_{k=n+1}^{N} f(k,L) F_1(k) \big[g_s(k,L) s_m(k,L) + g_w(k,L) w_m(k,L) \big], \end{aligned} \tag{5.4.13c}$$

$$w_m(N,L) = \frac{p_s(N,L) s_m(N,L)}{g_w(N,L) + p_w(N,L)}, \tag{5.4.13d}$$

$$\begin{aligned} w_m(N,l) &= \frac{1}{g_w(N,l) + p_w(N,l)} \Bigg\{ p_s(N,l) s_m(N,l) \\ &\quad + h_2(N,l) \sum_{k=l+1}^{L} (1 - f(N,k)) F_2(k) \big[g_s(N,k) s_m(N,k) + g_w(N,k) w_m(N,k) \big] \Bigg\}, \end{aligned} \tag{5.4.13e}$$

$$w_m(n,L) = \frac{1}{g_w(n,L)+p_w(n,L)}\Bigg\{p_s(n,L)s_m(n,L) + h_1(n,L)\sum_{k=n+1}^{N} f(k,L)F_1(k)\big[g_s(k,L)s_m(k,L)+g_w(k,L)w_m(k,L)\big]\Bigg\}. \tag{5.4.13f}$$

Now $w_m(n,l)$ is defined as the average number of tows of size n and length l on top roller m per unit time, and $s_m(n,l)$ is the average number of tows of size n and length l on the bottom roller before interacting with top roller m per unit time. Conditions (5.4.13a) and (5.4.13d) describe tows that remain the maximum size and length, conditions (5.4.13b) and (5.4.13e) describe tows that remain the maximum size but change length, and conditions (5.4.13c) and (5.4.13f) describe tows that remain the maximum length but change size.

Our solution strategy is similar to in the previous section. Given the bottom roller distribution $s_m(n,l)$ of tows entering from the left we first solve governing equations (5.4.12b), (5.4.13d), (5.4.13e), and (5.4.13f) for $w_m(n,l)$. Then the distribution $s_{m+1}(n,l)$ exiting to the right is determined explicitly by the governing equations (5.4.12a), (5.4.13a), (5.4.13b), and (5.4.13c), and fed in as the entry distribution for the next region.

5.4.2 Results

In this section we discuss simulations of equations (5.4.12)-(5.4.13), and so we have to define our transition probabilities, noting we have the constraints (5.4.1) along with

$$0 \le g_w(n,l),\ g_s(n,l),\ p_w(n,l),\ p_s(n,l),\ f(n,l),\ h(n,l) \le 1, \tag{5.4.14a}$$

$$g_w(n,l)+p_w(n,l)\le 1, \quad g_s(n,l)+p_s(n,l)\le 1. \tag{5.4.14b}$$

We assume that tows are more likely to split and break if they consist of more individual fibres and are longer, and so to begin we choose the probabilities

$$g_w(n,l) = \alpha_w\frac{(n-1)(l-1)}{(N-1)(L-1)}, \quad g_s(n,l) = \alpha_s\frac{(n-1)(l-1)}{(N-1)(L-1)}, \tag{5.4.15a}$$

$$p_w(n,l) = \beta_w, \quad p_s(n,l) = \beta_s, \quad h_1(n,l) = h_1, \quad h_2(n,l) = h_2, \tag{5.4.15b}$$

$$f(n,l) = \frac{n-1}{n+l-2}, \tag{5.4.15c}$$

where (5.4.15c) has been chosen as an example function that satisfies (5.4.1), and assumes that longer tows are more likely to break than split. We will discuss alternative

functions later in this section. We assume an initial distribution of tows of

$$s_1(n,l) = \left(\frac{nl}{NL}\right)^2, \tag{5.4.16}$$

and so the tows are more likely to be of larger sizes and lengths when entering this section of the carding machine. Similar results are observed for different initial distributions.

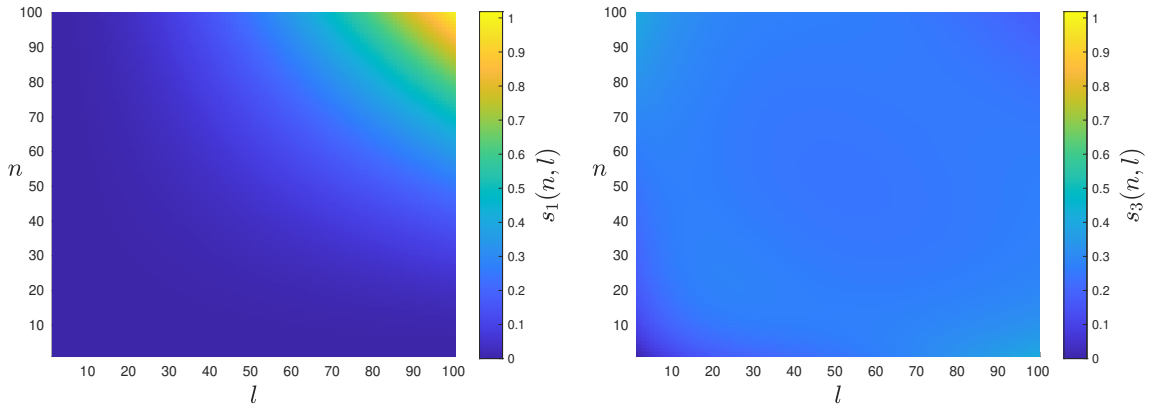
Solutions for the constitutive relations (5.4.15) are shown in figure 5.11, where we have arbitrarily chosen $N = L = 100$ for the simulations. We can therefore think of n in units of 100 filaments. We see that as the tows interact with more top rollers (stepping up in m) the fibres are gradually split and broken, until most of them are of a small size and length. We step up to $m = 6$ so we are modelling a carding machine with five pairs of top rollers. We note that at $m = 3$, shown in figure 5.11b, the distribution has become relatively uniform, before it becomes much more concentrated at small n and l at $m = 6$, in figure 5.11d. We note that the distribution is symmetric about $n = l$ in figure 5.11 because we have assumed symmetry in our transition probabilities. In practice this isn't realistic, and will be discussed in more detail later in this section when we look at alternative forms for our transition probabilities.

In figures 5.12, 5.13, and 5.14 we plot the results at $m = 6$ for different parameter values, as we did for the constant-length model in the previous section. We see that increasing the probability of either splitting or breaking, i.e. increasing α_s or α_w, leads to tows of smaller size and length, as expected.

We note that β_s is the probability of a tow moving from the bottom roller to the top, and β_w is the probability of a tow moving the other way, and that we expect this transfer to depend on the centrifugal force of the rollers [36]. Using the typical parameter values shown in table 1.1 we note that

$$\frac{V_s^2}{R_s} > \frac{V_w^2}{R_w}, \tag{5.4.17}$$

where V_s and R_s are the surface velocity and radius of the swift, and V_w and R_w are the surface velocity and radius of the worker. This means the centrifugal force of the swift is greater than that of the worker, and we therefore expect $\beta_s \geq \beta_w$. We see from figures 5.13 and 5.14 that for tows of smaller length and size it is advantageous to have high transfer from bottom to top, and low transfer from top to bottom, so that tows travel through the 'nip' regions more times.



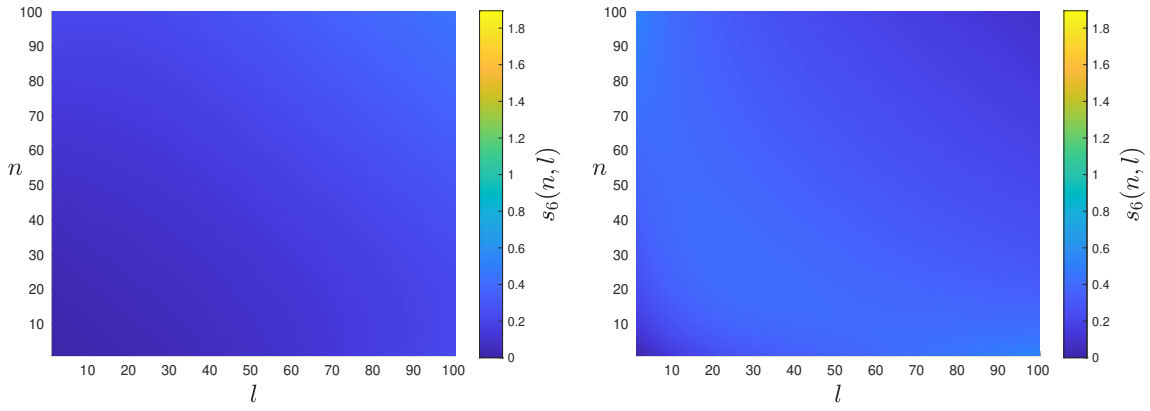
(a) Plot at $m = 1$.

(b) Plot at $m = 3$.

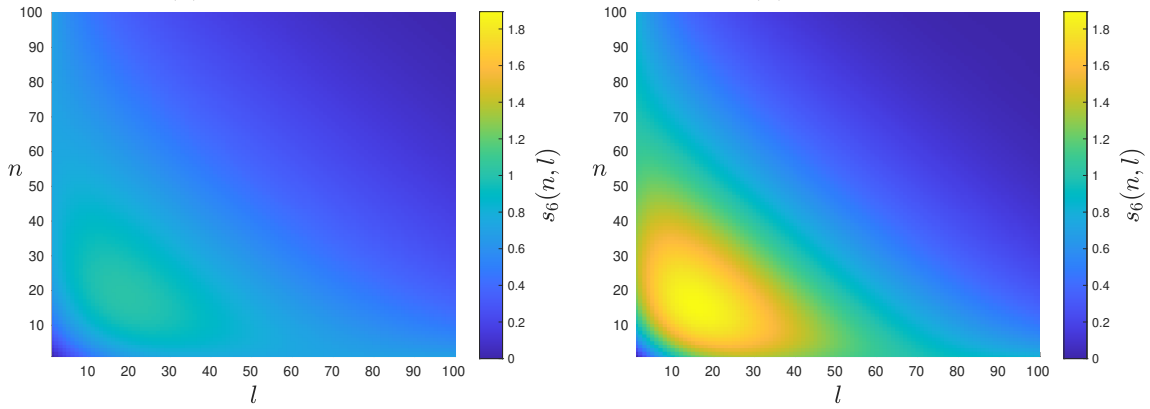
(c) Plot at $m = 5$.

(d) Plot at $m = 6$.

Figure 5.11: Plots of distribution $s_m(n, l)$ at successive positions $m = 1, ..., 6$. Plotted for $\alpha_w = \alpha_s = 0.5$, $\beta_w = \beta_s = 0.1$, and $h_1 = h_2 = 0.5$.

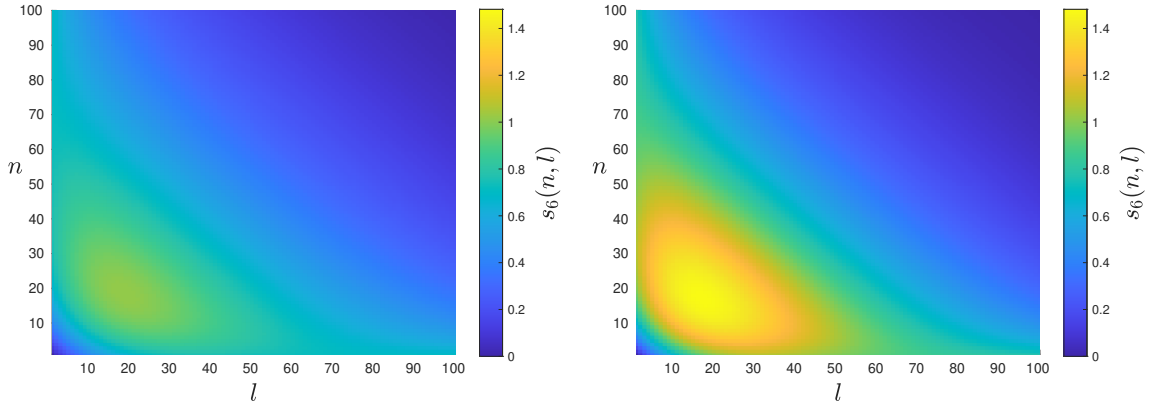


(a) $\alpha_w = \alpha_s = 0.1$. (b) $\alpha_w = \alpha_s = 0.3$.



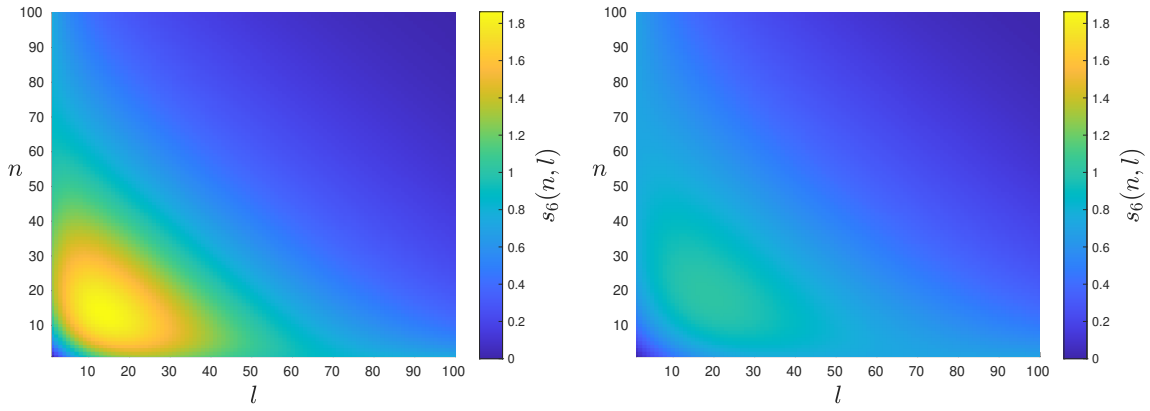
(c) $\alpha_w = \alpha_s = 0.5$. (d) $\alpha_w = \alpha_s = 0.7$.

Figure 5.12: Plots of distribution $s_6(n, l)$ for different α_w and α_s, with $\beta_w = \beta_s = 0.1$, and $h_1 = h_2 = 0.5$.



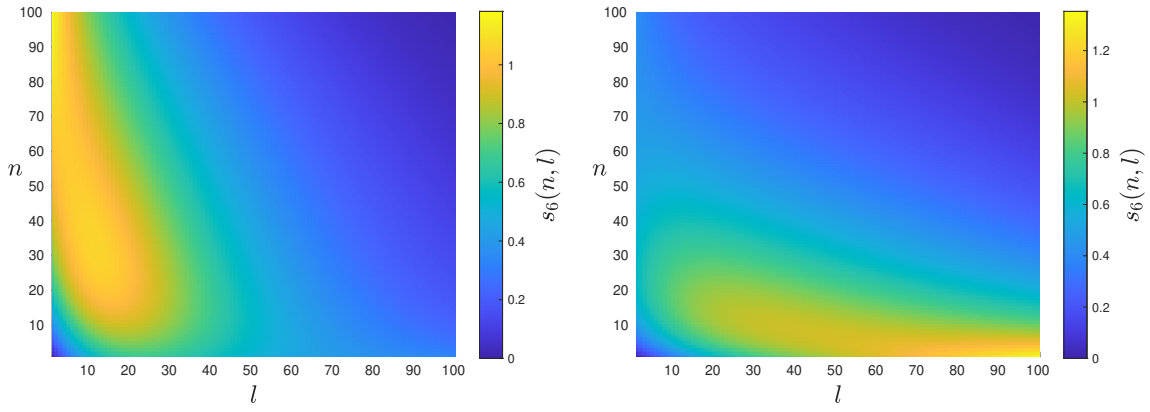
(a) $\beta_s = 0.1$. (b) $\beta_s = 0.2$.

Figure 5.13: Plots of distribution $s_6(n, l)$ for different β_s, with $\alpha_w = \alpha_s = 0.5$, $\beta_w = 0.1$, and $h_1 = h_2 = 0.5$.



(a) $\beta_w = 0.05$. (b) $\beta_w = 0.1$.

Figure 5.14: Plots of distribution $s_6(n,l)$ for different β_w, with $\alpha_w = \alpha_s = 0.5$, $\beta_s = 0.1$, and $h_1 = h_2 = 0.5$.



(a) $\gamma = 1.5$. (b) $\gamma = 2/3$.

Figure 5.15: Plots of distribution $s_6(n,l)$ for different γ, with $\alpha_w = \alpha_s = 0.5$, $\beta_s = 0.1$, and $h_1 = h_2 = 0.5$.

We can vary the probability f by defining it as

$$f(n,l) = \left(\frac{n-1}{n+l-2}\right)^{\gamma}, \tag{5.4.18}$$

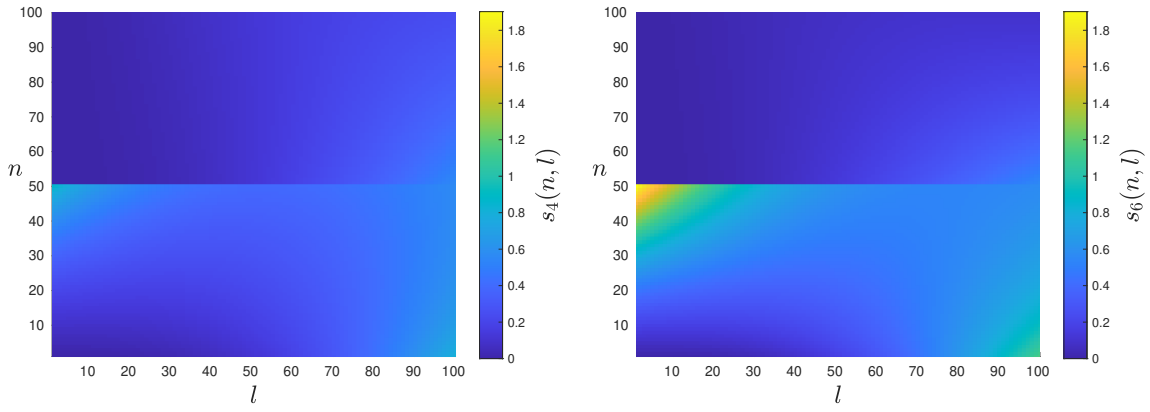
so we can change whether the tow is more likely to split or break, by changing the value of γ. This effect can be seen in figure 5.15, where we plot the final distribution $s_6(n,l)$. We see that for $\gamma > 1$, i.e. smaller f, we end up with shorter tows of larger sizes, and for $\gamma < 1$ the distribution shows longer tows of smaller sizes.

Another form of f that satisfies conditions (5.4.1) is

$$f = \begin{cases} 1, \ n > n_{\text{crit}}, \\ 0, \ n < n_{\text{crit}}, \end{cases} \tag{5.4.19}$$

for some critical tow size n_{crit}. We assume here that thick tows are far more likely to split than break and thin tows are far more likely to break. Equation (5.4.19) represents the limiting case of an abrupt transition from certain splitting to certain breaking at a critical tow size n_{crit}. We plot the results using this new probability (5.4.19) in figure 5.16 for two different values of n_{crit}. We see that for a lower n_{crit} we get more splitting than breaking, and therefore there are longer, thinner tows in the final distribution.

In practice, comparison with experimental data would be required to determine the parameters α_w, α_s, β_w, β_s, h_1, h_2, γ, and n_{crit}. In chapter 4 we showed that the splitting of a tow depends on the properties of the machine, such as tooth radius, tooth force/velocity, and the properties of the tows, such as the bending stiffness, and the coefficient of friction between a tooth and a tow. These properties will therefore be important in determining parameters α_w and α_s. There are many studies looking at transfer between rollers in the carding machine, with a roller's "collecting power" stated to depend on the roller velocity, tooth number density, and tooth angles [49]. These machine properties will therefore be important in defining our "transfer" parameters β_w, β_s, h_1, and h_2. The general model (5.4.12)-(5.4.13) provides us with a tool that could in practice be used to predict the properties of the final tow distribution after carding, given the initial properties of the tows and the machine. In chapter 6 we present a case study of how experimental data could be used to inform this type of model.



(a) $s_4(n,l)$ for $n_{\text{crit}} = N/2$.

(b) $s_6(n,l)$ for $n_{\text{crit}} = N/2$.

(c) $s_4(n,l)$ for $n_{\text{crit}} = N/4$.

(d) $s_6(n,l)$ for $n_{\text{crit}} = N/4$.

Figure 5.16: Plots of distributions $s_4(n,l)$ and $s_6(n,l)$ for different critical sizes, n_{crit}, with $\alpha_w = \alpha_s = 0.3$, $\beta_w = \beta_s = 0.1$, and $h_1 = h_2 = 0.5$.

5.5 A Continuous Model for Carbon Fibre Tows

5.5.1 Governing Equations

The tow length l is, in reality, a continuous variable and, due to the large value of N, it is sensible to approximate tow size n as a continuous variable as well. We initially take the continuum limit by approximating the sums in (5.4.12) as integrals, but note that this approximation could be improved by using the Euler-Maclaurin sum formula [6, 46]. The discrete governing equations (5.4.12) thus become

$$\begin{aligned} s_{m+1}(n,l) &= \left(1 - g_s(n,l) - p_s(n,l)\right) s_m(n,l) + p_w(n,l) w_m(n,l) \\ &\quad + \left(1 - h_2(n,l)\right) \int_l^L (1 - f(n,y)) F_2(y,l) \big[g_s(n,y) s_m(n,y) + g_w(n,y) w_m(n,y) \big] \mathrm{d}y \\ &\quad + \left(1 - h_1(n,l)\right) \int_n^N f(z,l) F_1(z,n) \big[g_s(z,l) s_m(z,l) + g_w(z,l) w_m(z,l) \big] \mathrm{d}z, \end{aligned} \tag{5.5.1}$$

$$\begin{aligned} w_m(n,l) = \frac{1}{g_w(n,l) + p_w(n,l)} \Bigg\{ & p_s(n,l) s_m(n,l) \\ & + h_2(n,l) \int_l^L (1 - f(n,y)) F_2(y,l) \big[g_s(n,y) s_m(n,y) + g_w(n,y) w_m(n,y) \big] \mathrm{d}y \\ & + h_1(n,l) \int_n^N f(z,l) F_1(z,n) \big[g_s(z,l) s_m(z,l) + g_w(z,l) w_m(z,l) \big] \mathrm{d}z \Bigg\}, \end{aligned} \tag{5.5.2}$$

where, after making analogous assumptions to the discrete case, we require

$$F_1(x) = F_2(x) = \frac{2}{x}, \tag{5.5.3}$$

to ensure mass is conserved. Equations (5.5.1) and (5.5.2) are the continuous limit of the discrete equations (5.4.12a) and (5.4.12b) respectively, where n and l are now defined as the continuous size and continuous length of a tow. In this continuous case our probabilities must satisfy

$$f(0,l) = 0, \quad f(n,0) = 1, \quad g_w(0,0) = g_s(0,0) = 0, \tag{5.5.4}$$

along with inequalities (5.4.14) to ensure we cannot have negative sizes and lengths.

We normalise using the scalings

$$n = Nx, \quad l = Ly, \quad s_m = S s_m^*, \quad w_m = S w_m^*. \tag{5.5.5}$$

The resulting dimensionless governing equations are

$$
\begin{aligned}
s^*_{m+1}(x,y) &= \left(1 - g_s(x,y) - p_s(x,y)\right) s^*_m(x,y) + p_w(x,y) w^*_m(x,y) \\
&\quad + 2\left(1 - h_2(x,y)\right) \int_y^1 \left(\frac{1 - f(x,y^*)}{y^*}\right) \Big[g_s(x,y^*) s^*_m(x,y^*) \\
&\qquad\qquad + g_w(x,y^*) w^*_m(x,y^*) \Big] \mathrm{d}y^* \\
&\quad + 2\left(1 - h_1(x,y)\right) \int_x^1 \frac{f(x^*,y)}{x^*} \Big[g_s(x^*,y) s^*_m(x^*,y) \\
&\qquad\qquad + g_w(x^*,y) w^*_m(x^*,y) \Big] \mathrm{d}x^*, \qquad (5.5.6a)
\end{aligned}
$$

$$
\begin{aligned}
w^*_m(x,y) &= \frac{1}{g_w(x,y) + p_w(x,y)} \Bigg\{ p_s(x,y) s^*_m(x,y) \\
&\quad + 2h_2(x,y) \int_y^1 \left(\frac{1 - f(x,y^*)}{y^*}\right) \Big[g_s(x,y^*) s^*_m(x,y^*) \\
&\qquad\qquad + g_w(x,y^*) w^*_m(x,y^*) \Big] \mathrm{d}y^* \\
&\quad + 2h_1(x,y) \int_x^1 \frac{f(x^*,y)}{x^*} \Big[g_s(x^*,y) s^*_m(x^*,y) + g_w(x^*,y) w^*_m(x^*,y) \Big] \mathrm{d}x^* \Bigg\}, \qquad (5.5.6b)
\end{aligned}
$$

with conditions

$$
s^*_{m+1}(1,1) = \left(1 - g_s(1,1) - p_s(1,1)\right) s^*_m(1,1) + p_w(1,1) w^*_m(1,1), \qquad (5.5.7a)
$$

$$
\begin{aligned}
s^*_{m+1}(1,y) &= \left(1 - g_s(1,y) - p_s(1,y)\right) s^*_m(1,y) + p_w(1,y) w^*_m(1,y) \\
&\quad + 2\left(1 - h_2(1,y)\right) \int_y^1 \left(\frac{1 - f(1,y^*)}{y^*}\right) \left[g_s(1,y^*) s^*_m(1,y^*) + g_w(1,y^*) w^*_m(1,y^*) \right] \mathrm{d}y^*, \qquad (5.5.7b)
\end{aligned}
$$

$$
\begin{aligned}
s^*_{m+1}(x,1) &= \left(1 - g_s(x,1) - p_s(x,1)\right) s_m(x,1) + p_w(x,1) w^*_m(x,1) \\
&\quad + 2\left(1 - h_1(x,1)\right) \int_x^1 \frac{f(x^*,1)}{x^*} \left[g_s(x^*,1) s^*_m(x^*,1) + g_w(x^*,1) w^*_m(x^*,1) \right] \mathrm{d}x^*, \qquad (5.5.7c)
\end{aligned}
$$

$$
w^*_m(1,1) = \frac{p_s(1,1) s_m(1,1)}{g_w(1,1) + p_w(1,1)}, \qquad (5.5.7d)
$$

$$
\begin{aligned}
w^*_m(1,y) &= \frac{1}{g_w(1,y) + p_w(1,y)} \Bigg\{ p_s(1,y) s^*_m(1,y) \\
&\quad + 2h_2(1,y) \int_y^1 \left(\frac{1 - f(1,y^*)}{y^*}\right) \left[g_s(1,y^*) s^*_m(1,y^*) + g_w(1,y^*) w^*_m(1,y^*) \right] \mathrm{d}y^* \Bigg\}, \qquad (5.5.7e)
\end{aligned}
$$

$$w_m^*(x,1) = \frac{1}{g_w(x,1)+p_w(x,1)}\Bigg\{ p_s(x,1)s_m^*(x,1) + 2h_1(x,1)\int_x^1 \frac{f(x^*,1)}{x^*}\left[g_s(x^*,1)s_m^*(x^*,1)+g_w(x^*,1)w_m^*(x^*,1)\right]\mathrm{d}x^*\Bigg\}. \tag{5.5.7f}$$

Analysis of the full problem (5.5.6)-(5.5.7) is discussed in section 5.5.3, but we first discuss a simplified version in the next section.

5.5.2 A Simple Model for Tow Size

In this section we simplify the analysis of our continuous model by removing the length dependence, noting that in this case, $f = 1$. The governing equations (5.5.6) reduce to

$$s_{m+1}(x) = (1-g_s(x)-p_s(x))\,s_m(x) + p_w(x)w_m(x) + 2\,(1-h_1(x))\int_x^1 \frac{1}{z}\left[g_s(z)s_m(z)+g_w(z)w_m(z)\right]\mathrm{d}z, \tag{5.5.8a}$$

$$w_m(x) = \frac{p_s(x)s_m(x) + 2h_1(x)\int_x^1 \frac{1}{z}\left[g_s(z)s_m(z)+g_w(z)w_m(z)\right]\mathrm{d}z}{g_w(x)+p_w(x)}. \tag{5.5.8b}$$

Assuming $h_1(x) = h_1$ is a constant, we can differentiate equations (5.5.8), resulting in the ODE system

$$\frac{\mathrm{d}w_m}{\mathrm{d}x} + H_1(x)w_m = H_{2,m}(x), \tag{5.5.9a}$$

$$\frac{\mathrm{d}s_{m+1}}{\mathrm{d}x} = H_{3,m}(x), \tag{5.5.9b}$$

where

$$H_1(x) = \frac{\frac{\mathrm{d}}{\mathrm{d}x}\left[g_w(x)+p_w(x)\right] + \frac{2h_1}{x}g_w(x)}{g_w(x)+p_w(x)}, \tag{5.5.10a}$$

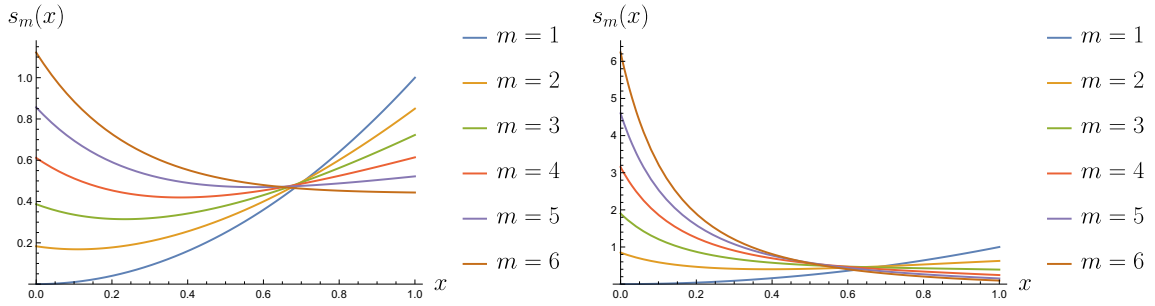
$$H_{2,m}(x) = \frac{\frac{\mathrm{d}}{\mathrm{d}x}\left[p_s(x)s_m(x)\right] - \frac{2h_1}{x}g_s(x)s_m(x)}{g_w(x)+p_w(x)}, \tag{5.5.10b}$$

$$H_{3,m}(x) = \frac{\mathrm{d}}{\mathrm{d}x}\left[(1-g_s(x)-p_s(x))s_m(x)+p_w(x)w_m(x)\right] - \frac{2(1-h_1)}{x}\left[g_s(x)s_m(x)+g_w(x)w_m(x)\right]. \tag{5.5.10c}$$

These ODEs are subject to the boundary conditions

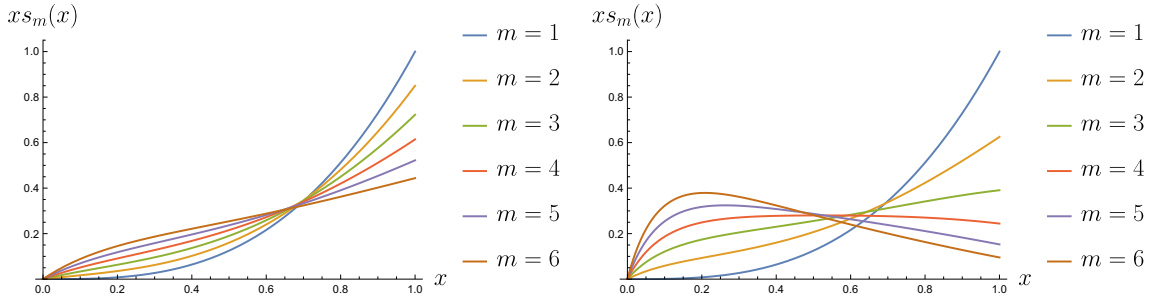
$$w_m(1) = k_1k_2^{m-1}s_1(1), \tag{5.5.11a}$$

$$s_m(1) = k_2^{m-1}s_1(1), \tag{5.5.11b}$$



(a) $\alpha_w = \alpha_s = 0.1$.

(b) $\alpha_w = \alpha_s = 0.3$.



(c) Volume density for $\alpha_w = \alpha_s = 0.1$.

(d) Volume density for $\alpha_w = \alpha_s = 0.3$.

Figure 5.17: Plots of continuous distribution, $s_m(x)$, and volume density, $xs_m(x)$, at successive positions $m = 1, ..., 6$ for $\beta_w = \beta_s = 0.1$, and $h_1 = 0.5$.

where we define the two constants

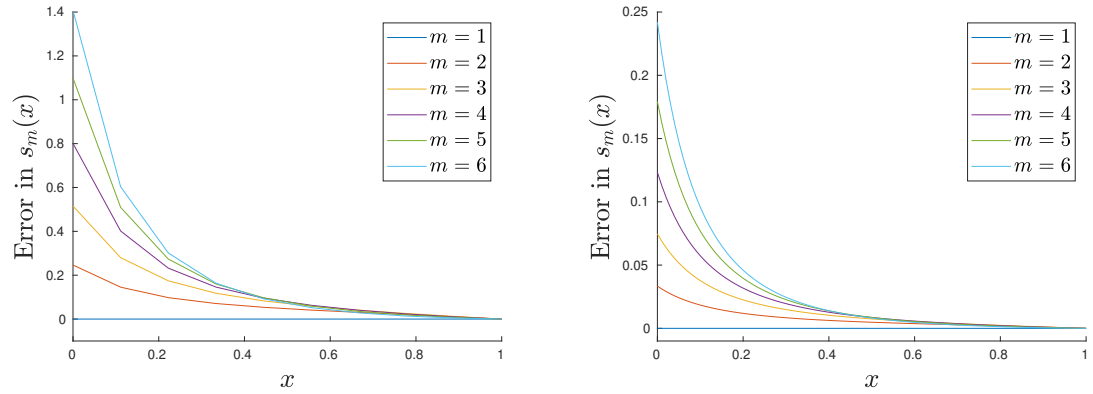
$$k_1 = \frac{p_s(1)}{g_w(1) + p_w(1)}, \tag{5.5.12a}$$

$$k_2 = \frac{g_w(1)\left(1 - g_s(1) - p_s(1)\right) + p_w(1)\left(1 - g_s(1)\right)}{g_w(1) + p_w(1)}. \tag{5.5.12b}$$

The probabilities must satisfy the conditions (5.5.4) and we choose probabilities that are analogous to those we had for the discrete case, in (5.3.12), so we have

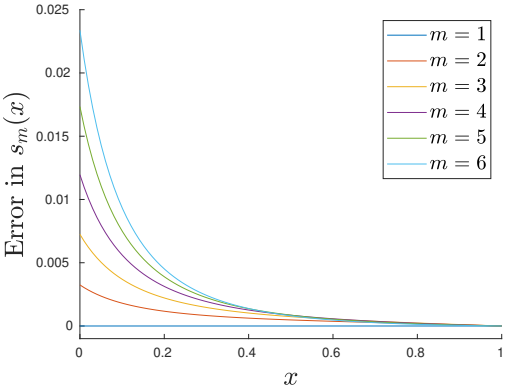
$$g_w(x) = \alpha_w x, \quad g_s(x) = \alpha_s x, \quad p_w(x) = \beta_w, \quad p_s(x) = \beta_s. \tag{5.5.13}$$

We plot solutions to the simplified continuous model (5.5.9)-(5.5.13) at different steps m in figure 5.17 for two different values of the parameters α_w and α_s. Comparing figures 5.17a-5.17d to figures 5.7a-5.7d we see that qualitatively the continuous model provides a good approximation of the discrete model. We plot the absolute error between the continuous model and the original discrete model from section 5.3, in figure 5.18. We see a significant decrease in the error as N is increased, and an increase in the error from $m = 1$ to $m = 6$. For higher m we still have a relatively large error that would require an improved approximation for the sums, such as the Euler-Maclaurin formula [6], to reduce; see the following section.

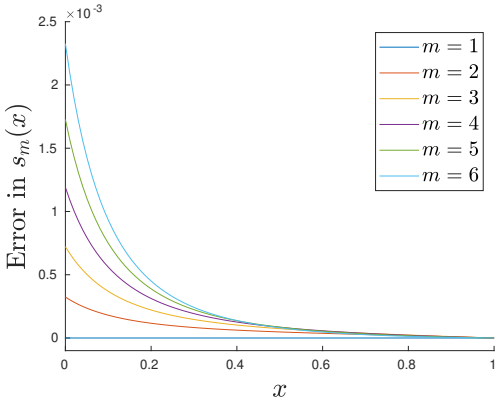


(a) $N = 10$.

(b) $N = 100$.



(c) $N = 10^3$.



(d) $N = 10^4$.

Figure 5.18: Plots of the absolute error in $s_m(x)$ between the continuous and discrete models for different m and N and $\alpha_w = \alpha_s = 0.3$, $\beta_w = \beta_s = 0.1$, and $h_1 = 0.5$.

We plot the maximum absolute error against $1/N$ in figure 5.19, where we see the error varying linearly against $1/N$. Ideally we would want an approximation at least of order $1/N^2$ which, as stated above, would require a slightly different approach. The method presented in this section however provides a useful, computationally inexpensive model for the general evolution of tow size.

5.5.3 Numerical Solution

5.5.3.1 Derivation of Numerical Scheme

In this section we return to the full dimensionless problem (5.5.6)-(5.5.7) including the length and size of tows. Our strategy is essentially to take the continuous limit of our discrete governing equations (5.4.12), and then discretize in a different way so we can efficiently solve the resulting system numerically. Using the Euler-Maclaurin

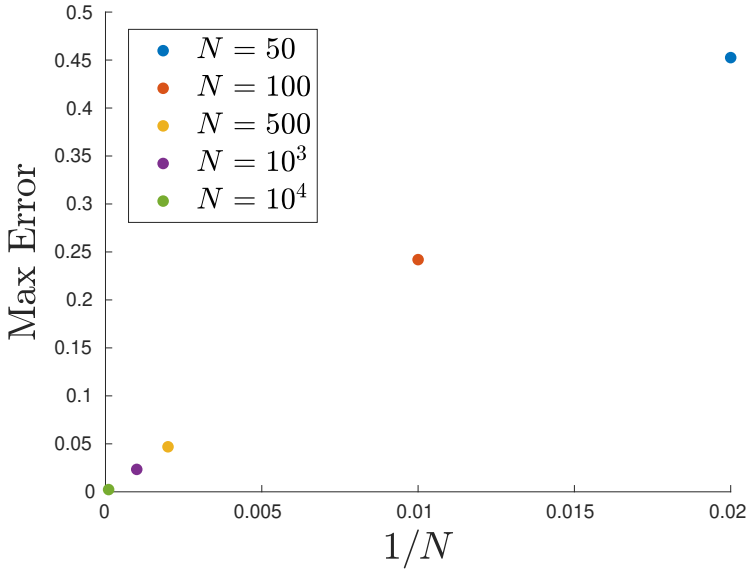


Figure 5.19: Plot of the maximum absolute error in $s_m(x)$ against $1/N$.

formula [6, 46] to $\mathcal{O}(1/N)$ we can improve on equations (5.5.6), resulting in

$$\begin{aligned} s_{m+1}(x,y) &= (1 - g_s(x,y) - p_s(x,y))\, s_m(x,y) + p_w(x,y) w_m(x,y) \\ &\quad + (1 - h_2(x,y)) \left[L \int_y^1 q_1(x,z) \mathrm{d}z + \frac{1}{2} (q_1(x,1) - q_1(x,y)) \right] \\ &\quad + (1 - h_1(x,y)) \left[N \int_x^1 q_2(z,y) \mathrm{d}z + \frac{1}{2} (q_2(1,y) - q_1(x,y)) \right], \end{aligned} \tag{5.5.14a}$$

$$\begin{aligned} w_m(x,y) &= \frac{1}{g_w(x,y) + p_w(x,y)} \Bigg\{ p_s(x,y) s_m(x,y) \\ &\quad + h_2(x,y) \left[L \int_y^1 q_1(x,z) \mathrm{d}z + \frac{1}{2} (q_1(x,1) - q_1(x,y)) \right] \\ &\quad + h_1(x,y) \left[N \int_x^1 q_2(z,y) \mathrm{d}z + \frac{1}{2} (q_2(1,y) - q_1(x,y)) \right] \Bigg\}, \end{aligned} \tag{5.5.14b}$$

where

$$q_1(x,y) = (1 - f(x,y))\, F_2(y) \left[g_s(x,y) s_m(x,y) + g_w(x,y) w_m(x,y) \right], \tag{5.5.15a}$$

$$q_2(x,y) = f(x,y) F_1(x) \left[g_s(x,y) s_m(x,y) + g_w(x,y) w_m(x,y) \right]. \tag{5.5.15b}$$

We then approximate the integrals in (5.5.14) using a different discretization, where we divide the domain up into B 'bins', each of size $N/B = L/B$. We thus obtain

$$\begin{aligned} s_{m+1}(b_n, b_l) &= (1 - g_s(b_n, b_l) - p_s(b_n, b_l))\, s_m(b_n, b_l) + p_w(b_n, b_l) w_m(b_n, b_l) \\ &+ (1 - h_2(b_n, b_l)) \left[\frac{1}{2} \left(1 - \frac{L}{B} \right) (q_1(b_n, B) - q_1(b_n, b_l)) + \frac{L}{B} \sum_{j=b_l+1}^{B} q_1(b_n, j) \right] \\ &+ (1 - h_1(b_n, b_l)) \left[\frac{1}{2} \left(1 - \frac{N}{B} \right) (q_2(B, b_l) + q_2(b_n, b_l)) + \frac{N}{B} \sum_{j=b_n+1}^{B} q_2(j, b_l) \right], \end{aligned} \tag{5.5.16a}$$

$$\begin{aligned} w_m(b_n, b_l) = \frac{1}{g_w(b_n, b_l) + p_w(b_n, b_l)} \Bigg\{ & p_s(b_n, b_l) s_m(b_n, b_l) \\ &+ h_2(b_n, b_l) \left[\frac{1}{2} \left(1 - \frac{L}{B} \right) (q_1(b_n, B) - q_1(b_n, b_l)) + \frac{L}{B} \sum_{j=b_l+1}^{B} q_1(b_n, j) \right] \\ &+ h_1(b_n, b_l) \left[\frac{1}{2} \left(1 - \frac{N}{B} \right) (q_2(B, b_l) - q_2(b_n, b_l)) + \frac{N}{B} \sum_{j=b_n+1}^{B} q_2(j, b_l) \right] \Bigg\}, \end{aligned} \tag{5.5.16b}$$

where

$$b_n = \frac{nB}{N},\ b_l = \frac{lB}{L}. \tag{5.5.17}$$

We note that we recover our initial model if we choose $B = N = L$.

5.5.3.2 Ignoring Length

If we ignore length, using our new discretization, equations (5.5.16) become

$$\begin{aligned} s_{m+1}(b_n) = &(1 - g_s(b_n) - p_s(b_n))\, s_m(b_n) + p_w(b_n) w_m(b_n) \\ &+ (1 - h(b_n)) \left[\frac{1}{2} \left(1 - \frac{N}{B} \right) (q(B) - q(b_n)) + \frac{N}{B} \sum_{j=b_n+1}^{B} q(j) \right], \end{aligned} \tag{5.5.18a}$$

$$\begin{aligned} w_m(b_n) = &\frac{1}{g_w(b_n) + p_w(b_n)} \Bigg\{ p_s(b_n) s_m(b_n) \\ &+ h(b_n) \left[\frac{1}{2} \left(1 - \frac{N}{B} \right) (q(B) - q(b_n)) + \frac{N}{B} \sum_{j=b_n+1}^{B} q(j) \right] \Bigg\}, \end{aligned} \tag{5.5.18b}$$

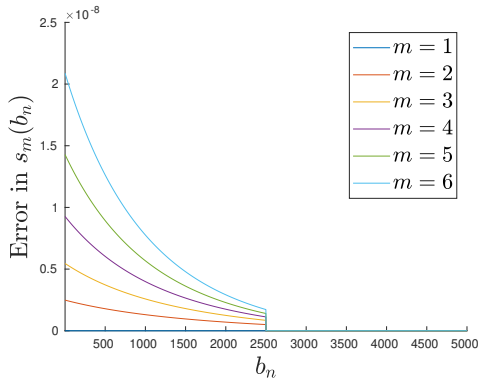
where

$$q(x) = F_1(x) \left[g_s(x) s_m(x) + g_w(x) w_m(x) \right]. \tag{5.5.19}$$

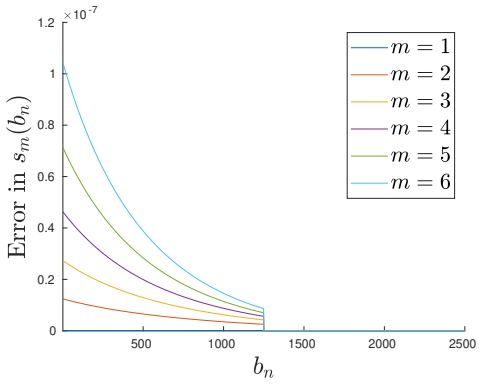
Using analogous probabilities to previously, and ensuring mass conservation, equations (5.5.18) can be written

$$
\begin{aligned}
w_m(b_n) = &\left(\frac{N-1}{\alpha_w\left(\frac{Nb_n}{B}-1\right)+\beta_w(N-1)+\alpha_w h\left(1-\frac{N}{B}\right)}\right)\\
&\times\Bigg\{\left(\beta_s-\frac{\alpha_s h}{N-1}\left(1-\frac{N}{B}\right)\right)s_m(b_n)\\
&+\frac{h}{N-1}\left(1-\frac{N}{B}\right)\left(\alpha_s s_m(B)+\alpha_w w_m(B)\right)\\
&+\frac{2hN}{B(N-1)}\sum_{j=b_n+1}^{B}\left(\alpha_s s_m(j)+\alpha_w w_m(j)\right)\Bigg\}, \qquad (5.5.20a)\\
s_{m+1}(b_n) = &\left(1-\alpha_s\left(\frac{\frac{Nb_n}{B}-1}{N-1}\right)-\beta_s-\frac{\alpha_s(1-h)}{N-1}\left(1-\frac{N}{B}\right)\right)s_m(b_n)\\
&+\left(\beta_w-\frac{\alpha_w(1-h)}{N-1}\left(1-\frac{N}{B}\right)\right)w_m(b_n)\\
&+\frac{(1-h)}{N-1}\left(1-\frac{N}{B}\right)\left(\alpha_s s_m(B)+\alpha_w w_m(B)\right)\\
&+\frac{2(1-h)N}{B(N-1)}\sum_{j=b_n+1}^{B}\left(\alpha_s s_m(j)+\alpha_w w_m(j)\right). \qquad (5.5.20b)
\end{aligned}
$$

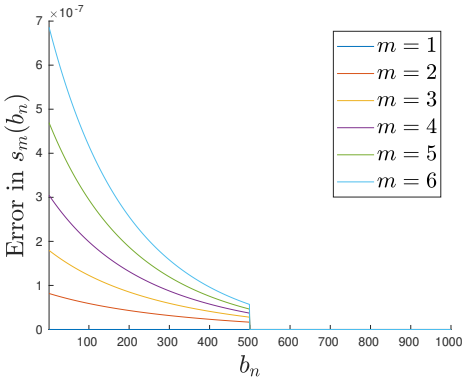
We note that for n close to N it does not make sense to use this new discretization as there will not be enough points to justify splitting them up into bins. We therefore run the old full discrete model, equations (5.3.14), for $n > n_c$, and the new discretization, equations (5.5.20), for $n < n_c$. We plot the absolute error between simulations of this method and the full model for all n in figure 5.20 for $n_c = N/2$, $N = 10^3$, and different numbers of bins, B. We note that we observe very small errors in our model, and given the savings in computational cost, discussed in more detail in the next section, this discretization method is worthwhile. We see from figure 5.21 that the maximum absolute error in this discretization decreases quadratically with the number of bins, B, increasing linearly with $1/B^2$. We see in figures 5.22 and 5.23 that the error increases with the value of n_c, however increasing the value of n_c does not increase the error as much as decreasing the value of B does. We note that to make this new discretization worthwhile it only makes sense to consider $n_c > N/2$. We conclude that using the old model for $n > n_{\text{crit}}$ is not required to maintain relative accuracy, and so in the next section we use our new discretization for all n and l.



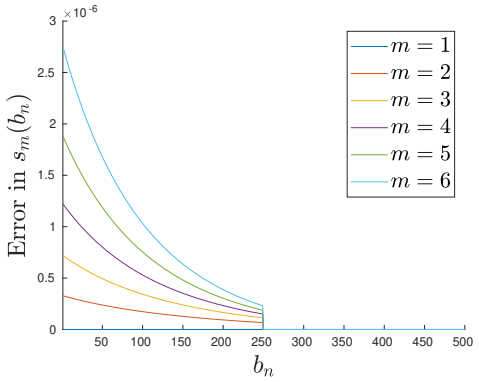
(a) Plot for $B = N/2$.



(b) Plot for $B = N/4$.



(c) Plot for $B = N/10$.



(d) Plot for $B = N/20$.

Figure 5.20: Plots of the absolute error in the distribution $s_m(b_n)$ using the new discretization (5.5.20) against b_n for different numbers of bins, B, and $n_c = N/2$.

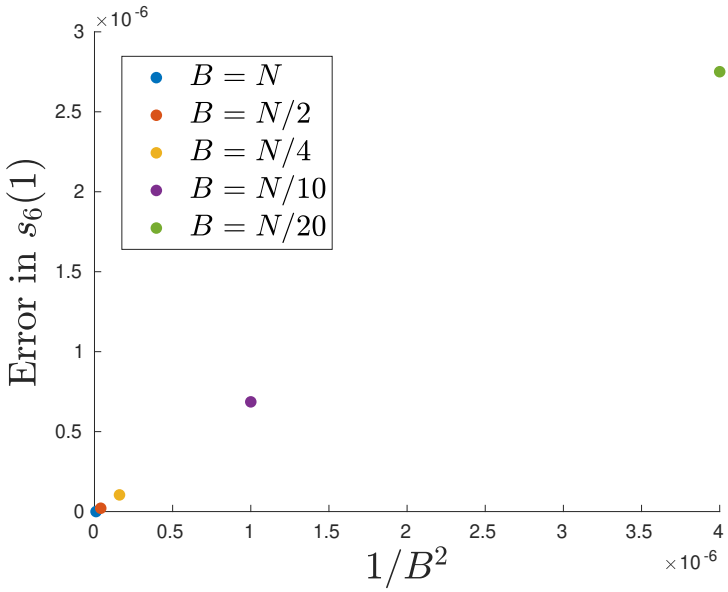
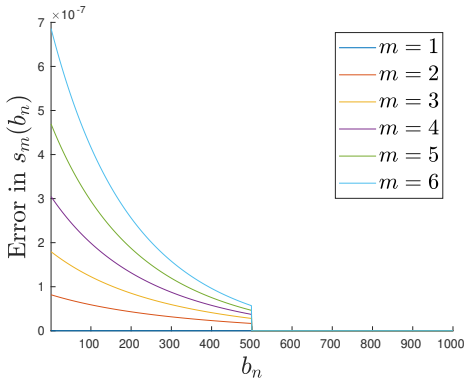
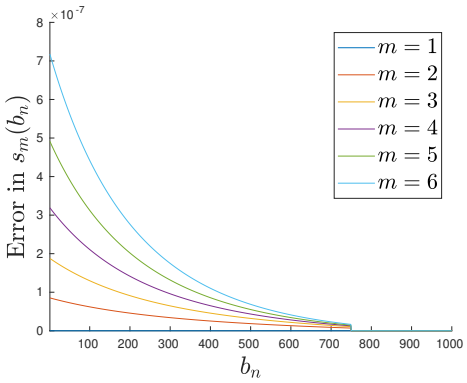


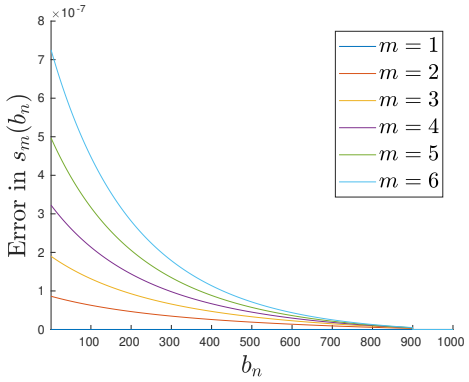
Figure 5.21: Plot of the maximum absolute error in the distribution, $s_6(1)$, against $1/B^2$ using the new discretization (5.5.20) and $n_c = N/2$.



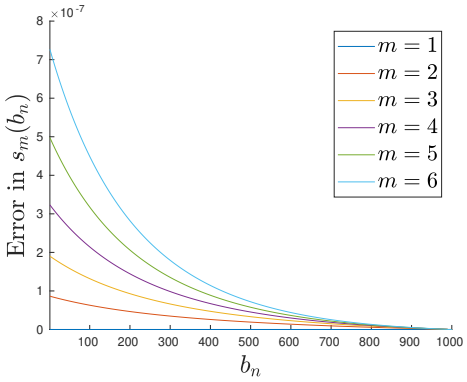
(a) Plot for $n_c = N/2$.



(b) Plot for $n_c = 3N/4$.



(c) Plot for $n_c = 9N/10$.



(d) Plot for $n_c = 99N/100$.

Figure 5.22: Plots of the absolute error in the distribution $s_m(b_n)$ using the new discretization (5.5.20) against b_n for different values of n_c and $B = N/10$.

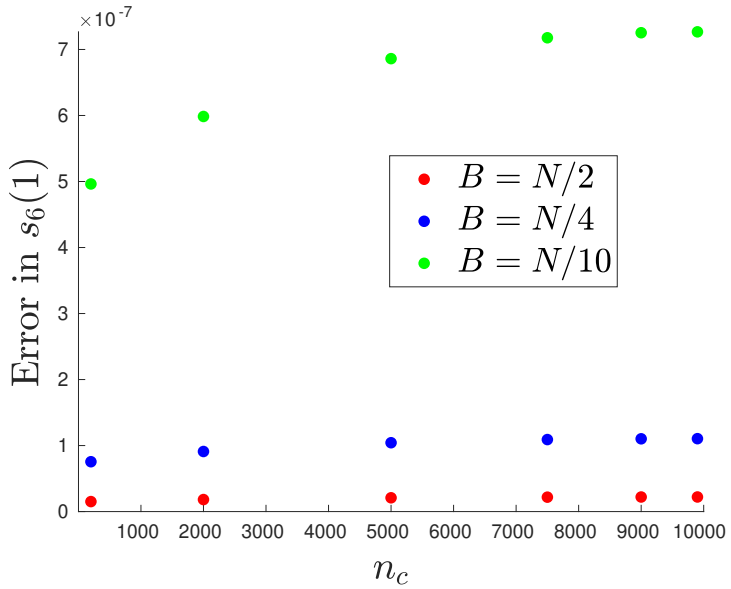
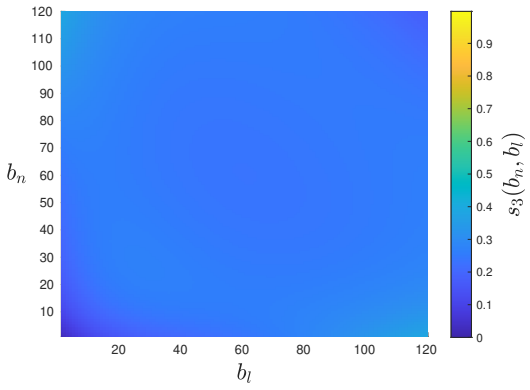
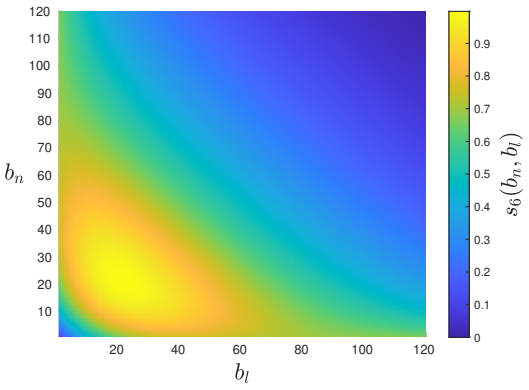


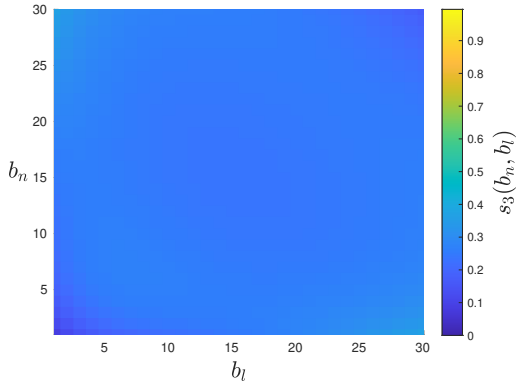
Figure 5.23: Plot of the maximum absolute error in the distribution, $s_6(1)$, using the new discretization (5.5.20) against n_c for different values of B and $N = 10^3$.



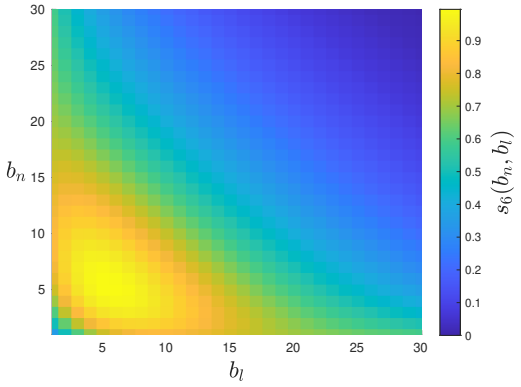
(a) $s_3(b_n, b_l)$ for $B = N/50$.



(b) $s_6(b_n, b_l)$ for $B = N/50$.



(c) $s_3(b_n, b_l)$ for $B = N/100$.



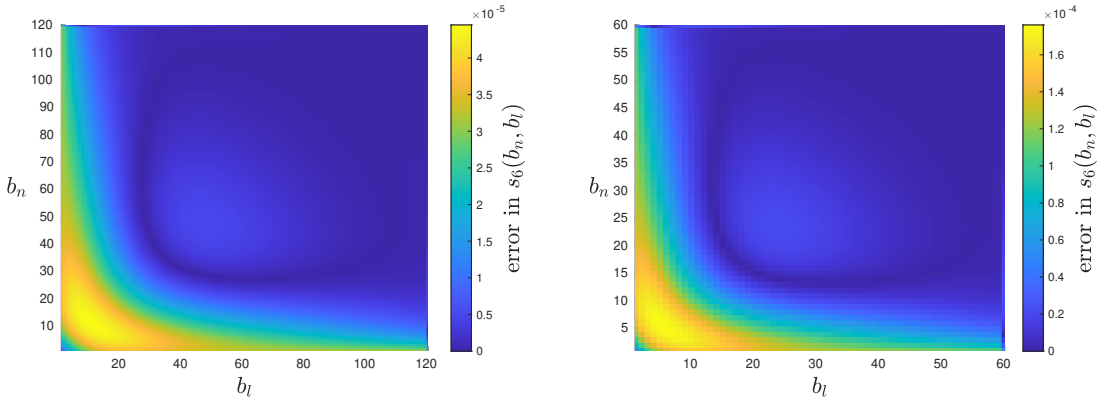
(d) $s_6(b_n, b_l)$ for $B = N/100$.

Figure 5.24: Plots of the distribution $s_m(b_n, b_l)$ using the new discretization (5.5.16) against b_n and b_l for different number of bins, B.

5.5.3.3 Size and Length

Returning to the full model including length, represented by equations (5.5.16), we use probabilities analogous to those for the full discrete model, in (5.4.15), and examine the error in this full model. We plot the solutions at $m = 3$ and $m = 6$ using this discretization in figure 5.24 for $N = L = 6000$ and two different values of B. We note that we use this new discretization for all n and l so no longer consider a critical value n_c. We see that the results for $B = N/50$ agree well with the previous results qualitatively, comparing to figures 5.11b and 5.11d. We plot the absolute errors in the final distribution in figure 5.25 for different values of B, where we again see small errors in our approximation. We plot the maximum error for different numbers of bins, B, in figure 5.26, and see that the maximum error is again proportional to $1/B^2$. We plot the computation time, t, for different numbers of bins, B, in figure 5.27, where we see significant savings in computational cost for lower values of B. Given these

computationtal savings, and the relatively low errors, this new discretization method provides us with a useful tool for efficiently calculating solutions to our model while maintaining relative accuracy.



(a) Plot for $B = N/50$.

(b) Plot for $B = N/100$.

Figure 5.25: Plots of the absolute error in the distribution $s_m(b_n, b_l)$ using the new discretization (5.5.16) against b_n and b_l for different numbers of bins, B.

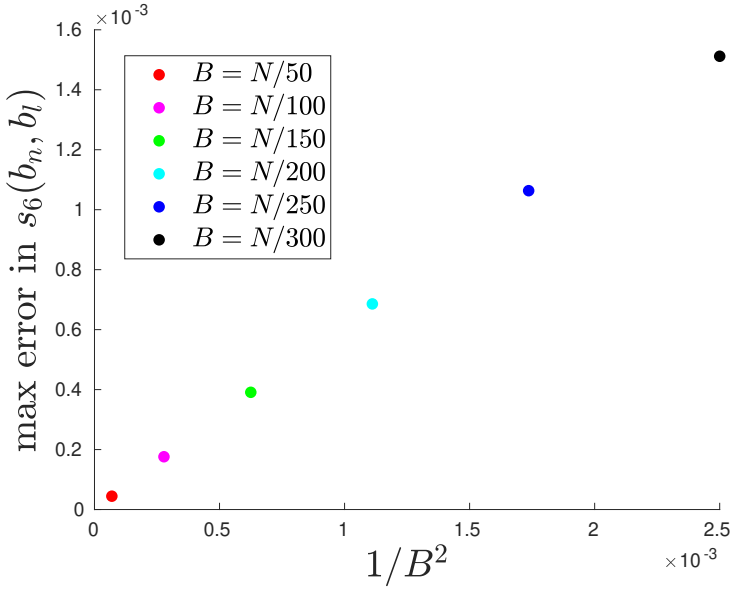


Figure 5.26: Plot of the maximum absolute error in the distribution, $s_6(b_n, b_l)$, against $1/B^2$ using the new discretization (5.5.16).

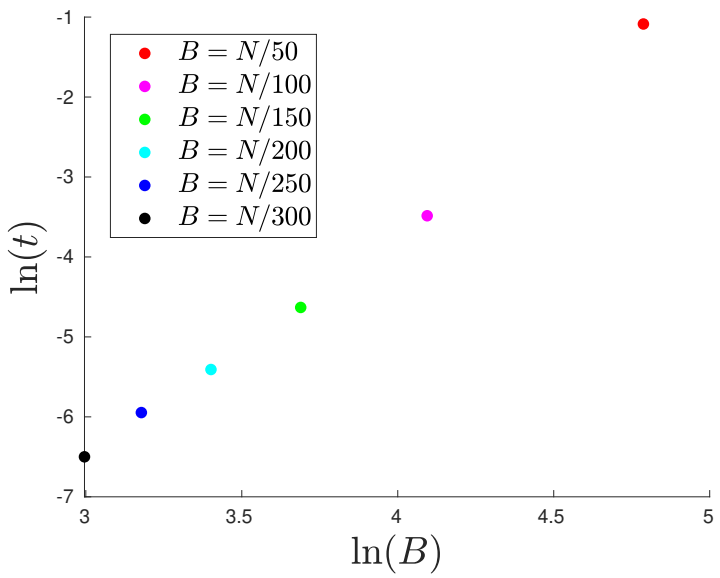


Figure 5.27: Plot of the computation time, t, versus number of bins, B.

5.6 A Simpler Model

5.6.1 Alternative Derivation

We now consider an alternative model for the process of tow splitting in the carding machine that is supported by experimental observations. We note that the models presented previously can be generalised to model any 'nip' regions between any two rollers in the carding machine. In this section we derive a more specific model that uses the geometry of the stripper-worker-swift region, which leads to a number of simplifications in the governing equations. We assume that when a distribution of tows enters the region between the stripper and the swift, the tows are first all put back on the swift by the stripper, before entering the region between the worker and swift. We additionally assume that all tows are transferred from the worker to the stripper, and the tow size distribution remains unchanged between the worker and stripper and the stripper and the swift. The new model is described in figures 5.28 and 5.29, where we define the probabilities

$g_s(n)$ = Probability a tow of size n on the swift interacts with the worker and splits,

$p_s(n)$ = Probability a tow of size n on the swift transfers to the worker without splitting,

$F(k, n)$ = Average number of daughter tows of size n produced when a tow of size k splits,

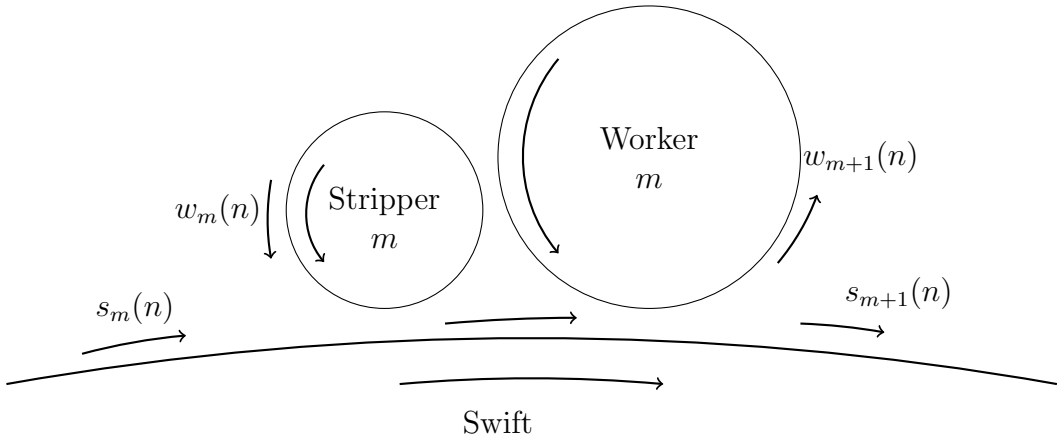


Figure 5.28: The probability distributions on the swift and a worker-stripper pair.

$h(n)$ = Probability a daughter tow of size n joins the worker.

We again assume the distribution of daughter tows is uniform, so to ensure mass is conserved we have $F(k) = 2/(k-1)$.

The master equations for this new model, after we assume $w_{m+1}(n) = w_m(n)$ as before, are

$$w_m(n) = \frac{p_s(n)s_m(n) + 2h(n)\sum_{k=n+1}^{N} \frac{g_s(k)}{k-1}\left(s_m(k) + w_m(k)\right)}{1 - p_s(n)}, \tag{5.6.1a}$$

$$w_m(N) = \frac{p_s(N)}{1 - p_s(N)} s_m(N), \tag{5.6.1b}$$

$$\begin{aligned} s_{m+1}(n) = {} & \left(1 - g_s(n) - p_s(n)\right)\left(s_m(n) + w_m(n)\right) \\ & + 2\left(1 - h(n)\right)\sum_{k=n+1}^{N} \frac{g_s(k)}{k-1}\left(s_m(k) + w_m(k)\right), \end{aligned} \tag{5.6.1c}$$

$$s_{m+1}(N) = \left(1 - g_s(N) - p_s(N)\right)\left(s_m(N) + w_m(N)\right). \tag{5.6.1d}$$

We note that these equations are equivalent to equations (5.3.10) in section 5.3 in the case of

$$g_w(n) = g_s(n),\ p_w(n) = 1 - g_s(n) - p_s(n), \tag{5.6.2}$$

i.e. the probability of splitting is independent of the roller a tow is on, and the probability of transferring from top to bottom is equal to the probability of a tow remaining on the bottom. This new formulation of the master equations is simpler than the one presented in section 5.3, reducing the number of transition probabilities and constitutive parameters to be determined.

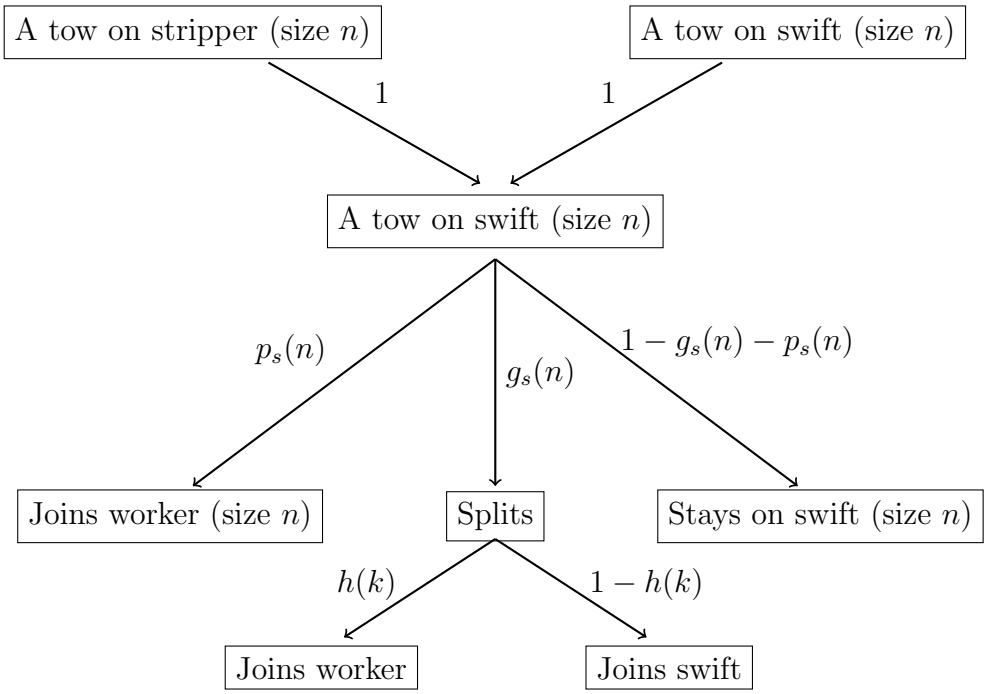
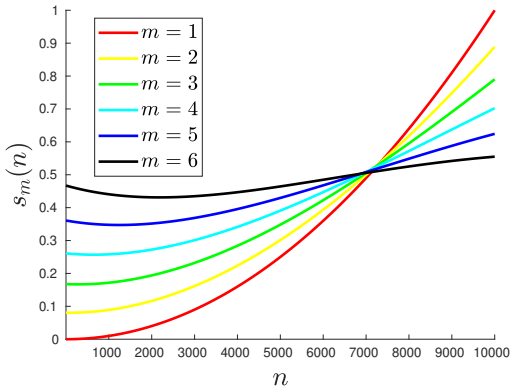


Figure 5.29: Diagram showing the new probabilistic model for the size of carbon fibre tows.

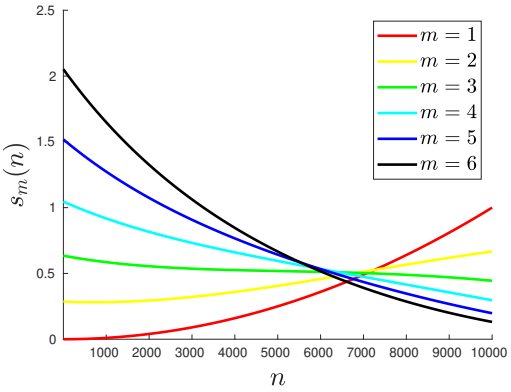
As before, we assume the probability of splitting is proportional to tow size, and the other probabilities are constant so that

$$g_s(n) = \alpha_s \left(\frac{n-1}{N-1} \right), \; p_s(n) = \beta_s, \; h(n) = h. \tag{5.6.3}$$

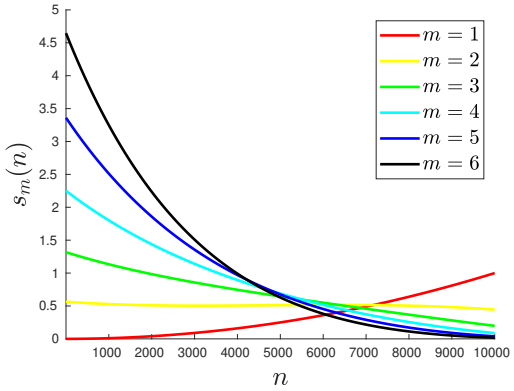
Simulations of governing equations (5.6.1) with probabilities (5.6.3) are presented in figures 5.30, 5.31, and 5.32. We present plots of the number density in figure 5.30 and volume density in figure 5.31. We observe similar behaviour to the previous model, noting in figure 5.32 that increasing the probability of transfer from the swift to the worker leads to more splitting. We see in figure 5.30 that increasing α_s leads to a distribution of smaller tows, with the distribution becoming more dominated by tows of the minimum size as α_s is increased. In figure 5.31 we see that for large α_s the majority of filaments are in tows above the minimum size, at around $N/5$ for $\alpha_s = 0.7$ for example. As with the previous model we observe the region around the maximum in the final volume density distribution becoming more narrow as α_s is increased, behaviour that will result in a more homogeneous web.



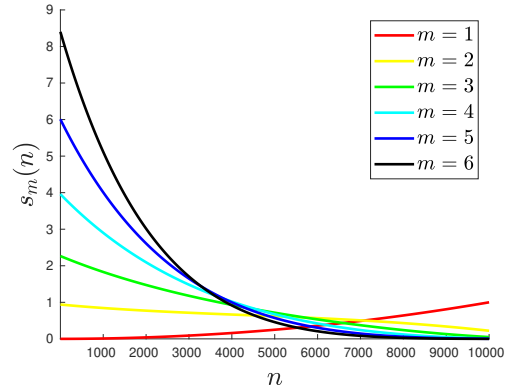
(a) $\alpha_s = 0.1$.



(b) $\alpha_s = 0.3$.

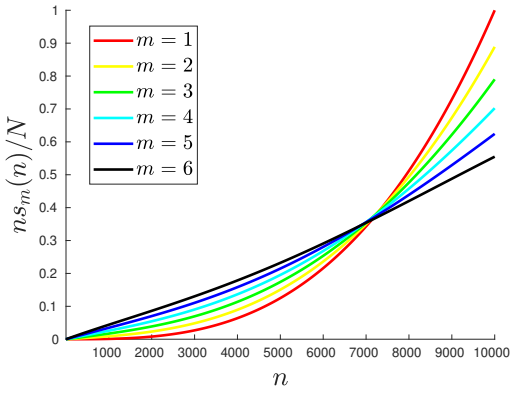


(c) $\alpha_s = 0.5$.

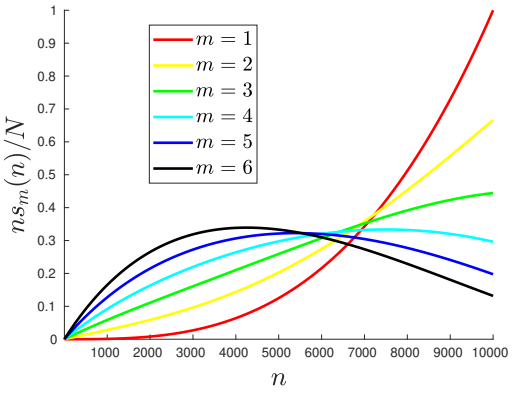


(d) $\alpha_s = 0.7$.

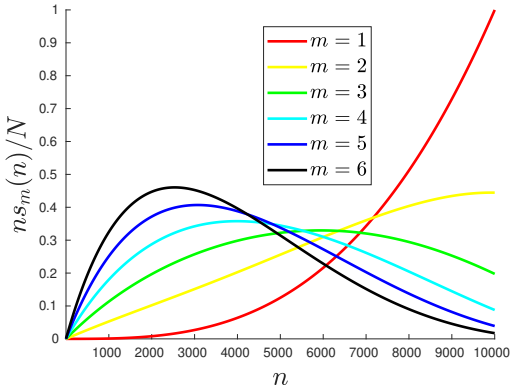
Figure 5.30: Plots of distribution $s_m(n)$, from equations (5.6.1) and (5.6.3), at successive positions for different values of α_s, $\beta_s = 0.1$, and $h = 0.5$.



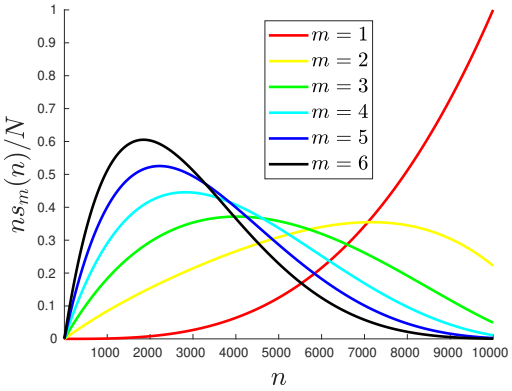
(a) $\alpha_s = 0.1$.



(b) $\alpha_s = 0.3$.

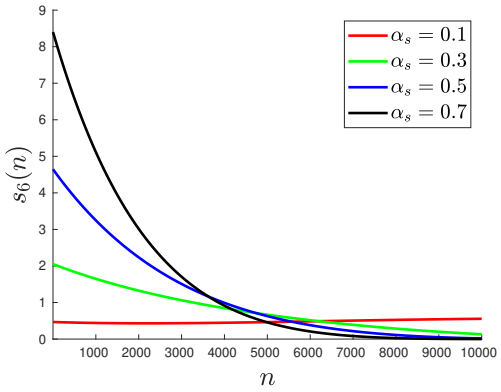


(c) $\alpha_s = 0.5$.

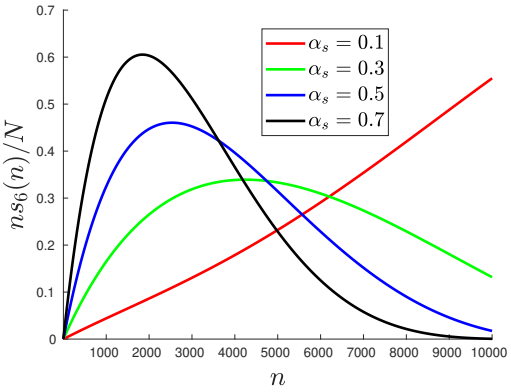


(d) $\alpha_s = 0.7$.

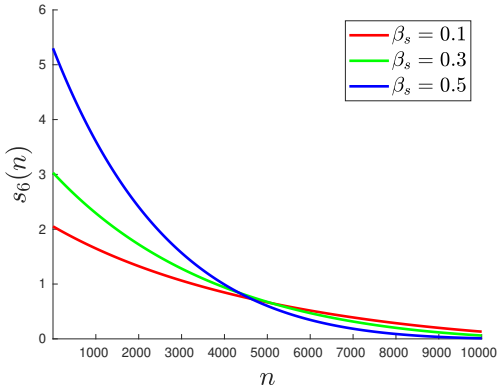
Figure 5.31: Plots of volume density $ns_m(n)/N$, from equations (5.6.1) and (5.6.3), at successive positions for different values of α_s, $\beta_s = 0.1$, and $h = 0.5$.



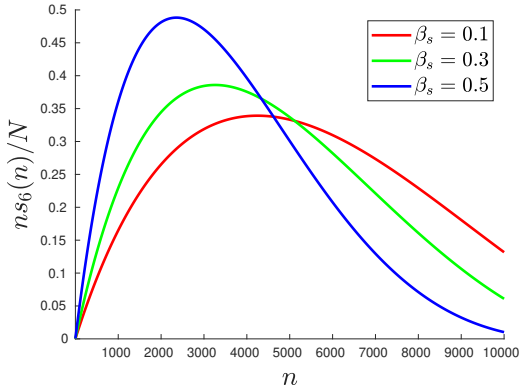
(a) Final distribution, $s_6(n)$, for different values of α_s and $\beta_s = 0.1$.



(b) Final volume density, $ns_6(n)/N$, for different values of α_s and $\beta_s = 0.1$.



(c) Final distribution, $s_6(n)$, for different values of β_s and $\alpha_s = 0.3$.



(d) Final volume density, $ns_6(n)/N$, for different values of β_s and $\alpha_s = 0.3$.

Figure 5.32: Plots of final distribution, $s_6(n)$, and volume density, $ns_6(n)/N$, from equations (5.6.1) and (5.6.3), for different values of α_s and β_s with $h = 0.5$.

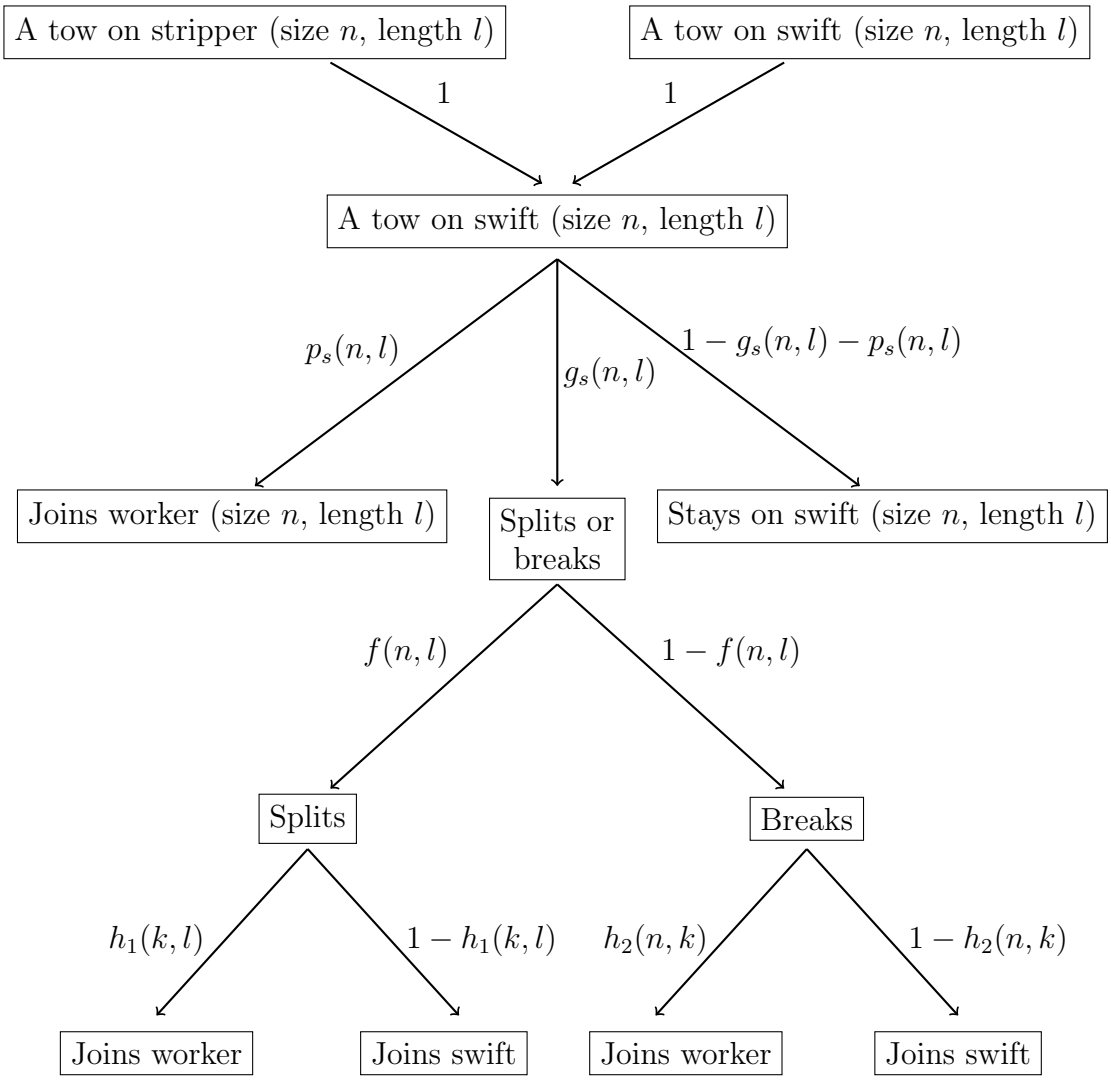


Figure 5.33: Diagram showing the new probabilistic model for the size of carbon fibre tows.

5.6.2 Extension to Include Length

In this section we extend the model presented in section 5.6.1 to include length. This model is described in figure 5.33, where we have distributions $s_m(n,l)$ and $w_m(n,l)$ as before, and the probabilities depend on n and l.

We define the probabilities as

$g_s(n,l)$ = Probability a tow of size n and length l on the swift interacts with the worker and either splits or breaks,

$p_s(n,l)$ = Probability a tow of size n and length l on the swift transfers to the worker without splitting or breaking,

$f(n,l)$ = Probability a tow splits, given that it either splits or breaks,

$h_1(n,l)$ = Probability a daughter tow of size n and length l joins the top roller,

$h_2(n,l)$ = Probability a daughter tow of size n and length l joins the top roller.

The master equations for this new model, after we assume $w_{m+1}(n,l) = w_m(n,l)$, the distribution of daughter tows is uniform, and mass is conserved, are

$$\begin{aligned} w_m(n,l) = \frac{1}{1-p_s(n,l)}\Bigg\{ & p_s(n,l)s_m(n,l) \\ & + 2h_2(n,l)\sum_{k=l+1}^{L}\left(1-f(n,k)\right)\frac{g_s(n,k)}{k-1}\left(s_m(n,k)+w_m(n,k)\right) \\ & + 2h_1(n,l)\sum_{k=n+1}^{N} f(k,l)\frac{g_s(k,l)}{k-1}\left(s_m(k,l)+w_m(k,l)\right)\Bigg\}, \end{aligned} \tag{5.6.4a}$$

$$\begin{aligned} s_{m+1}(n,l) = & \left(1-g_s(n,l)-p_s(n,l)\right)\left(s_m(n,l)+w_m(n,l)\right) \\ & + 2\left(1-h_2(n,l)\right)\sum_{k=l+1}^{L}\left(1-f(n,k)\right)\frac{g_s(n,k)}{k-1}\left(s_m(n,k)+w_m(n,k)\right) \\ & + 2\left(1-h_1(n,l)\right)\sum_{k=n+1}^{N} f(k,l)\frac{g_s(k,l)}{k-1}\left(s_m(k,l)+w_m(k,l)\right). \end{aligned} \tag{5.6.4b}$$

We note that the equations (5.6.4) are equivalent to (5.4.12) for $g_w(n,l) = g_s(n,l)$, and $p_w(n,l) = 1 - g_s(n,l) - p_s(n,l)$.

We define the transition probabilities as previously, namely

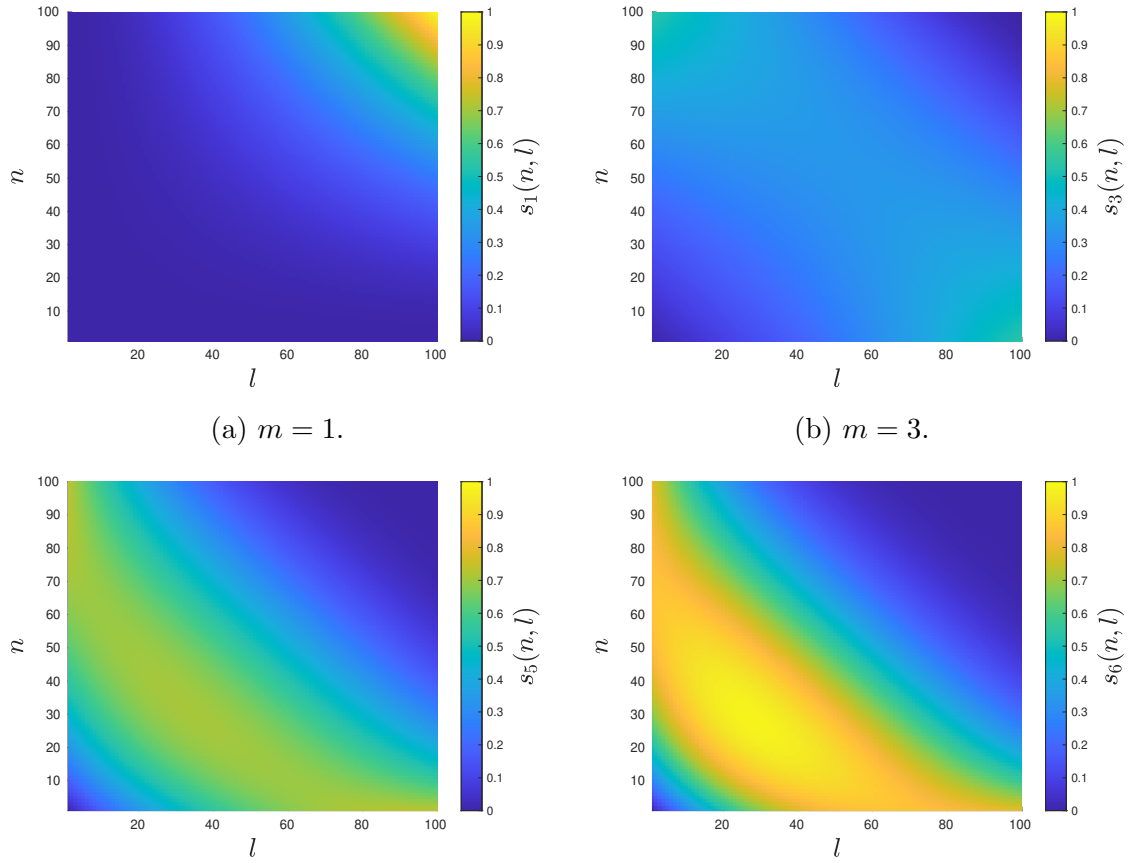
$$g_s(n,l) = \alpha_s \frac{(n-1)(l-1)}{(N-1)(L-1)}, \tag{5.6.5a}$$

$$p_s(n,l) = \beta_s,\ h_1(n,l) = h_1,\ h_2(n,l) = h_2, \tag{5.6.5b}$$

$$f(n,l) = \frac{n-1}{n+l-2}, \tag{5.6.5c}$$

and simulate equations (5.6.4) for $N = 100$. These simulations are shown in figure 5.34 where we see both the length and size of the tows decreasing through the machine as before. We observe similar qualitative behaviour to the previous formulation (see section 5.4) where we again have symmetry about $n = l$ because of the probability choices (5.6.5).

The new formulation presented in this section provides a simpler model for the distribution of tows in the stripper-worker-swift region of the carding machine, and



(a) $m = 1$. (b) $m = 3$.

(c) $m = 5$. (d) $m = 6$.

Figure 5.34: Plots of distribution $s_m(n, l)$ at successive positions $m = 1, ..., 6$ using the new formulation, defined by equations (5.6.4) and (5.6.5) for $\alpha_s = 0.7$, $\beta_s = 0.3$, and $h_1 = h_2 = 0.5$.

therefore leads to fewer probability parameters, α_s, β_s, h_1, and h_2. This method however is less generalised than the original formulation, which could be used to model any two rollers. To model the full carding machine a combination of these two models could be used, with different transition probabilities defined for each distinct 'nip' region. We use the new formulation in chapter 6, where we present a method for fitting the probability parameters to data.

5.7 Conclusions

In this chapter we have used a probabilistic approach to model carbon fibre tows in a carding machine, focusing on how the properties of tows such as size and length evolve. We defined distributions on top and bottom rollers, which represent the average

number of tows per unit time of a particular size. We modelled a worker-stripper pair as one roller, so that we could consider multiple sets of these 'pairs' interacting with the swift. We showed how the defined transition probabilities affect the evolution of tows, and the distribution at different points in the machine.

We introduced length as a variable in section 5.4, treating it in the same way as size for simplicity. We again modelled a worker-stripper pair as one roller, and defined probabilities for splitting, breaking, and transferring in the 'nip' regions between rollers. We showed that changing these probabilities changes the properties of the tow distribution throughout the machine, and discussed how these probabilities depend on the control parameters of the machine.

In section 5.5 we approximated n and l as continuous variables, using the large value of N to justify this approximation. We analysed this continuous model without length dependence, showing that it can be written as a system of ODEs. We then discussed the full problem that can be solved numerically by effectively splitting the large sums into 'bins'. The 'tow size' model is fundamentally discrete, but with a very large value of N, which motivates taking this continuum limit. If the resulting continuum model cannot be solved analytically, it must be discretized for a numerical solution which implies that we have gone in a circle. The rationale therefore is that we can choose a more efficient discretisation than the one provided by the physics, i.e. we can achieve acceptable accuracy (given all the other uncertainties in the model) with significantly lower computational cost. We then derived an alternative formulation of the process in section 5.6, using the observed properties of the strippers and workers, that yields a model with fewer probability parameters.

The natural next stage in this work is to use the tool and framework we have provided in this chapter, and conduct data analysis to fit the various probability parameters highlighted by the model. This includes collecting data on the lengths and tow sizes at different points in the machine so that the model can be used in the future to predict the properties of the final web, given the properties of the tows. A method for conducting this data analysis is outlined in chapter 6.

Chapter 6

A Data Case Study

6.1 Overview

In this chapter we present a case study that outlines a method for using experimental data, combined with the probabilistic model from chapter 5, to inform the carding setup and process. We use results from the other chapters, as well as some example data, to fit the parameters in our probabilistic model. This will give us insight into the experimental data that needs to be collected by Gen 2 Carbon in the future to inform a useful mathematical model.

In section 6.2 we review the model for tow size evolution presented in section 5.6.1, considering the continuous approximation of this discrete model. We then discuss the data required for our analysis in section 6.2.2, and present results in section 6.2.3. We follow the same procedure in section 6.3, reviewing the model derived in section 5.6.2 to describe variations in tow size and length. In section 6.3.2 we present a manufactured example of the experimental data required for the model, and then present results from fitting with our model in section 6.3.3.

The modelling approach here is first to pose simple but plausible constitutive relations for the transition probabilities, involving just a handful of unknown parameters. We then suppose that the initial and final tow distributions, for example $s_1(x)$ and $s_6(x)$, have been measured experimentally. We then use fitting to find the parameter values that, starting with the given initial distribution, give results that are as close as possible to the given final distribution. Since these experiments have not yet been carried out, in the first instance we test the approach using manufactured example data. These results are very preliminary at this stage and are intended as a proof of concept.

6.2 Tow Size

6.2.1 The Model

In section 5.6.1 we derived a model for the evolution of tow size distribution along the swift in the carding machine, namely

$$w_m(n) = \frac{p_s(n)s_m(n) + 2h(n)\sum_{k=n+1}^{N}\frac{g_s(k)}{k-1}\left(s_m(k)+w_m(k)\right)}{1-p_s(n)}, \tag{6.2.1a}$$

$$w_m(N) = \frac{p_s(N)}{1-p_s(N)}s_m(N), \tag{6.2.1b}$$

$$\begin{aligned} s_{m+1}(n) = {} & \left(1-g_s(n)-p_s(n)\right)\left(s_m(n)+w_m(n)\right) \\ & + 2\left(1-h(n)\right)\sum_{k=n+1}^{N}\frac{g_s(k)}{k-1}\left(s_m(k)+w_m(k)\right), \end{aligned} \tag{6.2.1c}$$

$$s_{m+1}(N) = \left(1-g_s(N)-p_s(N)\right)\left(s_m(N)+w_m(N)\right). \tag{6.2.1d}$$

Following a similar method to that in section 5.5.2, for large N we approximate n as a continuous variable, and assume $h(n) = h$ is a constant, allowing us to derive the dimensionless ODE system

$$\frac{\mathrm{d}w_m}{\mathrm{d}x} + \left(\frac{\frac{2hg_s(x)}{x} - \frac{\mathrm{d}p_s}{\mathrm{d}x}}{1-p_s(x)}\right)w_m(x) = \frac{\frac{\mathrm{d}}{\mathrm{d}x}\left[p_s(x)s_m(x)\right] - \frac{2hg_s(x)}{x}s_m(x)}{1-p_s(x)}, \tag{6.2.2a}$$

$$\begin{aligned} \frac{\mathrm{d}s_{m+1}}{\mathrm{d}x} = {} & \frac{\mathrm{d}}{\mathrm{d}x}\left[\left(1-g_s(x)-p_s(x)\right)\left(s_m(x)+w_m(x)\right)\right] \\ & - \frac{2(1-h)g_s(x)}{x}\left(s_m(x)+w_m(x)\right), \end{aligned} \tag{6.2.2b}$$

where $x = n/N$ is the dimensionless size. We have boundary conditions at $x = 1$, namely

$$w_m(1) = \left(\frac{p_s(1)}{1-p_s(1)}\right)\left(\frac{1-g_s(1)-p_s(1)}{1-p_s(1)}\right)^{m-1}s_1(1), \tag{6.2.2c}$$

$$s_m(1) = \left(\frac{1-g_s(1)-p_s(1)}{1-p_s(1)}\right)^{m-1}s_1(1). \tag{6.2.2d}$$

In section 3.2 we proposed a friction law that results in the force required to comb the fibres being proportional to the tooth velocity. We assume that this is the same case for a tow of fibres. In chapter 4 we then argued that the propensity of two halves of a tow to split depends on the curvature at the splitting point which itself increases with the applied force. We therefore take the probability of splitting, $g_s(x)$, to be a linear function of the velocity ratio between the rollers, $\bar{u}$, namely

$$g_s(x) = \alpha_s\left(1-\bar{u}\right)x, \quad p_s(x) = \beta_s, \tag{6.2.3}$$

where $\bar{u}$ is defined in chapter 2 as the velocity ratio between the worker and the swift. Thus, for two rollers moving at the same velocity there is no splitting, and splitting is more likely for a greater difference in the velocities (for example as the velocity of the worker decreases while keeping the swift velocity constant).

Substituting probabilities (6.2.3) into (6.2.2) yields a system of ODEs and boundary conditions that we solve for $w_1(x) - w_5(x)$ and $s_2(x) - s_6(x)$, given $s_1(x)$. The solution depends on three parameters, α_s, β_s, and h, that need to be determined using experimental data, as discussed in section 6.2.2.

6.2.2 Example Distributions

The first thing required to run our model is the initial tow size distribution moving onto the main cylinder, $s_1(x)$. In the absence of experimental measurements, in this section we simulate our model for two different manufactured initial distributions, shown in figure 6.1, where we say the velocity ratio for both examples is $\bar{u} = 0.1$. We fit a quadratic curve to our first distribution using least squares fit [64], also shown in figure 6.1a, in red. We find the equation of this line to be

$$s_1(x) = 0.0924024 - 0.0179705x + 3.83916x^2, \tag{6.2.4}$$

where the distribution is scaled so that

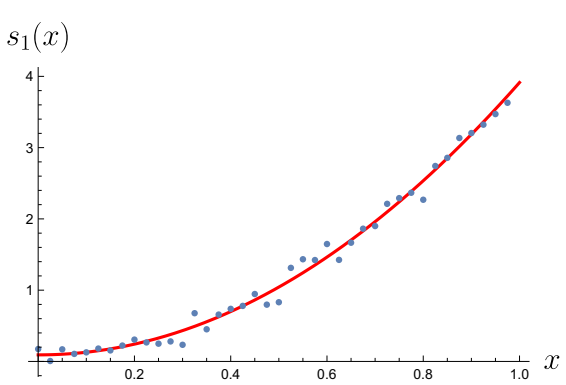
$$\int_0^1 x s_1(x) \mathrm{d}x = 1. \tag{6.2.5}$$

The second sample initial distribution is normal with mean 1 and variance 0.1, as illustrated in figure 6.1b. We solve the model (6.2.2) with the transition probabilities (6.2.3) and $\bar{u} = 0.1$. The results starting with both initial distributions, $s_1(x)$, are shown in figure 6.2, using example values of the unknown parameters α_s, β_s, and h.

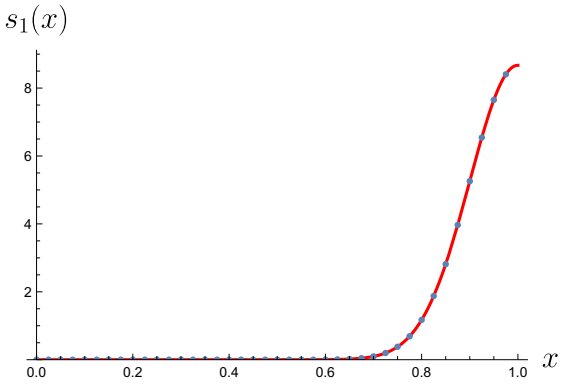
We now suppose that the final tow size distribution, $s_6(x)$, at the end of the machine, after all worker-stripper pairs has also been measured. Again, we manufacture two different example final distributions that are shown in figures 6.3a and 6.3b, corresponding to initial distributions in figures 6.1a and 6.1b respectively. To manufacture this data we simulate the model for the two different distributions for parameter values

$$\alpha_s = 0.3,\ \beta_s = 0.1,\ h = 0.5, \tag{6.2.6}$$

and add some noise to the final distributions $s_6(x)$, as can be seen in figure 6.3. In the next section we examine how such experimental data can in principle be used to fit the unknown parameters.

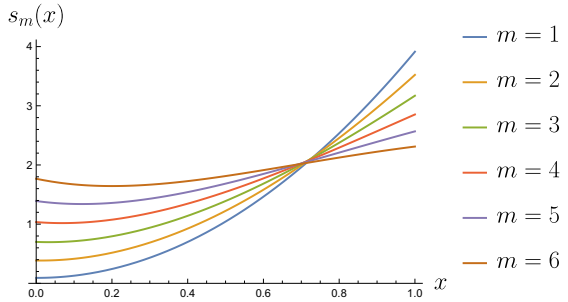


(a) Initial distribution, $s_1(x)$, and a line fitted to the data points, defined by (6.2.4).

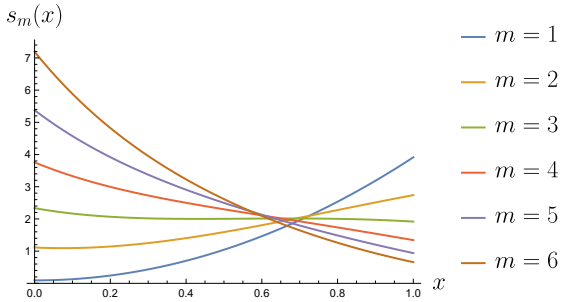


(b) Initial normal distribution, $s_1(x)$, with mean 1 and variance 0.1.

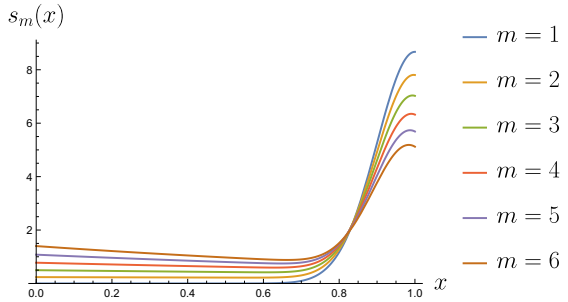
Figure 6.1: Plots of the example data for the initial distribution, $s_1(x)$.



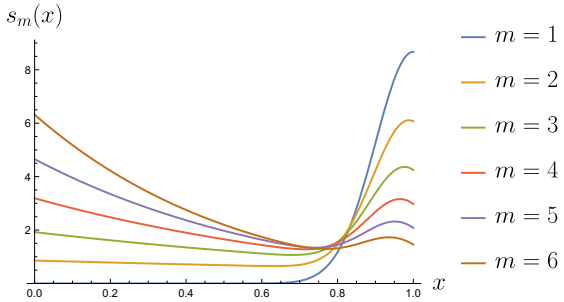
(a) First example plotted for $\alpha_s = 0.1$.



(b) First example plotted for $\alpha_s = 0.3$.

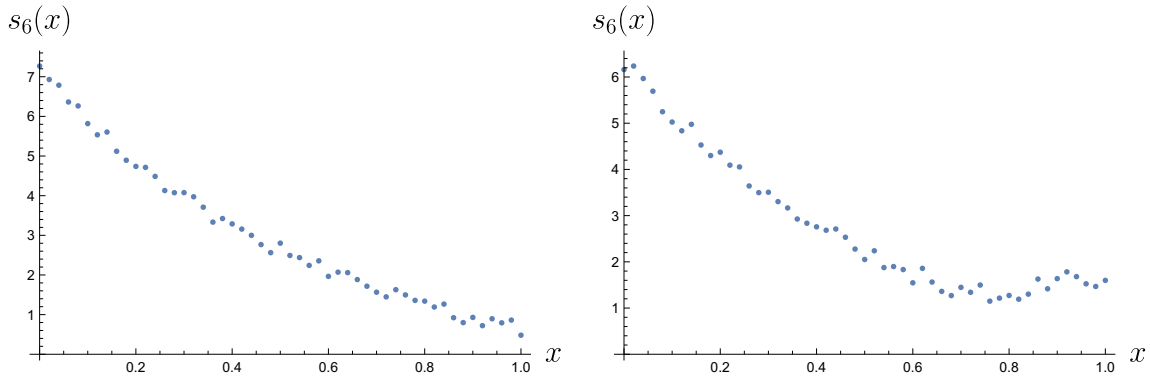


(c) Second example plotted for $\alpha_s = 0.1$.



(d) Second example plotted for $\alpha_s = 0.3$.

Figure 6.2: Plots of tow size distribution, $s_m(x)$, at successive positions $m = 1, ..., 6$, for both example initial distributions with $\bar{u} = 0.1$, $\beta_s = 0.1$, and $h = 0.5$.



(a) Example 1 (b) Example 2

Figure 6.3: Plots of the manufactured data for the final distribution, $s_6(x)$.

6.2.3 Fitting

We make use of the NonLinearModelFit and NMinimize functions in Mathematica [28] to fit the parameters α_s, β_s, and h to the distributions shown in figure 6.3. These inbuilt functions use global optimization to find a global minimum that results in the best least-squares fit to the data. We plot the solutions for the two examples in figure 6.4. This approach to both examples yields parameter choices of

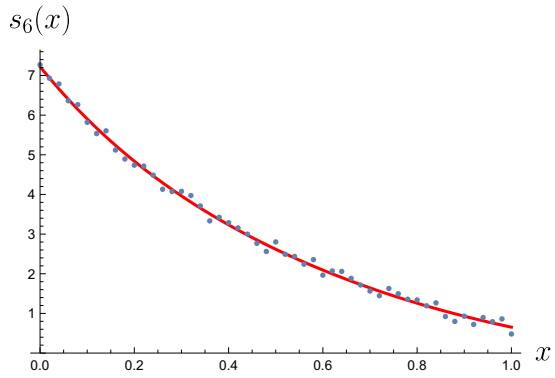
$$\alpha_s = 0.272786,\ \beta_s = 0.184113,\ h = 0.499342, \tag{6.2.7a}$$

$$\alpha_s = 0.300161,\ \beta_s = 0.107252,\ h = 0.472045, \tag{6.2.7b}$$

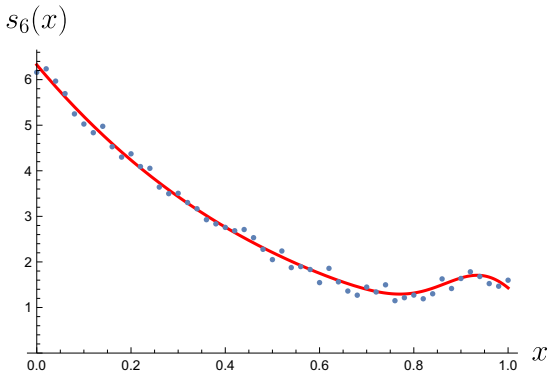
respectively, where we observe from figure 6.4 a qualitatively good fit to the example data. However we note that parameters (6.2.7) do not match original parameters (6.2.6) perfectly. This suggests a possible limitation to our method, discussed below.

We can now use these fitted parameter values in our model to compute solutions for different values of $\bar{u}$, and thus determine how the final distribution of tow sizes depends on the velocity ratio of the rollers. These results are shown in figure 6.5 where we see more breakup of tows for lower values of $\bar{u}$. This exercise illustrates how, once parameters have been fitted, the model can in principle be used to predict how the properties of the final tow distribution depend on the control parameters (such as the roller velocities) and the properties of the feedstock (for example the initial distribution).

We note that $s_6(x)$ is somewhat insensitive to variations in the probability parameters, providing a limitation to this approach. Further work could include a more in depth examination of parameter groupings, the collection of intermediate data for

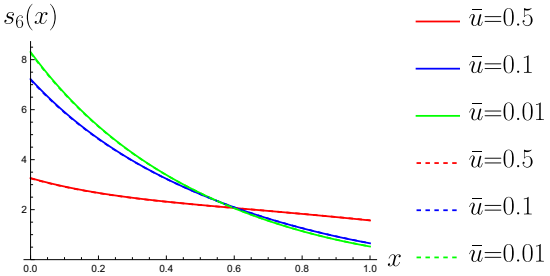


(a) Parameters (6.2.7a) for initial distribution (6.2.4).

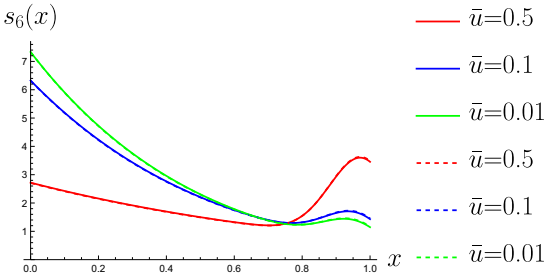


(b) Parameters (6.2.7b) for initial normal distribution.

Figure 6.4: The final data and fitted solutions.



(a) Parameters (6.2.7a) for initial distribution (6.2.4).



(b) Parameters (6.2.7b) for initial normal distribution.

Figure 6.5: Final distributions for both example simulations for the fitted parameters, α_s, β_s, and h (solid lines), and original parameters (6.2.6) (dashed lines), for different velocity ratios, $\bar{u}$.

the tow size distribution at more points along the machine, or running the machine for different roller velocities, and therefore different values of $\bar{u}$. Achieving the exact probability parameters may not be required however as long as good approximations to the desired distributions are achieved. This is shown in figure 6.5, as there is very little difference between the plots for different $\bar{u}$ for the original parameters (6.2.6), and the results using parameters (6.2.7). As long as the fitted distributions achieve a high degree of accuracy, this method could be used to predict the effect of machine control parameters on the breakup of tows.

6.3 Tow Size and Length

6.3.1 The Model

In this section we follow a similar method to that in section 6.2 to fit the model parameters in the size and length model. We use the simplified model that was derived in section 5.6.2 so that we have fewer parameters to fit. This model is defined by

$$w_m(n,l) = \frac{1}{1-p_s(n,l)}\Bigg\{p_s(n,l)s_m(n,l) + 2h_2(n,l)\sum_{k=l+1}^{L}(1-f(n,k))\,\frac{g_s(n,k)}{k-1}\,(s_m(n,k)+w_m(n,k)) + 2h_1(n,l)\sum_{k=n+1}^{N} f(k,l)\frac{g_s(k,l)}{k-1}\,(s_m(k,l)+w_m(k,l))\Bigg\}, \tag{6.3.1a}$$

$$s_{m+1}(n,l) = (1-g_s(n,l)-p_s(n,l))\,(s_m(n,l)+w_m(n,l)) + 2\,(1-h_2(n,l))\sum_{k=l+1}^{L}(1-f(n,k))\,\frac{g_s(n,k)}{k-1}\,(s_m(n,k)+w_m(n,k)) + 2\,(1-h_1(n,l))\sum_{k=n+1}^{N} f(k,l)\frac{g_s(k,l)}{k-1}\,(s_m(k,l)+w_m(k,l))\,, \tag{6.3.1b}$$

with conditions

$$w_m(N,L) = \frac{p_s(N,L)s_m(N,L)}{1-p_s(N,L)}, \tag{6.3.2a}$$

$$w_m(N,l) = \frac{1}{1-p_s(N,l)}\Bigg\{p_s(N,l)s_m(N,l) + 2h_2(N,l)\sum_{k=l+1}^{L}(1-f(N,k))\,\frac{g_s(N,k)}{k-1}\,(s_m(N,k)+w_m(N,k))\Bigg\}, \tag{6.3.2b}$$

$$w_m(n,L) = \frac{1}{1-p_s(n,L)}\Bigg\{p_s(n,L)s_m(n,L) + 2h_1(n,L)\sum_{k=n+1}^{N} f(k,L)\frac{g_s(k,L)}{k-1}\,(s_m(k,L)+w_m(k,L))\Bigg\}, \tag{6.3.2c}$$

$$s_{m+1}(N,L) = (1-g_s(N,L)-p_s(N,L))\,(s_m(N,L)+w_m(N,L))\,, \tag{6.3.2d}$$

$$s_{m+1}(N,l) = (1 - g_s(N,l) - p_s(N,l))\,(s_m(N,l) + w_m(N,l)) + 2\,(1 - h_2(N,l)) \sum_{k=l+1}^{L} (1 - f(N,k))\,\frac{g_s(N,k)}{k-1}\,(s_m(N,k) + w_m(N,k))\,, \tag{6.3.2e}$$

$$s_{m+1}(n,L) = (1 - g_s(n,L) - p_s(n,L))\,(s_m(n,L) + w_m(n,L)) + 2\,(1 - h_2(n,L)) \sum_{k=l+1}^{L} f(k,L)\frac{g_s(k,L)}{k-1}\,(s_m(k,L) + w_m(k,L))\,. \tag{6.3.2f}$$

As argued in section 6.2, we expect the breakup of tows to be driven by the difference in velocity between the worker and the swift. For simplicity, we take the probability of either splitting or breaking, $g_s(n,l)$, to be a linear function of the velocity ratio between the two rollers, with

$$g_s(n,l) = \alpha_s(1 - \bar{u})\frac{(n-1)(l-1)}{(N-1)(L-1)}. \tag{6.3.3}$$

The constant α_s then needs to be found using data. We note that (6.3.3) satisfies the constraint $g_s(1,1) = 0$.

We recall that $f(n,l)$ measures the relative probability of a tow splitting or breaking. We anticipate that decreasing $\bar{u}$ (increasing the velocity difference between rollers) means the tows are more likely to break than split, so that f should be an increasing function of $\bar{u}$. We also have the constraints

$$f(1,l) = 0,\ \ f(n,1) = 1, \tag{6.3.4}$$

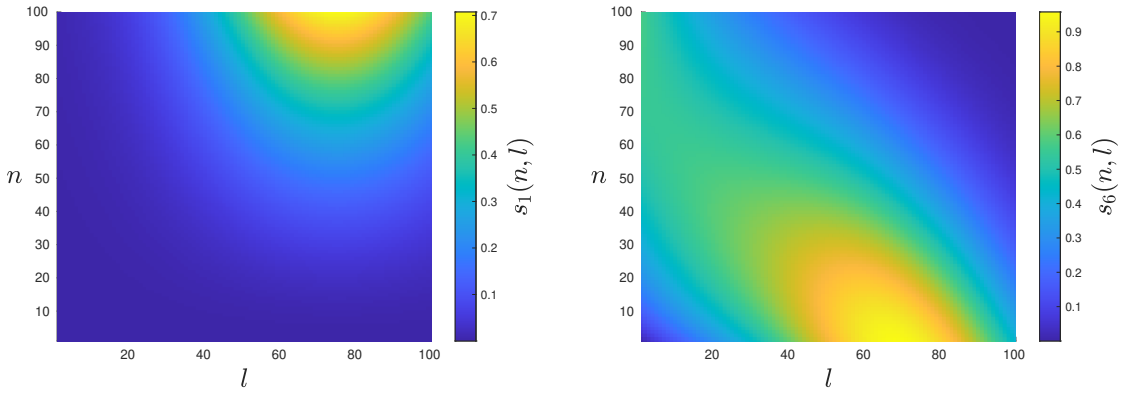
which we satisfy by proposing the constitutive relation

$$f(n,l) = \left(\frac{n-1}{n+l-2}\right)^{\frac{\gamma}{\bar{u}}}, \tag{6.3.5}$$

where γ is another parameter to be determined using the data. We assume the other probabilities from section 5.6.2 are constants, i.e.

$$p_s(n,l) = \beta_s, \quad h_1(n,l) = h_1, \quad h_2(n,l) = h_2. \tag{6.3.6}$$

The parameters that require data fitting to find are therefore α_s, γ, β_s, h_1, and h_2. In the next section we will discuss the data required to fit these parameters, and present an example.



(a) Manufactured initial data, at $m = 1$.

(b) Manufactured final data, at $m = 6$.

Figure 6.6: Manufactured initial and final data for the distribution of tows at $m = 1$ and $m = 6$, respectively.

6.3.2 Example Data

In this section we will discuss the experimental data required to proceed, beginning with the starting distributions of tows being fed onto the machine. There are a number of rollers before the tows make their way onto the swift and so, as before, we expect the initial tow size distribution to be dominated by bigger tows (bigger n), but with some spread. The general observations of tow lengths before carding suggest a normal distribution of lengths around a mean of $l \approx 80$mm. We assume $3L/4$ is this mean in our initial distribution, with standard deviation $L/4$, and therefore impose an initial distribution of tows given by

$$s_1(n,l) = 44.3193 \left(\frac{n}{N}\right)^2 \mathcal{N}\left(\frac{3L}{4}, \frac{L}{4}\right), \tag{6.3.7}$$

where $\mathcal{N}$ defines a normal distribution, and the constant 44.3193 is chosen to ensure the same total fibre mass as previous simulations in section 5.4. The distribution (6.3.7) is shown in figure 6.6a.

To proceed as before we then require samples of tows to be taken at the end of the process after all worker-stripper pairs, and the distribution of lengths and sizes to be measured. As in the previous section we manufacture this data by running our model at $\bar{u} = 0.1$ for parameter values $\alpha_s = 0.7$, $\beta_s = 0.2$, $h_1 = 0.5$, $h_2 = 0.5$, and $\gamma = 0.08$, with the aim of recovering these parameters through data fitting. The resulting final distribution of tow sizes and lengths is shown in figure 6.6b. In the next section we will use the data in figure 6.6 to fit our parameters, and simulate our model for different roller velocity ratios.

6.3.3 Fitting

We simulate the model (6.3.1)-(6.3.6) for the initial data in figure 6.6a and $\bar{u} = 0.1$. We solve the model in MATLAB [27], making use of the fmincon function to find the parameters that minimise the total absolute error between the solution and the data. The parameter values we find are

$$\alpha_s = 0.6861,\ \beta_s = 0.2158,\ \gamma = 0.0800,\ h_1 = 0.5000,\ h_2 = 0.5000, \tag{6.3.8}$$

and the final distribution these parameters yield is shown in figure 6.7. We see from (6.3.8) that the fitting method recovers the values of γ, h_1, and h_2 accurately, but there are errors in finding α_s and β_s. We assume these errors are present due to a lack of sensitivity of the final distribution on the parameters α_s and β_s. This can be seen from the small errors between the original and fitted parameter solutions in figure 6.8. As discussed in section 6.2 more analysis into the parameter groupings would need to be carried out to explain this property of the model. The small errors observed in figure 6.8 however suggest that even without recovering the original parameters this process can still provide us with informative results.

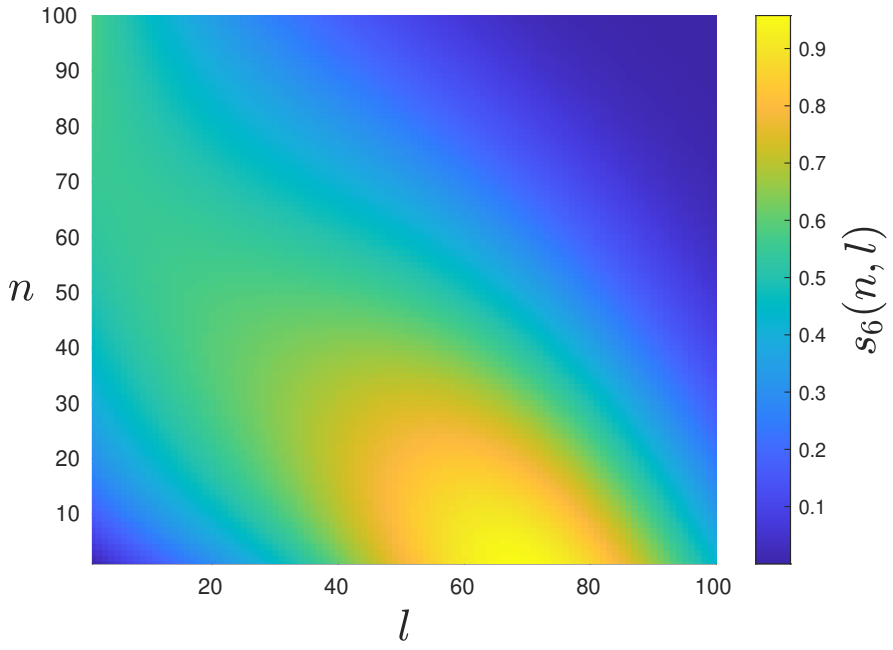


Figure 6.7: Final distribution for the parameters α_s, β_s, γ, h_1 and h_2 from (6.3.8) and $\bar{u} = 0.1$.

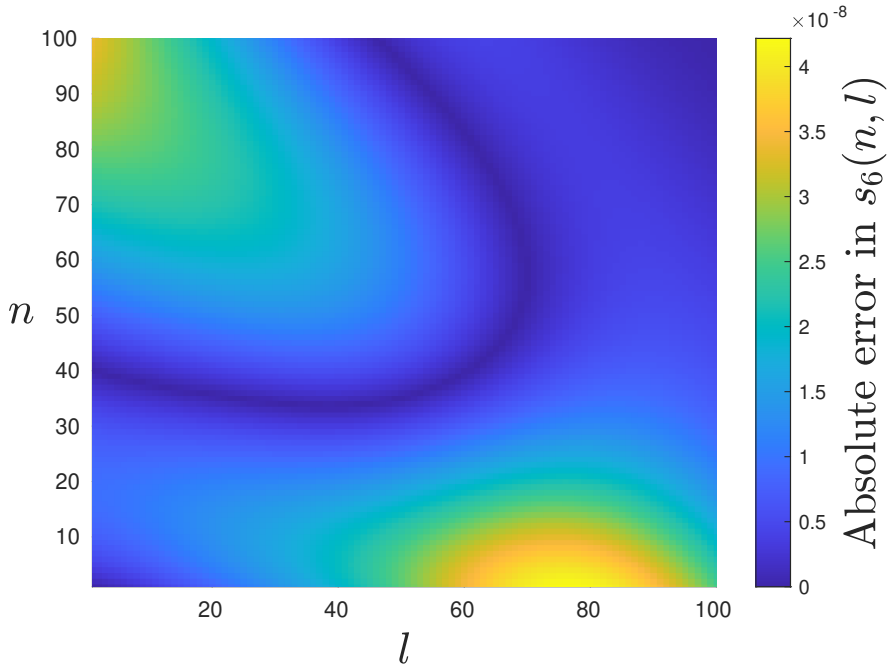
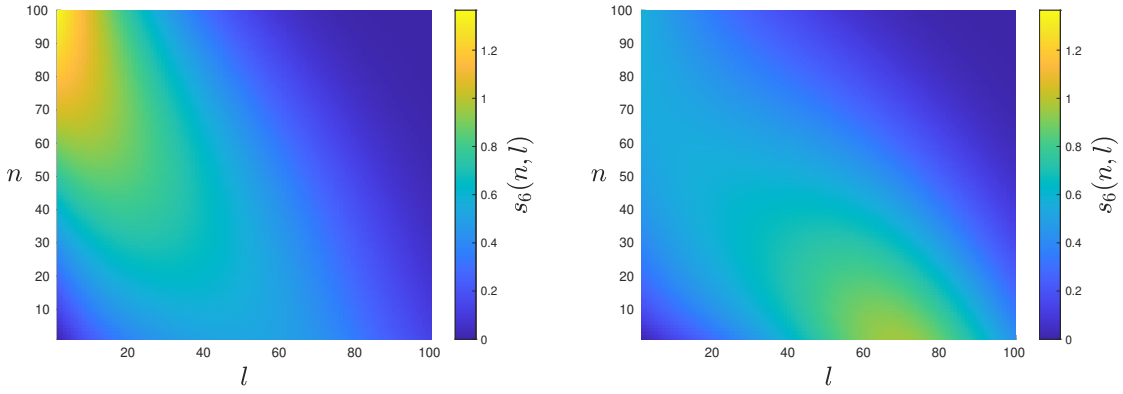


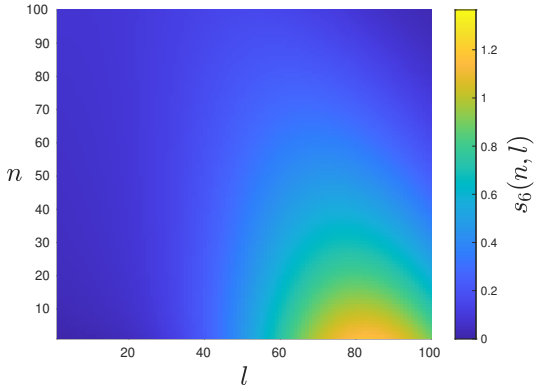
Figure 6.8: Absolute error in the final distribution for the parameters α_s, β_s, γ, h_1 and h_2 from (6.3.8) compared to the original chosen parameters, and $\bar{u} = 0.1$.

We use parameter values (6.3.8) to then simulate the model for different velocity ratios, $\bar{u}$, and show the resulting solutions in figure 6.9. We see that for very low $\bar{u}$, i.e. a large difference between the velocities, the average length of the tows decreases without decreasing the tow size significantly. Increasing $\bar{u}$ leads to less breakage, which is desired, however if $\bar{u}$ is increased too much there is not enough opening of tows (decrease in n) to achieve the desired homogeneity in the product. This observation suggests an 'optimal' value of $\bar{u}$ which depends on the desired balance between opening and breakage of tows. In principle, if the desired distribution is known, the parameter $\bar{u}$ could be fitted in order to optimise the carding action. This method could also be used in the future to set other control parameters, such as tooth density.

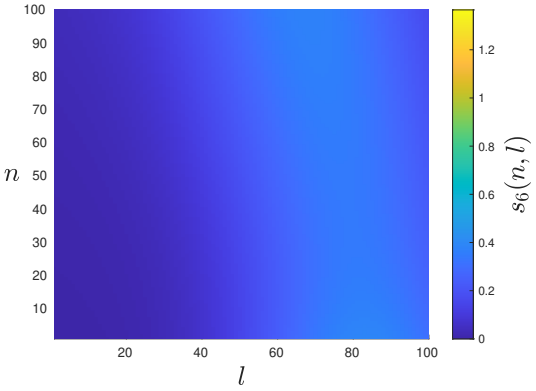


(a) $\bar{u} = 0.05$.

(b) $\bar{u} = 0.1$.



(c) $\bar{u} = 0.5$.



$\bar{u} = 0.8$.

Figure 6.9: Final distributions, $s_6(n, l)$, for different velocity ratios $\bar{u}$ and parameter values (6.3.8).

6.4 Conclusions

In this chapter we have outlined a method for fitting our models with experimental data. In section 6.2 we proposed a continuous approximation of the tow size distribution model derived in section 5.6.1, comprising of a system of ODEs. We proposed simple constitutive relations for the transition probabilities, resulting in a model depending on just three unknown parameters. We then showed how these parameter values can be fitted using knowledge of the initial and final tow size distributions. In principle these distributions can be measured experimentally but, in the absence of any usable data at this stage, we illustrated the method using some manufactured distributions.

This approach was extended in section 6.3 to include both size and length of tows, using the model derived in section 5.6.2. We followed a similar method, using data to fit our parameters. We then simulated the model for different velocity ratios, with results suggesting the existence of an 'optimal' velocity ratio between the rollers to achieve a balance between tow opening and breakage.

The exercise outlined in this chapter has provided a proof of concept for the probabilistic models we have developed. We have shown that combining experimental data and plausible constitutive laws allows us to fit the control parameters, and build the machine properties into the model. A possible limitation of this approach is that different parameter groups can yield very similar final distributions. This may not be a problem however as long as we can achieve the desired distributions with relative accuracy. To solve this possible issue however, further analysis could be done into the solutions and parameter groupings in the model. Additionally, including data at each stage along the swift (between each worker-stripper pair) and fitting the parameters to these distributions could provide more accurate results.

The method we have presented can be used to explore different roller velocities to achieve different tow size and length distributions in the carding process. This approach could be extended in the future to examine the effect of increasing or reducing the number of stripper-worker pairs, as well as building in other machine properties such as tooth number. Another natural extension would be to use these probabilistic approaches to model the whole carding process, including all cylinders, not just the strippers, workers, and swift. Each distinct region between pairs of rollers will have a different set of parameter values associated with it, the resulting model providing a detailed view of the behaviour of tows in the carding machine.

Chapter 7

Discussion, Conclusions and Further Work

7.1 Discussion and Conclusions

In this thesis we have presented a variety of models for the processing of recycled carbon fibre in the carding machine. The aim of this work is to provide insight into the physical processes behind the carding action, and the properties of both the machine and the carbon fibre that affect the final product. We have used the models to examine the behaviour of the web of carbon fibre in different regions and setups, and obtained tools that could be used in the future to adjust and optimise the carding process. We reviewed existing mathematical models for carding, mainly from the textile industry, and relevant models from a variety of other industries and applications. We used this existing work to inform and analyse our models.

In chapter 2 we began by reviewing the work of Lee [37, 38], who modelled the carding of polyester and cotton, and used this as the basis for a continuum model for a web of carbon fibre. We derived the governing equations, assuming that the order of the fibres increases due to the web being stretched, and examined the behaviour of this model in different geometries. A lubrication-type approximation was used to model the flow of the web through the crucial "nip" regions of the carding machine. We showed that the model can be reduced to 2D and, with the simplifying assumption of uniform viscosity, were then able to solve the resulting equations analytically. Relaxing the uniform viscosity assumption, we then presented a numerical scheme to solve the resulting coupled PDE system. The results indicate that a greater difference in the velocities of the swift and the worker lead to increased ordering of fibres. The full model showed that including the density and order of fibres in the viscosities has

a large effect on the results, and including these terms allowed us to examine the effect of different viscosity parameters.

We changed approaches to consider the web at a smaller scale in chapter 3, focusing on the forces on individual fibres, with the aim of understanding how the combing action of the teeth contributes to the ordering of fibres in the machine. We started by looking at a tooth moving at a constant velocity through two overlapped fibres and showed that the tooth can always move through the fibres, and therefore "comb" them. We proposed a friction law whereby the tension in the fibres is directly proportional to the velocity of the tooth, which suggests that a higher velocity is more likely to result in increased fibre breakage, if the tension in a fibre increases above its breaking stress. We then expanded this analysis to look at the case of three overlapping fibres. We showed that when the third fibre is perpendicular to the tooth velocity, the system cannot be combed out, but if it is at a slight angle the tooth will reduce the number of crossover points and the system will reduce to that of just two fibres. This work could be extended in the future to model a network of fibres, with combing describing the reduction in crossover points.

In chapters 4 and 5 we presented models for carbon fibre tows in the carding machine. Instead of the ordering of fibres being the key process, in this case the opening of tows, and splitting into smaller tows, was the focus. Splitting tows consisting of thousands of individual filaments into smaller tows (for example consisting of hundreds of filaments) needs to happen before a homogeneous, aligned web of fibres can be produced. In chapter 4 we derived a model for the opening of a single tow due to its interaction with a carding tooth. We assumed a tooth was already embedded in a tow, and thus presented a 2D model. We then used the theory of elasticity to model the tow as two joined elasticas being split apart [40, 58]. Our model yields key dimensionless parameters τ and μ, where μ is the coefficient of friction between a tooth and a tow, and τ is proportional to the force with which the tooth is pushed through the tow. We were then able to plot solution shapes of the elastica for different values of τ, particularly focusing on two cases; a single contact point between the tooth and the elastica, and a contact set between them. We used existing work on the splitting of mica [44] to argue that the curvature of the elastica at the splitting point determines whether the tow will open. This then provided results showing the force required to open tows for different critical curvatures and values of μ.

Models for a distribution of tows moving through different regions of the machine were derived in chapter 5. We compared the splitting of fibre tows to breakup processes in a number of applications, such as particles in a blender [48] and droplet

breakage [2, 70]. This motivated the derivation of a probabilistic model, where instead of stepping forward in time the tows step forward through different regions of the machine. This model highlighted key probabilities associated with the opening of tows, and the transfer of tows between rollers. We then extended this model to include the breaking of tows, i.e. a reduction in the length of the tows through the machine. We posed several probability functions associated with these processes, and showed the distributions of tow size and length these lead to. We then used the specific properties of the swift-stripper-worker region of the machine to derive a simpler model applicable to only this region.

In chapter 6 we worked through examples of how our probability parameters could be determined using experimental data. We used insights from chapters 2, 3, and 4 to inform the required probability functions. The combination of the models presented in this thesis give an overall picture of the different processes taking place in the carding machine, and provide insight into the important control parameters, for example roller velocities and tooth properties, in the formation of the final product.

In chapters 2 and 5 we modelled carbon fibre moving through the carding machine in two different ways; as a continuous web, and as tows consisting of discrete filaments. When tows are broken up in the carding machine the state of the material goes from being very discrete (see figure 1.5) to a continuous web (see figure 1.3). This suggests a combination of these two approaches would be appropriate to model the whole carding machine, for example with the probabilistic tow model at the start of the machine, where the main process is tow breakup, and with the continuum model after the tows reach a critical size, as the ordering and mixing of fibres become the key processes. This combined model could then give insights into how to optimise tow splitting in certain regions of the machine, and how to optimise fibre ordering in other regions.

7.2 Further Work

All of the models we have discussed could both be developed further, and combined with experimental data to help optimise the process of carding recycled carbon fibre. A more detailed experimental study into the webs of carbon fibre would be needed to evaluate the viscosity parameters $\mu_1 - \mu_2$, $\lambda_1 - \lambda_5$, which were chosen somewhat arbitrarily in chapter 2. This continuum model could be extended to include the mixing and movement of fibres across the rollers (into the page in figure 1.2). This would require analysis of the 3D model, possibly to include a diffusion-type term to model

random movement in this plane. Other extensions could include incorporating elastic and plastic behaviour, and focusing on the whole process, as opposed to just one region. This would involve nonuniform 'initial' conditions for the density and order of fibres. This kind of model could then provide a detailed prediction for the ordering of fibres in the final web. The current model however does provide information on the parameters (namely roller velocities) that contribute towards ordering.

The microscale combing models in chapter 3 motivate the development of a generalised model, for any arrangement and number of fibres. This would involve focusing on the crossover points between fibres, viewing 'combing' as the action of removing crossover points. A network model could be the best way to approach this challenge, with crossover points as nodes, and the fibres with tensions as the edges (or links). This type of approach could also be used to model the propagation of the tension forces through the network, and thus give a more detailed view of fibre breakage.

As discussed in chapter 4, our 2D model for the splitting of a tow could be extended to 3D to model the action of a tooth embedding itself within a tow. This would allow us to incorporate different tooth geometries as a variable in the model, giving another parameter to be optimised to achieve maximum opening.

The discussion in chapter 5, and derivation of a probabilistic model for a distribution of tows in the carding machine, describes a detailed tool that may be used to predict the properties of the final product produced by Gen 2 Carbon. To make this tool usable, the various probability parameters highlighted need to be fitted using carding data, as discussed in chapter 6. This data would include the lengths and sizes of tows at different points in the machine. After a detailed data analysis, this probabilistic model could then be combined with the continuum model of chapter 2 to provide a detailed model of how recycled carbon fibre behaves in the carding machine.

Appendix A

A Numerical Scheme for Method of Lines

In section 2.6.1 we discuss the numerical solution of a system of coupled PDEs using the method of lines. In this appendix we set out in detail the discretization of equations (2.6.11)-(2.6.17). We use central differences to approximate the derivatives in Z, using ghost points to maintain second-order accuracy at the boundaries. Our discretization is defined by

$$Z_i = (i-1)\Delta Z, \quad i = 1, ..., N, \quad \Delta Z = \frac{1}{N-1}. \tag{A.1}$$

Using this discretization, we derive the DAE system

$$f_1(X, Z_i)v_0(X, Z_{i+1}) + f_2(X, Z_i)v_0(X, Z_i) + f_3(X, Z_i)v_0(X, Z_{i-1}) = 0, \tag{A.2a}$$

$$f_1(X, Z_i)v_1(X, Z_{i+1}) + f_2(X, Z_i)v_1(X, Z_i) + f_3(X, Z_i)v_1(X, Z_{i-1}) = f_4(X, Z_i), \tag{A.2b}$$

$$f_1(X, Z_i)v_2(X, Z_{i+1}) + f_2(X, Z_i)v_2(X, Z_i) + f_3(X, Z_i)v_2(X, Z_{i-1}) = f_5(X, Z_i), \tag{A.2c}$$

$$\begin{aligned}\frac{\mathrm{d}y}{\mathrm{d}X}(X, Z_i) = \frac{h'(X)}{2m_3}\Bigg[&- \frac{2(m_3+1)\bar{u}}{1-\bar{u}}\left(\frac{v_0(X, Z_{i+1}) - v_0(X, Z_{i-1})}{2\Delta Z}\right) \\ &+ \alpha_1(X)\left(y - \frac{2(m_3+1)}{1-\bar{u}}\left(\frac{v_1(X, Z_{i+1}) - v_1(X, Z_{i-1})}{2\Delta Z}\right)\right) \\ &- \alpha_2(X)\left(1 + \frac{2(m_3+1)}{1-\bar{u}}\left(\frac{v_2(X, Z_{i+1}) - v_2(X, Z_{i-1})}{2\Delta Z}\right)\right)\Bigg],\end{aligned} \tag{A.2d}$$

$$
\begin{aligned}
&-\frac{2(m_3+1)}{1-\bar{u}}\left(\frac{v_1(X,Z_2)-v_1(X,Z_0)}{2\Delta Z}\right)\alpha_1(X)\\
&\qquad-\left(\frac{2(m_3+1)}{1-\bar{u}}\left(\frac{v_2(X,Z_2)-v_2(X,Z_0)}{2\Delta Z}\right)+1\right)\alpha_2(X)\\
&\qquad=\frac{2(m_3+1)\bar{u}}{1-\bar{u}}\left(\frac{v_0(X,Z_2)-v_0(X,Z_0)}{2\Delta Z}\right), \qquad \text{(A.2e)}\\
&\left(h(X)-\frac{2(m_3+1)}{1-\bar{u}}\left(\frac{v_1(X,Z_{N+1})-v_1(X,Z_{N-1})}{2\Delta Z}\right)\right)\alpha_1(X)\\
&\qquad-\left(\frac{2(m_3+1)}{1-\bar{u}}\left(\frac{v_2(X,Z_{N+1})-v_2(X,Z_{N-1})}{2\Delta Z}\right)+1\right)\alpha_2(X)\\
&\qquad=2m_3+\frac{2(m_3+1)\bar{u}}{1-\bar{u}}\left(\frac{v_0(X,Z_{N+1})-v_0(X,Z_{N-1})}{2\Delta Z}\right), \qquad \text{(A.2f)}\\
&\frac{\mathrm{d}\sigma}{\mathrm{d}X}=\alpha_1(X)h'(X)\sigma(X), \qquad \text{(A.2g)}\\
&\rho^2=-\frac{\sigma(X)}{1-\bar{u}}\left(\frac{y(X,Z_{i+1})-y(X,Z_{i-1})}{2\Delta Z}\right), \qquad \text{(A.2h)}\\
&\frac{\mathrm{d}\phi}{\mathrm{d}X}(X,Z_i)=\left(\frac{(1-(1-\bar{u})Z_i)\,\frac{\mathrm{d}y}{\mathrm{d}X}(X,Z_i)-v(X,Z_i)}{(1-(1-\bar{u})Z_i)\,(y(X,Z_{i+1})-y(X,Z_{i-1}))}\right)(\phi(X,Z_{i+1})-\phi(X,Z_{i-1}))\\
&\qquad+\frac{2\Delta Z\beta(1-\phi(X,Z_i))(1-\bar{u})}{1-(1-\bar{u})Z_i}\left[\frac{(1-(1-\bar{u})Z_i)\,\frac{\mathrm{d}y}{\mathrm{d}X}(X,Z_i)-v(X,Z_i)}{(1-(1-\bar{u})Z_i)\,(y(X,Z_{i+1})-y(X,Z_{i-1}))}\right]^+, \qquad \text{(A.2i)}
\end{aligned}
$$

for $i=1,...,N$, where

$$
\begin{aligned}
f_1(X,Z_i)=&2(m_3+1)-(1-\bar{u})\Delta Z\left[-\frac{4}{(1-(1-\bar{u})Z_i)}\right.\\
&\left.+\frac{2(m_3+1)}{(1-\bar{u})\Delta Z}\left(\frac{y(X,Z_{i+1})-2y(X,Z_i)+y(X,Z_{i-1})}{y(X,Z_{i+1})-y(X,Z_{i-1})}\right)\right], \qquad \text{(A.3a)}\\
f_2(X,Z_i)=&-4(m_3+1)-\frac{4m_3(1-\bar{u})\Delta Z}{(1-(1-\bar{u})Z_i)}\left(\frac{y(X,Z_{i+1})-2y(X,Z_i)+y(X,Z_{i-1})}{y(X,Z_{i+1})-y(X,Z_{i-1})}\right), \qquad \text{(A.3b)}\\
f_3(X,Z_i)=&2(m_3+1)+(1-\bar{u})\Delta Z\left[-\frac{4}{(1-(1-\bar{u})Z_i)}\right.\\
&\left.+\frac{2(m_3+1)}{(1-\bar{u})\Delta Z}\left(\frac{y(X,Z_{i+1})-2y(X,Z_i)+y(X,Z_{i-1})}{y(X,Z_{i+1})-y(X,Z_{i-1})}\right)\right], \qquad \text{(A.3c)}
\end{aligned}
$$

$$f_4(X,Z_i) =(2m_3+1)(1-\bar{u})\Delta Z\left(\frac{y(X,Z_{i+1})-y(X,Z_{i-1})}{2}\right) \tag{A.3d}$$

$$+\,y(X,Z_i)\left[\frac{2(1-\bar{u})^2\Delta Z^2}{1-(1-\bar{u})Z_i}\right.$$

$$\left.-\,2(1-\bar{u})\Delta Z\left(\frac{y(X,Z_{i+1})-2y(X,Z_i)+y(X,Z_{i-1})}{y(X,Z_{i+1})-y(X,Z_{i-1})}\right)\right], \tag{A.3e}$$

$$f_5(X,Z_i) =-\frac{2(1-\bar{u})^2\Delta Z^2}{1-(1-\bar{u})Z_i}+2(1-\bar{u})\Delta Z\left(\frac{y(X,Z_{i+1})-2y(X,Z_i)+y(X,Z_{i-1})}{y(X,Z_{i+1})-y(X,Z_{i-1})}\right). \tag{A.3f}$$

Boundary conditions (2.6.12a)-(2.6.12c) become

$$v_0(X,Z_1)=0,\ v_0(X,Z_N)=1, \tag{A.4a}$$

$$v_1(X,Z_1)=v_1(X,Z_N)=0, \tag{A.4b}$$

$$v_2(X,Z_1)=v_2(X,Z_N)=0, \tag{A.4c}$$

and we define ghost points in y and ϕ by

$$\frac{y(X,Z_0)+y(X,Z_2)}{2}=y(X,Z_1), \tag{A.5a}$$

$$\frac{y(X,Z_{N-1})+y(X,Z_{N+1})}{2}=y(X,Z_N), \tag{A.5b}$$

$$\frac{\phi(X,Z_0)+\phi(X,Z_2)}{2}=\phi(X,Z_1), \tag{A.5c}$$

$$\frac{\phi(X,Z_{N-1})+\phi(X,Z_{N+1})}{2}=\phi(X,Z_N). \tag{A.5d}$$

Equations (A.2), (A.3), (A.4), and (A.5) represent a DAE system that we solve using MATLAB's in-built solver ode15s [51], as discussed in section 2.6.1. The solution to this system of equations is described in section 2.6.1.3.

Appendix B

Analysis and Numerical Solution of the Full Lubrication Model

In this appendix we present the solution method of the full lubrication model defined by equations (2.6.22)-(2.6.24). We begin by conducting similar analysis to the density model, in section 2.6.1.2, and then solve the resulting system using the method of lines.

Again we want to solve on a fixed domain so we make the change of variables

$$X = x, \quad Z = \frac{1 - u(x,y)}{1 - \bar{u}}, \tag{B.1}$$

as in section 2.6.1.2, and introducing the unknown functions $\sigma(X)$ and $F(X)$, equations (2.6.22) become

$$\begin{aligned}(1-(1-\bar{u})Z)\,\frac{\partial y}{\partial Z}\frac{\partial \rho}{\partial X} + \left(v - (1-(1-\bar{u})Z)\,\frac{\partial y}{\partial Z}\right)\frac{\partial \rho}{\partial Z} \\ + \left(\frac{\partial v}{\partial Z} + (1-\bar{u})\frac{\partial y}{\partial X}\right)\rho = 0,\end{aligned} \tag{B.2a}$$

$$\frac{\partial \phi}{\partial X} = \frac{\frac{\partial y}{\partial X}}{\frac{\partial y}{\partial Z}}\frac{\partial \phi}{\partial Z} - \frac{v}{(1-(1-\bar{u})Z)\,\frac{\partial y}{\partial Z}}\frac{\partial \phi}{\partial Z} + \frac{\beta(1-\phi)}{(1-(1-\bar{u})Z)}\left[\frac{(1-(1-\bar{u})Z)\,\frac{\partial u}{\partial X} - v}{(1-(1-\bar{u})Z)\,\frac{\partial y}{\partial Z}}\right]^{+}, \tag{B.2b}$$

$$\rho^2 = -\frac{\sigma(X)}{(1+A_1\phi)(1-\bar{u})}\frac{\partial y}{\partial Z}, \tag{B.2c}$$

$$\begin{aligned}\frac{\partial v}{\partial Z} = \left(\frac{1-\bar{u}}{A_5 + A_6\phi}\right)\Bigg\{ &-(A_2 + A_3\phi)\frac{\partial y}{\partial X} + A_4\frac{\phi v}{1-(1-\bar{u})Z} \\ &- (1+A_1\phi)\left(\frac{F(X)}{\sigma(X)} - \frac{y\sigma'(X)}{\sigma(X)}\right)\Bigg\},\end{aligned} \tag{B.2d}$$

where we note that the term

$$\frac{(1-(1-\bar{u})Z)\,\frac{\partial u}{\partial X}-v}{(1-(1-\bar{u})Z)\,\frac{\partial y}{\partial Z}}, \tag{B.3}$$

is always negative for $X<0$ and always positive for $X>0$. We therefore only need to include this term in the model for $X>0$.

We note that, as for the previous model, our aim here is to derive a set of algebraic equations when we discretize in Z, and then have an explicit ODE for stepping forwards in X. We note that the difference now is that the equation for ϕ is coupled with the other equations, and therefore we have to take into account the extra term for $X>0$ in the derivation of our system. Combining equations (B.2) and rearranging gives the governing equations

$$\begin{aligned}\mathcal{L}_1 v = &\left(\frac{1-\bar{u}}{A_5+A_6\phi}\right)\left[(1+A_1\phi)\left(\frac{2(1-\bar{u})}{1-(1-\bar{u})Z}-\frac{\frac{\partial^2 y}{\partial Z^2}}{\frac{\partial y}{\partial Z}}\right)-\left(\frac{A_3(1+A_1\phi)}{A_2+A_3\phi}-A_1\right)\frac{\partial\phi}{\partial Z}\right]\\ &\times\left(\frac{y\sigma'(X)}{\sigma(X)}-\frac{F(X)}{\sigma(X)}\right)+\frac{(1-\bar{u})(1+A_2+(A_1+A_3)\phi)}{A_5+A_6\phi}\frac{\sigma'(X)}{\sigma(X)}\frac{\partial y}{\partial Z},\end{aligned} \tag{B.4a}$$

$$\begin{aligned}\mathcal{L}_2 v = &\left(\frac{1-\bar{u}}{A_5+A_6\phi}\right)\left[(1+A_1\phi)\left(\frac{2(1-\bar{u})}{1-(1-\bar{u})Z}-\frac{\frac{\partial^2 y}{\partial Z^2}}{\frac{\partial y}{\partial Z}}\right)-\left(\frac{A_3(1+A_1\phi)}{A_2+A_3\phi}-A_1\right)\frac{\partial\phi}{\partial Z}\right]\\ &\times\left(\frac{y\sigma'(X)}{\sigma(X)}-\frac{F(X)}{\sigma(X)}\right)+\frac{(1-\bar{u})(1+A_2+(A_1+A_3)\phi)}{A_5+A_6\phi}\frac{\sigma'(X)}{\sigma(X)}\frac{\partial y}{\partial Z}\\ &-\frac{A_1(1-\bar{u})^2\beta(1-\phi)}{(A_5+A_6\phi)(1-(1-\bar{u})Z)}\left(\frac{y\sigma'(X)}{\sigma(X)}-\frac{F(X)}{\sigma(X)}\right),\end{aligned} \tag{B.4b}$$

where we define the operators $\mathcal{L}_1$ and $\mathcal{L}_2$ as

$$\begin{aligned}\mathcal{L}_1 v \equiv &\frac{\partial^2 v}{\partial Z^2}+\left[-\frac{(1-\bar{u})(2A_2+(A_4+2A_3)\phi)}{(A_5+A_6\phi)(1-(1-\bar{u})Z)}+\frac{2(1-\bar{u})}{1-(1-\bar{u})Z}-\frac{\frac{\partial^2 y}{\partial Z^2}}{\frac{\partial y}{\partial Z}}\right.\\ &\left.+\left(\frac{A_6}{A_5+A_6\phi}-\frac{A_3}{A_2+A_3\phi}\right)\frac{\partial\phi}{\partial Z}\right]\frac{\partial v}{\partial Z}\\ &+\left(\frac{1-\bar{u}}{(A_5+A_6\phi)(1-(1-\bar{u})Z)}\right)\left[-\frac{3A_4(1-\bar{u})\phi}{1-(1-\bar{u})Z}-(A_2+(A_3-A_4)\phi)\frac{\frac{\partial^2 y}{\partial Z^2}}{\frac{\partial y}{\partial Z}}\right.\\ &\left.-\frac{A_2A_4}{A_2+A_3\phi}\frac{\partial\phi}{\partial Z}\right]v,\end{aligned} \tag{B.5a}$$

$$\mathcal{L}_2 v \equiv \frac{\partial^2 v}{\partial Z^2} + \Bigg[- \frac{(1-\bar{u})(2A_2 + (A_4 + 2A_3)\phi)}{(A_5 + A_6\phi)(1-(1-\bar{u})Z)} + \frac{2(1-\bar{u})}{1-(1-\bar{u})Z} - \frac{\frac{\partial^2 y}{\partial Z^2}}{\frac{\partial y}{\partial Z}} + \left(\frac{A_6}{A_5 + A_6\phi} - \frac{A_3}{A_2 + A_3\phi} \right) \frac{\partial \phi}{\partial Z} - \frac{A_1(1-\bar{u})\beta(1-\phi)}{(1+A_1\phi)(1-(1-u)\bar{Z})} \Bigg] \frac{\partial v}{\partial Z} + \left(\frac{1-\bar{u}}{(A_5 + A_6\phi)(1-(1-\bar{u})Z)} \right) \Bigg[- \frac{3A_4(1-\bar{u})\phi}{1-(1-\bar{u})Z} - (A_2 + (A_3 - A_4)\phi) \frac{\frac{\partial^2 y}{\partial Z^2}}{\frac{\partial y}{\partial Z}} - \frac{A_2 A_4}{A_2 + A_3\phi} \frac{\partial \phi}{\partial Z} + \frac{A_1(1-\bar{u})(((A_4 - A_3)\phi - A_2)\beta(1-\phi)}{(1+A_1\phi)(1-(1-\bar{u})Z)} \Bigg] v, \tag{B.5b}$$

and equation (B.4a) is used when $X < 0$ and equation (B.4b) is used when $X > 0$. We again split the vertical velocity into three components so it is defined by

$$v = v_0 \bar{u} h'(X) + \frac{\sigma'(X)}{\sigma(X)} v_1 + \frac{F(X)}{\sigma(X)} v_2. \tag{B.6}$$

This then allows us to write our governing equations as

$$\mathcal{L}_1 v_0 = 0, \quad \text{for} \quad X < 0, \tag{B.7a}$$

$$\mathcal{L}_2 v_0 = 0, \quad \text{for} \quad X > 0, \tag{B.7b}$$

$$\mathcal{L}_1 v_1 = \left(\frac{1-\bar{u}}{A_5 + A_6\phi} \right) \Bigg[(1 + A_1\phi) \left(\frac{2(1-\bar{u})}{1-(1-\bar{u})Z} - \frac{\frac{\partial^2 y}{\partial Z^2}}{\frac{\partial y}{\partial Z}} \right) - \left(\frac{A_3(1+A_1\phi)}{A_2 + A_3\phi} - A_1 \right) \frac{\partial \phi}{\partial Z} \Bigg] y + \frac{(1-\bar{u})(1 + A_2 + (A_1 + A_3)\phi)}{A_5 + A_6\phi} \frac{\partial y}{\partial Z}, \quad \text{for} \quad X < 0, \tag{B.7c}$$

$$\mathcal{L}_2 v_1 = \left(\frac{1-\bar{u}}{A_5 + A_6\phi} \right) \Bigg[(1 + A_1\phi) \left(\frac{2(1-\bar{u})}{1-(1-\bar{u})Z} - \frac{\frac{\partial^2 y}{\partial Z^2}}{\frac{\partial y}{\partial Z}} \right) - \left(\frac{A_3(1+A_1\phi)}{A_2 + A_3\phi} - A_1 \right) \frac{\partial \phi}{\partial Z} \Bigg] y + \frac{(1-\bar{u})(1 + A_2 + (A_1 + A_3)\phi)}{A_5 + A_6\phi} \frac{\partial y}{\partial Z} - \frac{A_1(1-\bar{u})^2\beta(1-\phi)}{(A_5 + A_6\phi)(1-(1-\bar{u})Z)} y, \quad \text{for} \quad X > 0, \tag{B.7d}$$

$$\mathcal{L}_1 v_2 = -\left(\frac{1-\bar{u}}{A_5+A_6\phi}\right)\left[(1+A_1\phi)\left(\frac{2(1-\bar{u})}{1-(1-\bar{u})Z}-\frac{\frac{\partial^2 y}{\partial Z^2}}{\frac{\partial y}{\partial Z}}\right)-\left(\frac{A_3(1+A_1\phi)}{A_2+A_3\phi}-A_1\right)\frac{\partial\phi}{\partial Z}\right] + \frac{(1-\bar{u})(1+A_2+(A_1+A_3)\phi)}{A_5+A_6\phi}\frac{\partial y}{\partial Z}, \quad \text{for} \quad X<0, \tag{B.7e}$$

$$\mathcal{L}_2 v_2 = -\left(\frac{1-\bar{u}}{A_5+A_6\phi}\right)\left[(1+A_1\phi)\left(\frac{2(1-\bar{u})}{1-(1-\bar{u})Z}-\frac{\frac{\partial^2 y}{\partial Z^2}}{\frac{\partial y}{\partial Z}}\right)-\left(\frac{A_3(1+A_1\phi)}{A_2+A_3\phi}-A_1\right)\frac{\partial\phi}{\partial Z}\right] + \frac{A_1(1-\bar{u})^2\beta(1-\phi)}{(A_5+A_6\phi)(1-(1-\bar{u})Z)}, \quad \text{for} \quad X>0, \tag{B.7f}$$

$$\frac{\mathrm{d}\sigma}{\mathrm{d}X} = \alpha_1(X)h'(X)\sigma(X), \tag{B.7g}$$

$$F(X) = \alpha_2(X)h'(X)\sigma(X), \tag{B.7h}$$

$$\frac{\partial y}{\partial X} = \frac{h'(X)}{A_2+A_3\phi}\left\{\bar{u}\left(\frac{A_4\phi}{1-(1-\bar{u})Z}v_0-\frac{A_5+A_6\phi}{1-\bar{u}}\frac{\partial v_0}{\partial Z}\right) + \alpha_1(X)\left((1+A_1\phi)y+\frac{A_4\phi}{1-(1-\bar{u})Z}v_1-\left(\frac{A_5+A_6\phi}{1-\bar{u}}\right)\frac{\partial v_1}{\partial Z}\right) + \alpha_2(X)\left(-(1+A_1\phi)+\frac{A_4\phi}{1-(1-\bar{u})Z}v_2-\left(\frac{A_5+A_6\phi}{1-\bar{u}}\right)\frac{\partial v_2}{\partial Z}\right)\right\}, \tag{B.7i}$$

$$\frac{\partial\phi}{\partial X} = \frac{1}{1-(1-\bar{u})Z}\left\{\frac{\frac{\partial\phi}{\partial Z}}{\frac{\partial y}{\partial Z}}\left((1-(1-\bar{u})Z)\frac{\partial y}{\partial X}-h'(X)\left(\bar{u}v_0+\alpha_1(X)v_1+\alpha_2(X)v_2\right)\right) + \beta(1-\phi)(1-\bar{u})\left[\frac{\frac{\partial y}{\partial X}}{\frac{\partial y}{\partial Z}}-\frac{h'(X)\left(\bar{u}v_0+\alpha_1(X)v_1+\alpha_2(X)v_2\right)}{(1-(1-\bar{u})Z)\frac{\partial y}{\partial Z}}\right]^+\right\}, \tag{B.7j}$$

$$\rho^2 = -\frac{\sigma(X)}{(1+A_1\phi)(1-\bar{u})}\frac{\partial y}{\partial Z}, \tag{B.7k}$$

with boundary conditions

$$v_0(X,0)=0,\ v_0(X,1)=1, \tag{B.8a}$$

$$v_1(X,0)=v_1(X,1)=0, \tag{B.8b}$$

$$v_2(X,0)=v_2(X,1)=0, \tag{B.8c}$$

$$y(X,0)=0,\ y(X,1)=h(X). \tag{B.8d}$$

Implementing boundary conditions (B.8d) in equation (B.7i) allows us to find functions $\alpha_1(X)$ and $\alpha_2(X)$ as the solutions of the system

$$\left(\frac{A_5 + A_6\phi(X,0)}{1-\bar{u}}\right)\bar{u}\frac{\partial v_0}{\partial Z}(X,0) = -\left(\frac{A_5 + A_6\phi(X,0)}{1-\bar{u}}\right)\frac{\partial v_1}{\partial Z}(X,0)\alpha_1(X) - \left(\left(\frac{A_5 + A_6\phi(X,0)}{1-\bar{u}}\right)\frac{\partial v_2}{\partial Z}(X,0) + (1 + A_1\phi(X,0))\right)\alpha_2(X), \tag{B.9a}$$

$$\begin{aligned} A_2 + (A_3 - A_4)\phi(X,1) + \left(\frac{A_5 + A_6\phi(X,1)}{1-\bar{u}}\right)\bar{u}\frac{\partial v_0}{\partial Z}(X,1) \\ = \left((1 + A_1\phi(X,1))h(X) - \left(\frac{A_5 + A_6\phi(X,1)}{1-\bar{u}}\right)\frac{\partial v_1}{\partial Z}(X,1)\right)\alpha_1(X) \\ - \left((1 + A_1\phi(X,1)) + \left(\frac{A_5 + A_6\phi(X,1)}{1-\bar{u}}\right)\frac{\partial v_2}{\partial Z}(X,1)\right)\alpha_2(X). \end{aligned} \tag{B.9b}$$

Equations (B.7)-(B.9) is a system of PDEs which can be solved using the method of lines, and reduce to equations (2.6.11)-(2.6.17) when the viscosity parameter values satisfy $A_1 = A_3 = A_4 = A_6 = 0$. We discuss the solution method and results of this system in section 2.6.2.2.

Bibliography

[1] D. J. Aldous. Deterministic and stochastic models for coalescence (aggregation and coagulation): a review of the mean-field theory for probabilists. *Bernoulli*, 5(1):3–48, 1999.

[2] J. Banasiak. Conservative and shattering solutions for some classes of fragmentation models. *Mathematical Models and Methods in Applied Sciences*, 14(4):483–501, 2004.

[3] J. Banasiak and W. Lamb. Coagulation, fragmentation and growth processes in a size structured population. *Discrete and Continuous Dynamical Systems-Series B*, 11(3):563–585, 2009.

[4] R. Becker and W. Döring. Kinetische behandlung der keimbildung in übersättigten dämpfen. *Annalen der physik*, 416(8):719–752, 1935.

[5] N. Brilliantov, P. L. Krapivsky, A. Bodrova, F.Spahn, H. Hayakawa, V. Stadnichuk, and J.Schmidt. Size distribution of particles in Saturn's rings from aggregation and fragmentation. *Proceedings of the National Academy of Sciences*, 112(31):9536–9541, 2015.

[6] P. L. Butzer and R. L. Stens. The Euler-Maclaurin summation formula, the sampling theorem, and approximate integration over the real axis. *Linear Algebra and its Applications*, 52-53:141–155, 1983.

[7] M. C. Calderer and C. Liu. Poiseuille flow of nematic liquid crystals. *International Journal of Engineering Science*, 38(9-10):1007–1022, 2000.

[8] G. A. Carnaby. Fiber breakage during carding: Part i: Theory. *Textile Research Journal*, 54(6):366–369, 1984.

[9] G. Chen, T. Huang, and W. Liu. Poiseuille flow of nematic liquid crystals via the full Ericksen–Leslie model. *Archive for Rational Mechanics and Analysis*, 236(2):839–891, 2020.

[10] A. Cherkassky. A two-dimensional mathematical model of the carding process. *Textile Research Journal*, 64(3):169–175, 1994.

[11] B. Cornelissen, M. B. de Rooij, B. Rietman, and R. Akkerman. Frictional behavior of carbon fiber tows: a contact mechanics model of tow–tow friction. *Textile Research Journal*, 84(14):1476–1488, 2014.

[12] B. Cornelissen, B. Rietman, and R. Akkerman. Frictional behaviour of high performance fibrous tows: Friction experiments. *Composites Part A: Applied Science and Manufacturing*, 44:95–104, 2013.

[13] R. J. Dyson and O. E. Jensen. A fibre-reinforced fluid model of anisotropic plant cell growth. *Journal of Fluid Mechanics*, 655:472–503, 2010.

[14] J. L. Ericksen. Liquid crystals with variable degree of orientation. *Archive for Rational Mechanics and Analysis*, 113(2):97–120, 1991.

[15] P. G. De Gennes and J. Prost. *The physics of liquid crystals*, volume 83. Oxford University Press, 1993.

[16] J. Green and A. Friedman. The extensional flow of a thin sheet of incompressible, transversely isotropic fluid. *European Journal of Applied Mathematics*, 19(3):225–257, 2008.

[17] I. M. Griffiths, C. D. Bain, C. J. W. Breward, D. M. Colegate, P. D. Howell, and S. L. Waters. On the predictions and limitations of the Becker–Döring model for reaction kinetics in micellar surfactant solutions. *Journal of colloid and interface science*, 360(2):662–671, 2011.

[18] I. M. Griffiths, C. J. W. Breward, D. M. Colegate, P. J. Dellar, P. D. Howell, and C. D. Bain. A new pathway for the re-equilibration of micellar surfactant solutions. *Soft Matter*, 9(3):853–863, 2013.

[19] L. T. Harper, T. A. Turner, N. A. Warrior, and C. D. Rudd. Characterisation of random carbon fibre composites from a directed fibre preforming process: The effect of tow filamentisation. *Composites Part A: Applied Science and Manufacturing*, 38(3):755–770, 2007.

[20] J. R. Harris, J. A. D. Wattis, and J. V. Wood. A comparison of different models for mechanical alloying. *Acta Materialia*, 49(19):3991–4003, 2001.

[21] S. He, L. Cheng, W. Xue, Z. Hua, L. Chen, and Z. Lu. An improvement design of groove-wound clothing on the licker-in—Part 1. Theoretical analysis and modeling validation. *Textile Research Journal*, 89(5):782–790, 2019.

[22] M. Hengstermann, N. Raithel, A. Abdkader, M. M. B. Hasan, and C. Cherif. Development of new hybrid yarn construction from recycled carbon fibers for high performance composites. Part-1: basic processing of hybrid carbon fiber/polyamide 6 yarn spinning from virgin carbon fiber staple fibers. *Textile Research Journal*, 86(12):1307–1317, 2016.

[23] C. R. Holloway, D. J. Smith, and R. J. Dyson. Linear Rayleigh–Bénard stability of a transversely isotropic fluid. *European Journal of Applied Mathematics*, 30(4):659–681, 2019.

[24] P. Howell, G. Kozyreff, and J. R. Ockendon. *Applied Solid Mechanics*, pages 413–417. Number 43. Cambridge University Press, 2009.

[25] P. Howell, G. Kozyreff, and J. R. Ockendon. *Applied Solid Mechanics*, pages 187–195. Number 43. Cambridge University Press, 2009.

[26] J. Huang, X. Guo, B. F. Edwards, and A. D. Levine. Cut-off model and exact general solutions for fragmentation with mass loss. *Journal of Physics A: Mathematical and General*, 29(23):7377, 1996.

[27] The MathWorks Inc. MATLAB version: R2023a, 2023.

[28] Wolfram Research, Inc. Mathematica, Version 13.3. Champaign, IL, 2023.

[29] S. Jlassi, F. Berthet, and G. Bernhart. Investigation of mechanical properties of nonwoven second generation composite material elaborated through a mixture of carbon fibers and filament lengths. In *Proceedings of the ECCM18—18th European Conference on Composite Materials, Athens, Greece*, 2018.

[30] M. F. Khurshid, A. Abdkader, and C. Cherif. Processing of waste carbon and polyamide fibres for high-performance thermoplastic composites: influence of carding parameters on fibre orientation, fibre length and sliver cohesion force. *Journal of the Textile Institute*, 111(9):1277–1287, 2020.

[31] M. F. Khurshid, M. Hasan, A. Abdkader, and C. Cherif. Processing of waste carbon and polyamide fibers for high performance thermoplastic composites: A

novel manufacturing technology for unidirectional tapes structure. *Journal of Industrial Textiles*, 51(4):7256S–7276S, 2022.

[32] M. F. Khurshid, M. Hengstermann, M. Hasan, A. Abdkader, and C. Cherif. Recent developments in the processing of waste carbon fibre for thermoplastic composites–a review. *Journal of Composite Materials*, 54(14):1925–1944, 2020.

[33] M. F. Khursid, A. Abdkader, and C. Cherif. Process development for uni directional tape structure based on recycled carbon fiber and thermoplastic fibers for fiber reinforced plastics. In *Proceedings of the 19th World Textile Conference-Autex 2019*, 2019.

[34] T. Komori and K. Makishima. Numbers of fiber-to-fiber contacts in general fiber assemblies. *Textile Research Journal*, 47(1):13–17, 1977.

[35] T. Komori and K. Makishima. Estimation of fiber orientation and length in fiber assemblies. *Textile Research Journal*, 48(6):309–314, 1978.

[36] C. F. J. Kuo, Y. C. Chou, and T. Y. Lin. Automatic control of roller carding machine. part i: Modeling and validation of roller carding machine. *Textile Research Journal*, 82(1):3–10, 2012.

[37] M. E. M. Lee. *Mathematical models of the carding process*. PhD thesis, University of Oxford, 2001.

[38] M. E. M. Lee and H. Ockendon. A continuum model for entangled fibres. *European Journal of Applied Mathematics*, 16(2):145–160, 2005.

[39] M. E. M. Lee and H. Ockendon. The transfer of fibres in the carding machine. *Journal of Engineering Mathematics*, 54:261–271, 2006.

[40] R. Levien. The elastica: a mathematical history. Technical report, Electrical Engineering and Computer Sciences University of California at Berkeley, 2008.

[41] B. Li and N. A. G. Johnson. Limits to the speed of fibre withdrawal from a fibre assembly or pin bed. *The Journal of The Textile Institute*, 88(4):428–439, 1997.

[42] A. E. H. Love. *A Treatise on the Mathematical Theory of Elasticity*. Cambridge University Press, 1927.

[43] G. Maltin and M. Mayer Jr. Simplified analysis of the disentanglement of a fiber clump. *Textile Research Journal*, 41(8):685–691, 1971.

[44] J. W. Obreimoff. The splitting strength of mica. *Proceedings of the Royal Society of London. Series A, Containing Papers of a Mathematical and Physical Character*, 127(805):290–297, 1930.

[45] G. Oliveux, L. O. Dandy, and G. A. Leeke. Current status of recycling of fibre reinforced polymers: Review of technologies, reuse and resulting properties. *Progress in Materials Science*, 72:61–99, 2015.

[46] A. M. Ostrowski. On the remainder term of the Euler-Maclaurin formula. *Journal Für Die Reine Und Angewandte Mathematik*, 239–240:268–286, 1969.

[47] T. G. Rogers. Squeezing flow of fibre-reinforced viscous fluids. *Journal of Engineering Mathematics*, 23(1):81–89, 1989.

[48] C. M. Rooney, I. M. Griffiths, C. Brunner, J. Potter, M. Wood-Lee, and C. P. Please. Dynamics of particle chopping in blenders and food processors. *Journal of Engineering Mathematics*, 112(1):119–135, 2018.

[49] J. P. Rust and H. M. Gutierrez. Mathematical modeling and simulation for carding. *Textile Research Journal*, 64(10):573–578, 1994.

[50] J. Saha, J. Kumar, and S. Heinrich. On the approximate solutions of fragmentation equations. *Proceedings of the Royal Society A: Mathematical, Physical and Engineering Sciences*, 474(2209):20170541, 2018.

[51] L. F. Shampine, M. W. Reichelt, and A. J. Kierzenka. Solving index-1 DAEs in MATLAB and Simulink. *SIAM Review*, 41(3):538–552, 1999.

[52] M. Smoluchowski. Mathematical theory of the kinetics of the coagulation of colloidal solutions. *Zeitschrift für Physikalische Chemie*, 92:129–168, 1917.

[53] A. J. M. Spencer. Deformations of fibre-reinforced materials. *Oxford Science Research Papers*, 1972.

[54] A. J. M. Spencer. Fibre-streamline flows of fibre-reinforced viscous fluids. *European Journal of Applied Mathematics*, 8(2):209–215, 1997.

[55] V. Stadnichuk, A. Bodrova, and N. Brilliantov. Smoluchowski aggregation–fragmentation equations: Fast numerical method to find steady-state solutions. *International Journal of Modern Physics B*, 29(29):1550208, 2015.

[56] D. Vella, A. Boudaoud, and M. Adda-Bedia. Statics and inertial dynamics of a ruck in a rug. *Physical Review Letters*, 103(17):174301, 2009.

[57] S. Wall and C. Elvingson. Equilibrium and kinetic properties of mixed micelles. *The Journal of Physical Chemistry*, 89(12):2695–2705, 1985.

[58] C. Y. Wang. A critical review of the heavy elastica. *International Journal of Mechanical Sciences*, 28(8):549–559, 1986.

[59] X. Wang and N. A. G. Johnson. Investigation of combing forces. part iii: Disentangling twisted fibres - theory. *Journal of the Textile Institute*, 83(2):218–229, 1992.

[60] J. A. D. Wattis. Exact solutions for cluster-growth kinetics with evolving size and shape profiles. *Journal of Physics A: Mathematical and General*, 39(23):7283–7298, 2006.

[61] J. A. D. Wattis. An introduction to mathematical models of coagulation–fragmentation processes: a discrete deterministic mean-field approach. *Physica D: Nonlinear Phenomena*, 222(1-2):1–20, 2006.

[62] J. A. D. Wattis and P. V. Coveney. Sequence selection during copolymerization. *The Journal of Physical Chemistry B*, 111(32):9546–9562, 2007.

[63] J. A. D. Wattis and J. R. King. Asymptotic solutions of the Becker-Döring equations. *Journal of Physics A: Mathematical and General*, 31(34):7169, 1998.

[64] E. W. Weisstein. Least squares fitting. *https://mathworld. wolfram. com/*, 2002.

[65] L. D. Wibberly. *Modeling fiber dynamics and transport in the carding process.* PhD thesis, University of Virginia, 1999.

[66] L. D. Wibberly and W. W. Roberts Jr. Modeling the diffusive transport of bulk fiber mass in a card. *Textile Research Journal*, 67(4):296–308, 1997.

[67] E. J. Wood. 5. Principles of wool carding. *The Australian Wool Education Trust*, 2009.

[68] E. J. Wood, P. Stanley-Boden, and G. A. Carnaby. Fiber breakage during carding: Part ii: Evaluation. *Textile Research Journal*, 54(7):419–424, 1984.

[69] B. Xiao, T. Zaima, K. Shindo, T. Kohira, J. Morisawa, Y. Wan, G. Yin, I. Ohsawa, and J. Takahashi. Characterization and elastic property modeling of discontinuous carbon fiber reinforced thermoplastics prepared by a carding and stretching system using treated carbon fibers. *Composites Part A: Applied Science and Manufacturing*, 126:105598, 2019.

[70] R. M. Ziff. New solutions to the fragmentation equation. *Journal of Physics A: Mathematical and General*, 24(12):2821, 1991.

[71] R. M. Ziff and E. D. McGrady. Kinetics of polymer degradation. *Macromolecules*, 19(10):2513–2519, 1986.